Torsional Alfvén waves in the Earth's core

Grace Alexandra Cox

Submitted in accordance with the requirements for the degree of
Doctor of Philosophy

The University of Leeds
School of Earth and Environment

August 2015

The candidate confirms that the work submitted is her own, except where work that has formed part of jointly-authored publications has been included. The contribution of the candidate and the other authors to this work has been explicitly indicated overleaf. The candidate confirms that appropriate credit has been given within the thesis where reference has been made to the work of others.

To my family

Declaration

This research has been carried out by a team which has included Grace Cox, Phil Livermore, Jon Mound and Steve Tobias. Chapter 1 contains some material from the publication

- **Cox, G. A., and Brown, W. J.** (2013). Rapid dynamics of the Earth's core. *Astronomy & Geophysics*, 54(5), 5-32.

Both Will Brown and Grace Cox wrote the article; only material written by Grace Cox is contained within this thesis.

Chapters 2 and 3 contain material from the publication

- **Cox, G. A., Livermore, P. W., and Mound, J. E.** (2014) Forward models of torsional waves: dispersion and geometric effects. *Geophysical Journal International*, 196(3), 1311-1329.

In this work, Grace Cox wrote the necessary codes, conducted the simulations and wrote the article. Phil Livermore and Jon Mound undertook advisory roles.

The work contained in chapter 4 made use of a code written by Will Brown, which was described in the article cited as Brown et al. (2013).

Acknowledgements

First and foremost, I would like to express my gratitude to my supervisors Phil Livermore and Jon Mound, who have been incredibly generous with their time, support and sound advice. I am also grateful to you both for your thorough proofreading of many documents over the years, including this manuscript. I must also extend my thanks to Chris Davies and Steve Tobias, who have always been willing to provide academic wisdom, encouragement and a sympathetic ear. It was through your kindness, understanding and persistence that I have completed this thesis.

The Deep Earth research group at Leeds has provided an intellectually stimulating environment for my studies, a constant source of explanations and great ideas. The vast knowledge contained within the group has enriched, amazed and, at times, utterly confused me! It has been an honour and a privilege to work with you for the last few years. Thank you all.

To my co-conspirator Will Brown, I offer my thanks for answering many, many daft questions and for providing me with his jerk detection code. Your continued good humour and patience is much appreciated. In the same vein, I must thank Richard Rigby for his assistance with all things IT-related, and for the hours he has spent troubleshooting my computer after I have 'broken things'.

This work was funded by a NERC studentship. I am also grateful for funding from the RAS, AGU, SEDI and CIDER, which has permitted my attendance at various conferences and workshops. I would like to thank the members of the Geodynamo group at ISTerrre, Grenoble for their hospitality during my visit.

Many friends and colleagues have helped and supported me throughout my years at Leeds. I will not list their names here, as I would undoubtably omit someone important. Suffice to say, you know who you are... Last, but not least, I thank my family. Your continued love and support has made this possible. I doubt that I will ever be able to convey my appreciation fully, but I owe you all my eternal gratitude.

Abstract

Torsional Alfvén waves are theoretically predicted to exist in Earth's outer core, have been inferred from geophysical data and observed in geodynamo simulations. They provide an indirect means of investigating core dynamics, core properties and core-mantle coupling mechanisms. In this study, we produce 1-D forward models of torsional waves in Earth's core and study the wave-induced secular variation (SV).

We find that torsional waves undergo significant dispersion during propagation that arises due to their geometric setting, with long wavelength features being more dispersive than short wavelength features. Other key propagation features observed in our models are phase shifts at Earth's rotation axis, low amplitude wakes trailing behind sharply defined pulses, reflections from the tangent cylinder and internal wave reflections caused by strong magnetic field gradients. These combined dispersive effects may lead to difficulties in resolving the excitation mechanism of any torsional waves identified in geophysical data.

Fast torsional waves with amplitudes and timescales consistent with a recent study of the 6 yr ΔLOD signal (Gillet et al., 2010) induce very rapid, small (maximum $\sim$2 nT/yr at Earth's surface) SV signals that likely could not be resolved in observations of the Earth's SV. Slow torsional waves with amplitudes and timescales consistent with, for example, Zatman & Bloxham (1997), Hide et al. (2000) produce larger SV signals that reach amplitudes of $\sim$20 nT/yr at Earth's surface. We applied the two-part linear regression jerk detection method developed by Brown et al. (2013) to the SV induced by slow torsional waves, using the same parameters as used on real SV, which identified several synthetic jerk events. As the local magnetic field morphology dictates which regions are sensitive to zonal core flow, and not all regions are sensitive at the same time, the modelled waves are not able to induce global contemporaneous jerk events such as that observed in 1969. The synthetic jerks are only observed on regional scales and generally occur in a single SV component. Also, the identified events are periodic due to waves passing beneath locations periodically and the SV signals are smoothly varying. These smooth signals are more consistent with the geomagnetic jerks envisaged by Demetrescu & Dobrica (2005, 2014) than the sharp 'V' shapes that are typically associated with geomagnetic jerks.

Contents

List of Figures **vii**

1 Introduction **1**
1.1 Overview . . . 1
1.2 Earth's deep interior . . . 2
1.3 The geomagnetic field and its source region . . . 4
1.4 Internal magnetic field generation . . . 12
1.4.1 General equations . . . 12
1.4.2 Taylor's constraint . . . 16
1.4.3 The torsional wave equation . . . 19
1.5 Torsional waves in the core . . . 20
1.6 Torsional waves in geodynamo models . . . 25
1.7 Aims and structure of the thesis . . . 29

2 1-D modelling: numerical methods **31**
2.1 Analytic solutions to simplified wave equations . . . 32
2.1.1 1-D wave equation in Cartesian coordinates . . . 32
2.1.2 1-D torsional waves in a cylinder . . . 33
2.2 Numerical schemes . . . 36
2.2.1 Normal mode projections . . . 36
2.2.1.1 Convergence testing . . . 37
2.2.2 Finite difference codes . . . 44
2.2.2.1 The second-order staggered leapfrog method . . . 47
2.2.2.2 The third-order Adams Bashforth method . . . 49
2.3 Regularity and boundary conditions . . . 50
2.4 Benchmarking . . . 53
2.4.1 1-D 'wave on a string' benchmark . . . 53
2.4.2 Torsional waves in a cylinder . . . 56
2.5 Code geometries . . . 64
2.6 Magnetic field profiles . . . 64

3 1-D modelling: torsional wave propagation 67
3.1 Parameters and scalings 67
3.2 Model i: torsional waves in a cylinder 68
3.3 Model ii: torsional waves in a sphere 71
3.4 Model iii: torsional waves in a spherical shell 76
3.5 Comparision 77
3.6 Dispersion 79
3.7 Model iv: torsional waves in a magnetic field with spatially varying $\{B_s^2\}$ 83
3.8 Local wave speed 85
3.9 The failure of Huygens' principle and dispersion in 2-D 87
3.10 Phase shift at the boundaries 90
3.11 Implications for torsional waves in the Earth's core 96

4 Geophysical signatures of torsional waves 99
4.1 Torsional waves and geomagnetic jerks 100
4.2 Method 102
4.3 Background magnetic fields 107
4.4 Benchmarking and resolution testing 112
4.5 SV patterns 116
4.6 Synthetic observatory data 124
4.7 Discussion and conclusions 142

5 Concluding remarks 145
5.1 Conclusions 145
5.2 Future extensions 149

References 151

Appendix A Derivation of the torsional wave equation 161

Appendix B Synthetic SV series and jerk results 167

List of Figures

1.1 A 1-D density structure of the Earth according to the Preliminary Reference Earth Model (PREM) of Dziewonski & Anderson (1981). The left axis gives depth in km, the right axis gives pressure in GPa, the upper horizontal axis gives seismic wave velocity in km/s for S- and P- waves and the lower horizontal axis gives density in 1000 kg/m^3. Figure taken from Romanowicz (2008). 3

1.2 The radial magnetic field in 2010 at (a) Earth's surface and (b) Earth's CMB according to the COV-OBS model (Gillet et al., 2013). Red represents positive magnetic field (outwards) and blue represents negative magnetic field (inwards). The maps are in Robinson projection and the scales are in (a) nT and (b) µT. 10

1.3 The radial secular variation in 2010 at (a) Earth's surface and (b) Earth's CMB according to the COV-OBS model (Gillet et al., 2013). Red represents positive SV and blue represents negative SV. The maps are in Robinson projection and the scales are in (a) nT/yr and (b) µT/yr. . . 11

1.4 Vertical (meridional) slices through the core. (a) Geometry of the geostrophic cylinders (GCs) defined in a cylindrical coordinate system. The symbols s, ϕ and z describe, respectively, radial distance from the rotation axis, azimuth and height. The cylinder half height is denoted z_T. All of the fluid on the same cylindrical surface of radius s has the same velocity $u_\phi(s)$. After Dumberry (2009). (b) The Earth's core is divided into three regions. I) The region of the outer core (OC) that is outside the tangent cylinder. II) The region of the outer core that lies inside the tangent cylinder and above the inner core (IC). III) The region of the outer core that lies inside the tangent cylinder and below the inner core. The tangent cylinder is shown as a dashed line between region I and regions II and III. 17

1.5 Torsional waves: azimuthal accelerations of rigid coaxial cylindrical surfaces. Each cylindrical surface moves with a different speed and is coupled to adjacent surfaces by the radial magnetic field B_s. Note that cylinder height decreases with increasing distance from the rotation axis. 20
1.6 The axisymmetric, equatorially symmetric part of decadal geostrophic core flow, inferred from secular variation at the CMB (Zatman & Bloxham (1997)). The colour scale is in km/yr; red represents positive velocity and blue represents negative velocity. 22
1.7 Representation of core angular momentum of 20 cylindrical shells as a function of latitude. The two peaks in mid-latitude coincide with the two geomagnetic jerk events that occurred during the studied interval (1912 and 1969). Based on the observed propagation pattern, Hide et al. (2000) suggested that the signal is transmitted from the equatorial to the polar regions. Taken from Hide et al. (2000). 23
1.8 (a) Comparison of bandpass-filtered ΔLOD time series with a six-year signal. The green line is observed LUNAR97 data, the black line is predicted core flow models and the red line is the result of the torsional wave assimilation of the flow coefficients (b) Time versus cylindrical radius map of bandpass-filtered angular velocity. The colour scale ranges between -0.4 km/yr (blue) and +0.4 km/yr (yellow) with contours every 0.02 km/yr. The observed six year signal is carried by wave-like patterns travelling from the tangent cylinder (the horizontal dashed black line at $s = 0.35$) to the outer core equator ($s = 1$). Taken from Gillet et al. (2010). 24
1.9 Velocity of geostrophic cylinders during the time interval in model E6 of Wicht & Christensen (2010). The time averaged velocity has been subtracted for each cylinder to highlight faster variations. White lines indicate the path waves should take when propagating with the Alfvén velocity. 26
1.10 Taylorisation measure during the selected time interval in model E6 of Wicht & Christensen (2010). 27
1.11 Contour plot of azimuthal velocity, as a function of time and cylindrical radius, showing torsional waves propagating from the tangent cylinder at the predicted Alfvén speed, from Teed et al. (2013). 27
1.12 Contour plot of azimuthal velocity, as a function of time and cylindrical radius, showing torsional waves propagating at the predicted Alfvén speed in four different models. The fifth model (e), is included as an example of a model in which no torsional waves were observed. Taken from Teed et al. (2015). 28

2.1 The absolute magnitude of the coefficients of the first 100 normal modes, $|c_m|$, for the projection of the initial profile given by equation (2.29) onto sine functions. 39
2.2 The L^2-norm, given by equation (2.28), of the difference between a projection of the initial profile described by equation (2.29) onto a certain number of sine modes, n, and a projection onto $n+5$ modes. The values on the horizontal axis show the lower resolution projection. For example, the leftmost data point shows the norm of the difference between a projection using 5 modes and a projection using 10 modes and the rightmost point shows the norm between projections using 100 and 105 normal modes. 40
2.3 The absolute magnitude of the coefficients of the first 100 normal modes, $|b_m|$, for the projection of the initial profile given by equation (2.30), defined as a function of s in cylindrical geometry, onto Bessel functions. 42
2.4 The L^2-norm, given by equation (2.31), of the difference between a projection of the initial profile described by equation (2.30) onto a certain number of Bessel modes, n, and a projection onto $n+5$ modes. The values on the horizontal axis show the lower resolution projection. For example, the leftmost data point shows the norm of the difference between a projection using 5 modes and a projection using 10 modes and the rightmost point shows the norm between projections using 100 and 105 normal modes. 43
2.5 The grid on which wave equations are discretised when using the staggered leapfrog finite difference scheme. Note that the space and time mesh points are shifted with respect to each other by half an interval. . 48
2.6 Profiles of the velocity Ψ of a 'wave on a string' during its evolution with no-slip boundary conditions applied at both ends of the domain. The red continuous line represents the normal mode (analytic) solution to the wave equation and the blue crosses represent the results obtained using an FD numerical scheme. The wave amplitude and the time have no intrinsic scale. 58
2.7 Contour plot of the velocity Ψ of a 'wave on a string' with no-slip boundary conditions applied at both ends, with time on the horizontal axis and x on the vertical axis. Red corresponds to positive velocity and blue corresponds to negative velocity. The wave group speed c is equal to 1 in this model. 59

2.8 Contour plot of the velocity of a 'wave on a string' with stress-free boundary conditions applied at both ends, with time on the horizontal axis and x on the vertical axis. Red corresponds to positive velocity and blue corresponds to negative velocity. The wave group speed c is equal to 1 in this model. 60
2.9 Profile of the velocity u_ϕ of a torsional wave propagating in a cylinder of unit radius. The red continuous line represents the normal mode (analytic) solution to the wave equation and the blue crosses represent the results obtained using the AB3 FD scheme. The wave amplitude has no intrinsic scale. 62
2.10 Contour plot of the velocity u_ϕ of torsional waves in a cylinder of unit radius, with time on the horizontal axis and cylindrical radius on the vertical axis. Red corresponds to positive velocity and blue corresponds to negative velocity. The no-slip condition was imposed on the outer boundary. 63
2.11 The spatially varying $\{B_s^2\}$ profile used in the full sphere model (iv). . . 66

3.1 Contour plot of the velocity u_ϕ of torsional waves in a cylinder, with time on the horizontal axis and cylindrical radius on the vertical axis. Red corresponds to positive velocity and blue corresponds to negative velocity. The two vertical lines show the times at which profiles are shown in Figs. 3.3 and 3.4 (one year before and one year after the waves reflect from the boundaries). 69
3.2 Velocity profiles of the waves at the start of evolution (blue), after one core transit (green), after two core transits (red) and after three core transits (cyan) in a cylinder. 70
3.3 Velocity profiles of the waves one year before (a', blue) and after (b', red) reflection at the outer boundary of a cylinder of radius r_c. The annotations correspond to those in Fig. 3.1 and the times at which the profiles were taken are shown in that figure as two vertical black lines. . 70
3.4 Velocity profiles of the waves one year before (a and b, blue) and after (c and d, red) reflection at the outer boundary of a cylinder of radius r_c. The annotations correspond to those in Fig. 3.1 and the times at which the profiles were taken are shown in that figure as two vertical black lines. 71

3.5 Contour plot of the velocity u_ϕ of torsional waves in a full sphere, with time on the horizontal axis and cylindrical radius on the vertical axis. Red corresponds to positive velocity and blue corresponds to negative velocity. The horizontal black dashed line represents the location of the tangent cylinder at $s = 1221$ km to aid comparison with the spherical shell case in Fig. 3.11. The two vertical lines show the times at which profiles are shown in Figs. 3.7 and 3.8 (one year before and one year after the waves reflect from the boundaries). 72
3.6 Velocity profiles of the waves at the start of evolution (blue), after one core transit (green), after two core transits (red) and after three core transits (cyan) in a full sphere. 72
3.7 Velocity profiles of the waves one year before (a', blue) and after (b', red) reflection at the equator of the core mantle boundary ($s = r_c$) in a full sphere. The annotations correspond to those in Fig. 3.5 and the times at which the profiles were taken are shown in that figure as two vertical black lines. 73
3.8 Velocity profiles of the waves one year before (a and b, blue) and after (c and d, red) reflection at the rotation axis in a full sphere. The annotations correspond to those in Fig. 3.5 and the times at which the profiles were taken are shown in that figure as two vertical black lines. 74
3.9 Contour plot of the angular momentum density $u_\phi s^2 z_T$ of torsional waves in a full sphere, with time on the horizontal axis and cylindrical radius on the vertical axis. Red corresponds to positive angular momentum density and blue corresponds to negative angular momentum density. . . 75
3.10 The total angular momentum at each time step of the full sphere model, normalised by the angular momentum of the initial profile. 75
3.11 Contour plot of the velocity u_ϕ of torsional waves in an equatorially symmetric spherical shell, with time on the horizontal axis and cylindrical radius on the vertical axis. Red corresponds to positive velocity and blue corresponds to negative velocity. The horizontal black dashed line represents the location of the tangent cylinder at $s = 1221$ km. 76
3.12 Velocity profiles of the waves at the start of evolution (blue), after one core transit (green), after two core transits (red) and after three core transits (cyan) in an equatorially symmetric spherical shell. 77

3.13 Contour plot of the difference in velocity u_ϕ when full sphere velocities were subtracted from the spherical shell case. Time is on the horizontal axis and cylindrical radius is on the vertical axis. Red corresponds to positive velocity differences and blue corresponds to negative velocity differences. The horizontal black dashed line represents the location of the tangent cylinder at $s = 1221$ km. Note the weak positive reflection (in yellow) from the tangent cylinder at time T$\sim$0.6 years. 78

3.14 Contour plots of α, as defined by equation (3.3), over one complete transit time (6 years) in the full sphere model. Black regions ($\alpha < 1$) are locally 'dispersive', since term 1 is smaller than at least one of the other terms. Coloured regions are locally 'non-dispersive', with the magnitude of term 1 at least equal to that of the other terms in the blue regions and exceeding the other terms by at least a factor of 10 in the red regions. White regions show areas where the terms are very small and calculating the ratio is numerically intractable. 80

3.15 The percentage of the domain that is non-dispersive over one core transit time (6 years) in the full sphere (crosses) and shell (circles) geometries according to the four different thresholds on α: 1 (blue), 2 (green), 5 (red) and 10 (cyan) as a function of initial pulse width. Lower σ values correspond to narrower initial velocity profiles. 82

3.16 Contour plot of the velocity u_ϕ of torsional waves in a full sphere with the steady background magnetic field shown in Fig. 2.11, with time on the horizontal axis and cylindrical radius on the vertical axis. Red corresponds to positive velocity and blue corresponds to negative velocity. . 83

3.17 Contour plots of α, as defined by equation (3.5), over one complete transit time (6 years) in the full sphere model with varying $\{B_s^2\}$. Black regions ($\alpha < 1$) are locally 'dispersive', since term 1 is smaller than at least one of the other terms. Coloured regions are locally 'non-dispersive', with the magnitude of term 1 at least equal to that of the other terms in the blue regions and exceeding the other terms by at least a factor of 10 in the red regions. White regions show areas where the terms are very small and calculating the ratio would therefore be numerically intractable. 85

3.18 Contour plots of the magnitude of the ratio of term 1 to (a) term 2 (b) term 3 (c) term 4 and (d) term 5, from the RHS of equation (3.2), over one complete transit time (6 years) in the full sphere model. Black regions are locally 'dispersive', since the relevant term is larger than term 1. Coloured regions are locally 'non-dispersive', with the magnitude of term 1 at least equalling that of the other term in the blue regions and exceeding the other term by at least a factor of 10 in the red regions. White regions show areas where the terms are very small and calculating the ratio is numerically intractable. 89

3.19 (a) Comparison of the outgoing wave in a cylinder of radius 1 at time $t = 1$ (after reflection at the rotation axis) according to the normal mode solution given by equation (3.10) (blue line) and the phase shifted asymptotic approximation to the normal mode solutions, given by equations (3.12) and (3.16) (red line). (b) Comparison of the incoming wave in a cylinder of radius 1 at time $t = 1$ (after reflection at the outer boundary $s = 1$) according to the normal mode solution given by equation (3.10) (blue line) and the phase shifted asymptotic approximation to the normal mode solutions, given by equations (3.12) and (3.16) (red line). . 93

3.20 (a) Velocity profiles of the waves one year before (blue) and after (red) reflection at the rotation axis in the full sphere model (ii). The annotations correspond to those in Fig. 3.5 and the times at which the profiles were taken are shown in that figure as two vertical black lines. The black dashed line is the Hilbert transform of the incoming wave (the blue line). Note that the Hilbert transform is somewhat similar to the outgoing wave (the red line). (b) Velocity profiles of the waves one year before (blue) and after (red) reflection at the rotation axis in a full sphere model with a narrow initial profile ($\sigma = 0.01$). The black dashed line is the Hilbert transform of the incoming wave (the blue line). Note the increased similarity of the Hilbert transform to the outgoing wave (the red line). 95

4.1 The general morphology of a geomagnetic jerk as seen in, from left to right, the magnetic field, the SV (first time-derivative of the field), the SA (second time-derivative of the field) and the impulse (third time-derivative of the field). 101

4.2 The Z ($= -B_r$) component of the geomagnetic field at the CMB according to the COV-OBS field model Gillet et al. (2013) (a) Snapshot of the field in 2010 (b) 50 year time-averaged field (1960-2010) and (c) 130 year time-averaged field (1840-2010). The scale is in μT; red indicates positive field (entering the core) and blue indicates negative field (exiting the core). 110
4.3 The (a) X, (b) Y and (a) Z components of the geomagnetic field at the CMB in 2010 according to the COV-OBS field model Gillet et al. (2013). The Gauss coefficients up to spherical harmonic degree 14 were used to calculate the field. The scale is in μT; red indicates positive field and blue indicates negative field. 111
4.4 The initial wave profile given by equation (2.60) in cylindrical coordinates mapped onto 100 collocation points (Gauss nodes) for GLQ (top) and the spatial power spectrum of the velocity (bottom). The spectrum has no units because the velocity has no intrinsic scale. 114
4.5 A torsional wave that has split into two pulses, see $t = 2$ yr of Fig. 3.5 in §3.3, mapped onto 100 collocation points (Gauss nodes) for GLQ (top) and the spatial power spectrum of the velocity (bottom). The spectrum has no units because the velocity has no intrinsic scale. 115
4.6 (a) The ϕ-derivative of the radial component of the geomagnetic field at the CMB in 2010 according to the COV-OBS field model Gillet et al. (2013) (b) The radial SV, $\dot{b}_r$, induced by the interaction of the field shown in (a) with a bulk rotation of the core fluid with respect to the mantle of -0.005 rad/yr ($-0.2864°$/yr) (c) The radial SV of the geomagnetic field at the CMB in 2010 according to the COV-OBS field model. The scale is in μT/yr; red indicates more positive field (more exiting the core) and blue indicates more negative field (more entering the core). 120
4.7 The spatial power spectrum, evaluated at the CMB radius, of torsional wave-induced SV. The waves in this model had a core transit time of 6 yr and an initial pulse amplitude of 0.4 km/yr. 121
4.8 Maps of the radial component of the SV induced by torsional waves with a 6 yr core transit time and an initial wave pulse amplitude of 0.4 km/yr. The SV is evaluated at the CMB and the colour scale is from -150 nT/yr to 150 nT/yr. The torsional wave profile is shown on the right, with cylindrical radius (km) on the horizontal axis and zonal velocity (km/yr) on the vertical axis. 123
4.9 The locations of the 24 magnetic observatories at which synthetic time series of wave-induced SV will be produced. 125

4.10 Time series of the z component of the SV induced at the CMB by torsional waves with a 6 yr core transit time and an initial pulse amplitude of 0.4 km/yr at (top) Bangui, (middle) Eskdalemuir and (bottom) Port Stanley. 126
4.11 Time series of the z component of the SV induced at Earth's surface by torsional waves with a 6 yr core transit time and an initial pulse amplitude of 0.4 km/yr at (top) Bangui, (middle) Eskdalemuir and (bottom) Port Stanley. 127
4.12 Contour plot of the velocity u_ϕ of torsional waves in a full sphere, with time on the horizontal axis and cylindrical radius on the vertical axis. Red corresponds to positive velocity and blue corresponds to negative velocity. The colour scale is from -6 km/yr to 6 km/yr; the initial wave pulse had an amplitude of 4 km/yr and the waves have a 60 yr core transit time. 130
4.13 Maps of the x component of the SV induced by torsional waves with a 60 yr core transit time and an initial wave pulse amplitude of 4 km/yr. The SV is evaluated at the Earth's surface and the colour scale is from -10 nT/yr to 10 nT/yr. The torsional wave profile is shown on the right, with cylindrical radius (km) on the horizontal axis and zonal velocity (km/yr) on the vertical axis. 135
4.14 Maps of the y component of the SV induced by torsional waves with a 60 yr core transit time and an initial wave pulse amplitude of 4 km/yr. The SV is evaluated at the Earth's surface and the colour scale is from -20 nT/yr to 20 nT/yr. The torsional wave profile is shown on the right, with cylindrical radius (km) on the horizontal axis and zonal velocity (km/yr) on the vertical axis. 137
4.15 Maps of the z component of the SV induced by torsional waves with a 60 yr core transit time and an initial wave pulse amplitude of 4 km/yr. The SV is evaluated at the Earth's surface and the colour scale is from -25 nT/yr to 25 nT/yr. The torsional wave profile is shown on the right, with cylindrical radius (km) on the horizontal axis and zonal velocity (km/yr) on the vertical axis. 139
4.16 The spatial power spectrum, evaluated at Earth's surface, of torsional wave-induced SV. The waves in this model had a core transit time of 60 yr and an initial pulse amplitude of 4 km/yr. 140

4.17 The top panel of these figures shows a time series of a single component of the SV signal (in nT/yr) at (a) Hermanus and (b) San Juan throughout the 200 years of the torsional wave forward model shown in Fig. 4.12. The observatory name and window length are displayed at the top of each subfigure, and identified jerk events are shown as a red 'V' shape fitted to the SV series. The bottom panel shows the calculated PDF from the two-part linear regression, with the chosen threshold cut-off value of 0.2 shown as a green line. The positive and negative errors on the PDF are filled in underneath the PDF curve in red and black, respectively . . 141

A.1 Simplified geometry of the core 164

B.1 The z component of the SV induced at the CMB by torsional waves with a 6 yr core transit time and an initial pulse amplitude of 0.4 km/yr. Time is on the horizontal axis, SV is on the vertical axis and the observatory name is at the top of each subfigure. The locations of the observatories are shown in Fig. 4.9. 174

B.2 Jerk identification in the $\dot{x}$ component at Earth's surface with a 5 yr window. 174

B.3 Jerk identification in the $\dot{y}$ component at Earth's surface with a 5 yr window. 176

B.4 Jerk identification in the $\dot{z}$ at Earth's surface component with a 5 yr window. 177

B.5 Jerk identification in the $\dot{x}$ component at Earth's surface with a 10 yr window. 180

B.6 Jerk identification in the $\dot{z}$ component at Earth's surface with a 10 yr window. 183

B.7 Jerk identification in the $\dot{x}$ component at Earth's surface with a 15 yr window. 187

B.8 Jerk identification in the $\dot{z}$ component at Earth's surface with a 15 yr window. 190

B.9 Jerk identification in the $\dot{x}$ component at Earth's surface with a 20 yr window. 192

B.10 Jerk identification in the $\dot{z}$ component at Earth's surface with a 20 yr window. 194

Chapter 1

Introduction

1.1 Overview

Earth's magnetic field has existed for at least the last 3.5 billion years and is the largest feature of our planet. Extending from within the solid inner core to the bow shock, where it meets the solar wind approximately 90 000 km from Earth's surface, it shields Earth's inhabitants and orbiting satellites from potentially harmful solar radiation (e.g. Cole, 2003). Observations show striking spatial and temporal variations in the strength of this protective shield. The fluctuations in time, called secular variation (SV), occur on a wide range of time scales, from daily interactions with the ionosphere to the millions of years between polarity reversals. Most SV at approximately annual or longer periods is associated with the geodynamo, the process that generates a large-scale self-sustaining magnetic field from fluid motion inside Earth's outer core (Larmor, 1919, Elsasser, 1946). Progress in understanding the dynamics of the core, and the associated signals in the magnetic field, is hindered by the fact that the core is too remote to be probed directly and that numerical dynamo simulations are unable to reach the relevant parameter regime due to computational limitations (Davies et al., 2011, King & Buffett, 2013). This thesis focusses on probing rapid outer core dynamics using torsional Alfvén waves, a type of magnetohydrodynamic (MHD) wave that is predicted to exist in Earth's core on decadal timescales, observed in dynamo models, and inferred from various geophysical datasets.

This chapter introduces the geomagnetic field and its source region to the reader, and provides the geophysical context for the work undertaken. Following a brief description

of the observed magnetic field and relevant core properties, continuous forms of the MHD equations are presented, along with a discussion of torsional wave theory. Next, an overview of torsional waves inferred from geophysical data and identified in previous numerical geodynamo simulations is provided. The chapter concludes with a list of the thesis aims and an outline of its structure.

1.2 Earth's deep interior

The structure and composition of Earth's interior cannot be measured directly; models are based on three major sources of information. First, the seismic profile of Earth and its interpretation (see Fig. 1.1), second, comparisons of primitive meteorite compositions and the known compositions of Earth's crust and mantle, and third, models of melting relationships and the behaviour of Earth minerals at high pressure and temperature. Whilst a range of interior models are permitted by the available data, the one that is most consistent with geochemical constraints and the seismological structure of the Earth comprises a silicate upper and lower mantle of similar composition and an Fe-Ni (iron-nickel) core containing between 5% and 15% of a low-atomic-weight element (e.g. Birch, 1964, McDonough & Sun, 1995). Proposed candidates for the light element in the core include silicon, sulphur, oxygen, hydrogen and carbon (e.g. Poirier, 1994, Li & Fei, 2003, Hirose et al., 2013). Seismologists in the early twentieth century used observations of a peculiar pattern in the distribution of shear wave (S-wave) arrivals after large earthquakes to deduce that the metallic core is molten (Oldham, 1906, Jeffreys, 1926). Further seismic observations by Lehmann (1936) revealed the existence of Earth's solid inner core, which is gradually crystallising outwards at a rate of approximately 0.3 mm/yr due to secular cooling of the whole planet (e.g. Shimizu et al., 2005).

A 1-D density structure of the Earth (e.g. Dziewonski & Anderson, 1981) is shown in Fig. 1.1, which shows a trend of increasing seismic velocity with increasing depth through the mantle. The upper green and brown layers represent the mantle; the seismic wave discontinuities at 410 km and 660 km arise due to phase transitions of mantle minerals at increasing pressures and temperatures (e.g. Shearer, 1995). The D" region in the lowermost mantle is thought to be a compositionally distinct boundary layer between the silicate mantle and the iron-nickel outer core, and possibly consists of

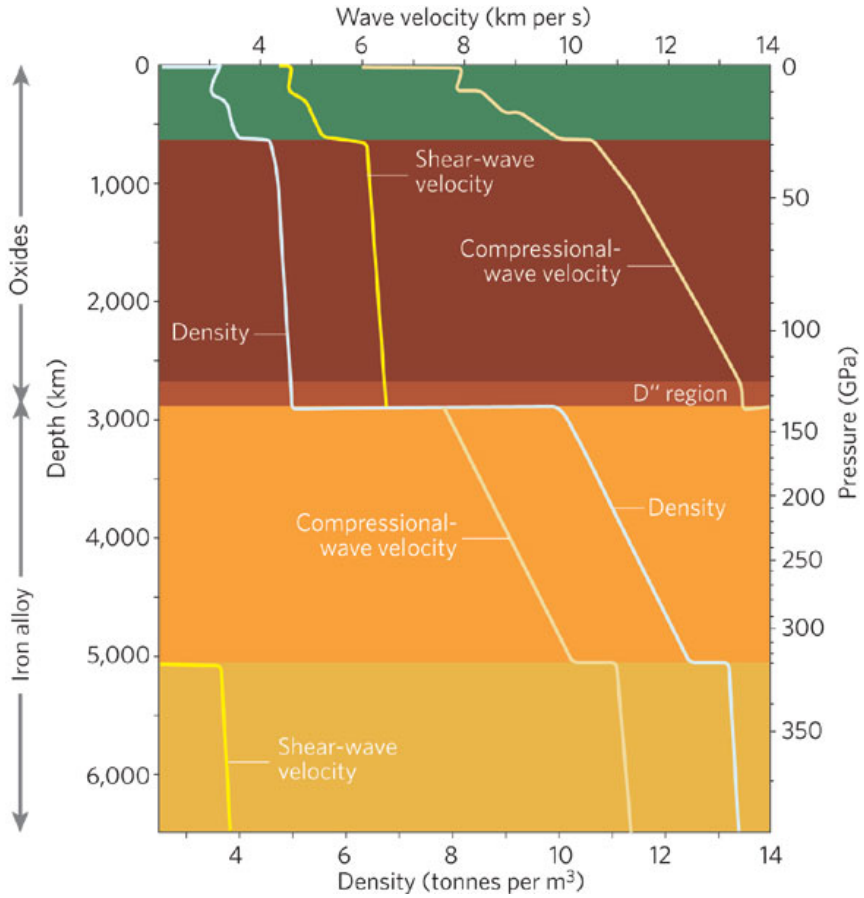

Figure 1.1: A 1-D density structure of the Earth according to the Preliminary Reference Earth Model (PREM) of Dziewonski & Anderson (1981). The left axis gives depth in km, the right axis gives pressure in GPa, the upper horizontal axis gives seismic wave velocity in km/s for S- and P- waves and the lower horizontal axis gives density in 1000 kg/m^3. Figure taken from Romanowicz (2008).

post-perovskite, which is a high-pressure phase of magnesium silicate (Murakami et al., 2004, Oganov & Ono, 2004, Iitaka et al., 2004). The two yellow-orange layers represent the outer and inner cores. The strong velocity contrast across the core mantle boundary (CMB) arises due to the phase change and the transition from silicate mantle rocks to the dense iron-nickel alloy of the core. The S-wave velocity goes to zero in the outer core because shear waves cannot be supported in a liquid. The density contrast at the inner core boundary (ICB) arises due to the phase change and because light elements are preferentially incorporated into the liquid phase upon crystallisation of the inner core (e.g. Alfè et al., 2000). This leaves an outer core fluid that is enriched in light element relative to the inner core, resulting in a denser Fe-Ni solid core.

At the high temperatures and pressures attained throughout Earth's core, an iron-

nickel alloy is thought to have a very low viscosity (de Wijs et al., 1998), comparable to that of water at room temperature and pressure, and recent estimates predict a very high electrical conductivity (Pozzo et al., 2012, Gomi et al., 2013). This recent upward revision of the conductivity estimates core has profound consequences for the our understanding of the core's thermal history and power requirements of the geodynamo, though these high values are still the subject of some debate (Zhang et al., 2015). The fluid in the core is likely undergoing vigorous convective motions due to both thermal and compositional sources (see Gubbins & Roberts, 1987). The thermal buoyancy sources arise because the liquid outer core is heated from below by the inner core and cooled from above by the mantle as the whole planet cools and latent heat is released at the ICB as the inner core slowly crystallises. Compositional buoyancy sources arise when the light elements are excluded from the inner core during crystallisation. These light elements are unstable near the ICB because they are less dense than the ambient fluid and so they rise up through the outer core. The combination of thermal and compositional buoyancy ensures that core convection is vigorous and thus the core is thought to be well-mixed.

Larmor (1919) first proposed that these fluid motions in Earth's electrically conducting outer core are responsible for the majority of the observed geomagnetic field by means of a dynamo mechanism, which converts the kinetic energy of the fluid into magnetic energy. Given an initial seed magnetic field, such as the interplanetary field, the moving conducting fluid in the core generates an electric field and an associated magnetic field. This magnetic field then interacts with the fluid motions, which then generate further electric and magnetic fields. In this way, a large-scale self-sustaining planetary magnetic field is generated and maintained against decay. In the next section, the method used to identify the source region of an observed magnetic field is described, along with a brief discussion of the structure of the observed geomagnetic field.

1.3 The geomagnetic field and its source region

Fixed ground-based measurements of the geomagnetic field have been made at the Earth's surface for several centuries, though spatial coverage was historically limited to primarily the northern hemisphere (see Jackson et al., 2000). The earliest measurements consisted of nautical logs, which recorded declination (the angle between

geographic and magnetic north). By the seventeenth century, these measurements were commonplace, and measurements of inclination (the angle between the magnetic field vector and the horizontal) became widespread in the eighteenth century. After the pioneering work of Gauss (1832), and his subsequent papers describing new instrumentation for magnetic observations, continuous measurements of the horizontal and total magnetic field vector intensities became widespread at land-based observatories (e.g. Gauss, 1834, 1839, Gauss & Weber, 1840). This resulted in a shift of the spatial bias of measurements from sea to land, though still in the northern hemisphere and Europe in particular. In the twentieth century, magnetic observatories adopted a new convention of measuring the X, Y and Z (north, east and vertically downwards, respectively) components of the magnetic field. In recent years, satellite measurements have provided high-precision magnetic data with excellent spatial and temporal coverage, albeit of limited duration. Notable satellite missions include MagSat (1979-1980), Ørsted (1990 to present), CHAMP (2000-2010) and the recently launched Swarm constellation of satellites (2013 to present). The observatory and satellite data are supplemented by less precise measurements of the remanent magnetic fields recorded in lake sediments and lavas, and in archaeological artefacts that can become magnetised as they cool from high temperatures. These palaeomagnetic measurements have lower temporal resolution, and uneven spatial coverage, but they provide evidence for the field's existence for at least the last 3.5 Ga (e.g. McElhinny & Senanayake, 1980, Biggin et al., 2011) and are key to understanding long-term geomagnetic field behaviour.

An observed planetary magnetic field is the superposition of several sources in the planetary environment ('external sources') and the planetary interior ('internal sources'). Examples of external sources include currents flowing in the ionosphere and magnetosphere, whilst internal sources include motion of an electrically conducting core, magnetisation of crustal rocks and induced currents in the planetary interior due to time-varying external magnetic fields (Olsen et al., 2010a). According to Gauss's mathematical theory of magnetic fields in a region containing no electric currents or moving charged particles ('source-free' regions), an observed magnetic field can be treated as a potential field (a solution to Laplace's equation) and separated into its internal and external contributions. The observed geomagnetic field can be treated as such a potential field if Earth's mantle is presumed to be a source-free region (i.e. electrically insulating). This is likely a valid assumption for most of the mantle, with the possi-

ble exception of the D" layer in the lowermost mantle (e.g. Shankland et al., 1993). Such mathematical analyses show that at least $\sim$ 97% of the field observed at the surface has an internal origin, except during periods of high solar activity when interactions between the solar wind and the ionosphere and magnetosphere are stronger than usual (Olsen & Stolle, 2012). Magnetised material in crustal rocks accounts for only a few percent of the observed field, on average, though the local crustal signal can reach hundreds or thousands of nanotesla (nT) close to the surface. For comparison, the internally-generated geomagnetic field varies from approximately $-65\,000$ nT to 65 000 nT at Earth's surface (see Fig. 1.2a).

The depth to the internal source region may be estimated using a method called magnetic sounding (Hide, 1978), which uses the spatial power spectrum of the observed internally generated magnetic field. The spatial power spectrum at Earth's surface is the squared magnitude of the magnetic field as a function of spherical harmonic degree

$$R_l = (l+1) \sum_{m=0}^{l} \left[\left(g_l^m\right)^2 + \left(h_l^m\right)^2 \right], \tag{1.1}$$

where l is the degree, m is the order and g_l^m and h_l^m are the Schmidt quasi-normalised spherical harmonic coefficients of the magnetic field (Lowes, 1974). Low degree terms are large-scale (e.g. the degree one dipole), with the length scale of higher harmonic degrees becoming progressively smaller. Hence, the power spectrum tells us about the relative importance of different length scales of the field. At Earth's surface, the power spectrum consists of two regimes. Up to degree 14, the field is dominated by low degree terms and there is rapid rolloff of the power with increasing degree. This 'red' spectrum is consistent with a field generated inside the liquid outer core. Higher degree (smaller scale) features of the core field are obscured by the signals from crustal rocks. Hide (1978) proposed that at the edge of the generating region, magnetic field should be created with equal power at all length scales and so the spatial power spectrum should be 'white' (flat). The utility of the spatial power spectrum is that it can be calculated at any radius outside the generating region, which means that determining the radius at which the spectrum becomes independent of spherical harmonic degree would give an estimate for the CMB radius if the outer core were indeed the source region of the geomagnetic field. Hide & Malin (1981) used this method on the geomagnetic data available at the time to calculate the depth to the source region of Earth's field, obtain-

ing values that were consistent with the seismologically determined outer core radius. The early estimates from geomagnetic sounding, as well as modern estimates based on high quality SV data (e.g. Langlais et al., 2014), remain in excellent agreement with the outer core radius determined by seismology, such as that given by the Preliminary Reference Earth Model (PREM, Dziewonski & Anderson, 1981).

Not only did the study of Hide & Malin (1981) add further weight to Larmor's dynamo hypothesis, the level of agreement between the geomagnetically and seismologically determined radii also suggests that the mantle is a good electrical insulator, which provides some justification for using Gauss's theory to model the geomagnetic field as a potential field. By treating the internally generated magnetic field as a potential field and fitting spherical harmonics to observations, we can construct maps of the magnetic field and its time variations at any radius outside the generating region by 'upward' or 'downward' continuation of the observationally-constrained surface field. This extrapolation of the field to different radii involves multiplying the power spectrum at the surface, given by equation (1.1), by a factor of $(a/r)^{2l+4}$ where a is Earth's radius and r is the radius of interest (Lowes, 1974). 'Upward continuation' is used to examine field structure above Earth's surface ($r > a$) and 'downward continuation' is used to examine its structure at the edge of the outer core ($r = c$, where c is the CMB radius). Fig. 1.2a shows a contour map of the radial magnetic field at Earth's surface in 2010 according to COV-OBS, a stochastic magnetic field model that was constrained by observatory and satellite data spanning the period 1840 to 2010 (Gillet et al., 2013). The surface geomagnetic field is dominated by a dipole tilted approximately 11° from Earth's rotation axis, with the south magnetic pole in the northern geographic hemisphere. The magnitude of the field observed at the surface varies from approximately 25 000 nT near the equator to approximately 65 000 nT near the poles. As shown in Fig. 1.2b, the radial magnetic field at the CMB has a much higher amplitude and is considerably more complex than the surface field. There are many visible small-scale features, the most prominent of which are high amplitude flux patches under Canada and Siberia in the northern hemisphere and under equatorially symmetric locations near Antarctica in the southern hemisphere. Several prominent patches of high amplitude positive radial magnetic field are seen near the geographic equator and similar high amplitude negative patches occur at approximately 20°N. Finally, two reverse flux patches (field patches of the opposite direction to the surrounding field) are seen under the tip of South America

and the tip of Africa.

It is of interest to look at the temporal behaviour of the geomagnetic field as well as its spatial structure. Magnetic signals in basalts at spreading mid-ocean ridges have revealed irregular polarity reversals throughout the last $\sim$ 200 Myr. These are the most dramatic of the field fluctuations; the axial dipole component changes sign, and magnetic field strength decreases by up to 75% (e.g. Merrill & McFadden, 1999). These changes are thought to occur over several millennia, though recent work by Sagnotti et al. (2014) suggests that a reversal may occur in less than a century. The longest timescale associated with the geomagnetic field is the rate at which polarity reversals occur, which could be several times in a million years or there may be long periods in which it does not reverse, such as during the Cretaceous normal superchron that lasted for almost 40 Myr (e.g. Constable, 2000).

Several time-varying magnetic field models have been constructed using observations of the geomagnetic field as constraints. Such models include *gufm* (Jackson et al., 2000), which was constrained by historical records for the period 1590 to 1990, and the CALSxk series (Korte & Constable, 2003, Korte et al., 2005, 2011) of models, which were constrained by the available palaeomagnetic data for the last 3k, 7k and 10k years. On timescales of centuries to millennia, the most obvious feature of SV is the westward drift of several features in the equatorial Atlantic. This feature was first noticed by Halley (1692), and was later quantified by Bullard et al. (1950) who estimated the drift rate as approximately $0.2\,^\circ\,\mathrm{yr}^{-1}$. As well as such directional changes, the geomagnetic field intensity has been gradually decreasing over the last 150 yr. During this period, the axial dipole field strength has decreased by approximately 10% (e.g. Bloxham et al., 1989). Figs 1.3a and 1.3b show snapshots of the SV in 2010 according to the COV-OBS model of Gillet et al. (2013). As with the magnetic field, the SV at the CMB is higher amplitude and on much smaller length scales compared to the surface SV. An interesting point is that the Pacific hemisphere has much weaker SV than the Atlantic hemisphere. At the CMB, reverse flux patches move from equator to pole (e.g. Terra-Nova et al., 2015), simultaneously intensifying, a phenomenon that is possibly correlated with the decay of the axial dipole moment observed at the surface (Gubbins, 1987).

On timescales of months to years, rapid changes in SV (the second temporal derivative of the magnetic field) have been observed in various locations (e.g. Courtillot & Valet,

1995, Le Huy et al., 1998). Some of these 'geomagnetic jerks' are of global extent (Alexandrescu et al., 1996), but many jerks occur on a regional basis (Brown et al., 2013). These rapid magnetic field changes are thought to be a result of rapid core dynamics, and have previously been linked to a set of axisymmetric core motions called torsional oscillations (Bloxham et al., 2002), which are thought to occur in Earth's core on decadal timescales and produce signals in SV and Earth's rotation rate (defined in terms of length-of-day, LOD). Recent work by Holme & de Viron (2013) has linked signals in LOD, and its time-derivative, with contemporaneous geomagnetic jerk events. However, the origin of geomagnetic jerks has not yet been identified conclusively and questions remain as to whether torsional oscillations can produce the kind of core flow required to cause SV matching observed patterns. The subject of this thesis is the theory behind torsional waves, their propagation characteristics and the SV signals that they can produce. The next section of this chapter is an overview of how magnetic fields are generated in planetary cores and a discussion of the torsional waves in Earth's core.

(a) Earth's surface

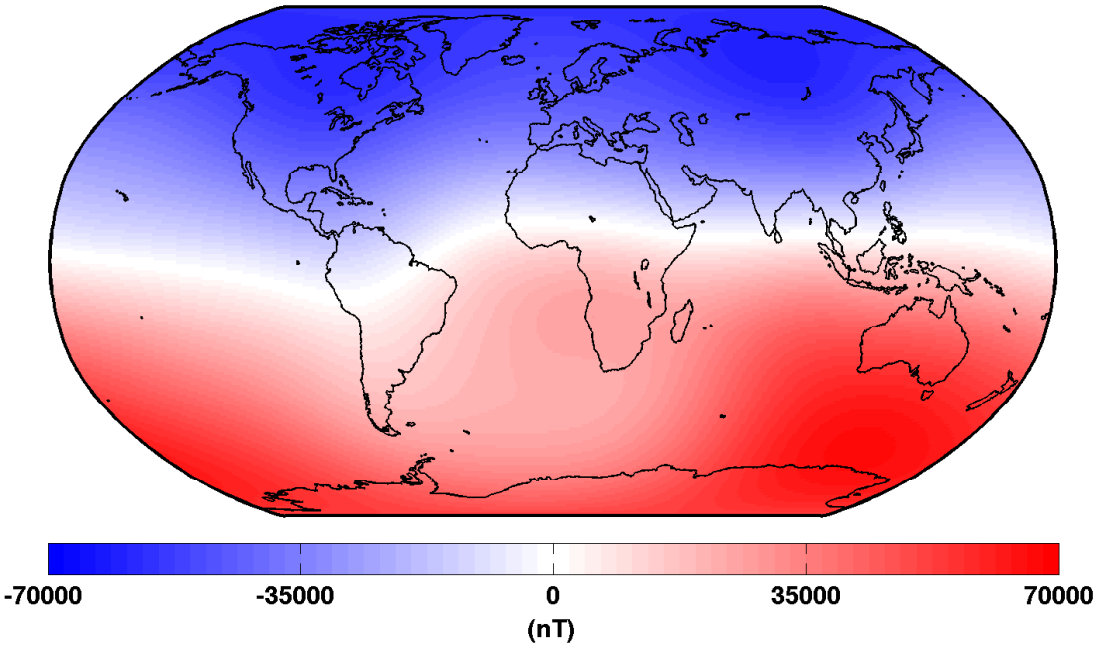

(b) CMB

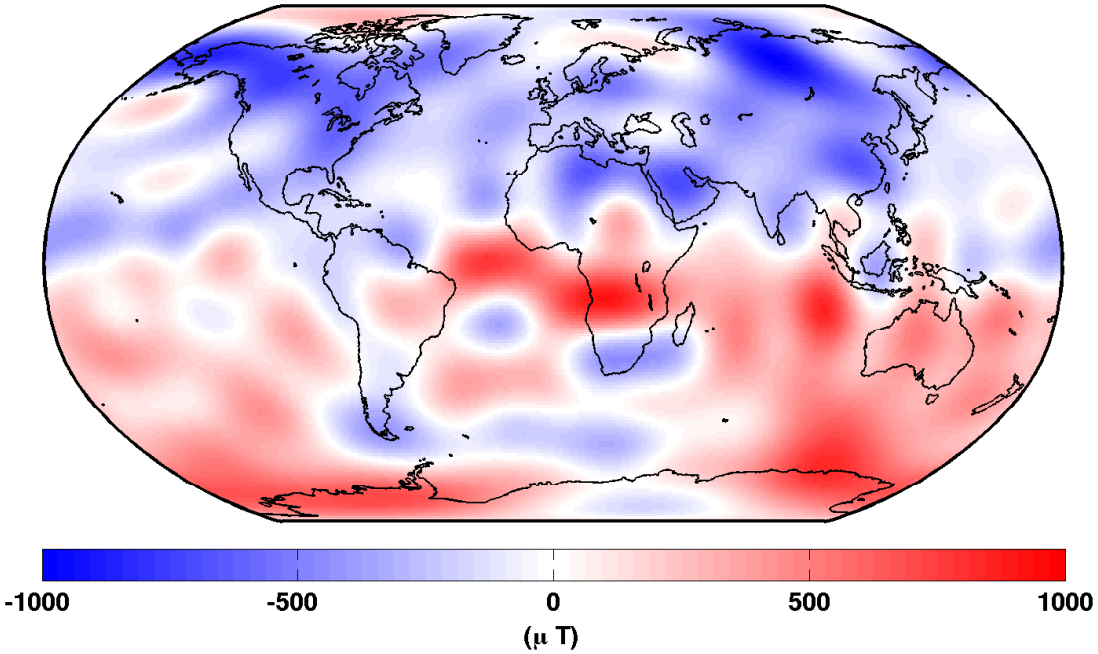

Figure 1.2: The radial magnetic field in 2010 at (a) Earth's surface and (b) Earth's CMB according to the COV-OBS model (Gillet et al., 2013). Red represents positive magnetic field (outwards) and blue represents negative magnetic field (inwards). The maps are in Robinson projection and the scales are in (a) nT and (b) μT.

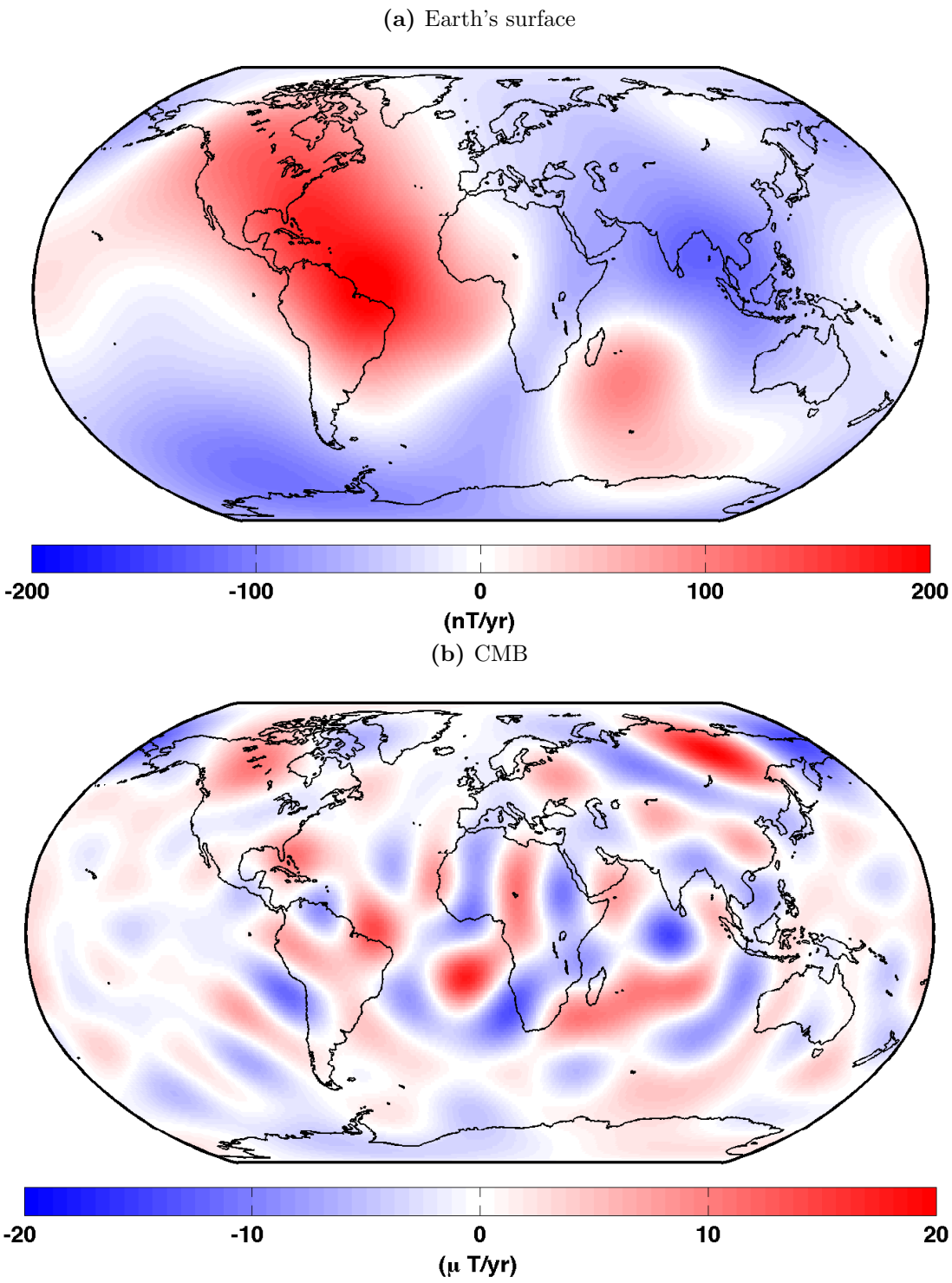

Figure 1.3: The radial secular variation in 2010 at (a) Earth's surface and (b) Earth's CMB according to the COV-OBS model (Gillet et al., 2013). Red represents positive SV and blue represents negative SV. The maps are in Robinson projection and the scales are in (a) nT/yr and (b) μT/yr.

1.4 Internal magnetic field generation

The dynamo process in the outer core is governed by the physical laws that encapsulate the mutual interaction of magnetic fields and the flow of an electrically conducting fluid. This theoretical framework is known as magnetohydrodynamics (MHD) and consists of the pre-Maxwell equations of electrodynamics, Ohm's law for a moving conductor and conservation laws for mass, momentum and energy (e.g. Davidson, 2001). These equations, along with their application to the Earth's core, are the subject of this section. Continuous forms of the MHD equations are presented, followed by a discussion of torsional wave theory (a derivation of the torsional wave equation may be found in Appendix A).

In the following discussion, the electrically conducting fluid of the Earth's outer core is confined between two concentric spheres of outer radius r_c and inner radius r_i, which correspond to the core-mantle-boundary (CMB) and inner-core-boundary (ICB) respectively. Unless stated otherwise, spherical polar coordinates (r, θ, ϕ) are used, where r is radius, θ is colatitude and ϕ is azimuth, and the position vector at a point on the sphere is denoted $\boldsymbol{r}$. Extensive use is also made of cylindrical polar coordinates (s, ϕ, z), where s is cylindrical radius, ϕ is azimuth and z is height. The spheres co-rotate about the vertical axis (z) with a constant angular velocity $\boldsymbol{\Omega}$.

1.4.1 General equations

Maxwell's equations of electrodynamics govern the behaviour of associated electric and magnetic fields in a moving conductor. As the fluid velocities in the core are much less than the speed of light, it is common practice to ignore relativistic effects and use the simpler pre-Maxwell form of the laws of electrodynamics. The differential form of Faraday's law, Ampère's law and the solenoidal condition are, respectively,

$$\nabla \times \boldsymbol{E} = -\frac{\partial \boldsymbol{B}}{\partial t}, \tag{1.2}$$

$$\nabla \times \boldsymbol{B} = \mu_0 \boldsymbol{J}, \tag{1.3}$$

and

$$\nabla \cdot \boldsymbol{B} = 0. \tag{1.4}$$

These describe the relationship between an electric field $\boldsymbol{E}$, a magnetic field $\boldsymbol{B}$ and an electric current density $\boldsymbol{J}$, where μ_0 is the permeability of free space ($4\pi \times 10^{-7}\,\mathrm{H/m}$). However, Maxwell's equations are not a complete system of equations; a closure relation is required to link the electric field, magnetic field and current density with each other. This coupling relation is known as Ohm's law, and is given for a conductor moving with velocity $\boldsymbol{u}$

$$\boldsymbol{J} = \sigma(\boldsymbol{E} + \boldsymbol{u} \times \boldsymbol{B}), \tag{1.5}$$

where σ is the electrical conductivity. Taking the curl of (1.5) and using (1.2) and (1.3) eliminates the electric field and current density, which yields a transport equation for the magnetic field called the magnetic induction equation

$$\frac{\partial \boldsymbol{B}}{\partial t} = \underbrace{\boldsymbol{\nabla} \times (\boldsymbol{u} \times \boldsymbol{B})}_{\text{(a)}} + \underbrace{\eta \nabla^2 \boldsymbol{B}}_{\text{(b)}}, \tag{1.6}$$

where $\eta = 1/\mu_0\sigma$ is the magnetic diffusivity. The induction equation gives the change in magnetic field at a fixed point due to two processes: advection and diffusion. Term (a) is the advection term, which describes the transport of magnetic field lines by fluid motion and term (b) describes the modification of magnetic flux by electromagnetic diffusion. The relative importance of these two processes is measured by the magnetic Reynolds number, R_m, which is defined as

$$R_m = \frac{UL}{\eta} = \frac{L^2}{\eta} \Big/ \frac{L}{U} = \frac{\tau_u}{\tau_\eta}, \tag{1.7}$$

where τ_u is the advection timescale (the time taken for core fluid to traverse the core), τ_η is the magnetic diffusion timescale, and U and L are typical velocity and length scales respectively. When $R_m \gg 1$, the change in magnetic field is predominantly due to advection of field lines by fluid motion, whereas $R_m \ll 1$ implies that sources can create higher magnetic flux, or Ohmic decay can destroy existing flux, more rapidly than the fluid motion can redistribute it. Roberts & Scott (1965) first argued that the core can be treated as a perfect conductor on secular variation timescales because the dynamical timescale of observed features, such as westward drift, is much shorter than the magnetic diffusion time, which is on the order of several millennia (or 200 000 yr

for the whole core). In this case, the magnetic field lines can be thought of as being 'frozen in' to the core fluid, and the induction equation reduces to its frozen-flux form

$$\frac{\partial \boldsymbol{B}}{\partial t} = \boldsymbol{\nabla} \times (\boldsymbol{u} \times \boldsymbol{B}). \tag{1.8}$$

Turning to continuum mechanics for a representation of the electrically conducting fluid in the core, we now assume that the fluid is Newtonian and that convection may be represented using the Boussinesq approximation, which states that density variations in the core fluid are small enough to be neglected, except for those involved in the buoyancy term. Then, the conservation of mass equation is

$$\nabla \cdot \boldsymbol{u} = 0, \tag{1.9}$$

and the conservation of momentum in a frame of reference rotating with the mantle can be written in the form of a Navier-Stokes equation, which is an expression of Newton's second law of motion:

$$\rho_0 \underbrace{\left(\frac{\partial \boldsymbol{u}}{\partial t} + \boldsymbol{u} \cdot \nabla \boldsymbol{u} \right)}_{\text{(a)}} + \underbrace{2\rho_0 \boldsymbol{\Omega} \times \boldsymbol{u}}_{\text{(b)}} = -\nabla p + \rho' \boldsymbol{g} + \boldsymbol{J} \times \boldsymbol{B} + \rho_0 \nu \nabla^2 \boldsymbol{u}, \tag{1.10}$$

where ρ' is the departure from the hydrostatic reference density ρ_0, $\boldsymbol{\Omega}$ is the rotation vector of the Earth, p is the non-hydrostatic contribution to pressure, $\boldsymbol{g}$ is the acceleration due to gravity and ν is the kinematic viscosity. In this work, gravity is assumed to vary linearly as $\boldsymbol{g} = -g\boldsymbol{r}$, where g is acceleration due to gravity at the CMB and the negative gradient indicates decreasing (i.e. stronger inward directed field) $\boldsymbol{g}$ with increasing radius.

Term (a) in equation (1.10) represents the material derivative of the momentum and term (b) represents the Coriolis force, which arises due to the rotation of the Earth. The right hand side of (1.10) is the sum of all the applied forces that cause changes in momentum. From left to right, these forces are pressure, buoyancy, the Lorentz force and viscous forces.

Equation (1.10) may be written in non-dimensional form by scaling length by the radius of the core r_c, time by the magnetic diffusion timescale r_c^2/η, the magnetic field by $\sqrt{\Omega \rho_0 \mu_0 \eta}$ and temperature by ΔT, the adiabatic temperature difference from the

ICB to the CMB. This non-dimensionalisation gives

$$R_o\left(\frac{\partial \boldsymbol{u}}{\partial t}+\boldsymbol{u}\cdot\nabla\boldsymbol{u}\right)+2\hat{\boldsymbol{z}}\times\boldsymbol{u}=-\nabla p+R_a\Theta\boldsymbol{r}+\boldsymbol{J}\times\boldsymbol{B}+E\nabla^2\boldsymbol{u}, \tag{1.11}$$

where the non-dimensional numbers $E=\nu/\Omega r_c^2$, $R_o=\eta/\Omega r_c^2$ and $R_a=\alpha g_0\Delta T r_c^2/\Omega\eta$ are, respectively, the Ekman number, Rossby number and Rayleigh number, Θ is the buoyancy and α is the coefficient of thermal expansion. Note that in this work, we neglect compositional buoyancy sources and consider an outer core that undergoes purely thermal convection due to heating from below and cooling from above. Typical values for these numbers in the Earth's core are $E\approx 10^{-15}$, $R_o\approx 10^{-9}$ and $R_a\approx 10^9$ (e.g. Gubbins & Roberts, 1987). The small magnitudes of E and R_o compared to R_a imply that, to leading order, the inertial and viscous effects are unimportant and the non-dimensional Navier-Stokes equation can be reduced to the following

$$2\hat{\boldsymbol{z}}\times\boldsymbol{u}=-\nabla p+R_a\Theta\boldsymbol{r}+\boldsymbol{J}\times\boldsymbol{B}. \tag{1.12}$$

The above equation represents the behaviour of the fluid in the slow, long term inviscid limit and is called the magnetostrophic balance (see §1.4.2 and Hollerbach (1996) for further details).

Another force balance, called geostrophic, arises in the absence of the Lorentz and buoyancy forces from the magnetostrophic balance. This balance is written as

$$2\hat{\boldsymbol{z}}\times\boldsymbol{u}=-\nabla p, \tag{1.13}$$

whose curl yields the Taylor-Proudman theorem (Proudman, 1916, Taylor, 1917)

$$\frac{\partial \boldsymbol{u}}{\partial z}=\boldsymbol{0}, \tag{1.14}$$

which states that the fluid motion must be independent of z. Therefore, the Coriolis force plays a key role in determining the large scale dynamics of the outer core because rapid rotation tends to prevent large variations in velocity parallel to the rotation axis. In spherical geometry, the Taylor-Proudman theorem implies that the only permitted flow is purely zonal, i.e. in the azimuthal direction (Bullard & Gellman, 1954), and this constraint requires that core fluid moves in rigid cylinders, coaxial with the rotation axis. This flow is called geostrophic and the cylinders of fluid, defined in a cylindrical

basis $(\boldsymbol{e}_s, \boldsymbol{e}_\phi, \boldsymbol{e}_z)$, are correspondingly named geostrophic cylinders (GCs), shown in Figs 1.4a and 1.4b.

1.4.2 Taylor's constraint

Theoretical considerations suggest that the geodynamo is in the strong field regime, in which the dominant force balance is the magnetostrophic balance of equation (1.12) (e.g. Hollerbach (1996); Roberts (2007)). This balance is of considerable interest because it describes the slow (millennial timescales) evolution of the magnetic field, and may explain dynamics such as geomagnetic reversals and the longstanding dominance of the axially symmetric dipolar component of the field (Livermore et al., 2011). Superimposed on this background state are more rapid dynamics such as torsional Alfvén waves. As Taylor identified in 1963, any magnetic field evolving in the magnetostrophic balance must satisfy a stringent class of constraints at all times. Taylor's constraint is a condition on the morphology of the geomagnetic field inside the core and it is derived by considering the ϕ-component of the equation describing the magnetostrophic balance (1.12) averaged over cylindrical surfaces aligned with the Earth's rotation axis (GCs). By only considering the azimuthal component of the magnetostrophic balance, we restrict ourselves to flows that are not directly affected by the Coriolis force (Taylor, 1963). In dimensional form, this is written as

$$\int \oint 2\rho_0(\boldsymbol{\Omega} \times \boldsymbol{u})_\phi d\Sigma = -\int \oint (\nabla p)_\phi d\Sigma + \int \oint (\rho' \boldsymbol{g})_\phi d\Sigma + \int \oint (\boldsymbol{J} \times \boldsymbol{B})_\phi d\Sigma, \quad (1.15)$$

where $d\Sigma = s d\phi dz$ is an element of surface area in cylindrical coordinates (s, ϕ, z), see Fig. 1.4a.

The pressure gradient term vanishes because the integrand is an exact derivative

$$\int \oint (\nabla p)_\phi d\Sigma = \int \left(\int_0^{2\pi} \frac{\partial p}{\partial \phi} d\phi \right) dz = 0.$$

The buoyancy integral also vanishes because gravity is purely radial

$$\int \oint (\rho' \boldsymbol{g})_\phi d\Sigma = 0.$$

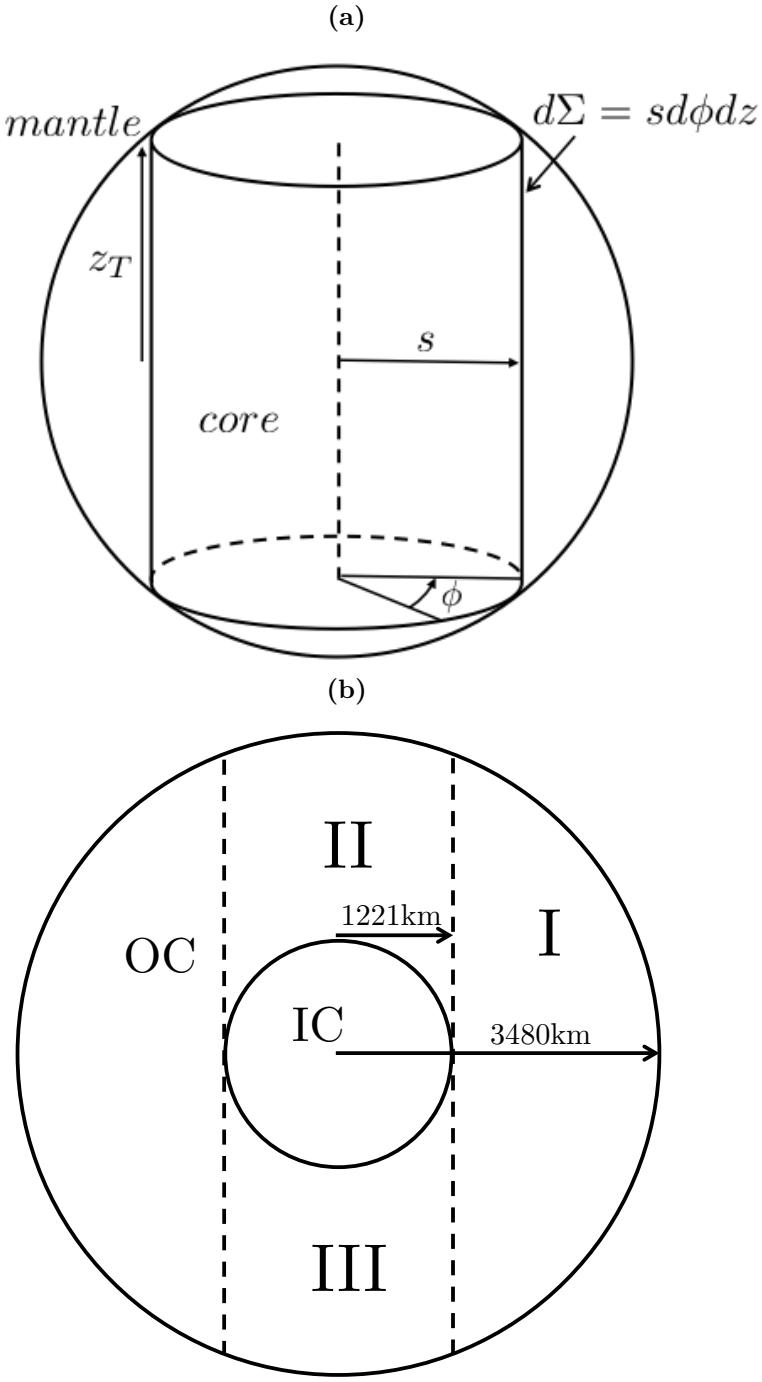

Figure 1.4: Vertical (meridional) slices through the core. (a) Geometry of the geostrophic cylinders (GCs) defined in a cylindrical coordinate system. The symbols s, ϕ and z describe, respectively, radial distance from the rotation axis, azimuth and height. The cylinder half height is denoted z_T. All of the fluid on the same cylindrical surface of radius s has the same velocity $u_\phi(s)$. After Dumberry (2009). (b) The Earth's core is divided into three regions. I) The region of the outer core (OC) that is outside the tangent cylinder. II) The region of the outer core that lies inside the tangent cylinder and above the inner core (IC). III) The region of the outer core that lies inside the tangent cylinder and below the inner core. The tangent cylinder is shown as a dashed line between region I and regions II and III.

The Coriolis term can be written in the following form due to conservation of mass

$$2\rho_0 \int \oint (\boldsymbol{\Omega} \times \boldsymbol{u})_\phi d\Sigma = 2\rho_0 \Omega \int \oint u_s d\Sigma,$$

where u_s is the component of the velocity normal to the rotation axis (i.e. in the cylindrical radial direction). The GC can be extended to form a closed surface by including a spherical cap at both the top and bottom of the cylinder such that

$$\int \oint_{\mathrm{GC}} u_s d\Sigma = \int \oint_{\mathrm{GC}} u_n d\Sigma + \int \oint_{\mathrm{caps}} u_n d\Sigma,$$

where u_n is the normal component of the velocity. The non-penetration condition at the CMB requires that $\boldsymbol{u} \cdot \boldsymbol{n} = 0$ at the CMB, which means that the integral over the caps is zero. So, using the divergence theorem, we have the following volume integral

$$2\rho_0 \Omega \int \oint u_n d\Sigma = 2\rho_0 \Omega \int \int \oint (\nabla \cdot \boldsymbol{u}) dV,$$

which must equal zero by the conservation of mass equation (1.9). Therefore, only the Lorentz term in (1.15) does not identically vanish and we must have

$$\int \oint (\boldsymbol{J} \times \boldsymbol{B})_\phi d\Sigma = 0. \tag{1.16}$$

This imposes a condition on the morphology of the internal magnetic field and an associated dynamic state, which are called the Taylor constraint and Taylor state respectively. Taylor's constraint specifies that the magnetic field inside the core must be organised in such a way that the azimuthal Lorentz force vanishes when averaged over an arbitrary cylindrical surface that is coaxial with the rotation axis, which would occur by having $(\boldsymbol{J} \times \boldsymbol{B})_\phi = 0$ everywhere or regions of positive and negative $(\boldsymbol{J} \times \boldsymbol{B})_\phi$ cancelling each other out over the whole of Σ. Taylor (1963) suggested that not only must the field obey this constraint at some initial time, but that departures from a Taylor state would excite azimuthal accelerations of these rigid cylindrical surfaces in order to reestablish the Taylor state at all later times. Note that equation (1.16) contains only the Lorentz term; if Taylor's constraint is violated, another term must be added back in to the equation so that the Lorentz force is balanced by another force. Torsional Alfvén waves arise when inertial forces are used to balance $(\boldsymbol{J} \times \boldsymbol{B})_\phi$. Relative rotation of adjacent cylinders perturbs magnetic field lines (see the magnetic induction equation (1.6)) and the stretching of these field lines provides a restoring force to counter the

perturbation. Fluid inertia carries the cylinder past the equilibrium position and the restoring force then changes direction, thus allowing torsional waves to propagate along radial magnetic field lines with a velocity that is linearly dependent on the intensity of the radial magnetic field. The observation of torsional waves in geophysical data would indicate that the Earth's core is in a quasi-Taylor state, in which the azimuthal Lorentz force vanishes when averaged over a cylinder, except for the part involved in torsional waves (Dumberry & Bloxham, 2003).

1.4.3 The torsional wave equation

We have previously derived Taylor's constraint, equation (1.16), which specifies that the Lorentz torque vanishes when averaged over cylindrical surfaces. When the magnetic field does not precisely satisfy Taylor's constraint, inertia may be reintroduced into equation (1.16) and used to balance the azimuthal Lorentz force to obtain

$$\rho_0 \int_z \oint \frac{\partial \boldsymbol{u}_g}{\partial t} s d\phi dz = \int_z \oint (\boldsymbol{J} \times \boldsymbol{B})_\phi s d\phi dz, \tag{1.17}$$

for an incompressible fluid. Since we have integrated in the ϕ and z directions, the problem collapses to one dimension and the above equation (1.17), along with the induction equation, may be used to derive an equation for the time derivative of the geostrophic flow $\boldsymbol{u}_g$. The resulting 1-D torsional wave equation

$$\frac{\partial^2 \omega_g}{\partial t^2} = \frac{1}{s^3 \mu_0 \rho_0 z_T} \frac{\partial}{\partial s} \left(s^3 z_T \{B_s^2\} \frac{\partial \omega_g}{\partial s} \right) \tag{1.18}$$

was first established by Braginsky (1970), though the derivation in Appendix A follows that found in Légaut (2005) and Jault & Légaut (2005) (see Braginsky (1970) and Roberts & Aurnou (2011) for alternative derivations). In this wave equation, ω_g is the angular speed ($=u_\phi/s$ where u_ϕ is the linear velocity and s is the cylindrical radius), z_T is the cylinder half-height (see Fig. 1.4a), μ_0 is the permeability of free space, ρ_0 is the hydrostatic reference density and we have introduced the notation $\{B_s^2\} = \frac{1}{4\pi z_T} \int_{-z_T}^{+z_T} \oint B_s^2 d\phi dz$. As previously stated, the torsional wave problem has collapsed to one dimension due to integration in the ϕ and z directions. Although torsional waves may be modelled in 1-D, Cox et al. (2014) argue that they are fundamentally a 2-D phenomenon, such as symmetric waves on a circular drum for example, due to their convergence on an axis at $s = 0$. If torsional waves were fundamentally 1-D or 3-D,

they would converge on a point at the origin. Their convergence on an axis imposes many conditions on the velocity and its derivatives (see §2.3), which would otherwise be unnecessary. We will return to this point in §3.9 of chapter 3.

1.5 Torsional waves in the core

Assuming an electrically insulating mantle, measurements of the geomagnetic field and its time variations may be downward continued to the core-mantle boundary (CMB) and inverted to construct maps of flow at the core surface (Backus, 1968). Dynamical assumptions can be used to constrain the flow model. One such assumption is that the time-dependent zonal motions are geostrophic, which are constrained by the core geometry to be axisymmetric and often characterised by the rotation of nested concentric cylinders, Fig. 1.5. All of the fluid on the same geostrophic cylinder has the same azimuthal velocity, u_ϕ. Due to its simple geometry and the presumed rigidity of geostrophic cylinders, this part of flow may then be extrapolated into the core interior (e.g. Le Mouël (1984)).

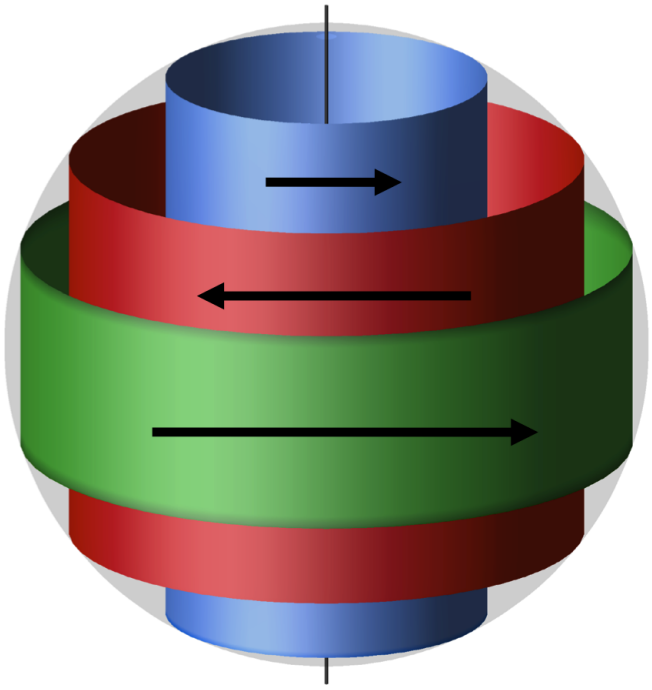

Figure 1.5: Torsional waves: azimuthal accelerations of rigid coaxial cylindrical surfaces. Each cylindrical surface moves with a different speed and is coupled to adjacent surfaces by the radial magnetic field B_s. Note that cylinder height decreases with increasing distance from the rotation axis.

Changes in core angular momentum can be calculated from core surface flow models. If the angular momentum of the core varies, there must be a corresponding variation in mantle angular momentum in order to satisfy the conservation law for this quantity. This leads to variations in length of day (ΔLOD). According to Jackson et al. (1993) and Jault et al. (1988), there is good correlation between changes in core angular momentum carried by geostrophic motions extracted from core flow models based on temporal changes in the geomagnetic field (secular variation), and observed changes in solid Earth angular momentum (ΔLOD) between 1920 and the present day. Braginsky (1970, 1984) first used torsional normal modes to explain observations of secular variation (SV) and decadal variations in ΔLOD. He made the link between theory and observations by deriving the torsional wave equation and predicted that torsional normal modes would have a period of approximately 60 years if B_s, the cylindrical radial (s) component of the magnetic field is $\sim$0.2 mT. The magnetic field strength and the Alfvén wave group velocity, V_A are related through the equation

$$V_A = \sqrt{\frac{\{B_s^2\}}{\mu_0 \rho_0}} \tag{1.19}$$

More recently, several authors have reported observational evidence to support the existence of torsional waves in the core (Hide et al., 2000, Pais & Hulot, 2000, Zatman & Bloxham, 1997, 1999). Zatman & Bloxham (1997, 1999) concluded that the core flow model that best fits the observed axially and equatorially symmetric component of SV consists of a steady flow plus several damped harmonic waves with periods of 53 and 76 years (Fig. 1.6).

The same authors subsequently repeated the analysis on a shorter but better temporally resolved dataset from 1957 to 2001, and noted three standing oscillations with periods of 13, 20 and 45 years (Zatman & Bloxham (1999)). In both studies, they interpreted these waves as torsional normal modes and inverted them to derive an estimate of the internal magnetic field strength responsible for the waves and an estimate of core viscosity. Pais & Hulot (2000) used a method developed by Le Mouël et al. (1985) for determining the core surface flow accounting for the observed SV and obtained results in agreement with Zatman & Bloxham (1997, 1999). Hide et al. (2000) calculated the core angular momentum based on flow velocity models of Jackson et al. (1993), which were inferred from SV observed between 1840 and 1990. They noted a dominant latitude

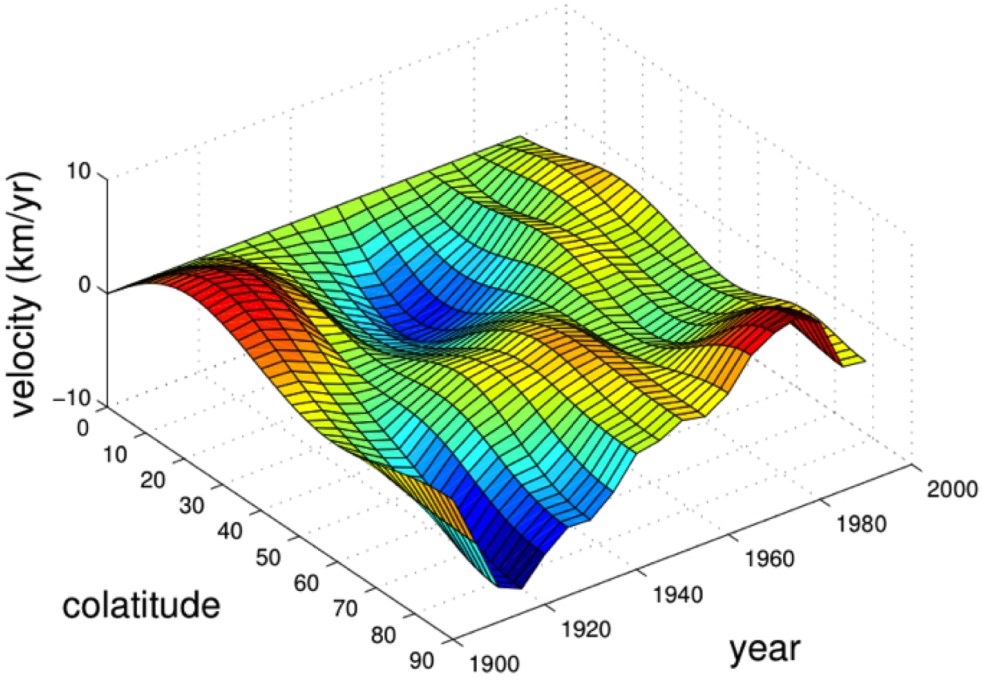

Figure 1.6: The axisymmetric, equatorially symmetric part of decadal geostrophic core flow, inferred from secular variation at the CMB (Zatman & Bloxham (1997)). The colour scale is in km/yr; red represents positive velocity and blue represents negative velocity.

dependent fluctuation with a 65 year period, with angular momentum propagating from the equatorial to the polar regions (Fig. 1.7). The direction of propagation of the waves had not been considered in prior studies because previous models were restricted to standing oscillations.

However, recent work by Gillet et al. (2010) suggests that torsional waves are faster than previously concluded. They inverted the *gufm1* magnetic model (Jackson et al., 2000) for core flow and found that a recurring torsional wave matches the observed phase and amplitude of the observed 6 year ΔLOD signal (Fig. 1.8).

As the propagation velocity of Alfvén waves is proportional to magnetic field strength (see equation (1.19)), this would suggest that the internal core field strength is higher than previously assumed. Indeed, having calculated an ensemble of admissible profiles of torsional wave speed as a function of cylindrical radius, Gillet et al. (2010) inferred an internal field strength of 4 mT, compared to $\sim$2.5 mT calculated by Buffett (2010), $\sim$0.3 mT by Buffett et al. (2009) and $\sim$0.4 mT by Zatman & Bloxham (1997). Interestingly, not only does the internal magnetic field strength differ from previous studies,

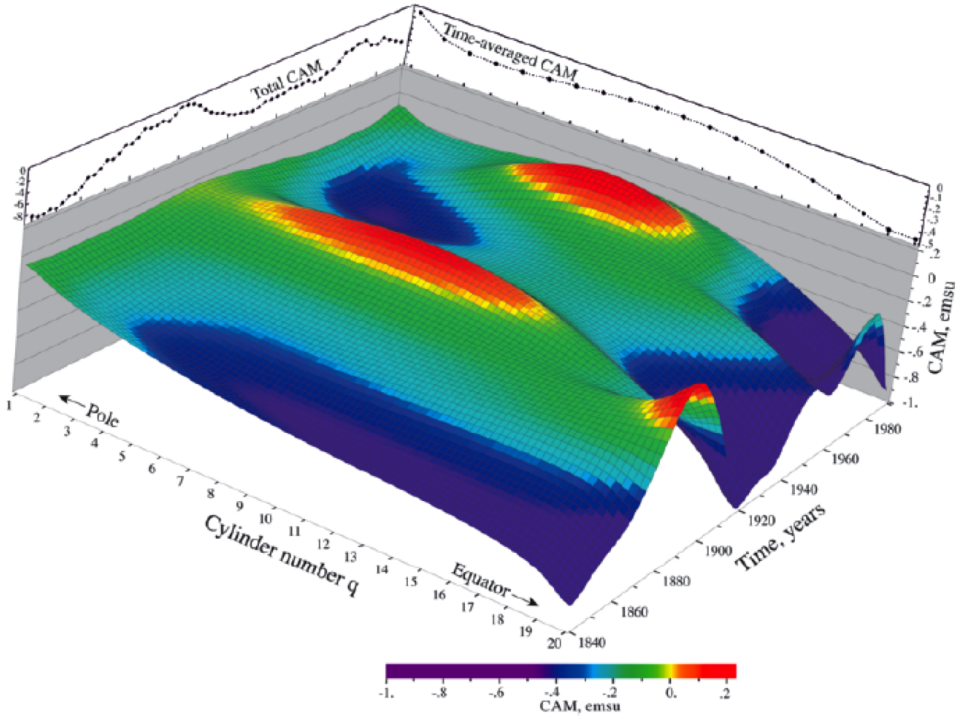

Figure 1.7: Representation of core angular momentum of 20 cylindrical shells as a function of latitude. The two peaks in mid-latitude coincide with the two geomagnetic jerk events that occurred during the studied interval (1912 and 1969). Based on the observed propagation pattern, Hide et al. (2000) suggested that the signal is transmitted from the equatorial to the polar regions. Taken from Hide et al. (2000).

but also the direction of propagation inferred by Gillet et al. (2010) is from the tangent cylinder outwards, rather than from the equator to the poles as suggested by Hide et al. (2000). The tangent cylinder is the imaginary cylinder that is coaxial with the rotation axis and just touches the inner core (see Fig. 1.4b). As previously mentioned, previous studies had reported that standing oscillations were a better fit to the observed data than propagating waves. However, when Gillet et al. (2010) considered only the ΔLOD time series filtered between five and eight years, they found that propagating waves best fit the data. Canet et al. (2009) derived a quasi-geostrophic model of rapid (secular variation timescales) core dynamics and used a variational data assimilation approach to link the model to the observed secular variation. Using both forward and adjoint models of torsional waves, which included both zonal and non-zonal velocity components, they concluded that torsional waves may be properly resolved using the last 10 years of satellite measurements of the geomagnetic field. Buffett et al. (2009) used normal mode analyses to recover the excitation source for torsional normal modes and identified the tangent cylinder as the main source region. A review of prior modelling

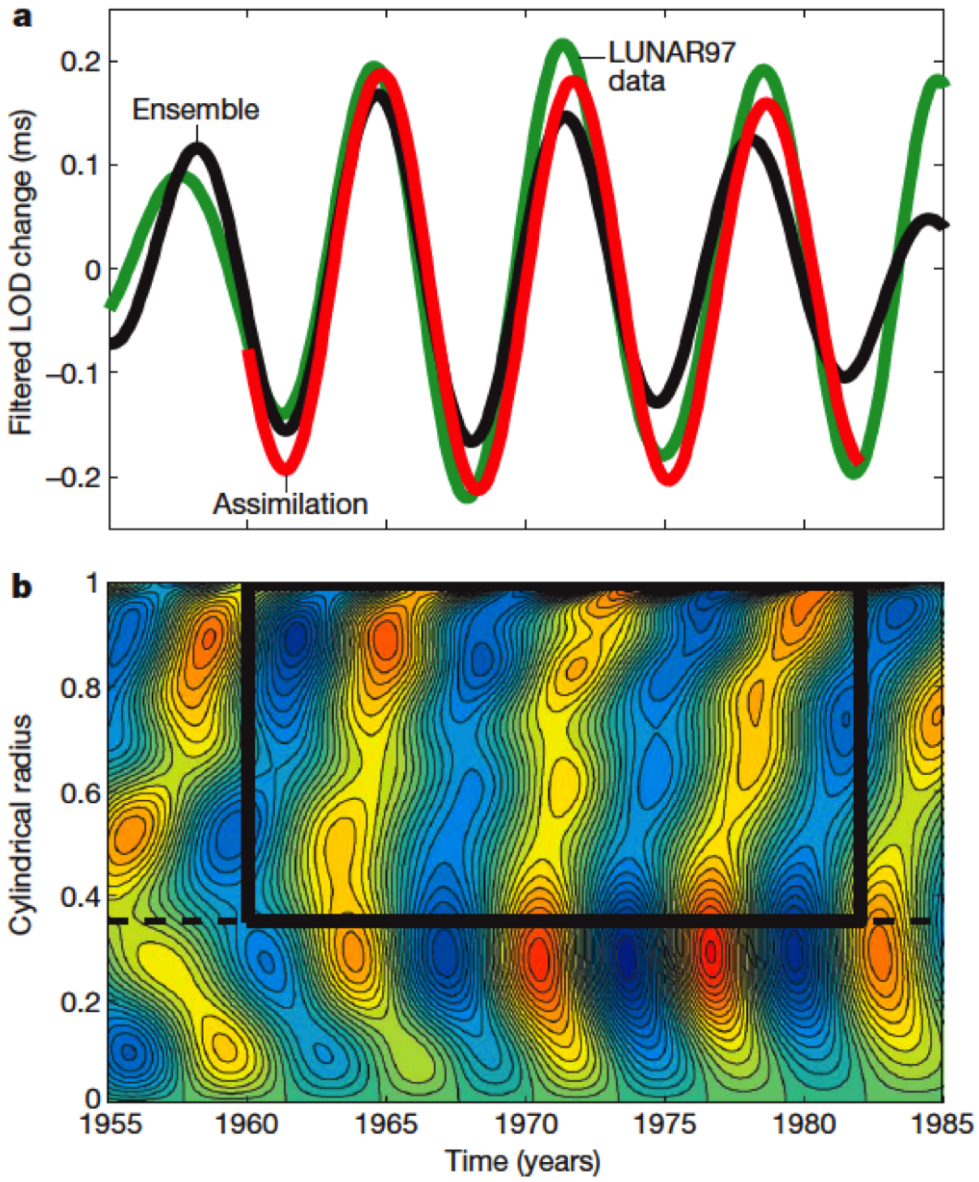

Figure 1.8: (a) Comparison of bandpass-filtered ΔLOD time series with a six-year signal. The green line is observed LUNAR97 data, the black line is predicted core flow models and the red line is the result of the torsional wave assimilation of the flow coefficients (b) Time versus cylindrical radius map of bandpass-filtered angular velocity. The colour scale ranges between -0.4 km/yr (blue) and +0.4 km/yr (yellow) with contours every 0.02 km/yr. The observed six year signal is carried by wave-like patterns travelling from the tangent cylinder (the horizontal dashed black line at $s = 0.35$) to the outer core equator ($s = 1$). Taken from Gillet et al. (2010).

attempts of torsional waves can be found in Jault & Légaut (2005).

1.6 Torsional waves in geodynamo models

Current knowledge of torsional waves based on geophysical observations is limited due to the sparsity of data, the non-uniqueness of observationally constrained core flow models (e.g. Holme, 2007) and the fact that, apart from the geostrophic flow, internal core dynamics remain inaccessible. An advantage of investigating torsional waves using numerical simulations of the geodynamo is that one can directly analyse the entire core flow field, examine force balances and look for Taylor states and/or torsional waves. Since the pioneering work of Glatzmaier & Roberts (1995), many numerical models of the geodynamo have been developed (for a detailed review see Christensen & Wicht (2007)). However, although geodynamo models are able to replicate some of the most important geomagnetic field features, such as polarity reversals, the simulations cannot run in the appropriate parameter regime for the Earth's core due to computational limitations. An important consequence of this is that the force balances involved in the models may differ from those expected in the Earth's core, which could prevent the excitation of torsional waves. In particular, even the most sophisticated geodynamo models operate with viscosities that are many orders of magnitude higher than estimated core values. If any waves were to develop in models with these high viscosities, they would be damped more quickly than expected in the Earth's core, which potentially means that torsional waves do not have the same importance in numerical models as in the core.

Nevertheless, several authors have reported evidence of torsional waves and/or quasi-Taylor states in geodynamo models (Kuang, 1999, Rotvig & Jones, 2002, Stellmach & Hansen, 2004, Takahashi et al., 2005, Wicht & Christensen, 2010). Kuang (1999) investigated the force balance in the Kuang-Bloxham dynamo model (Kuang & Bloxham, 1997) and concluded that torsional waves would develop in the model, and would be slightly damped by viscous dissipation. Dumberry & Bloxham (2003) obtained similar results using the same model and model parameters as in Kuang & Bloxham (1997). They observed rigid azimuthal accelerations when examining the torque balance on cylindrical surfaces, but concluded that they were not conventional torsional waves because Reynolds stresses, which are usually neglected, were relatively large and played a major role in wave dynamics by providing an alternative means of balancing the azimuthal Lorentz force. Wicht & Christensen (2010) provide a more detailed review of

the above work and other attempts to identify Taylor states and torsional waves in numerical simulations. They also present the results of a suite of geodynamo simulations, each performed at different parameters, with the aim of identifying torsional waves based on two criteria: first, the presence of wave-like structures propagating with the expected Alfvén velocity and second, a dominant azimuthal Lorentz force during propagation. Fig. 1.9 shows wave-like propagating structures in their best model, named E6, and Fig. 1.10 shows the Taylorisation during the same time period. Taylorisation is a measure of cancellation of the Lorentz torque, where $\mathcal{T} = 0$ is perfect Taylorisation (high cancellation) and $\mathcal{T} \approx 1$ is poor Taylorisation (effectively no cancellation).

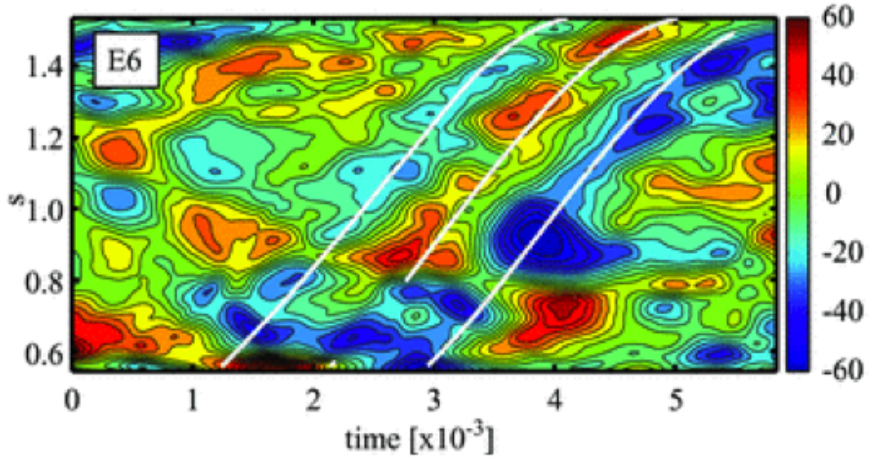

Figure 1.9: Velocity of geostrophic cylinders during the time interval in model E6 of Wicht & Christensen (2010). The time averaged velocity has been subtracted for each cylinder to highlight faster variations. White lines indicate the path waves should take when propagating with the Alfvén velocity.

As expected, the cancellation is relatively low during wave propagation, which corresponds to poor Taylorisation (high $\mathcal{T}$), because torsional waves are excited to reestablish the Taylor state. Wicht & Christensen (2010) were therefore able to confirm the predicted link between the magnetostrophic force balance, Taylor states and the existence of torsional waves.

Recent work by Teed et al. (2013) also focussed upon torsional waves in geodynamo simulations. Having performed 3-D simulations in a spherical shell in parameter regimes where Earth-like magnetic fields were produced, they identified torsional waves propagating at the theoretically predicted Alfvén speed in many of their simulations, an example of which is shown in Fig. 1.11. Waves propagated in the cylindrical radial direction, either inwards or outwards, and were sometimes excited at the tangent cylinder.

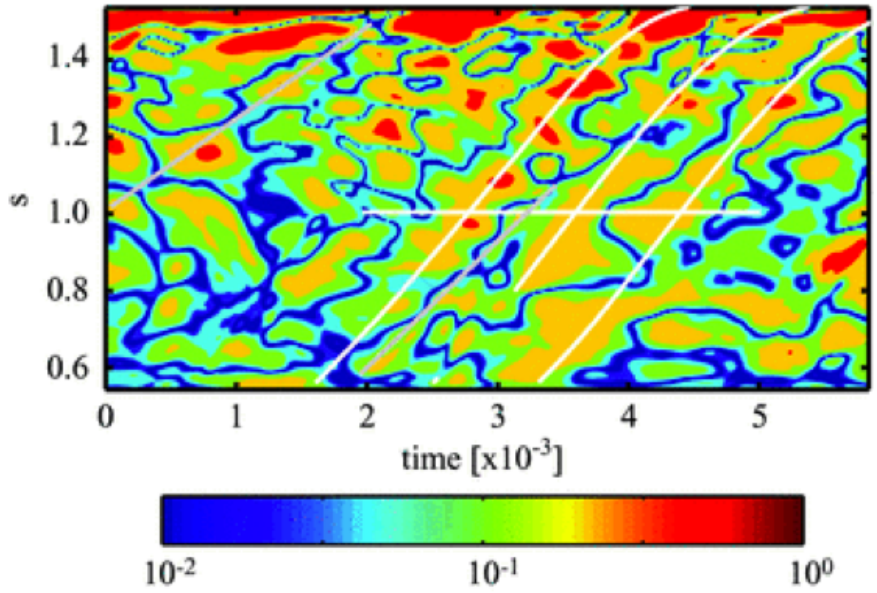

Figure 1.10: Taylorisation measure during the selected time interval in model E6 of Wicht & Christensen (2010).

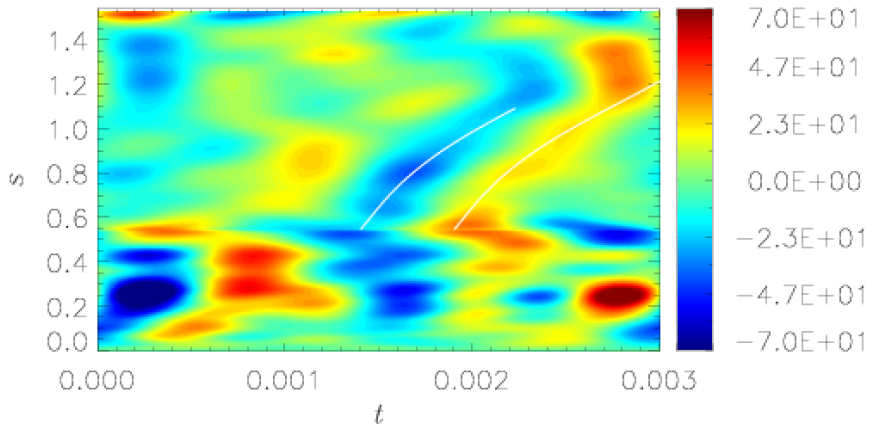

Figure 1.11: Contour plot of azimuthal velocity, as a function of time and cylindrical radius, showing torsional waves propagating from the tangent cylinder at the predicted Alfvén speed, from Teed et al. (2013).

Typical core transit times were between 4 and 6 years. Teed et al. (2013) noted that the frequency, location and direction of propagation of the waves were influenced by the choice of model parameters and also that excitation mechanisms for torsional waves were available throughout the outer core in their models. They calculated the driving terms for the observed torsional waves and concluded that both the Reynolds force and ageostrophic convection acting through the Lorentz force were important driving mechanisms. In a subsequent work focussing upon torsional waves in 3-D magneto-

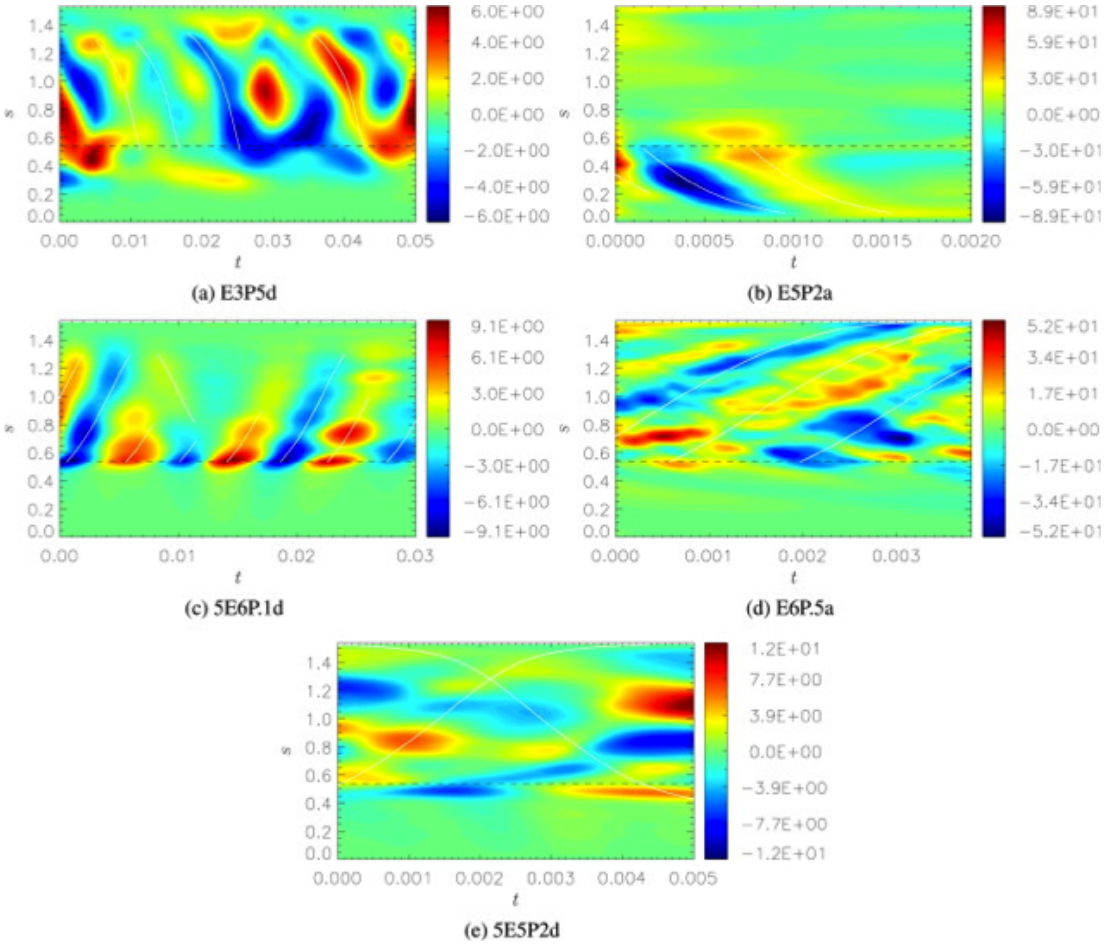

Figure 1.12: Contour plot of azimuthal velocity, as a function of time and cylindrical radius, showing torsional waves propagating at the predicted Alfvén speed in four different models. The fifth model (e), is included as an example of a model in which no torsional waves were observed. Taken from Teed et al. (2015).

convection simulations, Teed et al. (2015) investigated the driving forces of torsional waves at high and low Ekman numbers. At large Ekman numbers ($E \geq 10^{-5}$), they found that torsional waves are typically only a small fraction of the overall dynamics and are often driven by Reynolds forcing at various locations throughout the domain (see Fig. 1.12a). However, decreasing the Ekman number results in more prominent torsional waves that can be the dominant portion of the short timescale flow (see the models in Fig. 1.12b-d). The dominance of torsional waves in the models coincides with a transition to regimes in which wave excitation is found only at the tangent cylinder, is provided by the Lorentz force and gives rise to periodic wave patterns operating on approximately 4 to 5 year timescales. Teed et al. (2015) also noted that the core travel times of their waves became independent of rotation at low Ekman number, with many

converging to 'Earth-like' values of around 4 years.

1.7 Aims and structure of the thesis

The aim of this thesis is to use numerical simulations to answer the following questions regarding torsional Alfvén waves in Earth's core and their influence on geomagnetic secular variation:

1. What are the fundamental propagation characteristics of torsional Alfvén waves?
2. What are the implications of these propagation characteristics on torsional waves in Earth's core?
3. Are torsional wave-induced perturbations to the ambient magnetic field resolvable in SV data?
4. Can torsional waves produce signals in secular variation that are consistent with geomagnetic jerks?

Chapter 2 describes various analytic and numerical methods used to solve simple wave equations and discusses their application to the torsional wave equation. The development and testing of the numerical models used in this work is also discussed in that chapter. The results of the torsional wave forward models are presented and discussed in chapter 3, which elucidates the answers to questions 1 and 2 of the above list. Chapter 4 uses the results contained in the preceding chapter to produce synthetic geomagnetic secular variation data for propagating torsional waves. Questions 3 and 4 of the above list are answered in that chapter. The thesis ends in chapter 5 with some concluding remarks and suggestions for future extensions to the current study.

Chapter 2

1-D modelling: numerical methods

Many propagation phenomena can be mathematically described as solutions to a hyperbolic partial differential equation (PDE). Indeed, the 1-D Cartesian wave equation is the prototype hyperbolic PDE, and the torsional wave equation also belongs to this subset of time-dependent differential equations. Some simple PDEs can be solved analytically; for example, as is shown shortly, explicit solutions to the 1-D Cartesian wave equation (e.g. Morse & Feshbach, 1953) and to the torsional wave equation in a cylinder (constant z_T, Mound & Buffett (2007)) can be derived. However, explicit solutions to more complicated differential equations are often unknown and so their solutions must be approximated numerically. To do this, accurate numerical methods must be employed. There are several categories of numerical methods available, which include finite differences, finite elements and spectral methods. The application of certain analytic and finite difference methods to the 1-D Cartesian wave equation and the torsional wave equation is the subject of this chapter. We begin by solving the 1-D Cartesian wave equation and the equation describing torsional waves in a cylinder, analytically, to find the normal modes of the systems and discuss how these normal modes can be used to investigate how waves propagate over time. We then explore how various finite difference numerical schemes could be implemented to produce models of torsional waves. The accuracy and convergence of our proposed numerical algorithms are verified by benchmarking numerical results against the known analytic solutions for simple test cases. Finally, we describe how these benchmarked numerical methods

can be extended to solve the more challenging problem of torsional wave propagation in the Earth's core. Discussion of the results of these torsional wave models is left until the following chapter.

2.1 Analytic solutions to simplified wave equations

In this section, the 1-D Cartesian wave equation and a simplified version of the 1-D torsional wave equation are solved analytically. Although these equations are much simpler than those governing the evolution of torsional waves in the outer core, this is a useful exercise because knowledge of analytic solutions allows us to test proposed numerical algorithms before confronting more complicated physical problems.

2.1.1 1-D wave equation in Cartesian coordinates

The simplest possible wave (a 'wave on a string') is represented by the 1-D wave equation in Cartesian coordinates

$$\frac{\partial^2 \Psi(x,t)}{\partial t^2} = c^2 \frac{\partial^2 \Psi(x,t)}{\partial x^2}, \tag{2.1}$$

where Ψ is the wave velocity, x is the spatial coordinate, t is time and c is the wave group speed. This equation is readily solved using the separation of variables method, where we suppose that the solution $\Psi(x,t)$ constitutes a product of two separate functions of x and t. Substituting $\Psi(x,t) = X(x)T(t)$ into equation (2.1) gives

$$\frac{1}{c^2}\frac{1}{T(t)}\frac{d^2T(t)}{dt^2} = \frac{1}{X(x)}\frac{d^2X(x)}{dx^2} = -k^2, \tag{2.2}$$

where k is a constant. The spatial solution of equation (2.2) takes the form

$$X(x) = A_1 \cos(kx) + A_2 \sin(kx), \tag{2.3}$$

where A_1 and A_2 are arbitrary constants to be determined by the boundary conditions.

For example, assuming that a string of length L is fixed at both ends for all time, the no-slip boundary conditions $\Psi(0,t) = 0$ and $\Psi(L,t) = 0$ may be used to deduce that $A_1 = 0$ and $kL = m\pi$, where m is an integer. This gives the spatial solution below

$$X_m(x) = A_m \sin\left(\frac{m\pi x}{L}\right) \tag{2.4}$$

for a particular value of m.

The temporal part of equation (2.2) is

$$\frac{1}{T}\frac{\partial^2 T}{\partial t^2} = -\omega^2, \tag{2.5}$$

where $\omega = ck$, which has solutions of the form

$$T_m(t) = B_m \cos(\omega_m t) + C_m \sin(\omega_m t), \tag{2.6}$$

where B_m and C_m are arbitrary constants for each value of m.

For example, the initial condition $\frac{\partial \Psi}{\partial t}\Big|_{x,t=0} = 0$ gives $C_m = 0$ and so a solution to equation (2.1) is

$$\Psi_m(x,t) = A_m \sin\left(\frac{m\pi x}{L}\right) \cos(\omega_m t), \tag{2.7}$$

where each value of m describes a single normal mode (eigenvalue) of the system. The general solution is a linear sum over all possible values of m (i.e. over all of the normal modes)

$$\Psi(x,t) = \sum_{m=1}^{\infty} D_m \sin\left(\frac{m\pi x}{L}\right) \cos(\omega_m t), \tag{2.8}$$

where D_m is an arbitrary constant for each value of m.

2.1.2 1-D torsional waves in a cylinder

The canonical version of the 1-D torsional wave equation is

$$\frac{\partial^2 \omega_g}{\partial t^2} = \frac{1}{s^3 \mu_0 \rho_0 z_T} \frac{\partial}{\partial s}\left(s^3 z_T \{B_s^2\} \frac{\partial \omega_g}{\partial s}\right). \tag{2.9}$$

This section outlines an analytic solution of (2.9) when the equation is simplified by using a constant z_T, which corresponds to a completely fluid cylindrical core, and a constant $\{B_s^2\}$ profile. Taking the z_T and $\{B_s^2\}$ terms outside the spatial derivative gives

$$\frac{\partial^2 \omega_g}{\partial t^2} = \frac{\{B_s^2\}}{s^3 \mu_0 \rho_0} \frac{\partial}{\partial s} \left(s^3 \frac{\partial \omega_g}{\partial s} \right)$$

$$= \frac{\{B_s^2\}}{s^3 \mu_0 \rho_0} \left(s^3 \frac{\partial^2 \omega_g}{\partial s^2} + 3s^2 \frac{\partial \omega_g}{\partial s} \right)$$

$$= \frac{\{B_s^2\}}{\mu_0 \rho_0} \left(\frac{\partial^2 \omega_g}{\partial s^2} + \frac{3}{s} \frac{\partial \omega_g}{\partial s} \right). \tag{2.10}$$

Equation (2.10) can now be solved by separation of variables, supposing that the angular speed $\omega_g(s,t)$ constitutes a product of two separate functions of s and t such that $\omega_g(s,t) = \Phi(s)T(t)$. This substitution yields

$$\Phi(s) \frac{d^2 T(t)}{dt^2} = \frac{\{B_s^2\}}{\mu_0 \rho_0} T(t) \left(\frac{d^2 \Phi(s)}{ds^2} + \frac{3}{s} \frac{d\Phi(s)}{ds} \right), \tag{2.11}$$

where the functions for space and time are now found individually. We now define a constant $\alpha^2 = \{B_s^2\}/\mu_0 \rho_0$ and solve the torsional wave equation for general α.

$$\frac{1}{T} \frac{d^2 T}{dt^2} = \alpha^2 \left(\frac{1}{\Phi} \frac{d^2 \Phi}{ds^2} + \frac{3}{s\Phi} \frac{d\Phi}{ds} \right) = -k^2, \tag{2.12}$$

where k is a constant. The time equation

$$\frac{1}{T} \frac{d^2 T}{dt^2} = -k^2, \tag{2.13}$$

has solutions of the form

$$T(t) = A_1 \cos(kt) + A_2 \sin(kt), \tag{2.14}$$

where A_1 and A_2 are arbitrary constants. The spatial part of (2.12) is a modified Bessel equation

$$\frac{d^2 \Phi}{ds^2} + \frac{3}{s} \frac{d\Phi}{ds} + \left(\frac{k}{\alpha} \right)^2 \Phi = 0 \tag{2.15}$$

whose solutions take the form

$$\Phi(s) = \frac{1}{s} \left(B_1 J_1 \left(\frac{ks}{\alpha} \right) + B_2 Y_1 \left(\frac{ks}{\alpha} \right) \right), \tag{2.16}$$

where $J_1(ks/\alpha)$ and $Y_1(ks/\alpha)$ are Bessel functions of order one of the first and second kind respectively and B_1 and B_2 are arbitrary constants.

The boundary conditions are now used to remove any unphysical parts of the solutions at the origin and to determine the constants B_1, B_2 and k. The rotation axis of a cylindrical system is not a physical boundary, but a singular point of the cylindrical coordinate system. Care must be taken that the physical solution, itself regular at $s = 0$, is not subject to such singularities. Lewis & Bellan (1990) detail the mathematical constraints that impose regularity on the solution at the origin in cylindrical coordinates. They state that the general form for the ϕ-component of any axisymmetric vector, $\boldsymbol{u}$, in cylindrical coordinates is

$$u_\phi = sf(s^2), \tag{2.17}$$

where f is any smooth function of s^2, which implies that the linear velocity u_ϕ (where $\omega_g = u_\phi/s$) is zero at the rotation axis for all time. Setting $u_\phi = 0$ at $s = 0$ requires $B_2 = 0$ due to the singularity of Y_1, the Bessel function of the second kind, at the origin. Scaling the radius of the cylinder by a characteristic length scale leads to non-dimensional radius of $s = 1$. The no-slip boundary condition

$$u_\phi\Big|_{s=1} = 0 \tag{2.18}$$

at outer edge of the cylinder ($s = 1$) can then be used to find the eigenvalues, k, of the system. Thus, k/α are the zeroes of $J_1(s)$. The n-th mode of ω_g is described by

$$(\omega_g)_n = (A_1^n \sin(k_n t) + A_2^n \cos(k_n t))\frac{1}{s} J_1\left(\frac{k_n s}{\alpha}\right), \tag{2.19}$$

where the arbitrary constants A_1^n and A_2^n now depend on n. The general solution to equation (2.10) is then a sum over all the possible n values

$$\omega_g = \sum_{n=1}^{\infty} (A_1^n \sin(k_n t) + A_2^n \cos(k_n t))\frac{1}{s} J_1\left(\frac{k_n s}{\alpha}\right). \tag{2.20}$$

These normal mode solutions can be used to test the numerical schemes discussed in the next section before they are implemented to study the more complicated problem of torsional wave propagation in the Earth's core.

2.2 Numerical schemes

In this section, we discuss two independent methods of investigating wave evolution in both Cartesian and cylindrical coordinates. The first method is a normal mode approach in which an initial profile is projected onto a set of basis functions and then evolved through time. This method relies on knowledge of the analytic solutions to equations (2.1) and (2.9), which were derived in sections 2.1.1 and 2.1.2 respectively. The second method uses a time-stepping finite difference algorithm to study the evolution of an initial wave pulse.

2.2.1 Normal mode projections

As discussed in the previous section, the analytic spatial solutions to the 1-D wave equations previously considered take the form of sine waves in Cartesian coordinates and Bessel functions in cylindrical coordinates. These are therefore the appropriate basis functions onto which we project an initial profile f. We then exploit the orthogonality properties of these basis functions to calculate the coefficient of each mode (i.e. the contribution of each mode to the projection). To illustrate this point, consider an arbitrary initial profile described by an infinite sum of sine waves in Cartesian coordinates

$$f(x) = \sum_{m=1}^{\infty} c_m \sin(m\pi x), \tag{2.21}$$

where c_m is the contribution of a particular mode m. Multiplying both sides of equation (2.21) by $\sin(n\pi x)$ and integrating with respect to x gives

$$\int_0^1 f(x) \sin(n\pi x) dx = \int_0^1 \sum_{m=1}^{\infty} c_m \sin(m\pi x) \sin(n\pi x) dx, \tag{2.22}$$

from which it is easy to deduce that each coefficient, c_m, is given by

$$c_m = 2 \int_0^1 f(x) \sin(m\pi x) dx \tag{2.23}$$

since the sine function obeys the following orthogonality condition (e.g. Boas, 2006; pp. 575)

$$\int_0^1 \sin(m\pi x) \sin(n\pi x) dx = \frac{1}{2} \delta_{mn}, \tag{2.24}$$

where δ_{mn} is the Kronecker delta.

If an arbitrary initial profile f, satisfying the regularity condition of equation (2.17) and the no-slip boundary condition of equation (2.18), is now defined in cylindrical coordinates as a function of cylindrical radius, $f(s)$ is projected onto (2.20) by assuming that the profile may be constructed using an infinite sum of Bessel functions as follows

$$f(s) = \sum_{m=1}^{\infty} b_m J_\nu(\alpha_{\nu m} s), \tag{2.25}$$

where $\alpha_{\nu m}$ is the m-th zero of J_ν and $\nu = 1$. We then multiply both sides by a factor of $sJ_\nu(\alpha_{\nu n} s)$ and integrate both sides with respect to s. This allows us to make use of the following orthogonality property of the Bessel functions of the first kind (e.g. Boas, 2006; pp. 601)

$$\int_0^1 J_\nu(\alpha_{\nu m} s) J_\nu(\alpha_{\nu n} s) s ds = \frac{1}{2}[J_{\nu+1}(\alpha_{\nu m})]^2 \delta_{mn} \tag{2.26}$$

to find an expression for the coefficient of each mode

$$b_m = \frac{\int_0^1 f(s) J_\nu(\alpha_{\nu m} s) s ds}{\frac{1}{2}[J_{\nu+1}(\alpha_{\nu m})]^2}. \tag{2.27}$$

Of course, in practice it is not feasible to project onto an infinite sum of normal modes and we must therefore choose a number of modes that is both practical and gives a converged solution. A converged solution is one that does not change upon increasing resolution (adding more modes), which is essential because any initial misfit between the initial profile and its normal mode projection will be amplified with time. This amplification could then introduce spurious wave characteristics that are simply numerical artefacts. The relative magnitude of the normal mode coefficients and the convergence of the projections at different stages of the wave evolution were investigated in order to determine how many modes are required to represent the wave with sufficient accuracy (see the next section). Having chosen a suitable resolution, we then introduced the companion time dependent functions, complex exponentials, to evolve the wave through time and investigate its propagation.

2.2.1.1 Convergence testing

Before using normal mode projections to examine wave propagation, it is first necessary to determine how many normal modes are required to represent the initial profile with sufficient accuracy. This was done using two methods; first, by calculating the

coefficient magnitude of each mode and second, by examining the convergence of the L^2-norm between projections using successively larger numbers of modes. The second convergence test involves projecting onto a certain number of modes n, and then $n+5$ modes and calculating the L^2-norm of the difference between the two projections such that

$$\left\| f(x)_{n+5} - f(x)_n \right\|_2 = \left[\int_0^1 \left(f(x)_{n+5} - f(x)_n \right)^2 dx \right]^{\frac{1}{2}}, \tag{2.28}$$

where the subscripts on $f(x)$ denote the number of modes used in the projection. Perfect convergence would be when this norm falls to zero, which is not possible in practice because a perfect representation of the initial profile would require an infinite number of modes.

As a demonstration of this normal mode projection method, consider a Gaussian-like initial wave profile defined in Cartesian geometry as

$$f(x) = Ax^2(x-1)^2 e^{-\left(\frac{x-0.5}{0.1}\right)^2}, \tag{2.29}$$

where A is a constant chosen such that the maximum value of the profile is 1, see Fig. 2.6a. This initial profile is a smooth bell-shaped curve that is centred about $x = 0.5$, the midpoint of the domain, and satisfies our chosen boundary conditions. The absolute magnitude of the contributions of the first 100 normal modes are shown in Fig. 2.1.

There are two clear trends in the coefficient magnitudes, corresponding to the odd and even values of the number of the normal mode, m. The even m values have very low magnitudes of $\mathcal{O}(10^{-22})$ to $\mathcal{O}(10^{-30})$ in the plot; the normal mode calculations were performed in Maple using a precision of 30 digits. This implies that these coefficients are actually zero, rather than $\mathcal{O}(10^{-30})$, and that only the odd normal mode numbers contribute to the projection. Given the symmetry of the initial profile, this result is unsurprising and may be explained as follows. As described in section 2.2.1, the orthogonality properties of the basis functions are used to calculate each coefficient. The chosen initial profile is an even function (symmetric) about $x = 1/2$, the midpoint of the domain, whereas $\sin(m\pi x)$ is an odd function (antisymmetric) about $x = 1/2$ for even values of m. This means that the integral $\int_0^1 f(x) \sin(m\pi x) dx$ is zero for even m because the integrand is an odd function. For odd m, the integrand is an

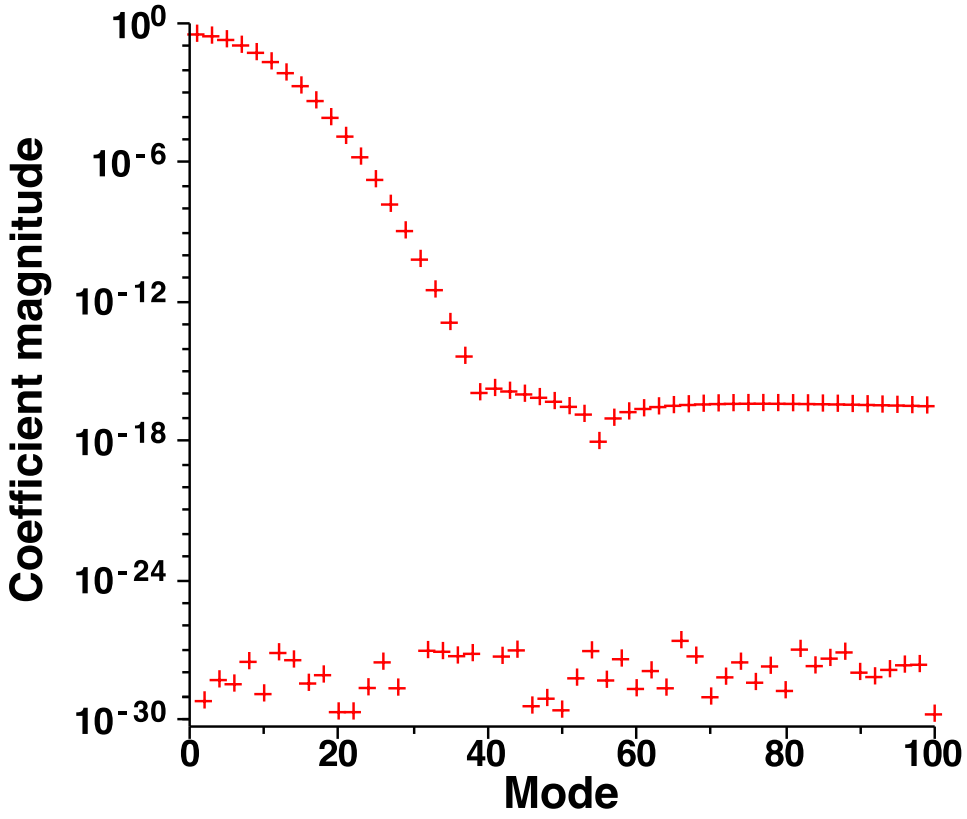

Figure 2.1: The absolute magnitude of the coefficients of the first 100 normal modes, $|c_m|$, for the projection of the initial profile given by equation (2.29) onto sine functions.

even function, because both the initial profile and $\sin(m\pi x)$ are even functions, and so non-zero coefficients c_m are obtained. These modes show a decrease in magnitude with increasing m, which is expected because the initial profile is a smooth bell-shaped curve and easily represented by the large-scale normal modes.

Fig. 2.2 shows the L^2-norm between the projection of the initial profile using successive numbers of normal modes (e.g. 5 and 10 modes, 10 and 15 modes and so on), with the final point showing the difference in the projection of 100 and 105 modes. The figure shows a rapid drop in this norm, which indicates that a well-resolved projection is achieved using the first few normal modes.

Perfect convergence is reached when this norm, or $|c_m|$, falls to zero because this means that adding more normal modes results in no change to the projection. In practice, this is not possible because a perfect projection requires an infinite number of modes. One convergence criterion that could be used is when $|c_m|$ reaches a certain threshold, below which any non-zero coefficients are considered as noise. For the purposes of the

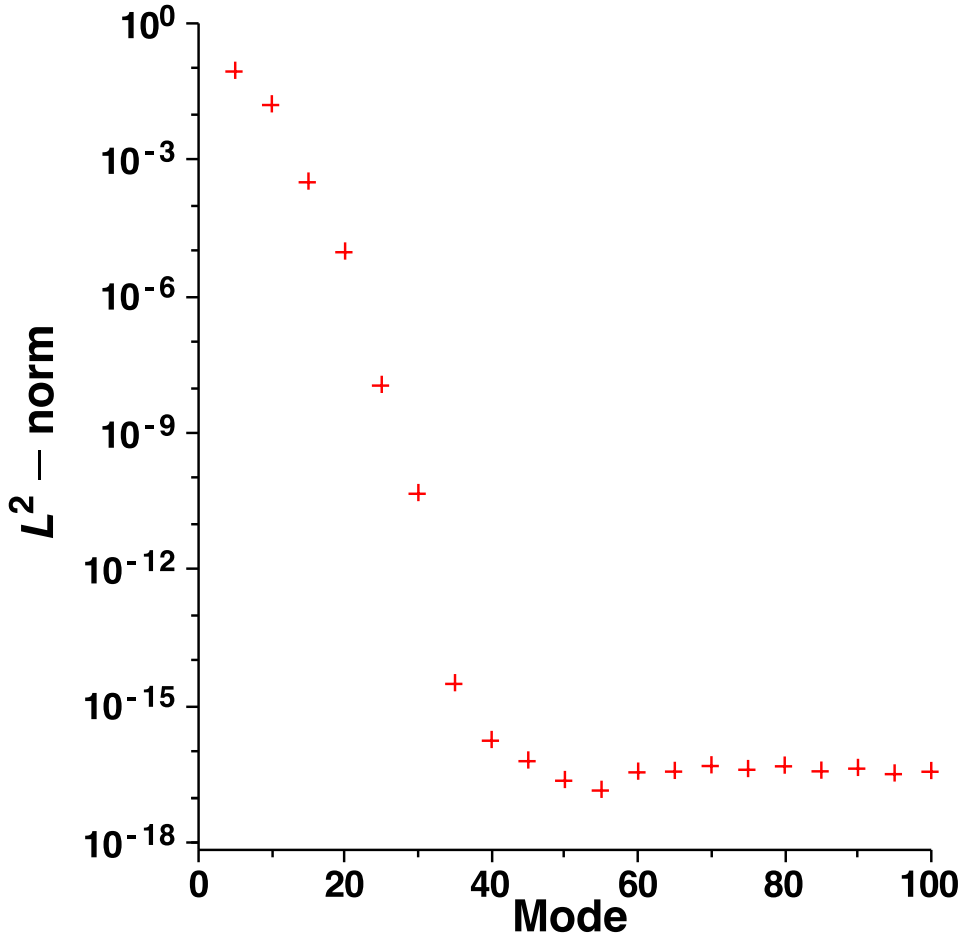

Figure 2.2: The L^2-norm, given by equation (2.28), of the difference between a projection of the initial profile described by equation (2.29) onto a certain number of sine modes, n, and a projection onto $n+5$ modes. The values on the horizontal axis show the lower resolution projection. For example, the leftmost data point shows the norm of the difference between a projection using 5 modes and a projection using 10 modes and the rightmost point shows the norm between projections using 100 and 105 normal modes.

discussion in this section, the threshold is set to 10^{-10}. In this case, both Figs. 2.1 and 2.2 show that approximately 30 normal modes, i.e. the first 15 normal modes with odd m, are sufficient to represent the initial profile given by equation (2.29).

Now considering the convergence of the projection of the same initial profile defined in a cylindrical geometry as

$$f(s) = As^2(s-1)^2 e^{-\left(\frac{s-0.5}{0.1}\right)^2}, \tag{2.30}$$

where A is a constant chosen such that the maximum value of the profile is 1, see Fig. 2.9a. Again, this initial profile is a smooth bell-shaped curve that is centred about

$s = 0.5$, the midpoint of the domain. The absolute magnitude of the contributions of the first 100 normal modes are shown in Fig. 2.3. In this geometry, projection of the initial profile requires normal modes with both odd and even m normal modes because the modes are not symmetric about $s = 1/2$. As in the Cartesian projection, there is a rapid drop off in the coefficient magnitudes $|b_m|$ because the chosen initial profile is smooth and easily represented by large-scale normal modes. Fig. 2.4 shows the L^2-norm between the projection of the wave profile using successive numbers of normal modes (e.g. 5 and 10 modes, 10 and 15 modes and so on), defined by

$$\left\| f(s)_{n+5} - f(s)_n \right\|_2 = \left[\int_0^1 \left(f(s)_{n+5} - f(s)_n \right)^2 ds \right]^{\frac{1}{2}}, \tag{2.31}$$

where the subscripts on $f(s)$ denote the number of modes used in the projection. The final point shows the difference in the projection of 100 and 105 modes. The figure shows a rapid drop in this norm, which indicates that a well-resolved projection is achieved using the first few normal modes. Again using a threshold value of 10^{-10}, both figures 2.3 and 2.4 show that the first 30 normal modes are sufficient to represent the initial profile.

The convergence tests described above are valid only for the specific initial profiles described by equations (2.29) and (2.30) and do not account for any time variation in the wave profiles. It should be noted that smaller scale features may be introduced into the system during wave propagation, which may not be well-resolved if the resolution adopted does not include enough normal modes. Convergence tests such as those described above were performed for every initial profile used in this work, and at several different times during wave evolution to ensure that the initial profile projection is sufficient to resolve all features that occur during wave evolution. Examples of wave evolutions obtained using the normal mode projection method will be discussed in the benchmarking section, 2.4.

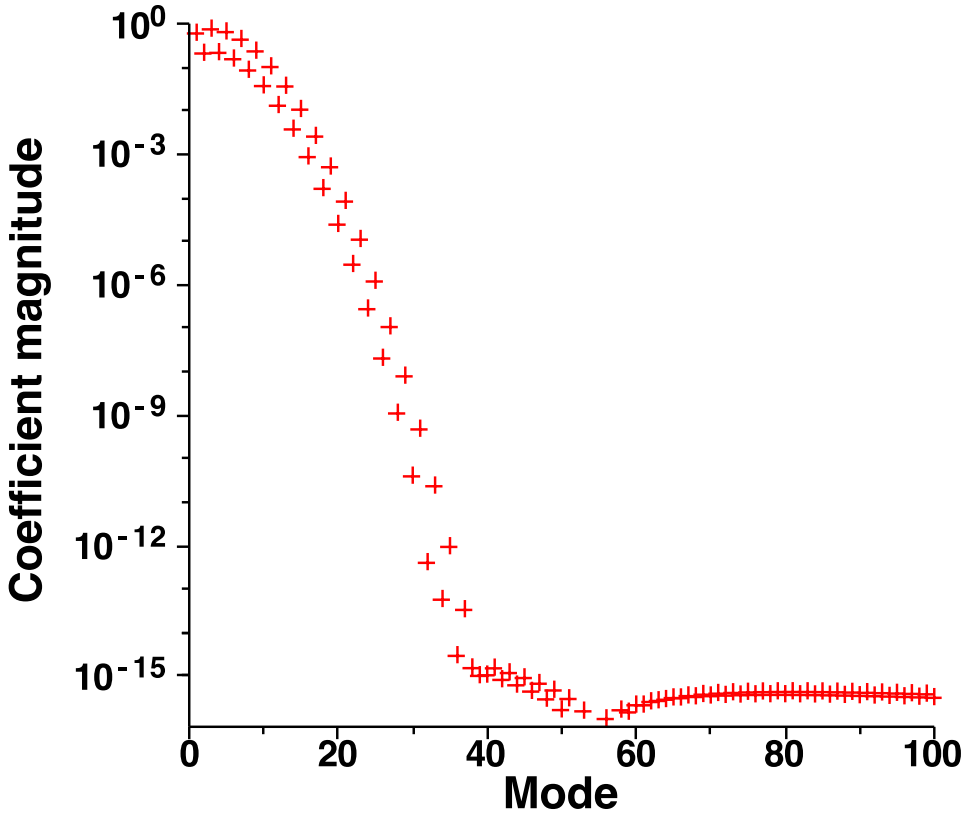

Figure 2.3: The absolute magnitude of the coefficients of the first 100 normal modes, $|b_m|$, for the projection of the initial profile given by equation (2.30), defined as a function of s in cylindrical geometry, onto Bessel functions.

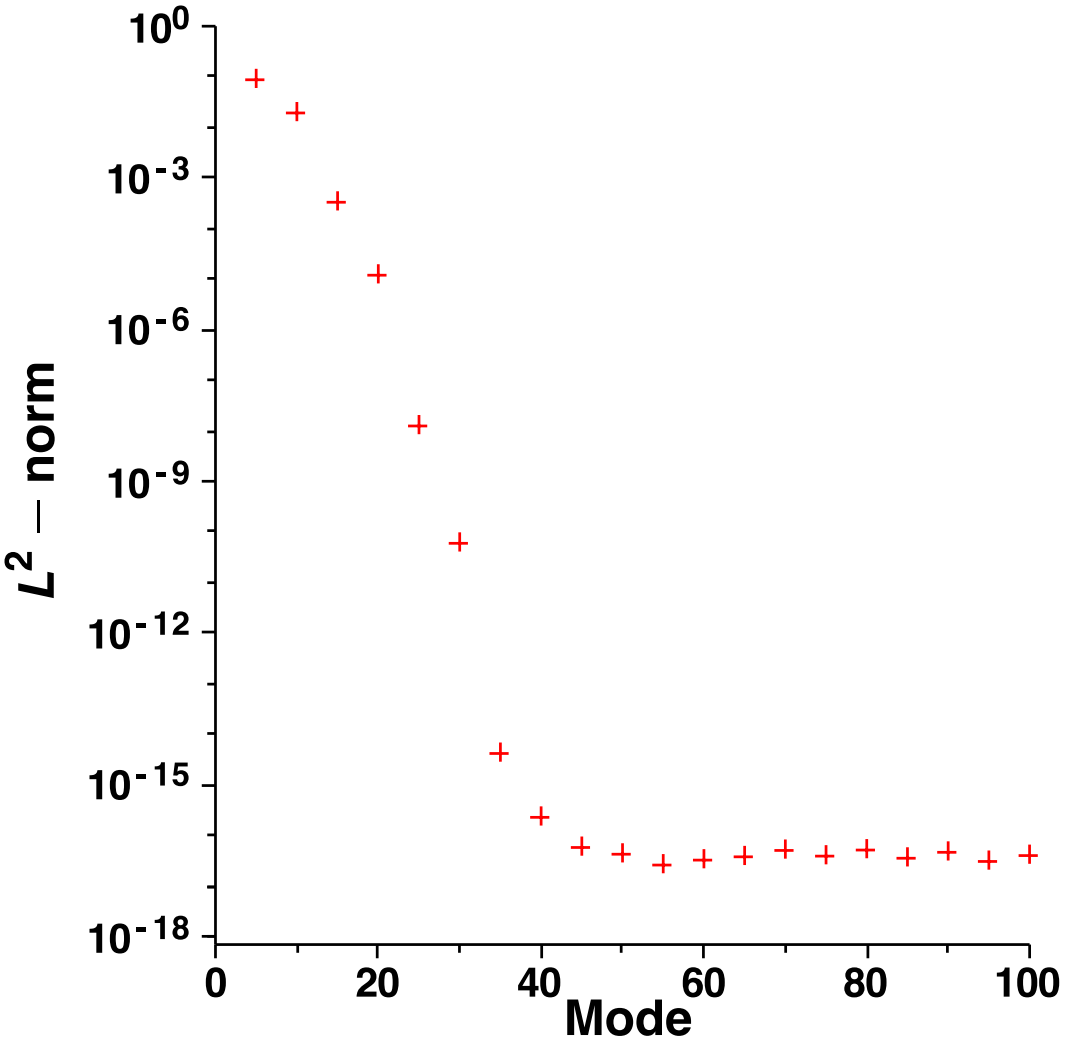

Figure 2.4: The L^2-norm, given by equation (2.31), of the difference between a projection of the initial profile described by equation (2.30) onto a certain number of Bessel modes, n, and a projection onto $n + 5$ modes. The values on the horizontal axis show the lower resolution projection. For example, the leftmost data point shows the norm of the difference between a projection using 5 modes and a projection using 10 modes and the rightmost point shows the norm between projections using 100 and 105 normal modes.

2.2.2 Finite difference codes

Finite difference (FD) methods are techniques that approximate the solution to differential equations by replacing the continuous derivatives by numerical differentiation formulae. These formulae are then applied to discrete meshes, with the value at one node, x_0 say, being dependent upon a linear combination of the sampled values at nearby points. To do this, we must discretise the problems under consideration in space and in time. As an example of this method, we now consider a 1-D Cartesian 'wave on a string' given by equation (2.1). In this geometry, we have a grid of N interior nodes x_i with constant spacing Δx such that $x_i = i\Delta x$, $i = 1..N$, where $\Delta x = \frac{L}{N+1}$ when the equations are solved in the spatial domain 0 to L. Time is discretised in a similar manner such that $t_j = j\Delta t$, where Δt is the time step. We then apply the following differentiation formulae to each node, except where the values are given by boundary conditions, in order to develop an appropriate numerical algorithm

$$\frac{\partial \Psi}{\partial x}(x_i, t_j) = \Psi'(x_i, t_j) = \frac{\Psi(x_{i+1}, t_j) - \Psi(x_{i-1}, t_j)}{2\Delta x} + \mathcal{O}((\Delta x)^2) \tag{2.32}$$

$$\frac{\partial^2 \Psi}{\partial x^2}(x_i, t_j) = \Psi''(x_i, t_j) = \frac{\Psi(x_{i+1}, t_j) - 2\Psi(x_i, t_j) + \Psi(x_{i-1}, t_j)}{(\Delta x)^2} + \mathcal{O}((\Delta x)^2) \tag{2.33}$$

$$\frac{\partial^2 \Psi}{\partial t^2} = \Psi''(x_i, t_j) = \frac{\Psi(x_i, t_{j+1}) - 2\Psi(x_i, t_j) + \Psi(x_i, t_{j-1})}{(\Delta t)^2} + \mathcal{O}((\Delta t)^2). \tag{2.34}$$

The FD scheme may be explicit, which calculates the state of the system at a later time based on the current state, or implicit, which uses both the current and later state. Although explicit schemes are easier to implement and less numerically intensive than implicit schemes, they often require very small time steps for numerical stability. A requirement for numerical stability is the Courant-Friedrichs-Lewy (CFL) condition

$$\gamma = \frac{c\Delta t}{\Delta x} \leq 1 \tag{2.35}$$

which relates the wave speed c, the stable time step and spatial resolution (e.g. Press et al., 1992; pp. 1034). However, not all stable schemes give accurate results. To obtain solutions that are accurate and converged, the spatial resolution must be sufficiently high and the time step must be small enough to resolve the intrinsic timescales of the

system. In the case of a wave equation, this timescale corresponds to the time taken for the wave to travel between adjacent nodes. The convergence of numerical solutions obtained by FD schemes was investigated by varying the time step and number of grid points in order to determine the appropriate resolution before producing forward models of waves. Details of an example FD scheme used to solve the Cartesian wave equation are given below. Substituting the FD approximations of equations (2.33) and (2.34) into the 1-D Cartesian wave equation, (2.1), and rearranging terms leads to the following iterative scheme

$$\Psi(x_i, t_{j+1}) = \alpha^2\Psi(x_{i+1}, t_j) + 2(1-\alpha^2)\Psi(x_i, t_j) + \alpha^2\Psi(x_{i-1}, t_j) - \Psi(x_i, t_{j-1}) \quad (2.36)$$

where $\alpha = c\Delta t/\Delta x$. Taking into account the no-slip boundary conditions discussed in section 2.1.1, this system may be rewritten in matrix form as follows

$$\boldsymbol{\Psi}^{j+1} = D\boldsymbol{\Psi}^j - \boldsymbol{\Psi}^{j-1} \quad (2.37)$$

where D is a tridiagonal matrix with elements

$$D = \begin{pmatrix} 2(1-\alpha^2) & \alpha^2 & & & \\ \alpha^2 & 2(1-\alpha^2) & \alpha^2 & & \\ & \alpha^2 & \ddots & \ddots & \\ & & \ddots & \ddots & \alpha^2 \\ & & & \alpha^2 & 2(1-\alpha^2) \end{pmatrix} \quad (2.38)$$

and the entries of $\boldsymbol{\Psi}^j$ are the numerical approximations at the interior nodes at time t_j

$$\boldsymbol{\Psi}^j = \begin{pmatrix} \Psi(x_1, t_j) \\ \Psi(x_2, t_j) \\ \vdots \\ \Psi(x_{N-1}, t_j) \\ \Psi(x_N, t_j) \end{pmatrix}. \quad (2.39)$$

This is a second-order implicit FD scheme; each iterate Ψ^{j+1} requires the values of the preceding two values, Ψ^j and Ψ^{j-1}. This poses a problem because initially we have no information about the second iterate (at time $t = \Delta t$), which is needed to start the sequence of iterations. In this scheme, the first iterate Ψ^1 is determined by the initial

position profile $f(x)$ and the second iterate Ψ^2 is either filled in using values calculated by normal mode projections or determined using an explicit first-order Euler step. One way to avoid this necessity is to write the second-order wave equation (2.1) as a system of first-order differential equations such that

$$\frac{\partial \Psi}{\partial t} = \frac{\partial v}{\partial x} \tag{2.40}$$

and

$$\frac{\partial v}{\partial t} = c^2 \frac{\partial \Psi}{\partial x}, \tag{2.41}$$

where v is an auxiliary variable. This leads to the following iterative system

$$\boldsymbol{v}^{j+1} = \frac{c^2 \Delta t}{(\Delta x)^2} E \boldsymbol{\Psi}^j + \boldsymbol{v}^j \tag{2.42}$$

where E is a tridiagonal matrix with elements

$$E = \begin{pmatrix} -2 & 1 & & & \\ 1 & -2 & 1 & & \\ & 1 & \ddots & \ddots & \\ & & \ddots & \ddots & 1 \\ & & & 1 & -2 \end{pmatrix} \tag{2.43}$$

and the entries of $\boldsymbol{\Psi}^j$ and $\boldsymbol{v}^j$ are, respectively, the numerical approximations to the solution and its first time derivative at the interior nodes at time t_j. As equations (2.40) and (2.41) are first-order in time, an initial profile for $\boldsymbol{\Psi}$ and $\boldsymbol{v}$ is sufficient to commence the sequence of iterations. The centred difference approximation to a first derivative, described by equation (2.32), is used to ensure that the scheme retains second-order accuracy in space and time. This technique of using an auxiliary variable to reduce the order of the system will prove useful when solving the torsional wave equation because it ensures that iterations can be started by specifying a single initial condition for each variable. The normal mode solutions to the torsional wave equation in Earth-like geometries are unknown, so this information cannot be used to 'infill' missing iterates at the start of wave propagation as is possible for simpler cases with known solutions.

Having considered the simplest possible case, the 1-D 'wave on a string', we now con-

sider the numerical schemes that can be used to solve the 1-D torsional wave equation given by (2.9). As previously discussed, its canonical form is

$$\frac{\partial^2 u_\phi}{\partial t^2} = \frac{1}{s^2 \mu_0 \rho_0 z_T} \frac{\partial}{\partial s} \left(s^3 z_T \{B_s^2\} \frac{\partial \left(\frac{u_\phi}{s} \right)}{\partial s} \right). \qquad \text{(2.9 revisited)}$$

Introducing an auxiliary variable, τ, we separate the second-order torsional wave equation (2.9) into two first-order differential equations as follows

$$\frac{\partial u_\phi}{\partial t} = \frac{1}{\mu_0 \rho_0 z_T s^2} \frac{\partial \tau}{\partial s}, \qquad (2.44)$$

$$\frac{\partial \tau}{\partial t} = s^3 z_T \{B_s^2\} \frac{\partial \left(\frac{u_\phi}{s} \right)}{\partial s}, \qquad (2.45)$$

following Canet et al. (2009). Equations (2.44) and (2.45) are solved, respectively, for u_ϕ and τ on separate staggered equally spaced grids using the finite difference schemes described below.

2.2.2.1 The second-order staggered leapfrog method

The leapfrog FD scheme is widely used for the study of wave propagation and is second-order in both space and time (e.g. Press et al., 1992; pp.1038-1042). It is an efficient method that achieves second-order accuracy with only one function evaluation per time step and does not produce instabilities by amplifying oscillatory motion (e.g. Durran, 1991)). In a staggered scheme, variables are solved on grids that are shifted with respect to each other by half an interval (see Fig. 2.5). The variables u_ϕ (denoted u here) and τ are centred on half-mesh points as follows

$$\tau_{j+\frac{1}{2}}^{n} = (z_T)_{j+\frac{1}{2}} \{B_s^2\}_{j+\frac{1}{2}} s_{j+\frac{1}{2}}^3 \left[\frac{1}{s_{j+\frac{1}{2}}} \left(\frac{u_{j+1}^{n-\frac{1}{2}} - u_j^{n-\frac{1}{2}}}{\Delta s} \right) - \frac{u_{j+1}^{n-\frac{1}{2}} + u_j^{n-\frac{1}{2}}}{2 s_{j+\frac{1}{2}}^2} \right] \qquad (2.46)$$

$$u_j^{n+\frac{1}{2}} = \frac{1}{\mu_0 \rho_0 (z_T)_j s_j^2} \left[\frac{\tau_{j-\frac{1}{2}}^{n} - \tau_{j+\frac{1}{2}}^{n}}{\Delta s} \right], \qquad (2.47)$$

where the superscripts denote the time step and the subscripts denote the spatial node at which the equations are solved. The values for velocity are calculated on the integer

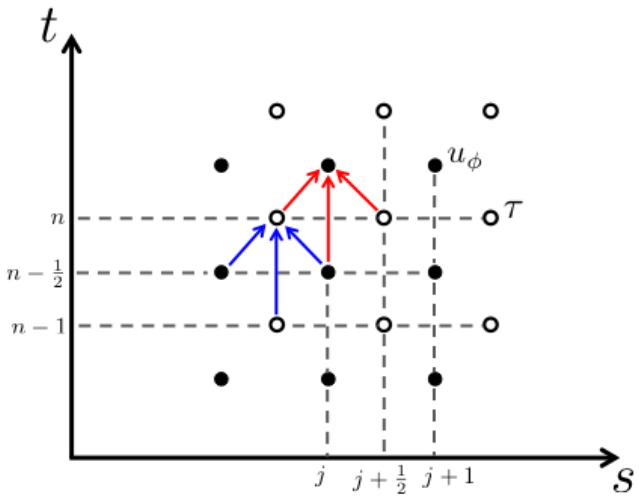

Figure 2.5: The grid on which wave equations are discretised when using the staggered leapfrog finite difference scheme. Note that the space and time mesh points are shifted with respect to each other by half an interval.

space nodes and half-integer time steps, whereas τ is calculated at the half-integer space nodes at the integer time steps so the time levels for one variable 'leapfrog' over time levels for the other variable. Substituting the above expressions into a forward Euler differencing, equations (2.33) and (2.34), gives these equations for the new values of τ and u_ϕ based on previously calculated values

$$\tau_{j+\frac{1}{2}}^{n+1} = \tau_{j+\frac{1}{2}}^{n} + (z_T)_{j+\frac{1}{2}}\{B_s^2\}_{j+\frac{1}{2}} s_{j+\frac{1}{2}}^3 \Delta t \left[\frac{1}{s_{j+\frac{1}{2}}} \left(\frac{u_{j+1}^{n+\frac{1}{2}} - u_j^{n+\frac{1}{2}}}{\Delta s} \right) - \frac{u_{j+1}^{n+\frac{1}{2}} + u_j^{n+\frac{1}{2}}}{2 s_{j+\frac{1}{2}}^2} \right] \tag{2.48}$$

and

$$u_j^{n+\frac{1}{2}} = u_j^{n-\frac{1}{2}} + \frac{\Delta t}{\mu_0 \rho_0 (z_T)_j s_j^2} \left[\frac{\tau_{j-\frac{1}{2}}^{n} - \tau_{j+\frac{1}{2}}^{n}}{\Delta s} \right]. \tag{2.49}$$

As this explicit scheme requires solutions at two previous times to calculate a new solution, a profile for each of u_ϕ and τ at times $t = \Delta t/2$ and $t = 0$, respectively, is sufficient to commence the sequence of iterations. Details of the initial and boundary conditions used in this study are given in section 2.3.

However, one problem with the leapfrog method is that its computational mode (a spurious part of the numerical solution that is not part of the physical solution) is

undamped (Durran, 1991). This undamped computational mode slowly amplifies to produce an instability called 'time-splitting' in numerical simulations of nonlinear fluid dynamics. One way to avoid this instability is the use of a Robert-Asselin filter (Robert (1966), Asselin (1972)), but this reduces the accuracy of the scheme from second-order to first-order.

2.2.2.2 The third-order Adams Bashforth method

The multistep differential equation solvers are a class of alternative time differencing schemes with damped computational modes (e.g. Press et al., 1992; pp. 942-946). Multistep methods approximate the solution to a differential equation by constructing a polynomial that passes through the solution at several previous time levels. The order of the scheme depends on how many previous values are required to calculate the new value. The third-order Adams-Bashforth scheme (AB3) belongs to this class of integration techniques and is an explicit finite difference scheme, requiring knowledge of the solution at three previous time steps in order to calculate the next solution. Like the leapfrog scheme, AB3 requires only one function evaluation per time step, though more storage is required due to the use of three previous time levels in every calculation. Its main advantages over the leapfrog scheme is that AB3 is not subject to the time-splitting instability and is of higher accuracy, being third-order in time $\mathcal{O}((\Delta t)^3)$ and second order in space $\mathcal{O}((\Delta s)^2)$. The maximum stable time step for AB3 is similar to that permitted by the filtered leapfrog scheme (Durran, 1991).

Considering an initial value problem of the form

$$\frac{d\psi}{dt} = F(\psi, t), \tag{2.50}$$

most numerical schemes, including the AB3 scheme, replace the differential equation for ψ with algebraic equations for the approximation to the true solutions at a set of discrete time levels. In this notation, we denote ξ_n as the approximate solution to (2.50) at time t_n where $t_n = n\Delta t$. The algebraic equations for the solution are solved repeatedly to step the solution forwards from the initial condition $\xi_0 = \psi_0$. The multistep methods approximate the solution to (2.50) by integrating the differential

equation over time intervals of Δt as follows

$$\psi(t_{n+1}) = \psi(t_n) + \int_{t_n}^{t_{n+1}} F(\psi(t), t)dt \tag{2.51}$$

and the algebraic equation of the particular numerical method provides an approximation to the integral of F (the right hand side of the differential equation). The AB3 method uses the following formula to approximate the solution to (2.50) at time t_{n+1}

$$\xi_{n+1} = \xi_n + \frac{\Delta t}{12}\left[23F(\xi_n) - 16F(\xi_{n-1}) + 5F(\xi_{n-2})\right]. \tag{2.52}$$

Reducing the second-order torsional wave equation (2.9) by splitting it into equations (2.44) and (2.45) gives two coupled first order time-dependent differential equations of the same form as (2.50). Equations (2.44) and (2.45) are solved, respectively, for u_ϕ and τ by time stepping the scheme described by (2.52), with the function F of the above example being replaced by the right-hand side of the relevant equation (2.44 or 2.45). The two equations are discretised in space and time on the same staggered equally spaced grids as that used in the leapfrog method, shown in Fig. 2.5. The time step Δt and the grid spacing Δs were chosen such that all models were converged. The sequence of iterations is started with an initial profile for each variable at time $t = 0$, an explicit first-order Euler step at time $t = \Delta t$ and a second-order Adams Bashforth step at time $t = 2\Delta t$. Details of the initial and boundary conditions used in this study are given in the next section.

2.3 Regularity and boundary conditions

The FD numerical schemes require that both u_ϕ and τ are defined on their respective spatial grids when iterations commence and that boundary conditions are imposed on u_ϕ at $s = 0$ and the outer boundary $s = r_c$. For models of torsional waves in the Earth's core, r_c corresponds to the equator of the core-mantle boundary (=3480 km). Despite the need for a boundary condition at $s = 0$, the rotation axis is not a physical boundary. As previously remarked upon in section 2.2.1, the rotation axis is a singular point of the cylindrical coordinate system. In order for the physical solution to remain regular at the origin, the ϕ-component of any axisymmetric vector in cylindrical coordinates

must satisfy

$$u_\phi = sf(s^2), \tag{2.17 revisited}$$

where f is any smooth function of s^2. The Taylor expansion of (2.17) includes only odd powers of s

$$u_\phi = a_0 s + a_1 s^3 + a_2 s^5 + ..., \tag{2.53}$$

from which it follows that $u_\phi = 0$ at the rotation axis. Dividing equation (2.17) by s and differentiating with respect to s yields

$$\frac{\partial(\frac{u_\phi}{s})}{\partial s}\Big|_{s=0} = 2sf'(s^2) = 0. \tag{2.54}$$

This means that the solution must satisfy constraints simultaneously imposed on both the velocity u_ϕ and $\frac{\partial\left(\frac{u_\phi}{s}\right)}{\partial s}$ at the rotation axis in cylindrical coordinates. Further differentiation of equation (2.54) would yield an infinite hierarchy of higher order conditions that must also be satisfied at $s = 0$. Numerically, we impose only the regularity condition $u_\phi = 0$ at $s = 0$ in our models; all other necessary conditions are automatically satisfied. Note that in subsequent discussions of torsional wave propagation we refer to interactions with, and reflections at, the 'boundary' at $s = 0$. The reader should regard these 'reflections' at the rotation axis as pseudo-reflections, because they occur at a singular point of the coordinate system and not at a physical boundary.

A boundary condition is also required for the outer boundary of the domain. Rigid boundaries, such as the Earth's CMB, require

$$\boldsymbol{u} \cdot \boldsymbol{n} = 0 \tag{2.55}$$

and

$$\boldsymbol{u} \times \boldsymbol{n} = \boldsymbol{0}, \tag{2.56}$$

where $\boldsymbol{n}$ is the normal vector to the velocity (e.g. Gubbins & Roberts, 1987). These are the 'no-slip' conditions, which state that flow cannot penetrate the boundary and that the tangential components of velocity must vanish at the boundary, implying that $\boldsymbol{u} = \boldsymbol{0}$ on the boundary. The no-slip condition is transmitted through the fluid via viscous effects, which cause fluid to adhere to a rigid boundary and give rise to shear stresses in the region immediately adjacent to the boundary. A thin boundary layer forms in this region, across which the velocity undergoes a rapid adjustment from its

mainstream value (in the bulk of the core fluid) to the value specified on the boundary. However, an inviscid fluid, as is considered in this work, has no viscosity and therefore feels no shear effects, even in the presence of a rigid boundary. In this case, the appropriate boundary condition is called 'stress-free', which replaces equation (2.56) with the requirement that the tangential stresses vanish on the boundary. For the azimuthal fluid flow involved in torsional waves, the stress-free condition is

$$\frac{\partial \omega_g}{\partial s}\Big|_{s=r_c} = 0 \tag{2.57}$$

(Jault & Légaut, 2005), which we impose at the equator of the CMB ($s = r_c$).

Theory predicts that with stress-free boundary conditions applied at the equator of the CMB, and no coupling between the fluid core and the mantle, total angular momentum of the core should be conserved. The total angular momentum of the waves, M_T, is the integral of the angular momentum density over the whole core

$$M_T = \int_0^{r_c} u_\phi s^2 z_T ds. \tag{2.58}$$

From the definition of $\frac{\partial u_\phi}{\partial t}$ given by equation (2.44), it follows that

$$\frac{\partial M_T}{\partial t} = \frac{1}{\mu_0 \rho_0} \int_0^{r_c} \frac{\partial \tau}{\partial s} ds = \frac{1}{\mu_0 \rho_0} [\tau]_0^{r_c}. \tag{2.59}$$

This integral vanishes if $\tau|_{s=r_c} = \tau|_{s=0}$ throughout wave evolution, which is guaranteed by the stress-free boundary condition at $s = r_c$ applied in equation (2.45) and, following Canet et al. (2009), by initially setting the variable τ to zero on the whole domain.

A Gaussian-like initial profile, that is not a normal mode solution to the torsional wave equation but satisfies the boundary and regularity conditions, is chosen for u_ϕ. Although the choice of initial profile is somewhat arbitrary, the Gaussian-like profile has several desirable properties; it is smooth, continuous and infinitely differentiable. Also, its simple shape allows the investigation of how the form of the pulse changes during the wave evolution. The initial profile is given by

$$u_\phi = A s^2 (s - r_c)^2 e^{-\left(\frac{s-(r_c/2)}{\sigma}\right)^2}, \tag{2.60}$$

where A is a constant chosen such that the maximum value of the profile is 1 and σ determines the width of the pulse. This profile is the same as that described in the

normal mode projection method section 2.2.1 when $\sigma = 0.1$.

2.4 Benchmarking

In this section, solutions to the 1-D Cartesian wave equation (2.1) and of torsional waves in a cylinder (2.9) obtained from the normal mode projection method and from finite difference schemes are shown. As the two methods are used to solve the same equation, but are mutually independent, comparison of the two sets of results provides a robust and convenient benchmark of the numerical schemes.

2.4.1 1-D 'wave on a string' benchmark

Fig. 2.6 shows profiles of a 1-D wave in Cartesian geometry at different times during its wave evolution, with the red continuous line representing the normal mode (analytic) solution to the wave equation and the blue crosses representing the results obtained using a leapfrog FD scheme on a staggered grid. In this test case, no-slip conditions ($\Psi = 0$) were used at both boundaries of the domain. There is excellent agreement between the analytic and numerical solutions, which is a demonstration of the suitability and accuracy of the implemented numerical methods. Fig. 2.7 is a space-time contour plot of the same wave evolution, with time along the horizontal axis and x on the vertical axis. Red indicates a positive wave amplitude and blue indicates a negative wave amplitude. The 1-D Cartesian wave equation does not define a magnitude for the velocity Ψ because it is linear and homogeneous, so the velocity in the plots is scaled by the amplitude of the initial pulse, which is given by equation (2.29). The FD scheme used 500 interior nodes, a time step of 0.00001 and a wave group speed of 1. The scheme therefore satisfies the CFL condition of equation (2.35) with $\gamma = 5 \times 10^{-3}$.

The wave begins as one large positive pulse that subsequently splits into two smaller pulses of equal amplitude (=0.5). These two pulses travel across the domain until they reflect from the no-slip boundaries at time $t = 0.5$. Upon reflection, the pulses change polarity (so that their amplitude becomes -0.5) and travel towards the midpoint of the domain. The two small negative pulses reach $x = 0.5$ at time $t = 1.0$ and form a large negative pulse that is the exact negative of the initial profile. The large negative pulse splits apart again and the two small pulses travel towards the domain boundaries.

Again, the pulses change sign upon reflection and two small positive pulses travel towards the midpoint of the domain. These two pulses join together to reform the original pulse when $t = 2.0$. The wave is symmetric about the midpoint $x = 0.5$ at all times. The recovery of the initial wave pulse is an expected result, as is the time at which this occurs. Any arbitrary wave can be decomposed into contributions from individual normal modes of the chosen system. For this 'wave on a string' example, the individual normal modes of the system all repeat with multiples of the same frequency and the initial wave profile is periodically recovered. As previously discussed, the general solution to equation (2.1) is a linear sum over all possible values of m

$$\Psi(x,t) = \sum_{m=1}^{\infty} A_m \sin\left(\frac{m\pi x}{L}\right)\cos(\omega_m t), \qquad \text{(2.8 revisited)}$$

whose m-th mode has a time dependence of $\cos(cm\pi t/L)$. If a wave travels at speed c along a string of length L, the m-th normal mode solution to the wave equation has period $T_m = 2L/mc$. Therefore, an arbitrary travelling wave solution of the system, which can be regarded as a superposition of the periodic normal modes, will itself be periodic in time and the whole system will repeat every time $t = 2L/c$. Substituting $t = t + \frac{2L}{c}$ leaves 2.8 (revisited) unchanged. In the example shown in this section, $L = 1$ and $c = 1$, and so the wave pattern should repeat every $t = 2.0$, as observed.

A solution to equation (2.1) will obey conservation of energy, which provides another test for numerical schemes. The total energy consists of the kinetic energy E_k plus the potential energy E_p such that

$$E(t) = \int_0^L E_k + E_p dx = \int_0^L \frac{1}{2}\left(\frac{\partial\Psi}{\partial t}\right)^2 dx + \frac{1}{2}c^2\int_0^L \left(\frac{\partial\Psi}{\partial x}\right)^2 dx. \qquad (2.61)$$

Differentiating equation (2.61) with respect to time gives

$$\begin{aligned}
\frac{dE}{dt} &= \int_0^L \frac{\partial \Psi}{\partial t}\frac{\partial^2 \Psi}{\partial t^2}dx + c^2 \int_0^L \frac{\partial \Psi}{\partial x}\frac{\partial^2 \Psi}{\partial x \partial t}dx \\
&= \int_0^L \frac{\partial \Psi}{\partial t}\frac{\partial^2 \Psi}{\partial t^2}dx + c^2 \left(\underbrace{\frac{\partial \Psi}{\partial t}\frac{\partial \Psi}{\partial x}\Big|_0^L}_{=0} - \int_0^L \frac{\partial \Psi}{\partial t}\frac{\partial^2 \Psi}{\partial x^2}dx \right) \\
&= \int_0^L \frac{\partial \Psi}{\partial t}\left(\underbrace{\frac{\partial^2 \Psi}{\partial t^2} - c^2\frac{\partial^2 \Psi}{\partial x^2}}_{=0 \text{ (since } \Psi \text{ is a solution to the wave equation)}} \right) dx \\
&= 0, \qquad (2.62)
\end{aligned}$$

which is the requirement for energy conservation because the total energy in the system must remain constant with time. The conservation of total energy was verified for both the normal mode and numerical solutions, to accuracies of 16 digits and a few parts in 10^5 respectively. Since the appropriate boundary condition for torsional waves in an inviscid core is stress-free (see §2.3), it is of interest to consider how a 1-D 'wave on a string' propagates with this condition imposed at the boundaries ($\frac{d\Psi}{dx} = 0$ at $x = 0$ and at $x = 1$). Fig. 2.8 is a space-time contour plot of the velocity of the 1-D 'wave on a string' with stress-free boundary condition imposed, using the same initial profile as the no-slip model discussed above. The initial wave pulse splits into two smaller pulses of amplitude 0.5 that traverse the domain and reflect from the boundaries. Upon reflection from the stress-free boundaries, there is no change of sign and the two positive wave pulses travel towards the midpoint of the domain, where they reform the initial pulse at time $t = 1.0$. The change in the time at which the initial pulse is recovered is due the application of the stress-free boundary condition. The analysis of initial pulse recovery previously discussed is valid only for no-slip boundaries because this was the boundary condition used to determine the general solution to the wave equation (2.1). The general solutions differs slightly if the stress-free boundary condition is used to determine the arbitrary constants.

2.4.2 Torsional waves in a cylinder

Fig. 2.10 shows profiles of a torsional wave in a cylinder of unit radius ($r_c = 1$) at different times during its wave evolution, with the red continuous line representing the normal mode (analytic) solution to the torsional wave equation and the blue crosses representing the results obtained using the AB3 finite difference scheme and the same resolution as in the previous Cartesian models (500 interior nodes and a time step of 0.00001). Fig. 2.10 is a space-time contour plot of the same wave evolution. In this example, the velocity obeys the regularity condition $u_\phi = 0$ at the rotation axis and the no-slip boundary condition $u_\phi = 0$ at the outer boundary $s = 1$. The no-slip boundary condition was imposed in this benchmarking test case because it is easier to implement exactly in the normal mode projection codes. Since the stress-free boundary condition of equation (2.57) is most appropriate for torsional waves modelled in an inviscid outer core, a numerical model using that boundary condition is discussed in the next chapter. As the purpose of this chapter is to describe the methods used to obtain results, we leave discussion of torsional wave evolution until the next chapter and comment only that there is excellent agreement between the analytic and numerical solutions.

Results from the second-order leapfrog (LF) finite difference scheme were also successfully benchmarked against the analytic solutions and AB3 results for torsional waves in a cylinder (not shown on figures because the LF results plot on top of the AB3 results). Conservation of angular momentum was also verified for both normal mode and numerical solutions. Although the solutions using the leapfrog and AB3 method matched closely, the third-order Adams Bashforth method was chosen to produce models of torsional waves in the Earth's core due to its strong damping of numerical instabilities. Unlike the leapfrog method, it is not subject to time-splitting instability and has significantly smaller associated phase speed errors (Durran, 1991).

Having established the suitability of the proposed numerical algorithms for solving the torsional wave equation in simple test cases, and benchmarked numerical results against analytic solutions, we now turn our attention to the model geometries and parameters required for numerical models of torsional waves in the Earth's core.

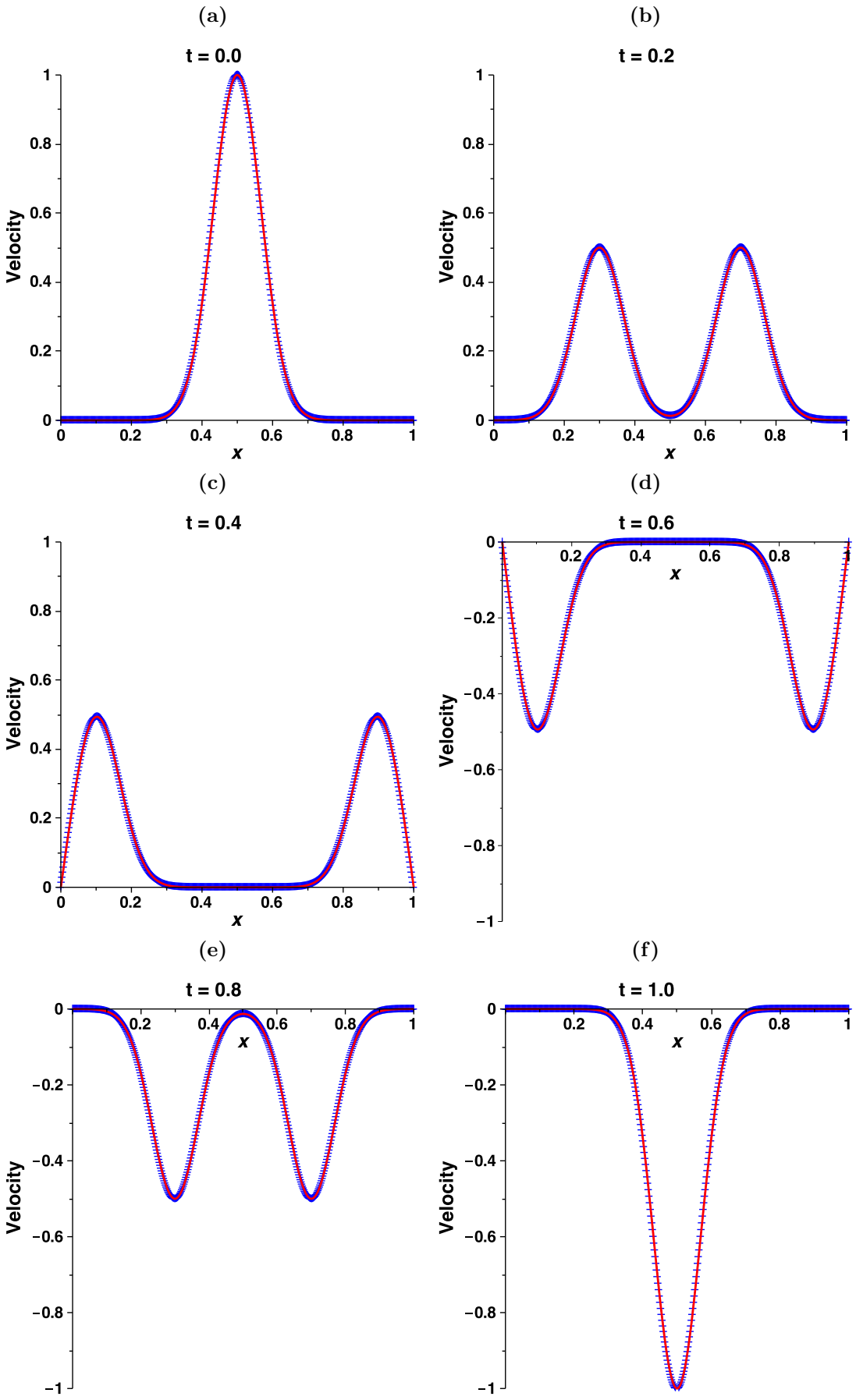
(a)
t = 0.0
Velocity
x
(b)
t = 0.2
Velocity
x
(c)
t = 0.4
Velocity
x
(d)
t = 0.6
Velocity
x
(e)
t = 0.8
Velocity
x
(f)
t = 1.0
Velocity
x

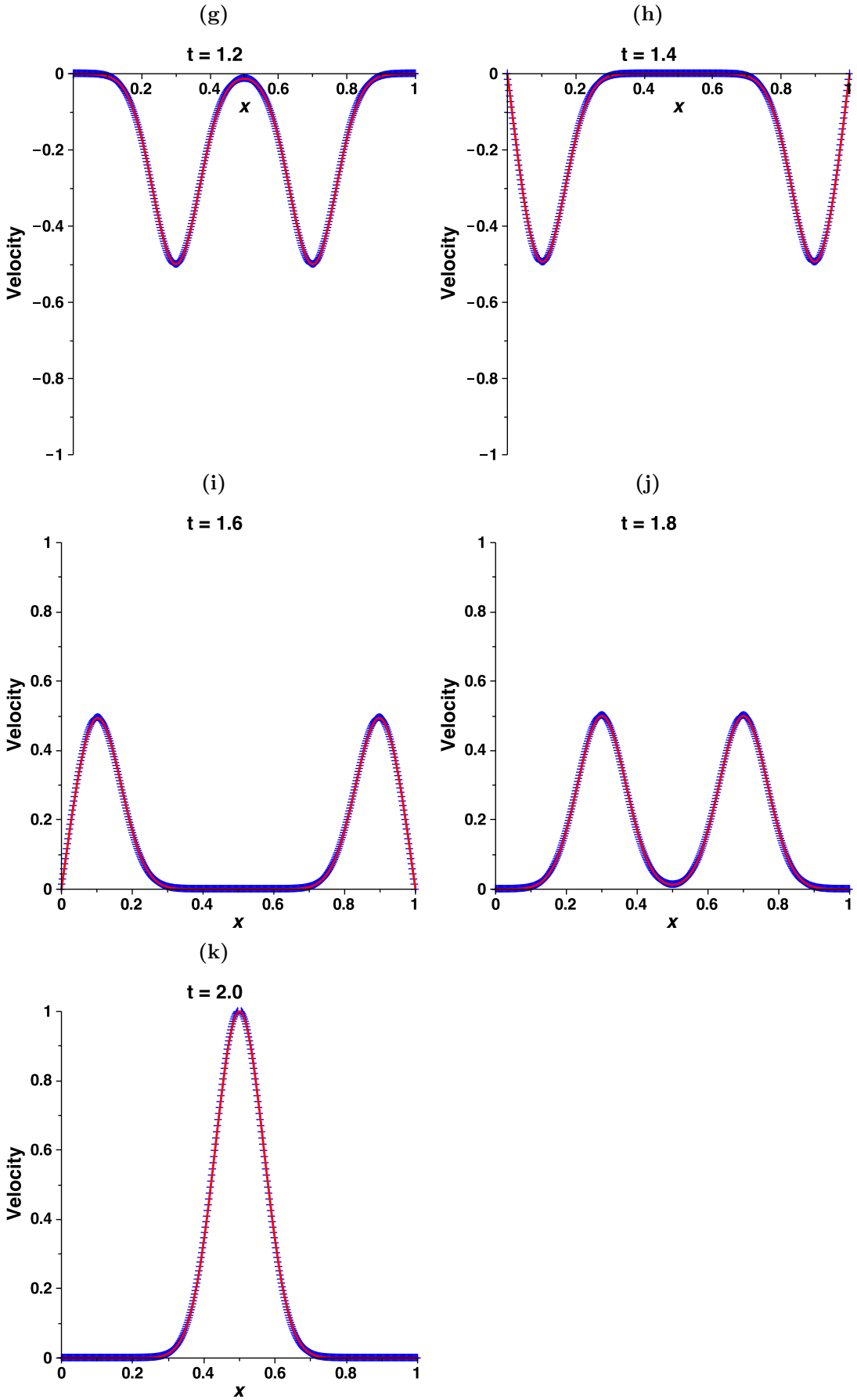

Figure 2.6: Profiles of the velocity Ψ of a 'wave on a string' during its evolution with no-slip boundary conditions applied at both ends of the domain. The red continuous line represents the normal mode (analytic) solution to the wave equation and the blue crosses represent the results obtained using an FD numerical scheme. The wave amplitude and the time have no intrinsic scale.

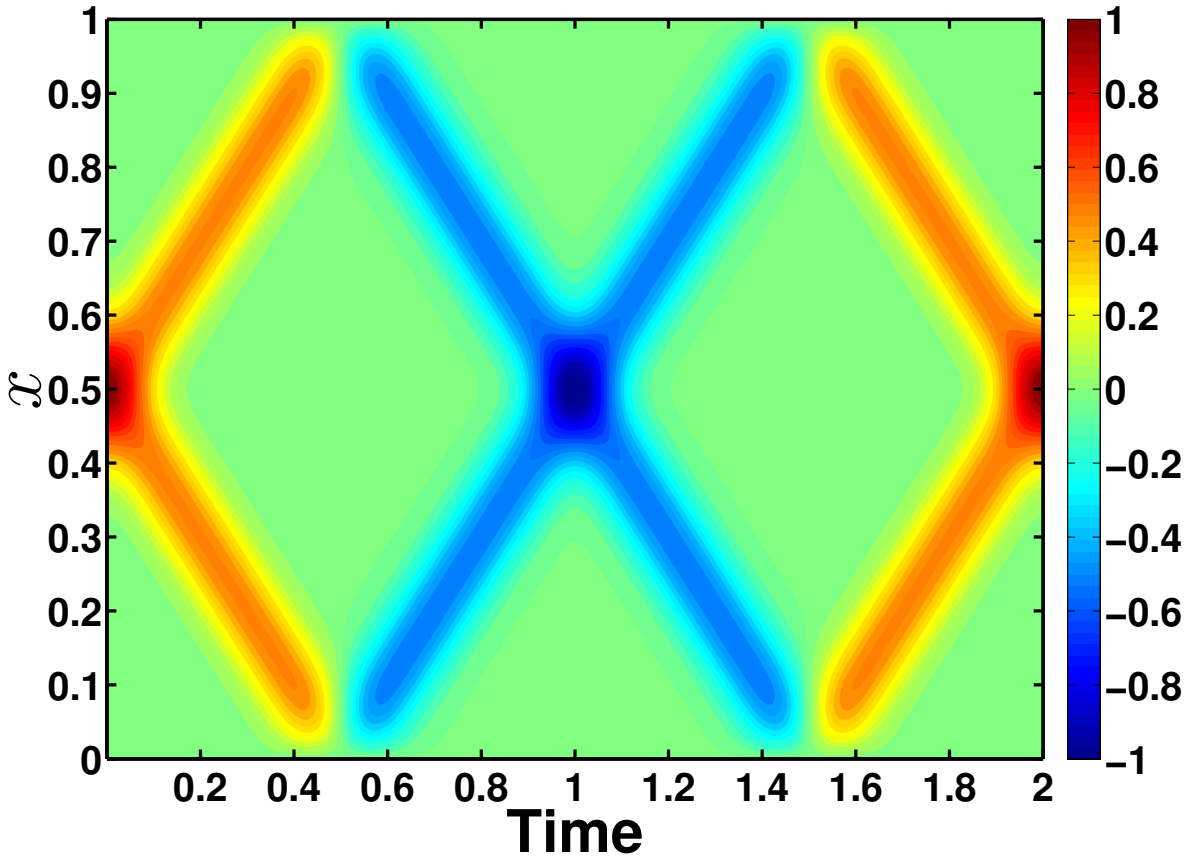

Figure 2.7: Contour plot of the velocity Ψ of a 'wave on a string' with no-slip boundary conditions applied at both ends, with time on the horizontal axis and x on the vertical axis. Red corresponds to positive velocity and blue corresponds to negative velocity. The wave group speed c is equal to 1 in this model.

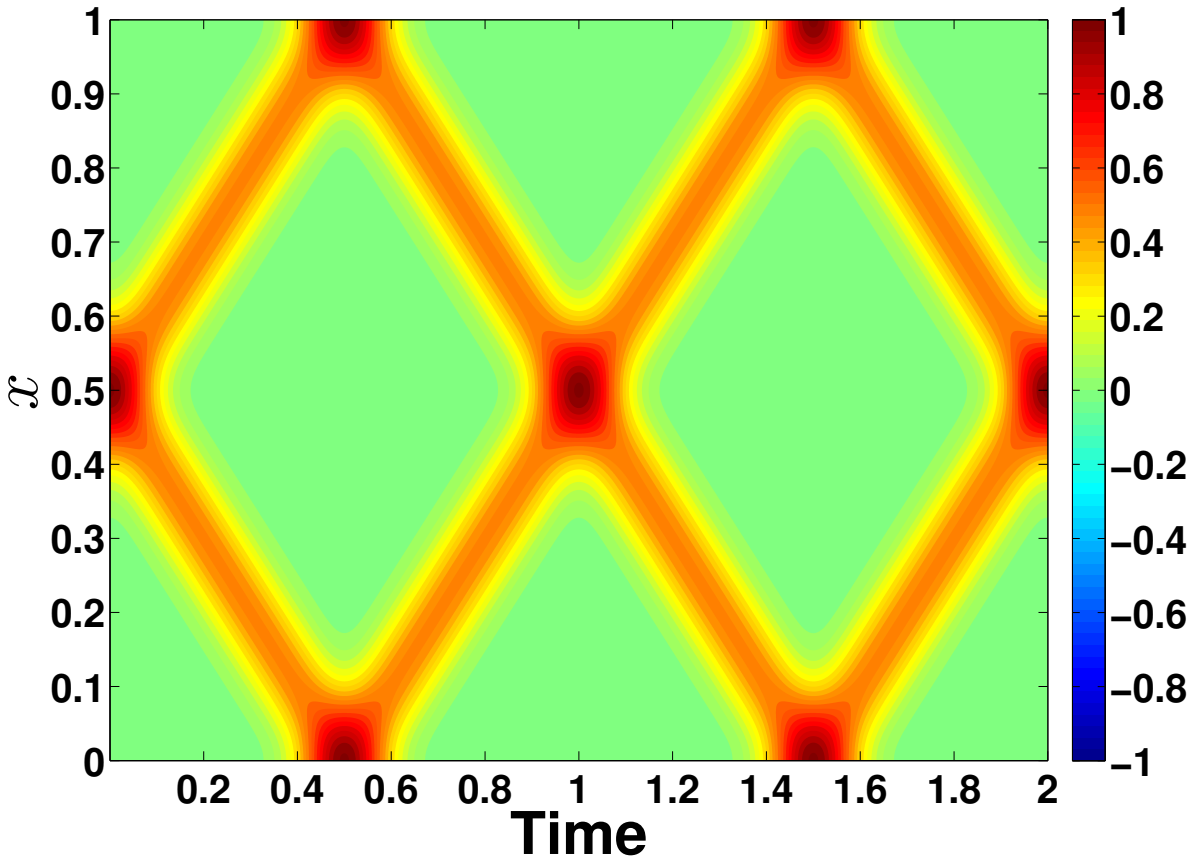

Figure 2.8: Contour plot of the velocity of a 'wave on a string' with stress-free boundary conditions applied at both ends, with time on the horizontal axis and x on the vertical axis. Red corresponds to positive velocity and blue corresponds to negative velocity. The wave group speed c is equal to 1 in this model.

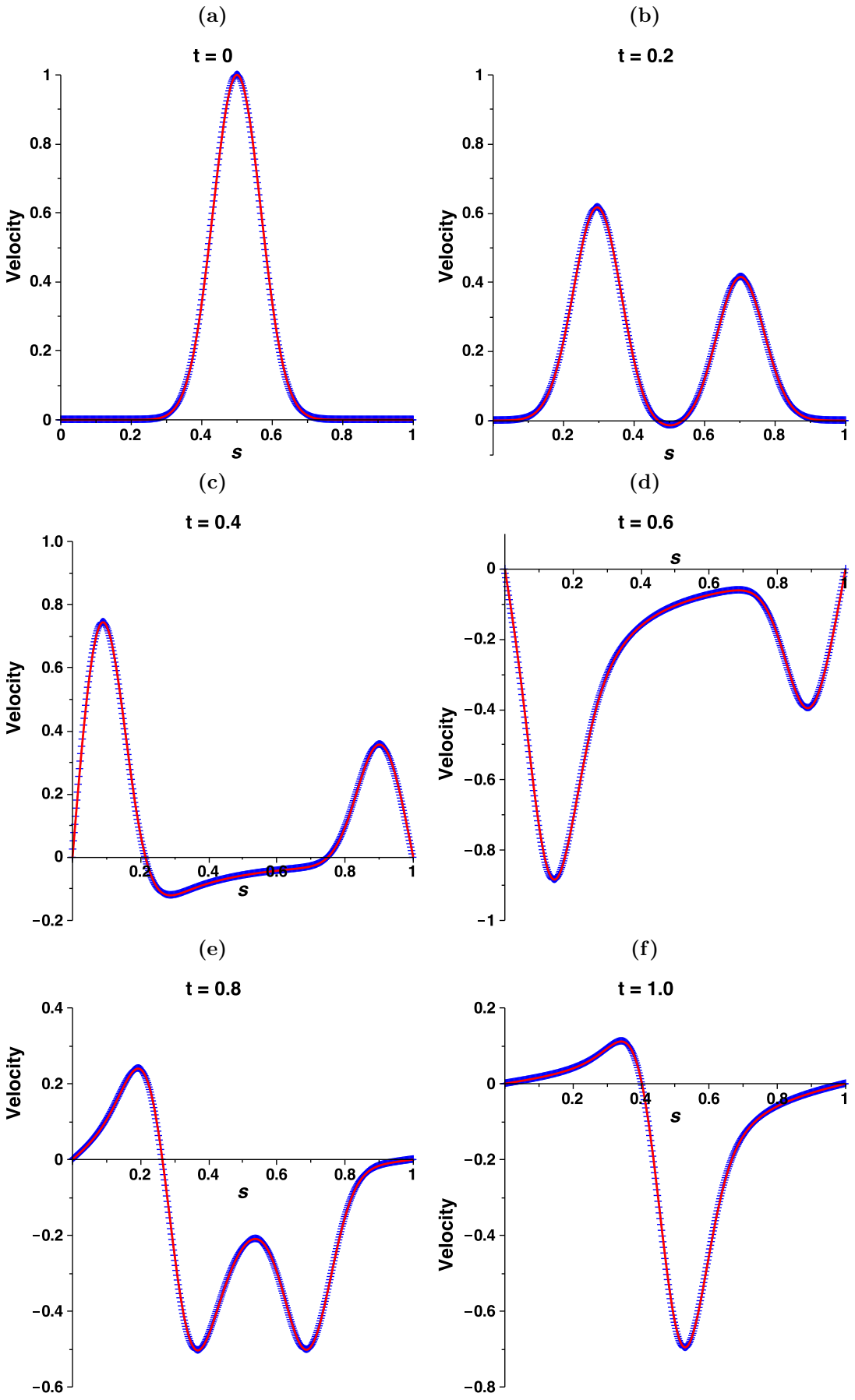
(a)
t = 0
Velocity
s
(b)
t = 0.2
Velocity
s
(c)
t = 0.4
Velocity
s
(d)
t = 0.6
Velocity
s
(e)
t = 0.8
Velocity
s
(f)
t = 1.0
Velocity
s

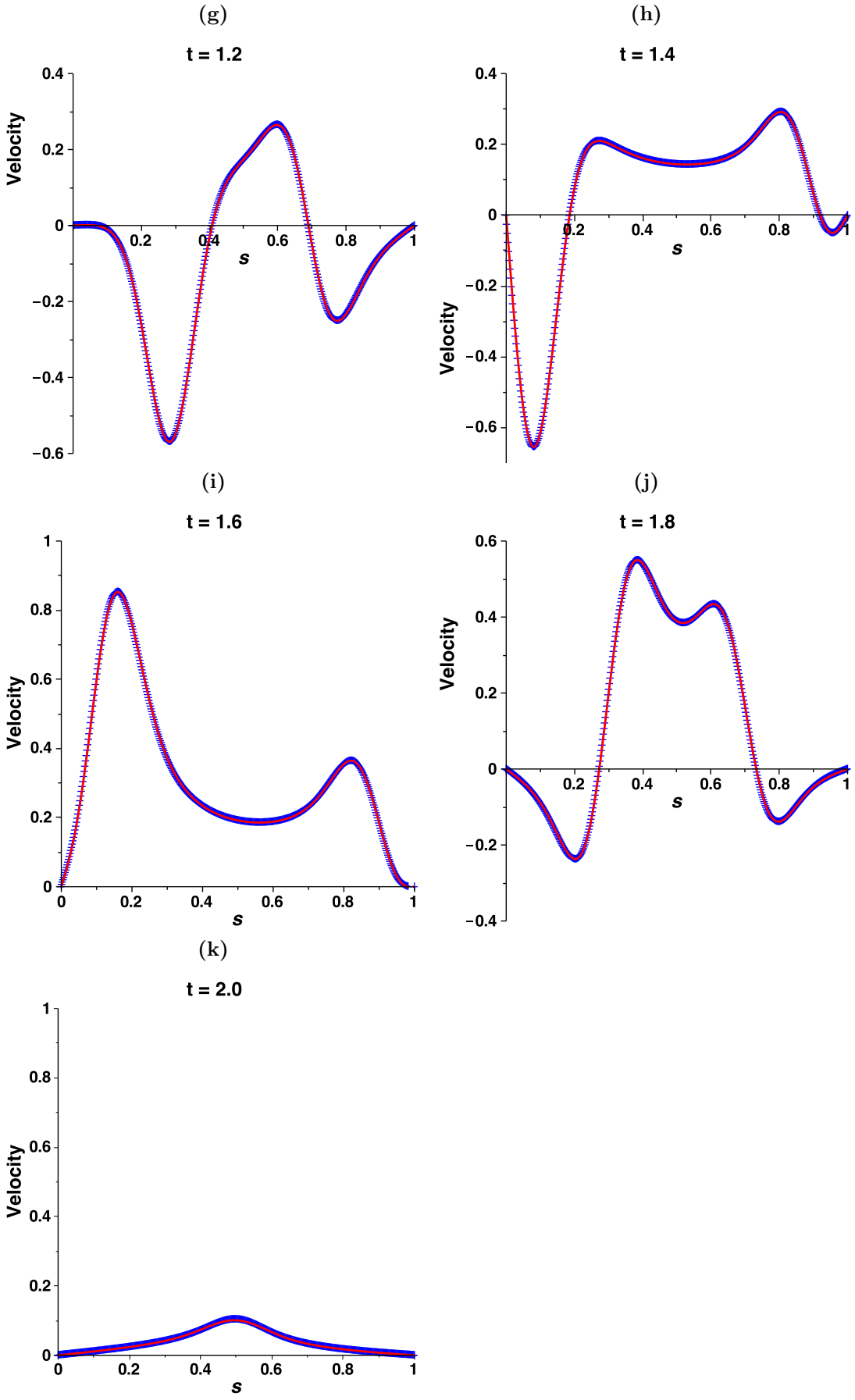

Figure 2.9: Profile of the velocity u_ϕ of a torsional wave propagating in a cylinder of unit radius. The red continuous line represents the normal mode (analytic) solution to the wave equation and the blue crosses represent the results obtained using the AB3 FD scheme. The wave amplitude has no intrinsic scale.

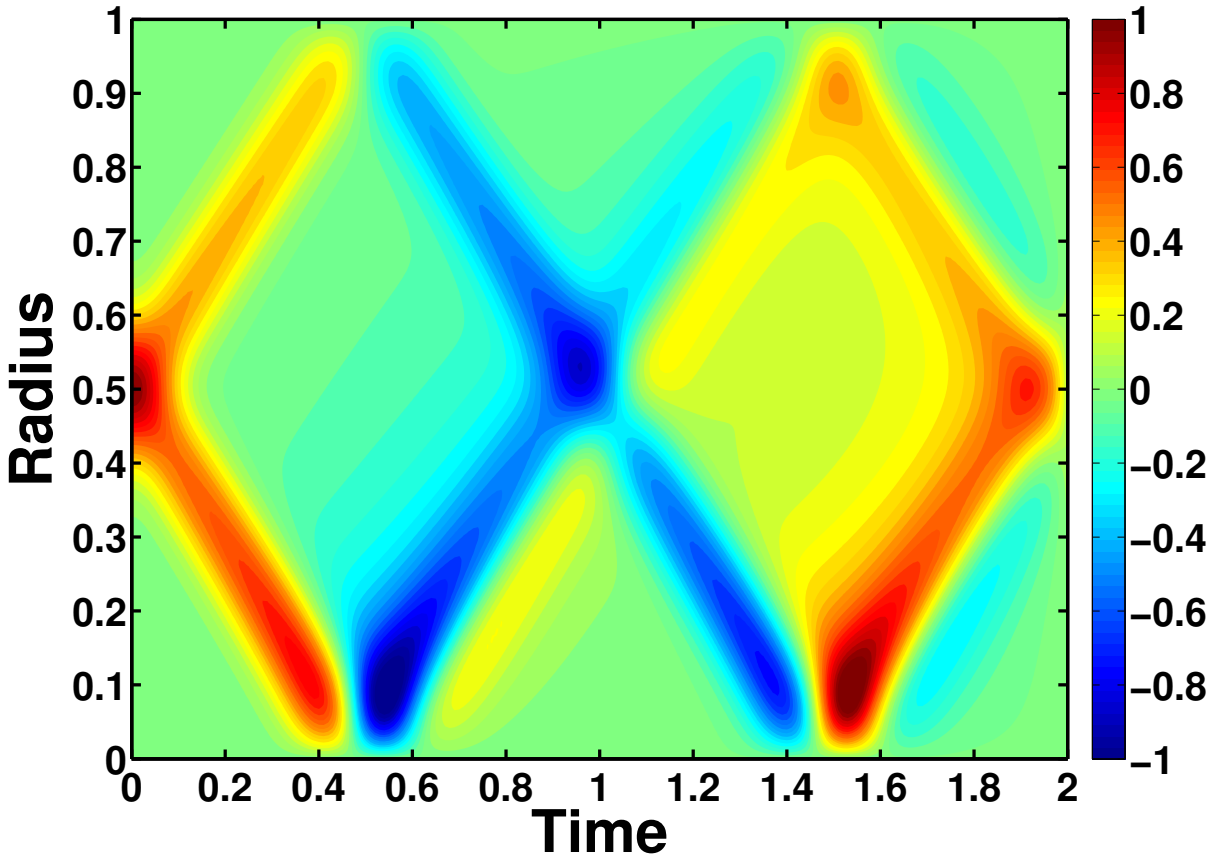

Figure 2.10: Contour plot of the velocity u_ϕ of torsional waves in a cylinder of unit radius, with time on the horizontal axis and cylindrical radius on the vertical axis. Red corresponds to positive velocity and blue corresponds to negative velocity. The no-slip condition was imposed on the outer boundary.

2.5 Code geometries

Following the successful benchmarking of the numerical schemes, three codes were developed to solve torsional wave equations better tailored to Earth's core. The geometries of these models are:

1. a cylinder of radius r_c, where r_c is the radius of the outer core (3480 km). The cylinder height z_T is constant in this geometry.

2. a full sphere (no inner core). The cylinder height decreases with increasing cylindrical radius such that $z_T = \sqrt{r_c^2 - s^2}$ (see Fig. 1.4a for a schematic).

3. an equatorially symmetric spherical shell (the velocities u_ϕ are identical in regions II and III in Fig. 1.4b). Outside the tangent cylinder, the cylinder height is the same as in the full sphere case. Inside the tangent cylinder, the height of the inner core is subtracted from the full sphere case, which gives a piecewise differentiable function for cylinder height

$$z_T = \begin{cases} \sqrt{r_c^2 - s^2} - \sqrt{r_i^2 - s^2} & \text{if } s < r_i \\ \sqrt{r_c^2 - s^2} & \text{if } s \geq r_i \end{cases} \tag{2.63}$$

   where r_i is the inner core radius (1221 km). The difference between the two models is purely geometric; there is no coupling mechanism between the inner and outer cores. Note that the height of the geostrophic cylinders tends to zero at the equator of the CMB ($s = r_c$, see Fig. 1.4b for a schematic).

2.6 Magnetic field profiles

For the majority of the work in the next chapter, we consider three models with a constant $\{B_s^2\}$ profile, one in a cylinder (model i), a second in full sphere (model ii) and the third in an equatorially symmetric spherical shell (model iii). In these models, the $\{B_s^2\}$ profile takes a constant value of 4 $(\text{mT})^2$. This value was chosen because it gives a core transit time of approximately 6 years, which is consistent with the work of Gillet et al. (2010). As stated in the derivation of the torsional wave equation in

Appendix A, the quantity $\{B_s^2\}$ is defined as

$$\{B_s^2\} = \frac{1}{4\pi z_T} \int_{-z_T}^{+z_T} \oint B_s^2 d\phi dz. \tag{2.64}$$

If the magnetic field were axisymmetric and independent of z, then equation (2.64) implies that

$$\begin{aligned} \{B_s^2\} =& \frac{2z_T}{4\pi z_T} \oint B_s^2 d\phi \\ &= \frac{4\pi z_T}{4\pi z_T} B_s^2 \\ &= B_s^2, \end{aligned} \tag{2.65}$$

which requires a non-zero B_s^2 at $s = 0$ if $\{B_s^2\} \neq 0$ at the rotation axis and therefore violates the divergence-free condition of the magnetic field. However for non-axisymmetric magnetic fields, the quantities B_s and $\{B_s^2\}$ are not subject to the same requirement; many different configurations of the magnetic field could give a profile of $\{B_s^2\}$ that is non-zero at the rotation axis (e.g. an equatorial dipole). We leave the structure of the radial magnetic field B_s used in models i, ii and iii unspecified, except to remark that a constant $\{B_s^2\}$ profile requires a non-axisymmetric magnetic field at $s = 0$ and that we anticipate many different asymmetric B_s profiles would have the same profile of $\{B_s^2\}$. The requirement of axial symmetry is geophysically unreasonable because observations of the geomagnetic field show that it is not axisymmetric, and indeed no axisymmetric magnetic field could be generated and maintained by a dynamo process (Cowling, 1934). Potential effects of variable $\{B_s^2\}$ are considered in a fourth model (model iv), which is in a full sphere geometry. Model (iv) uses the magnetic field profile shown in Fig. 2.11, which is based on a profile taken from a geodynamo simulation (Rob Teed, personal communication).

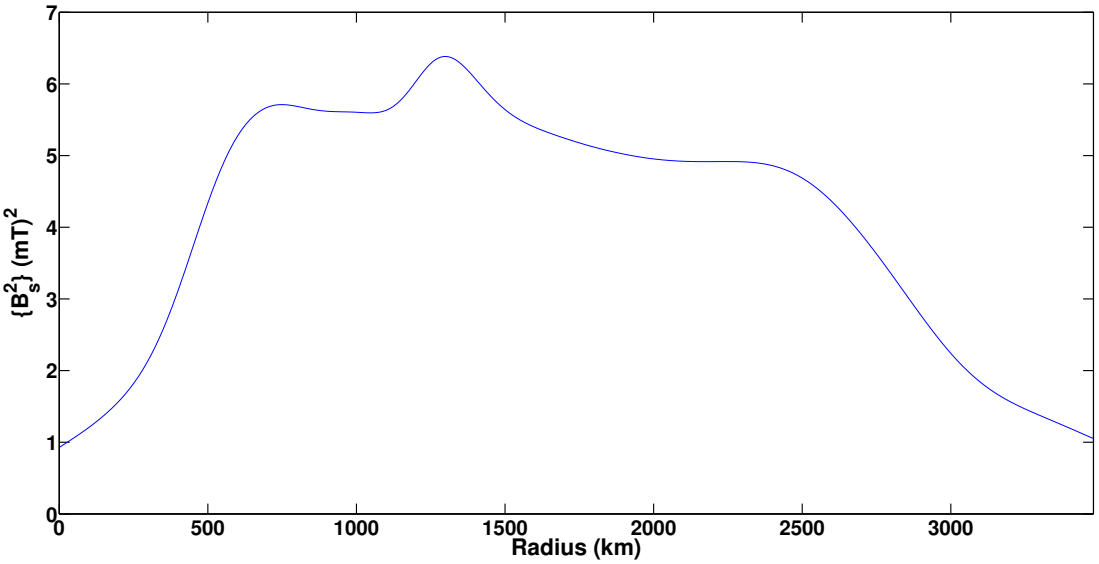

Figure 2.11: The spatially varying $\{B_s^2\}$ profile used in the full sphere model (iv).

Chapter 3

1-D modelling: torsional wave propagation

In this chapter, results from the previously described 1-D torsional wave models are presented. Models of torsional waves propagating in an ambient magnetic field whose radial component has a constant cylindrical average were produced in three geometries: first, a cylinder of fluid; second, a sphere of fluid; third, an equatorially symmetric spherical shell. A fourth model, in a sphere, examines torsional wave propagation in an ambient magnetic field whose cylindrical average is spatially varying. For these models, figures relating to the velocity u_ϕ are presented, along with a detailed discussion of the observed propagation characteristics. The key points of investigation include wave propagation, reflection and dispersion. The chapter concludes with a discussion on the implications of the observed features on the potential for identifying torsional waves in geophysical data. This final point is expanded upon in the next chapter, which focusses on the secular variation induced by torsional wave propagation.

3.1 Parameters and scalings

For the models discussed in this chapter, the scales of length, time and magnetic field have been non-dimensionalised, respectively, by the radius of the outer core 3480 km, 1 year and 1 mT. The time and length scales have been restored to their correct values on the contour plot axes, but the velocity u_ϕ has no intrinsic scale. The torsional wave equation does not define a magnitude for the velocity because it is linear and homo-

geneous, so the velocity in the following plots is scaled by the amplitude of the initial pulse, which is given by equation (2.60). Also required are values for the permeability of free space, μ_0, and a reference density ρ_0 (taken as 9900 kg/m^3 in this work). The torsional wave models do not include viscosity or dissipation terms that take into account coupling between the core and the mantle or between the inner core and the outer core. Neglecting the effects of a conducting layer at the base of the mantle and Ohmic and viscous dissipation allows us to isolate effects of core geometry and investigate their importance on torsional wave propagation. Models i-iv use the initial velocity profile described by equation (2.60), with $\sigma = 0.1$, which is smooth and has one positive peak at the midpoint of the domain ($s = r_c/2$). This is the same initial profile as in §2.2.1 and can be seen in the blue line of Figs. 3.2, 3.6 and 3.12.

3.2 Model i: torsional waves in a cylinder

Fig. 3.1 shows the evolution of this pulse in a cylinder of radius 3480 km. The first observation is that the initial waves are apparently non-dispersive and travel as distinct independent pulses before they first encounter the boundaries (0-3 years). The initial pulse splits into two smaller positive peaks, one of which travels outwards towards the equator (a') and the other travels inwards towards the rotation axis (a). After approximately 3 years, both pulses arrive at their respective boundaries and then reflect. When (a') reaches the outer boundary (the equator of the CMB), it reflects with no change of sign such that (b') is also positive, see Fig. 3.3 for profiles of the wave one year before and one year after reflection at the outer boundary. A strong positive pulse (a) followed by a very weak negative pulse (b) converges on the rotation axis, and the returning wave train consists of a strong trough (c) followed by a small peak (d), see Fig. 3.4 for profiles of the wave one year before and one year after reflection at the rotation axis. The reader is reminded that the rotation axis at $s = 0$ is not a physical boundary, but a singular point of the coordinate system. Therefore, 'reflections' of waves at this point should be regarded as pseudo-reflections. Note that the specific behaviour of the reflections will be considered in detail in §3.10. Having reflected from the boundaries, the two wave trains (b') and (c, d) traverse the core radius, meeting and interfering with each other after a further 3 years. The waves continue to reflect from the boundaries and interfere, each time taking approximately 6 years to traverse the

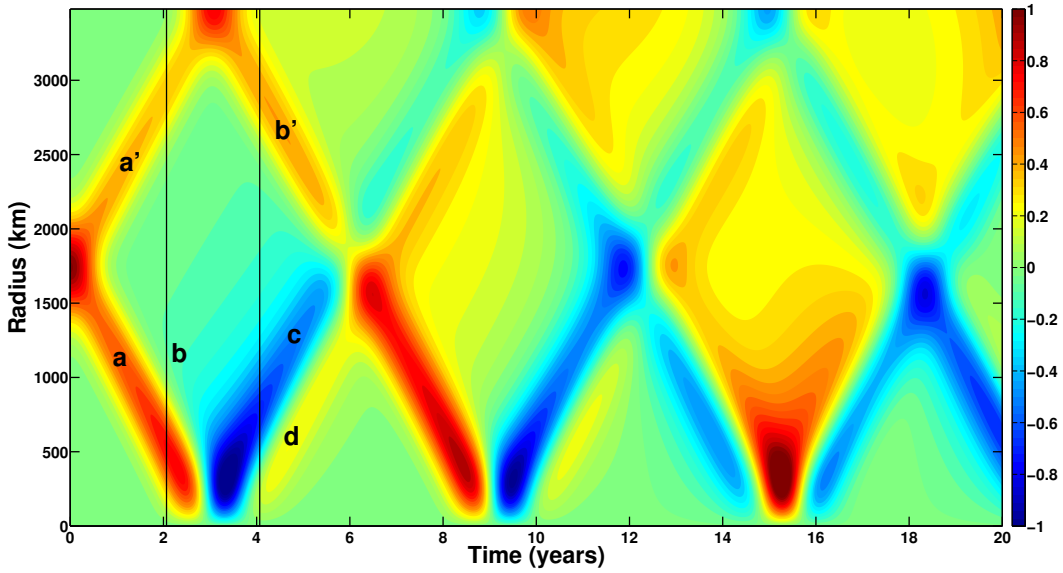

Figure 3.1: Contour plot of the velocity u_ϕ of torsional waves in a cylinder, with time on the horizontal axis and cylindrical radius on the vertical axis. Red corresponds to positive velocity and blue corresponds to negative velocity. The two vertical lines show the times at which profiles are shown in Figs. 3.3 and 3.4 (one year before and one year after the waves reflect from the boundaries).

entire core. Note that after one core transit time (6 years), some of the wave energy has spread throughout the domain and the wave no longer travels entirely as distinct pulses. An evolving wave packet shape through time would indicate that some form of dispersion is occurring. It seems that successive reflections at the boundaries increase the effects of this dispersion such that after 3 core transit times most of the energy has spread out and the wave bears little resemblance to the initial velocity profile (Fig. 3.2).

The propagation of torsional waves in a cylinder of fluid is not a geophysically realistic case due to the shape of the Earth's core, but it is an interesting study because the torsional wave equation (2.9) can be solved analytically for this problem (see §2.1.2). These analytic solutions were used to benchmark the numerical models implemented to produce torsional wave models. Having briefly considered waves in this geometry, the remainder of this chapter focusses upon wave propagation in more Earth-like settings, namely a full sphere of fluid and an equatorially symmetric spherical shell.

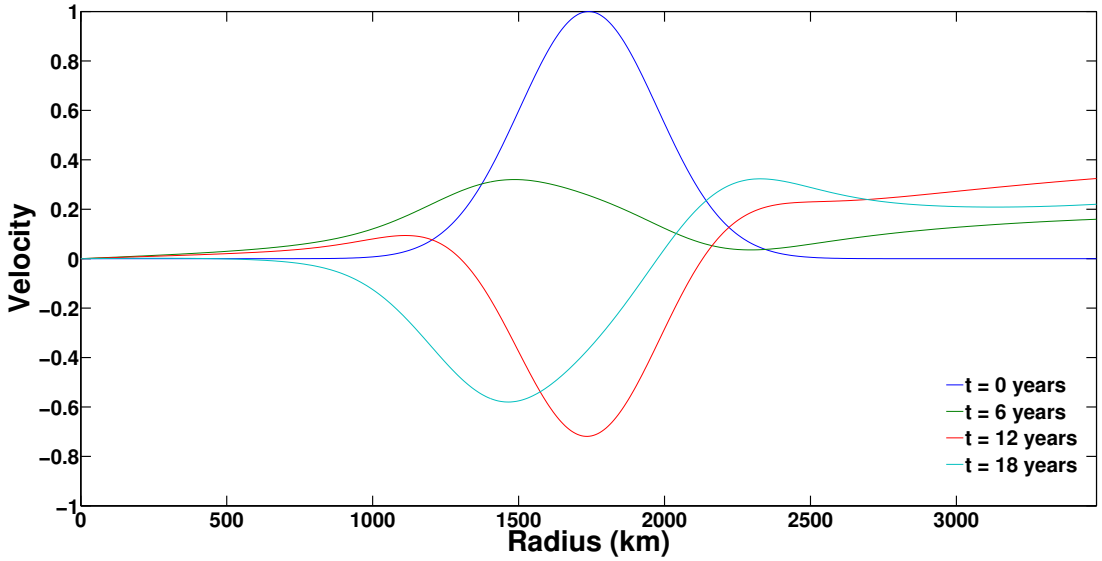

Figure 3.2: Velocity profiles of the waves at the start of evolution (blue), after one core transit (green), after two core transits (red) and after three core transits (cyan) in a cylinder.

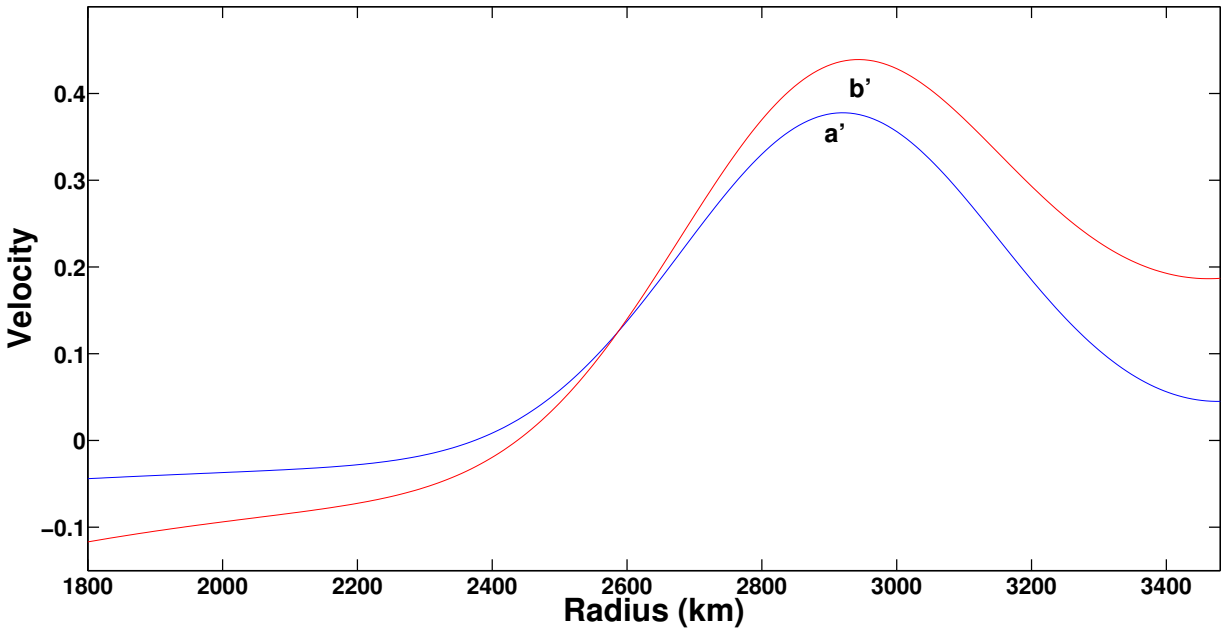

Figure 3.3: Velocity profiles of the waves one year before (a', blue) and after (b', red) reflection at the outer boundary of a cylinder of radius r_c. The annotations correspond to those in Fig. 3.1 and the times at which the profiles were taken are shown in that figure as two vertical black lines.

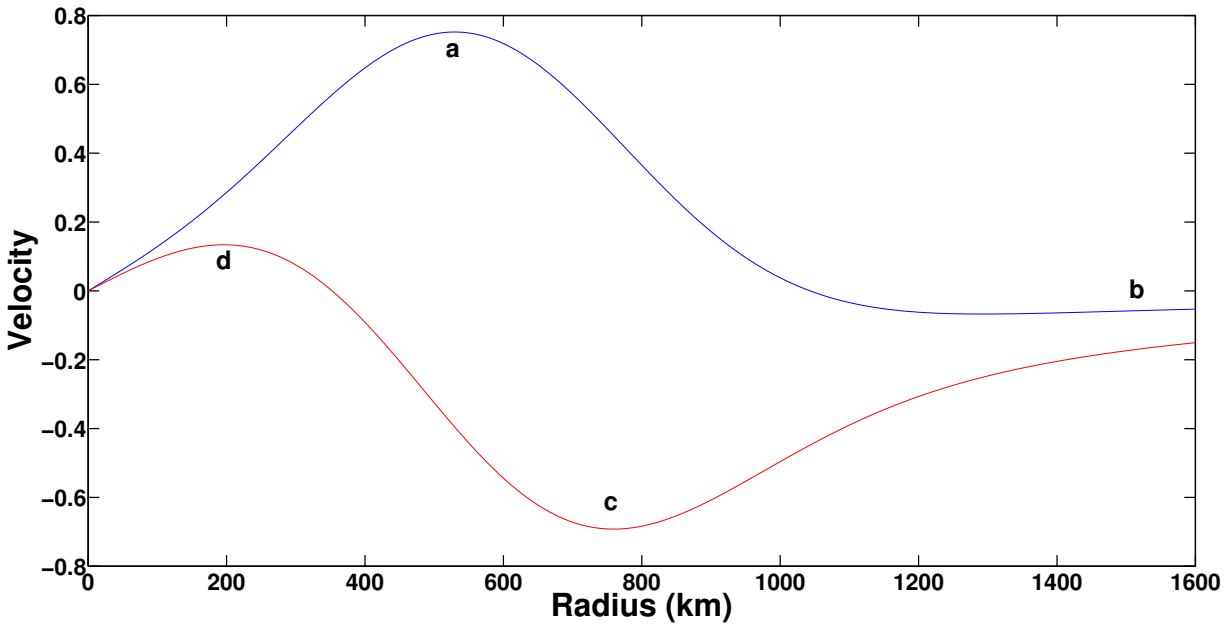

Figure 3.4: Velocity profiles of the waves one year before (a and b, blue) and after (c and d, red) reflection at the outer boundary of a cylinder of radius r_c. The annotations correspond to those in Fig. 3.1 and the times at which the profiles were taken are shown in that figure as two vertical black lines.

3.3 Model ii: torsional waves in a sphere

The wave evolution of torsional waves in a sphere is very similar to that of waves in a cylinder, see Fig. 3.5. Again, the initial wave pulse splits into an outwards travelling peak (a') and an inwards travelling peak (a). Pulse (a') hits the equator of the CMB after 3 years and reflects with no change of sign. The positive pulse (a), followed by the weak negative pulse (b), reflects at the rotation axis to form a strong trough (c) and a small peak (d). These waves meet (b') at approximately $t = 6$ years and interfere. As in the cylindrical case, waves have a core transit time of approximately 6 years and the pulses become more dispersed with increasing time, see Fig. 3.6 for profiles of the wave after one, two and three core transit times.

Figs. 3.7 and 3.8 show the velocity profiles across the core 1 year before and after the wave reflects from the boundaries in the full sphere geometry. Since we investigate the effects of core geometry on torsional waves, it is of interest to compare the boundary effects in the full sphere model results with those expected in the simplest possible geometry, which is 1-D Cartesian (a 'wave on a string'). In the latter case, after reflection at a stress-free boundary, the wave profiles at the same time before and after reflection, one year for example, are identical. At a no-slip boundary, the wave

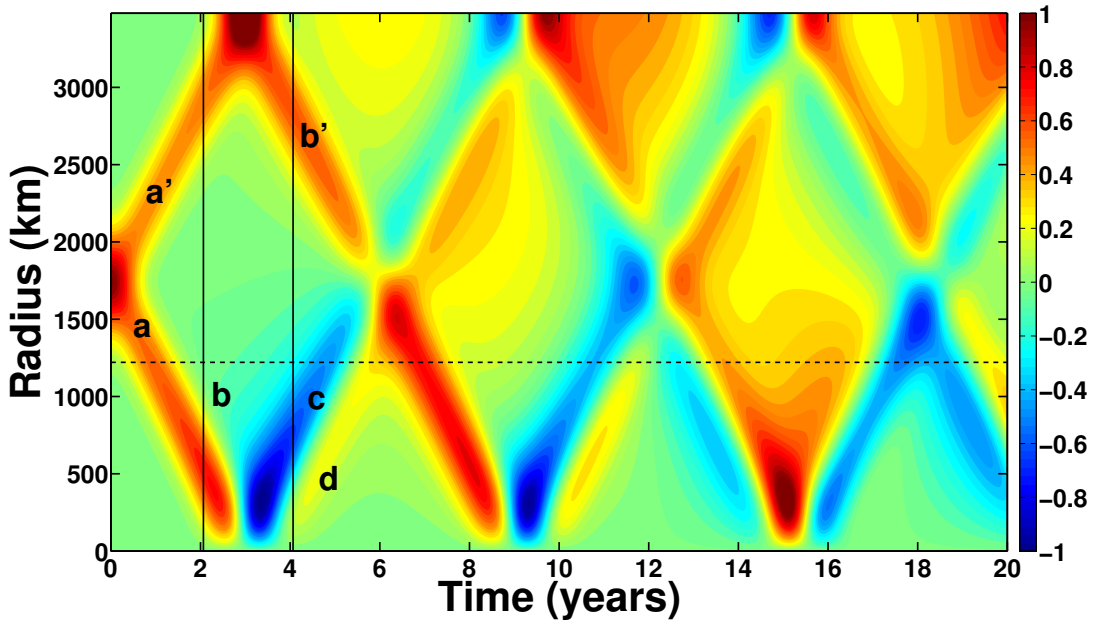

Figure 3.5: Contour plot of the velocity u_ϕ of torsional waves in a full sphere, with time on the horizontal axis and cylindrical radius on the vertical axis. Red corresponds to positive velocity and blue corresponds to negative velocity. The horizontal black dashed line represents the location of the tangent cylinder at $s = 1221$ km to aid comparison with the spherical shell case in Fig. 3.11. The two vertical lines show the times at which profiles are shown in Figs. 3.7 and 3.8 (one year before and one year after the waves reflect from the boundaries).

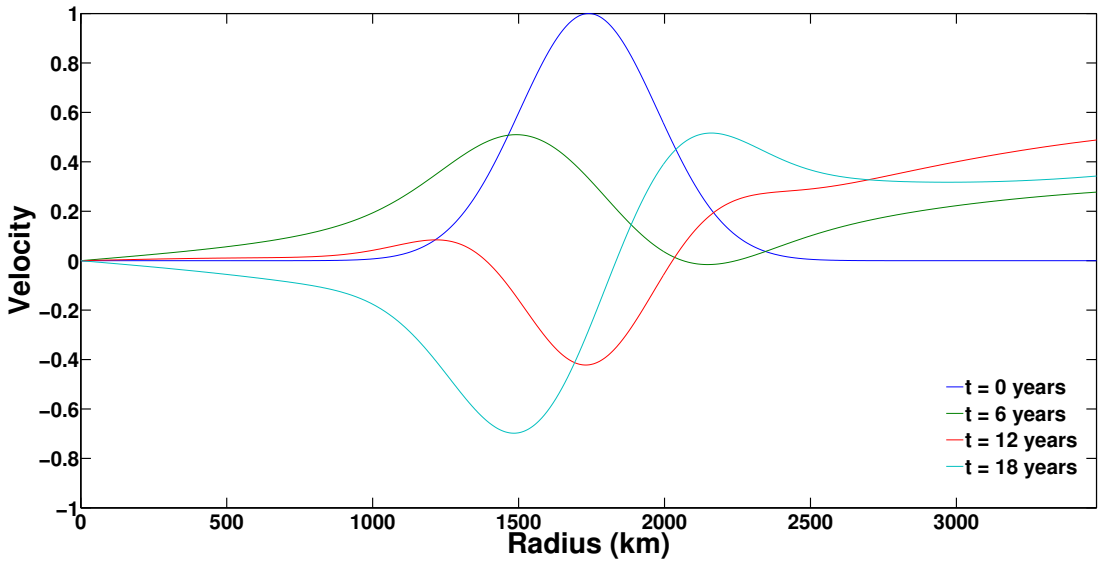

Figure 3.6: Velocity profiles of the waves at the start of evolution (blue), after one core transit (green), after two core transits (red) and after three core transits (cyan) in a full sphere.

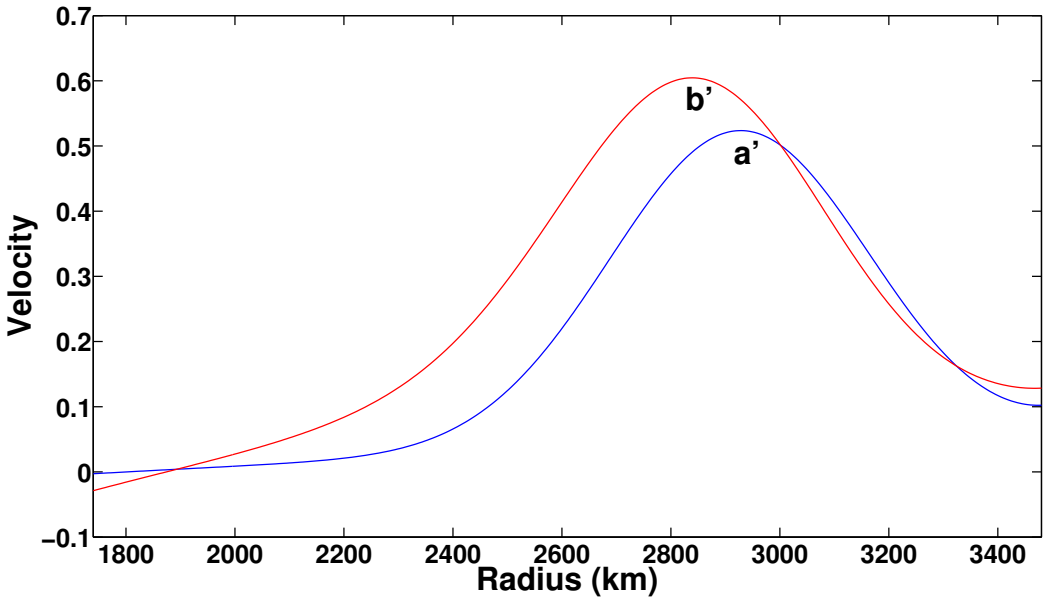

Figure 3.7: Velocity profiles of the waves one year before (a', blue) and after (b', red) reflection at the equator of the core mantle boundary ($s = r_c$) in a full sphere. The annotations correspond to those in Fig. 3.5 and the times at which the profiles were taken are shown in that figure as two vertical black lines.

changes sign and the reflected wave is the exact negative of the incoming wave. Since a stress-free boundary condition is applied at the equator of the CMB ($s = r_c$) in our torsional wave models, we might expect the incoming and reflected torsional wave profiles to match as they do in the Cartesian case. Although the incident (a') and reflected (b') wave profiles in Fig. 3.7 are of the same sign, the incoming pulse is not exactly recovered after reflection. At the rotation axis (see Fig. 3.8), the reflected wave profile (c, d) contains both positive and negative components, and is very different from the incident profile (a, b). We discuss this observation in more detail in §3.10.

Fig. 3.9 shows the transport of angular momentum density $u_\phi s^2 z_T$ through the core for the full sphere model discussed above. The plot of angular momentum density is similar to the contour plot of velocity shown in Fig. 3.5, in that the initial pulse is shown splitting apart into two pulses travelling in opposite directions and these pulses are subsequently shown reflecting from the domain boundaries. The amplitude of angular momentum density is low in the region close to the rotation axis due to the influence of the s^2 contribution to angular momentum density, which decreases with decreasing cylindrical radius more rapidly than u_ϕ increases. Though theoretically predicted, numerically exact conservation of angular momentum in models is unlikely due to computational error and due to the use of the canonical torsional wave equation,

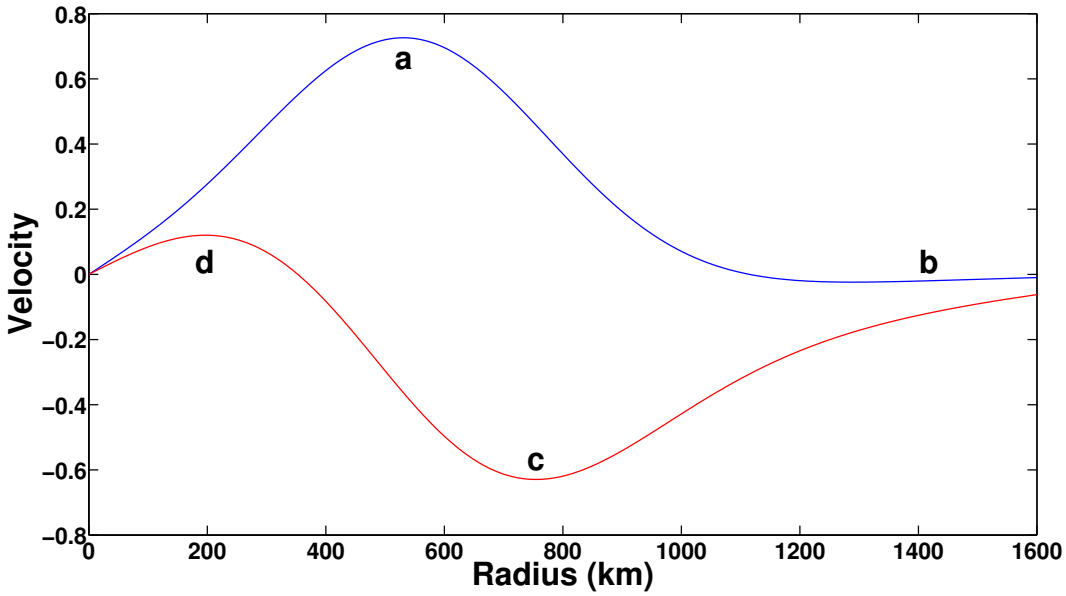

Figure 3.8: Velocity profiles of the waves one year before (a and b, blue) and after (c and d, red) reflection at the rotation axis in a full sphere. The annotations correspond to those in Fig. 3.5 and the times at which the profiles were taken are shown in that figure as two vertical black lines.

which omits the second term on the RHS of the torsional wave equation (A.21) derived in Appendix A. The total angular momentum of the initial wave pulse was compared to the total angular momentum of the wave profiles at every time step and we find that this quantity is conserved to a few parts in 10^4 for the models presented in this work, see Fig. 3.10 for a plot of this normalised angular momentum for the full sphere model described in this section. We produced similar plots for models using finer spatial grids and found that angular momentum is better conserved in models with better spatial resolution, which indicates that the spatial discretisation is largely responsible for the observed small fluctuations of angular momentum.

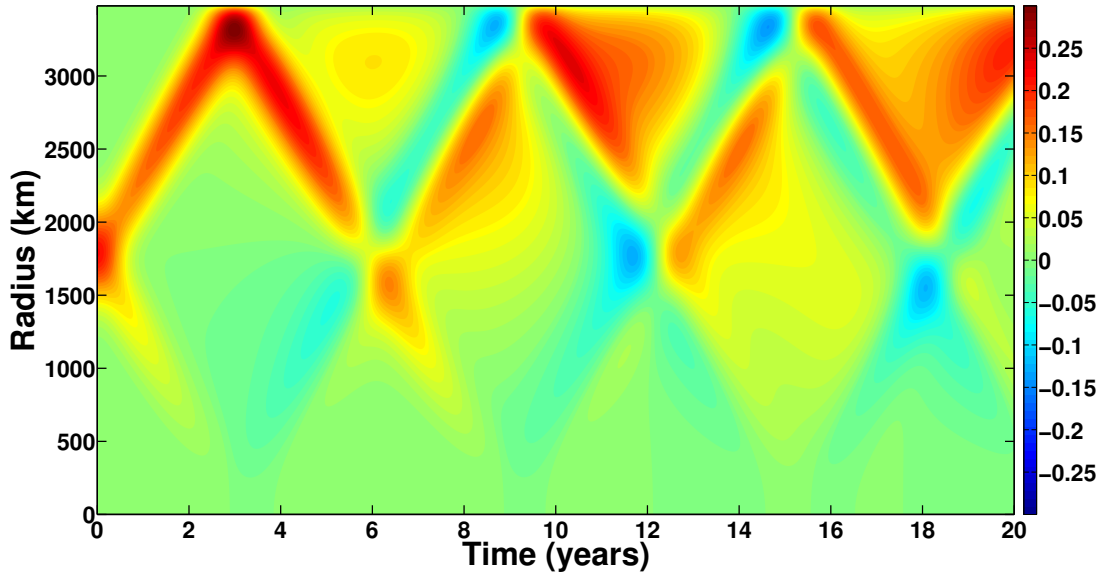

Figure 3.9: Contour plot of the angular momentum density $u_\phi s^2 z_T$ of torsional waves in a full sphere, with time on the horizontal axis and cylindrical radius on the vertical axis. Red corresponds to positive angular momentum density and blue corresponds to negative angular momentum density.

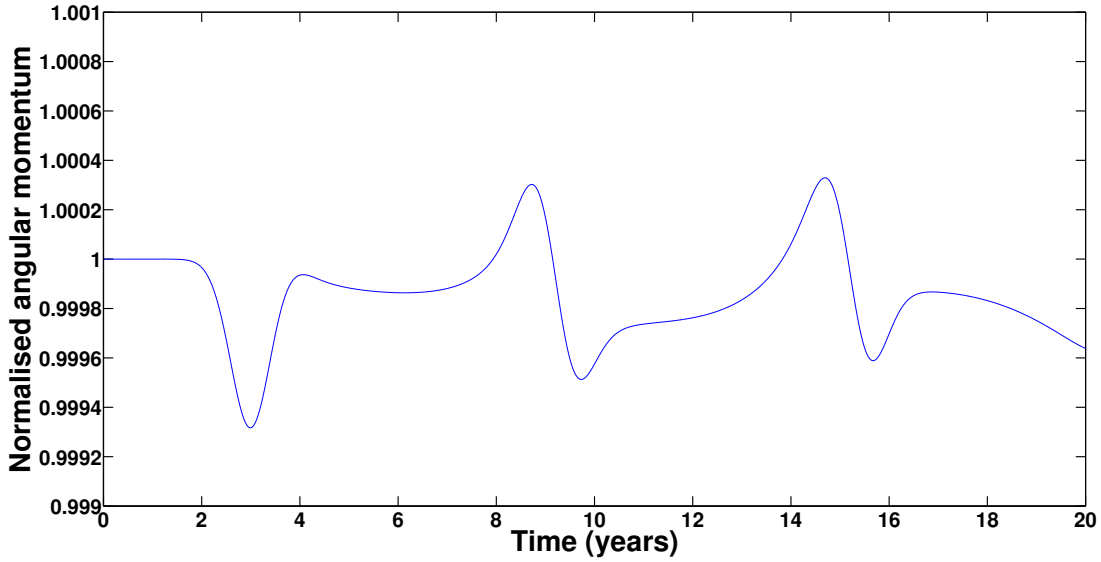

Figure 3.10: The total angular momentum at each time step of the full sphere model, normalised by the angular momentum of the initial profile.

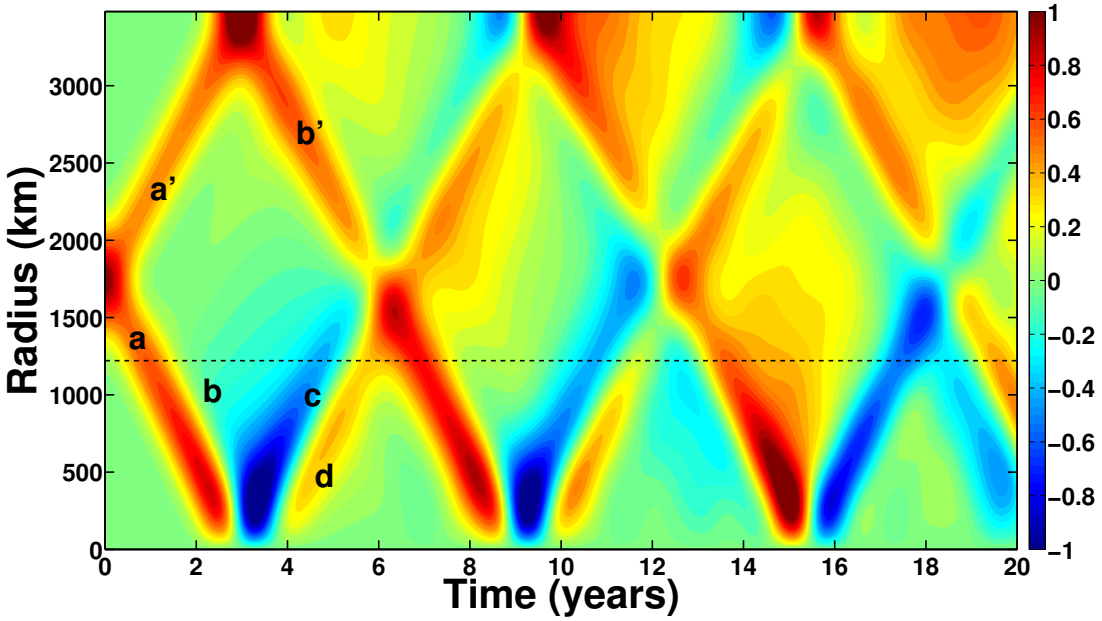

Figure 3.11: Contour plot of the velocity u_ϕ of torsional waves in an equatorially symmetric spherical shell, with time on the horizontal axis and cylindrical radius on the vertical axis. Red corresponds to positive velocity and blue corresponds to negative velocity. The horizontal black dashed line represents the location of the tangent cylinder at $s = 1221$ km.

3.4 Model iii: torsional waves in a spherical shell

The wave evolution in an equatorially symmetric spherical shell, Fig. 3.11, is very similar to that of a full sphere and of a cylinder. The initial wave pulse splits into an outwards travelling peak (a') and an inwards travelling peak (a). Pulse (a') hits the equator of the CMB after 3 years and reflects with no change of sign. The positive pulse (a), followed by the weak negative pulse (b), reflects at the rotation axis to form a strong trough (c) and a small peak (d). These waves meet (b') at approximately $t = 6$ years and interfere. As in the previous cases, waves have a core transit time of approximately 6 years and the pulses become more dispersed with increasing time.

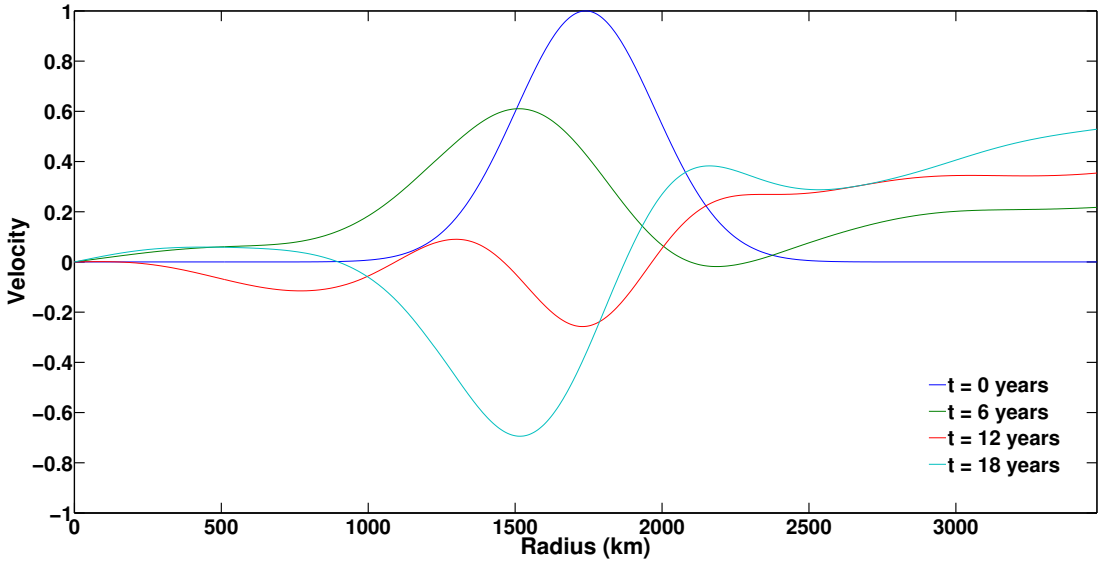

Figure 3.12: Velocity profiles of the waves at the start of evolution (blue), after one core transit (green), after two core transits (red) and after three core transits (cyan) in an equatorially symmetric spherical shell.

3.5 Comparision

An important observation is that the wave amplitude changes throughout propagation. In all three geometries, peaks (a) and (a') are not symmetric about $s = r_c/2$; the inwards travelling pulse (a) has a higher amplitude than the outwards travelling (a') when traversing the central regions of the domain, Figs. 3.1, 3.5 and 3.11. At the rotation axis, the amplitude of pulse (a) drops to zero due to the regularity condition, whilst the wave amplitude of pulse (a') is high in the region adjacent to the equator of the CMB. Jault & Légaut (2005) used geometric effects on the transport of angular momentum density to explain these variations of wave amplitude during torsional wave propagation through the core.

Although Figs. 3.5 and 3.11 appear quite similar, subtracting the full sphere velocities from the spherical shell velocities highlights some important differences between models (ii) and (iii) (Fig. 3.13). The first of these differences is a weak reflection at the tangent cylinder. After the initial pulse splits apart and pulse (a) hits the tangent cylinder, a very weak reflection of the same sign (A) can be seen travelling away from the inner core after time T$\sim$0.6 years. Pulse (A) is much weaker than the incident pulse (a), with a reflection coefficient of approximately 0.07. The second difference between the two models is that the wave amplitude is higher near the rotation axis in the

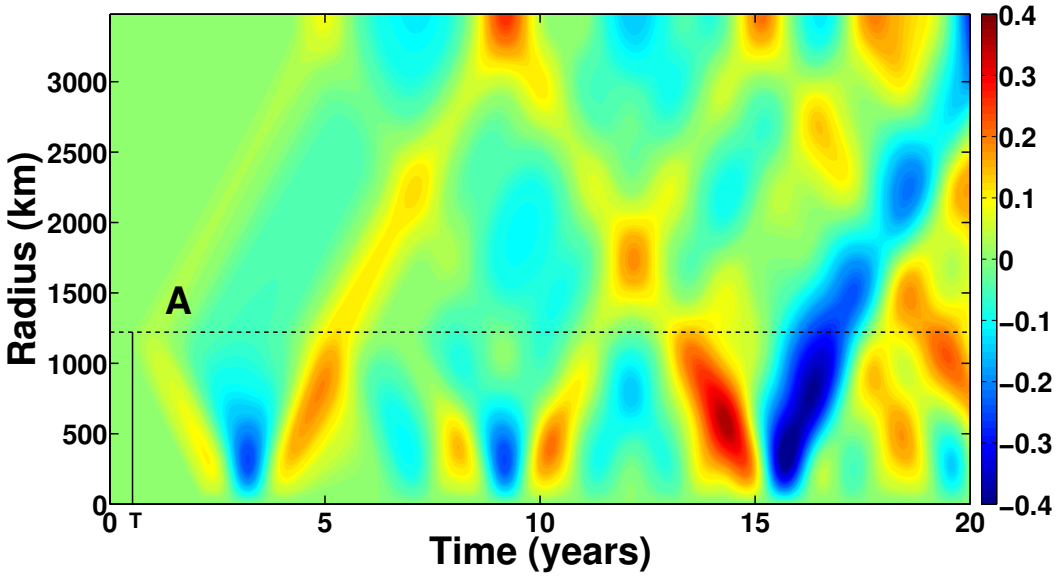

Figure 3.13: Contour plot of the difference in velocity u_ϕ when full sphere velocities were subtracted from the spherical shell case. Time is on the horizontal axis and cylindrical radius is on the vertical axis. Red corresponds to positive velocity differences and blue corresponds to negative velocity differences. The horizontal black dashed line represents the location of the tangent cylinder at $s = 1221$ km. Note the weak positive reflection (in yellow) from the tangent cylinder at time T$\sim$0.6 years.

equatorially symmetric spherical shell model than in the full sphere model (pulses a, b, c and d in Figs. 3.5 and 3.11, and the waves inside the tangent cylinder in Fig. 3.13). The amplitudes of the velocity differences between models (ii) and (iii) increases with increasing time in Fig. 3.13. This could be due to the successive reflections from the tangent cylinder that only occur in the spherical shell model. Alternatively, since it appears that the waves in both models are subject to dispersion, the increasing amplitude with time in the difference plot in Fig. 3.13 may indicate that the phase difference between the models is increasing with time.

In all three geometries, an interesting feature is observed in both the velocity and angular momentum density contour plots; after the initial pulse has separated, there remains a low amplitude negative tail connecting the two pulses in the centre of the domain. This central region never returns to its initial quiescent state after the passage of the torsional waves as one might expect, but the wavefronts leave a low amplitude negative trailing wake (labelled as pulse (b) in Figs. 3.1, 3.5 and 3.11). In the case of the general wave equation for a scalar field, the failure of Huygens' principle in even spatial dimensions gives rise to trailing wakes behind sharply defined wave pulses (Courant &

Hilbert (1962; pp. 765-766); Hadamard (1923; pp. 53, 176-177)). Since torsional waves are symmetric 2-D waves due to their convergence on an axis at $s = 0$, we interpret the observed trailing wakes in terms of Huygens' principle in §3.9.

3.6 Dispersion

In the archetypical 1-D Cartesian 'wave on as string' example, the second spatial derivative of the velocity Ψ is the only term on the right hand side (RHS) of the 1-D wave equation given by

$$\frac{\partial^2 \Psi(x,t)}{\partial t^2} = c^2 \frac{\partial^2 \Psi(x,t)}{\partial x^2}, \qquad \text{(2.1 revisited)}$$

D'Alembert first proposed that the solution to the above equation (2.1) takes the form of two superposed waves travelling in opposite directions with speed c such that

$$\Psi(x,t) = F(x - ct) + G(x + ct), \tag{3.1}$$

where F and G are two arbitrary twice differentiable functions that are found from the initial and boundary conditions. $F(x - ct)$ represents a wave travelling in the positive x-direction, whilst $G(x + ct)$ represents a wave travelling in the negative x-direction. Since the speed c remains constant and does not depend on wave number, the waves are non-dispersive. In other geometries, such as the cylindrically symmetric 2-D setting that we consider in this paper, the relevant wave equation includes additional terms on the RHS and the 1-D Cartesian (non-dispersive) case is approached when the relative magnitudes of these extra terms are small. Assuming a constant magnetic field profile $\{B_s^2\}$ across the core, expanding the RHS of the torsional wave equation gives

$$\frac{\partial^2 u_\phi}{\partial t^2} = \frac{\{B_s^2\}}{\mu_0 \rho_0} \left(\underbrace{\frac{\partial^2 u_\phi}{\partial s^2}}_{1} + \underbrace{\frac{1}{s}\frac{\partial u_\phi}{\partial s}}_{2} - \underbrace{\frac{s}{z_T^2}\frac{\partial u_\phi}{\partial s}}_{3} + \underbrace{\frac{u_\phi}{z_T^2}}_{4} - \underbrace{\frac{u_\phi}{s^2}}_{5} \right). \tag{3.2}$$

One measure of the dispersive properties of the modelled torsional waves is the ratio of the magnitude of the second spatial derivative (term 1) to the maximum value of the magnitude of the other four terms (terms 2-5) on the RHS of equation (3.2). We define

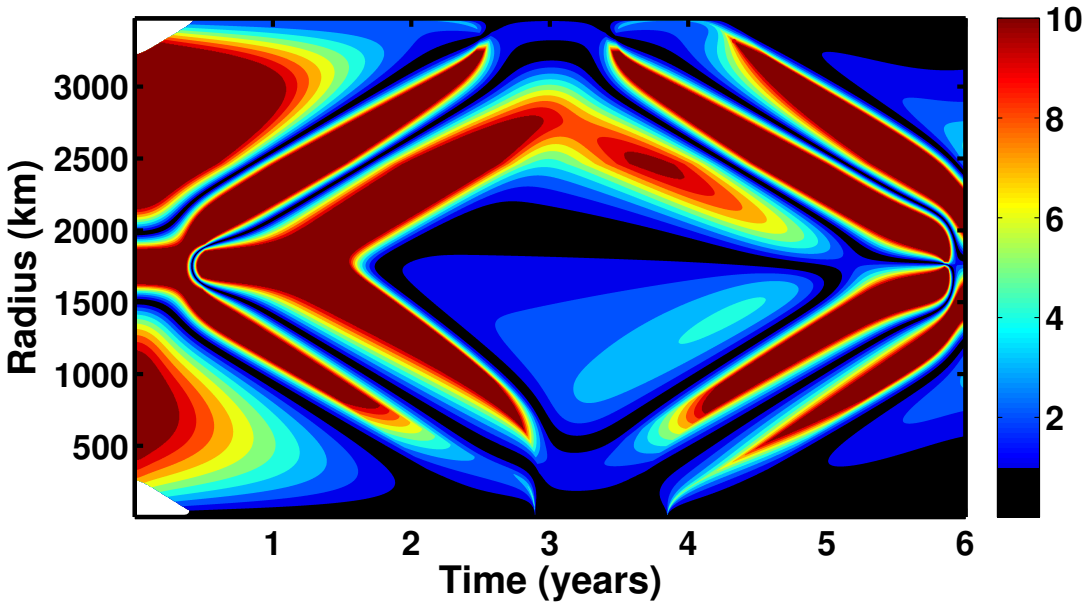

Figure 3.14: Contour plots of α, as defined by equation (3.3), over one complete transit time (6 years) in the full sphere model. Black regions ($\alpha < 1$) are locally 'dispersive', since term 1 is smaller than at least one of the other terms. Coloured regions are locally 'non-dispersive', with the magnitude of term 1 at least equal to that of the other terms in the blue regions and exceeding the other terms by at least a factor of 10 in the red regions. White regions show areas where the terms are very small and calculating the ratio is numerically intractable.

a measure α such that

$$\alpha = \frac{\left|\frac{\partial^2 u_\phi}{\partial s^2}\right|}{\max\left(\left|\frac{1}{s}\frac{\partial u_\phi}{\partial s}\right|, \left|\frac{s}{z_T^2}\frac{\partial u_\phi}{\partial s}\right|, \left|\frac{u_\phi}{z_T^2}\right|, \left|\frac{u_\phi}{s^2}\right|\right)}. \tag{3.3}$$

If α is sufficiently large, waves become effectively non-dispersive. For the purposes of the following discussion of our torsional wave models, we label waves as locally 'non-dispersive' if term 1 exceeds the largest of the other terms ($\alpha \geq 1$). The ratio α may be evaluated at every point in space during the wave evolution to determine what percentage of the spatial domain is dispersive or non-dispersive over a particular time duration.

Fig. 3.14 is a contour plot of α over one complete transit time (6 years) in the full sphere geometry. Black regions ($\alpha < 1$) are locally 'dispersive', since term 1 is smaller than at least one of the other terms. Coloured regions are locally 'non-dispersive' according to our definition, with the magnitude of term 1 at least equal to that of the other terms in the blue regions and exceeding the other terms by at least a factor of 10 in the red regions. White regions show areas where the terms are all very small and calculating

the ratio is numerically intractable. We see that in our geometry, geometric factors begin to dominate the second spatial derivative near the boundaries, especially near to the rotation axis, though the dispersion condition is also violated in central areas of the domain, where trailing wakes are observed. Since the condition given by equation (3.3) evaluates the extent to which the torsional wave equation itself is non-dispersive, rather than the solutions to the torsional wave equation, it is of interest to compare the predicted dispersive regions of the domain with the regions in which dispersion is seen in our model results. Comparing the contour plots of the first 6 years of wave evolution in Fig. 3.5 with the elements in Fig. 3.14, we find that wave dispersion, which manifests as an evolving wave pulse shape through time, coincides with regions of the domain where the second spatial derivative is dominated by another term, as predicted. We performed the same analysis, in both a sphere and spherical shell, using several initial velocity profiles of differing widths for threshold values on α of 1, 2, 5 and 10. Fig. 3.15 shows the percentage of the domain that is non-dispersive over one core transit time as a function of the initial pulse width. It shows that narrower Gaussian-like pulses (lower σ values) undergo less dispersion than wider pulses in both the full sphere and shell models. The models presented in Figs. 3.5 and 3.11 both used $\sigma = 0.1$. In the full sphere case, this corresponds to the domain being at most 84% non-dispersive over one transit time (using a threshold on α of 1). The spherical shell model is at most 83% non-dispersive over the same period, using a threshold on α of 1. Using the threshold value of 1 only ensures that the second derivative (term 1) is at least the same order of magnitude as the other terms, not that it is the dominant term of the RHS of the torsional wave equation. A more realistic condition would be that the second derivative must be at least an order of magnitude higher than the other terms to be considered the dominant term. Using this more stringent threshold value of 10, we find that the domains in models (ii) and (iii) are, respectively, only 40% and 42% non-dispersive over one core transit time.

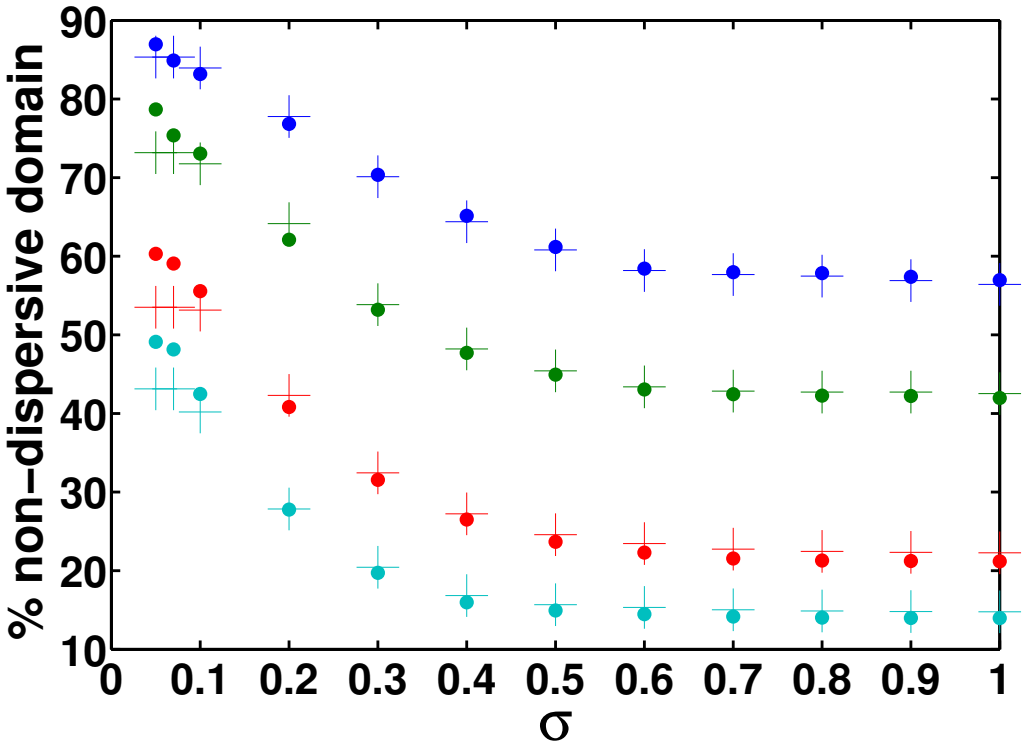

Figure 3.15: The percentage of the domain that is non-dispersive over one core transit time (6 years) in the full sphere (crosses) and shell (circles) geometries according to the four different thresholds on α: 1 (blue), 2 (green), 5 (red) and 10 (cyan) as a function of initial pulse width. Lower σ values correspond to narrower initial velocity profiles.

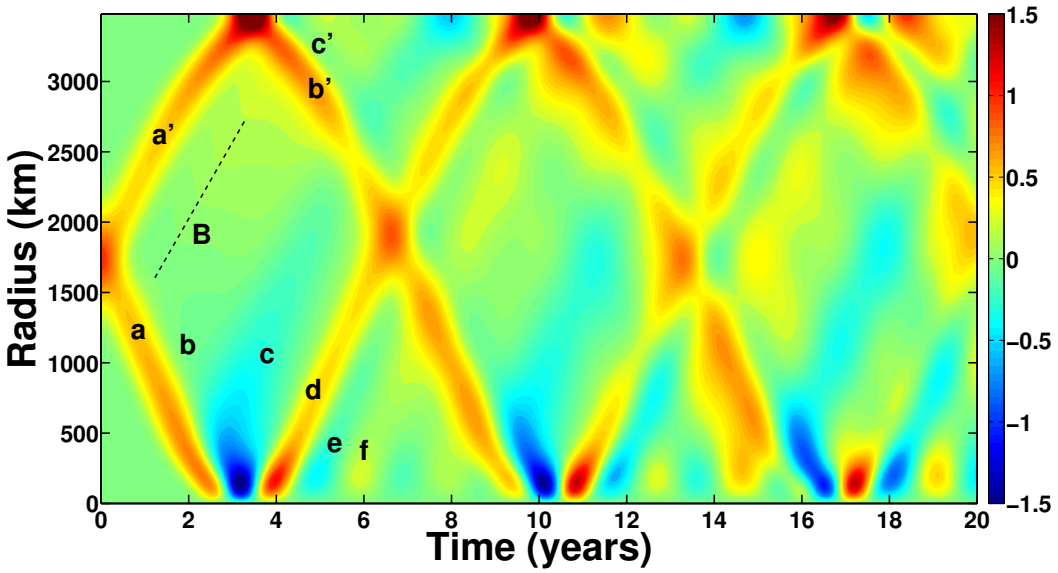

Figure 3.16: Contour plot of the velocity u_ϕ of torsional waves in a full sphere with the steady background magnetic field shown in Fig. 2.11, with time on the horizontal axis and cylindrical radius on the vertical axis. Red corresponds to positive velocity and blue corresponds to negative velocity.

3.7 Model iv: torsional waves in a magnetic field with spatially varying $\{B_s^2\}$

Since the magnetic field in the Earth's core is expected to vary on large length scales, it is of interest to study torsional wave evolution in an ambient magnetic field whose cylindrical average is spatially varying. Fig. 3.16 shows the first 20 years of torsional wave evolution in the spatially varying ambient magnetic field shown in Fig. 2.11.

As in previous results for constant $\{B_s^2\}$ models, the initial profile splits into two waves travelling in opposite directions, with a low amplitude tail connecting the two pulses in the centre of the domain. These pulses take just over 6 years to traverse the entire core. Waves reflect from the stress-free boundary at $s = r_c$ with no change of sign and with a partial change of sign at the rotation axis. We observe that wave energy becomes increasingly dispersed through the core with increasing time and that the initial profile is never recovered. In order to quantify this dispersion, two terms must be added to equation (3.2) to account for spatial variations of the $\{B_s^2\}$ profile. The fully expanded

torsional wave equation now reads

$$\frac{\partial^2 u_\phi}{\partial t^2} = \frac{1}{\mu_0 \rho_0}\left[\{B_s^2\}\left(\underbrace{\frac{\partial^2 u_\phi}{\partial s^2}}_{1} + \underbrace{\frac{1}{s}\frac{\partial u_\phi}{\partial s}}_{2} - \underbrace{\frac{s}{z_T^2}\frac{\partial u_\phi}{\partial s}}_{3} + \underbrace{\frac{u_\phi}{z_T^2}}_{4} - \underbrace{\frac{u_\phi}{s^2}}_{5}\right) + \underbrace{\frac{\partial u_\phi}{\partial s}\frac{\partial \{B_s^2\}}{\partial s}}_{6} - \underbrace{\frac{u_\phi}{s}\frac{\partial \{B_s^2\}}{\partial s}}_{7}\right], \tag{3.4}$$

which suggests that the following ratio

$$\alpha = \frac{\left|\frac{\partial^2 u_\phi}{\partial s^2}\right|}{\max\left(\left|\frac{\{B_s^2\}}{s}\frac{\partial u_\phi}{\partial s}\right|, \left|\frac{s\{B_s^2\}}{z_T^2}\frac{\partial u_\phi}{\partial s}\right|, \left|\frac{u_\phi\{B_s^2\}}{z_T^2}\right|, \left|\frac{u_\phi\{B_s^2\}}{s^2}\right|, \left|\frac{\partial u_\phi}{\partial s}\frac{\partial\{B_s^2\}}{\partial s}\right|, \left|\frac{u_\phi}{s}\frac{\partial\{B_s^2\}}{\partial s}\right|\right)} \tag{3.5}$$

should be evaluated at each point in space during wave evolution. We again use thresholds on α of 1, 2, 5 and 10, and find that over the first 6 years of wave propagation, the domain is 88%, 78%, 55% and 36% non-dispersive for these four thresholds for $\sigma = 0.1$. We note that these dispersion percentages are very similar to those obtained in the full sphere (ii) and spherical shell (iii) models with constant $\{B_s^2\}$ profiles, see Fig. 3.15. Fig. 3.17 shows the regions of the domain that are labelled 'dispersive' (black) and 'non-dispersive' (coloured) for model (iv). As in previous models, we see that dispersion mainly occurs near to the rotation axis due to geometric factors and, to a lesser extent, in central parts of the domain where trailing wakes are observed.

Although we observe the same geometric features in all of the models, there are some important differences in wave behaviour between the variable field model (iv) and the constant field models (ii) and (iii). First, the pulse trajectories in Fig. 3.16 are curved due to variations in the local Alfvén wave group velocity. Since the cylindrical average of the magnetic field $\{B_s^2\}$ varies across the core, and the local wave group speed depends on this quantity (see section 3.8), the pulses accelerate when the magnetic field strength is increasing and decelerate when the magnetic field is weakening. One consequence of this is that pulses (a) and (a') do not reach their respective boundaries at the same time, and that waves (c, d) and (b') no longer intercept each other in the centre of the domain as in the constant $\{B_s^2\}$ profile models. The second observed feature is an internal reflection, labelled as pulse B in Fig. 3.16, which likely arises due to the relatively steep magnetic field gradient at $s = 1300$ km (see the $\{B_s^2\}$ profile in Fig. 2.11). Third, we observe several pulses of alternating polarity near to

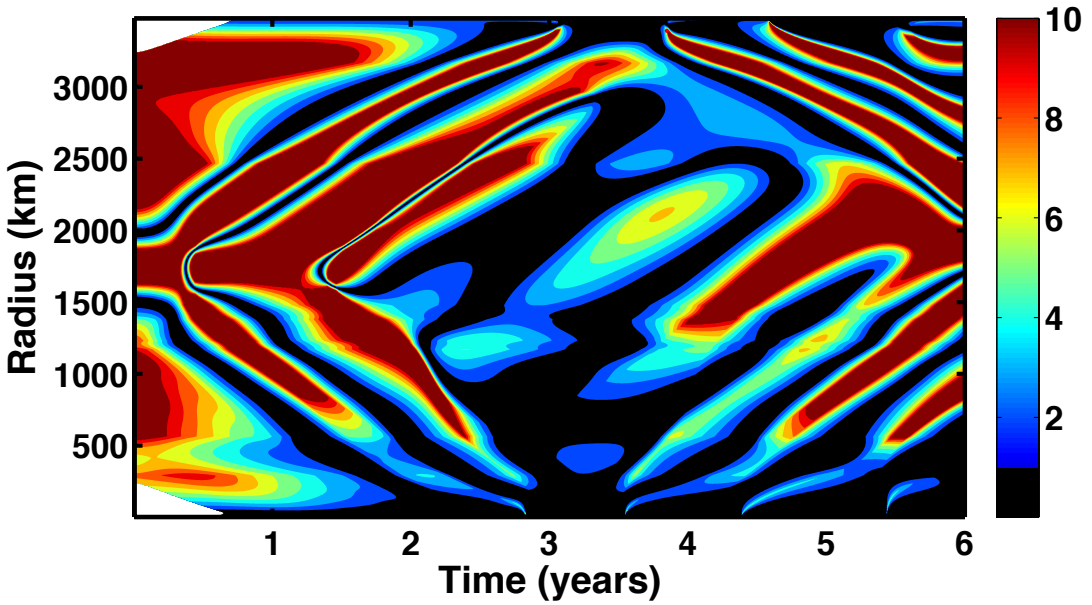

Figure 3.17: Contour plots of α, as defined by equation (3.5), over one complete transit time (6 years) in the full sphere model with varying $\{B_s^2\}$. Black regions ($\alpha < 1$) are locally 'dispersive', since term 1 is smaller than at least one of the other terms. Coloured regions are locally 'non-dispersive', with the magnitude of term 1 at least equal to that of the other terms in the blue regions and exceeding the other terms by at least a factor of 10 in the red regions. White regions show areas where the terms are very small and calculating the ratio would therefore be numerically intractable.

both the rotation axis and the equator after the first reflection of torsional waves at the boundaries (examples of these are labelled as (c'), (e) and (f)). We note that this effect is particularly prominent near the rotation axis, where the gradient of the magnetic field profile is steep. An explanation for the observed wave patterns is that strong magnetic field gradients cause continual reflections of propagating waves in the narrow region of the core between $s = 0$ and $s \approx 500$ km, resulting in waves being unable to exit this region.

3.8 Local wave speed

Dumberry (2009) investigated dispersion of torsional normal modes by substituting solutions of the following form into the torsional wave equation

$$u_\phi = U_0 e^{-i\omega t + iks},$$

where ω is the angular frequency and k is the wavenumber. For large k values, the

second spatial derivative (k^2 for the above form of solution) dominates the other terms on the RHS of the wave equation and we obtain

$$\omega^2 = \frac{\{B_s^2\}}{\mu_0 \rho_0} k^2,$$

from which the Alfvén wave group velocity

$$V_A = \frac{\partial \omega}{\partial k} = \sqrt{\frac{\{B_s^2\}}{\mu_0 \rho_0}} \tag{3.6}$$

may be recovered. In models (ii) - (iii) of travelling torsional waves, the cylindrical average of the radial magnetic field, $\{B_s^2\}$ was kept to a constant 4 $(\mathrm{mT})^2$. From the above Alfvén wave group velocity, it is possible to compare the theoretically predicted local wave speeds with those obtained in the models. Substituting the constants used in the models into equation (3.6) results in a predicted local wave speed of $\sim$0.018 m/s. Using the gradient of the wave travel path in our model results (the time taken for the pulse to traverse a particular distance), we obtain a local wave speed of $\sim$0.018 m/s as predicted. This group velocity was used to calculate the theoretical reflection time from the boundaries and used to produce Figs. 3.3, 3.4, 3.7 and 3.8, which show the wave velocity profiles one year before and after reflection.

In the results of model (iv), we observed all of the geometric effects observed in previous models with constant $\{B_s^2\}$ profiles, which included angular momentum effects, trailing wakes left behind wave pulses, geometric dispersion and phase shifts at the boundaries. In addition to these geometric effects, we also observed several features that arise due to magnetic field variations such as curved pulse travel paths, an internal reflection from the global field maximum and partially trapped waves near the boundaries. The trajectories of the pulses are curved due to variations in local Alfvén group velocity; we checked the local group velocity at several points during wave propagation by comparing the travel path gradients in the velocity contour plot (Fig. 3.16) with the predicted V_A according to equation (3.6), and found that the calculated and predicted values were in agreement.

3.9 The failure of Huygens' principle and dispersion in 2-D

The general wave equation for a scalar f is

$$\frac{\partial^2 f}{\partial t^2} = c^2 \nabla^2 f, \tag{3.7}$$

where c^2 is the wave group speed.

In sections 3.2-3.7, we commented upon the existence of dispersion and trailing wakes behind the wave pulses in our models. For the general wave equation above, the latter feature is related to what is termed the failure of Huygens' minor premise in even spatial dimensions. Huygens' minor premise states that a wave disturbance is localised in space and time (Hadamard, 1923; pp. 53). For example, a wave packet arriving at an initially quiescent location would depart after a finite time period leaving a quiescent state. This premise is known to hold for symmetric waves obeying equation (3.7) in odd spatial dimensions; for example, waves in 1-D are characterised by the solution (3.1), which has this property, as does the equivalent formula for spherically symmetric waves in 3-D

$$u = \frac{1}{r}\left[F_+(r+ct) + F_-(r-ct)\right], \tag{3.8}$$

where r is the spherical radius. However, it has been shown (Courant & Hilbert (1962; pp. 765-766); Hadamard (1923; pp. 53, 176-177)) that Huygens' minor premise fails in even dimensions and behind any wave pulse will be an infinite reverberation. Equation (3.7) can be written in cylindrical coordinates as

$$\frac{\partial^2 f}{\partial t^2} = c^2 \left(\frac{\partial^2 f}{\partial s^2} + \frac{1}{s}\frac{\partial f}{\partial s} \right), \tag{3.9}$$

and the second term on the RHS is linked to the failure of Huygen's principle in this geometric setting. Although torsional waves may be modelled in 1-D, 2-D or 3-D, we believe that they are fundamentally a 2-D phenomenon due to their convergence on an axis at $s = 0$. This convergence imposes many conditions on the velocity and its derivatives, and changes the shape of wave pulses due to phase shifts (see section 3.10). The torsional wave equation differs from the general cylindrically symmetric wave equation for a scalar, equation (3.9), for several reasons. First, torsional waves

are Alfvénic, meaning that the local wave group speed depends on the strength of the magnetic field at a particular location. This is taken into account by terms 6 and 7 on the RHS of equation (3.4). Second, the height of the geostrophic cylinders changes due to the spherical boundary of the CMB, which gives rise to terms 3 and 4 in equations (3.2) and (3.4). Finally, the velocity $\boldsymbol{u}$ is a vector field, of which torsional waves involve only the azimuthal component u_ϕ. Term 5 of equations (3.2) and (3.4) arises due to the vector nature of the velocity field. As term 2 on the RHS of the torsional wave equation (equations (3.2) and (3.4)) is the same as the term linked to the failure of Huygens' principle for the general wave equation (3.9), it is of interest to investigate where in the domain this term is large and whether these regions correspond to where trailing wakes are observed in our models. In order to do this, we produced individual contour plots of the ratio of term 1 to terms 2-5 on the RHS of equation (3.2) during one core transit time (6 years). These plots (Figs. 3.18a-d), have the same colour scale as figures 3.14 and 3.17.

Dispersion is observed in our torsional wave models as trailing wakes in the centre of the domain and as energy spreading out in the regions close to $s = 0$ and $s = r_c$ after a wave has passed through. From Figs. 3.18a-d, it seems that dispersion arises in our models due to the dominance of different terms in different regions of the domain. Terms 2 and 5 are large near to the rotation axis, whilst terms 3 and 4 are large near to the equator of the CMB. This suggests that all of these terms are sources of dispersion near the boundaries of the model domain. The regions in which term 2 is dominant, shown in Fig. 3.18a, correspond to the regions in the centre of the domain where we observe trailing wakes in our models. Since the other terms on the RHS of equation 17 are smaller than term 2 in the same regions at those times, we conclude that the failure of Huygens' principle in the geometric setting of torsional waves is related to the observed trailing wakes, and is therefore a source of dispersion in our models.

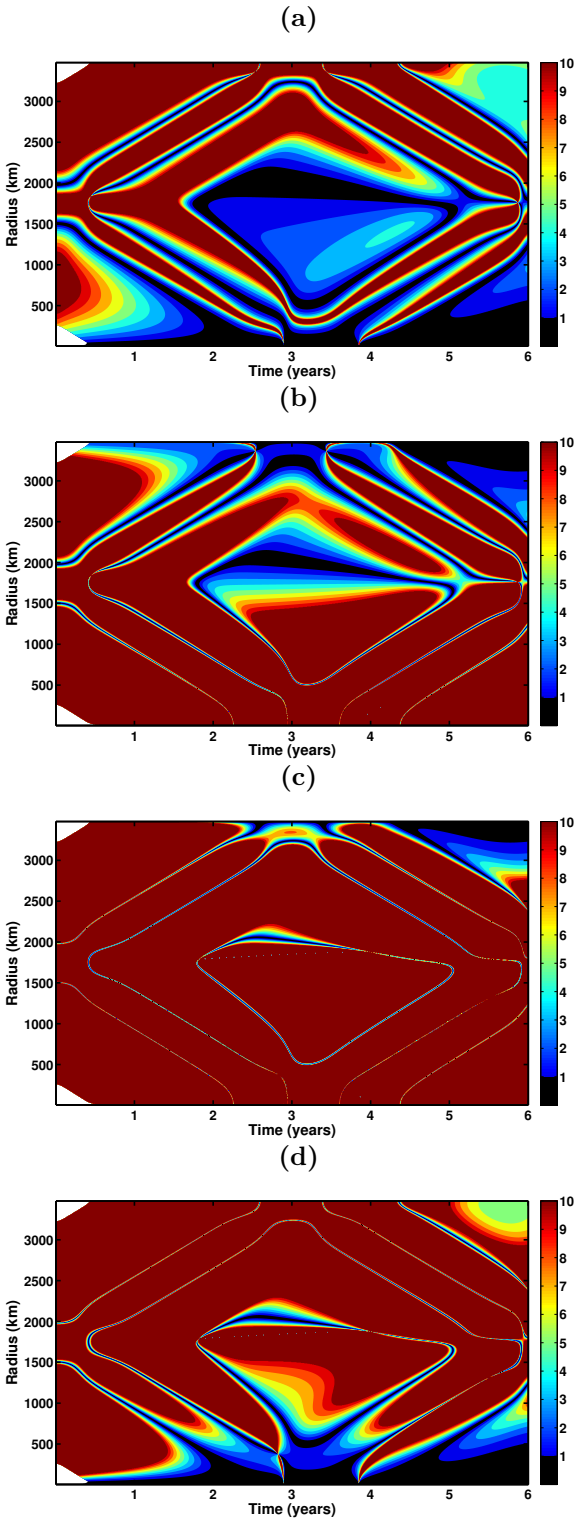

Figure 3.18: Contour plots of the magnitude of the ratio of term 1 to (a) term 2 (b) term 3 (c) term 4 and (d) term 5, from the RHS of equation (3.2), over one complete transit time (6 years) in the full sphere model. Black regions are locally 'dispersive', since the relevant term is larger than term 1. Coloured regions are locally 'non-dispersive', with the magnitude of term 1 at least equalling that of the other term in the blue regions and exceeding the other term by at least a factor of 10 in the red regions. White regions show areas where the terms are very small and calculating the ratio is numerically intractable.

3.10 Phase shift at the boundaries

In this section, we explain the change in wave profile upon reflection at the boundaries, which was reported in section 3 and Figs. 3.7 and 3.8. The reader is reminded that the rotation axis is not a physical boundary, but a singular point of the coordinate system at which an infinite set of constraints is satisfied, and as such, an explanation of the observed pseudo-reflection is not trivial. Morse & Feshbach (1953) investigated transient (wave) motion on a circular membrane of radius $r = a$ and, by considering normal modes, found that a wave undergoes a $\pi/4$ phase shift when traversing the region $r \approx 0$ to $r \approx a$. We now perform a similar analysis to that detailed in Morse & Feshbach (1953) for torsional normal modes, whose analytic form is known in a cylindrical container (constant z_T), and use phase shifts to explain wave behaviour at $s = 0$ and $s = r_c$.

For the purposes of the following discussion, we restrict ourselves to a simplified geometry consisting of a cylinder of radius 1, with constant $\{B_s^2\}$ such that the wave speed is 1. This case was considered in the benchmarking section of the previous chapter, see Fig. 2.9 for wave profiles and Fig. 2.10 for a space-time contour plot of the wave evolution. In this geometry, the general solution to the axisymmetric torsional wave equation is

$$u_\phi(s,t) = \sum_{j=1}^{\infty} N_j J_1(k_j s)\cos(k_j t), \tag{3.10}$$

where N_j are coefficients determined by the initial condition, J_1 is the first order Bessel function of the first kind and k_j is the j-th zero of J_1 (e.g. Mound & Buffett (2007)). These solutions satisfy the required regularity condition at the rotation axis and a no-slip condition ($u_\phi = 0$) at the outer boundary, rather than the stress-free condition that has previously been considered in this work. For large argument, $k_j s$, the asymptotic behaviour of J_1 is

$$J_1(k_j s) \approx \sqrt{\frac{2}{\pi k_j s}}\cos\left(k_j s - \frac{3\pi}{4}\right), \tag{3.11}$$

e.g. Abramowitz & Stegun (1984). Substitution of (3.11) into equation (3.10) gives the following general solution away from the rotation axis

$$u_\phi(s,t) \approx \frac{1}{2}\sum_{j=1}^{\infty} N_j \sqrt{\frac{2}{\pi k_j s}}\left[\cos\left(k_j(s-t) - \frac{3\pi}{4}\right) + \cos\left(k_j(s+t) - \frac{3\pi}{4}\right)\right], \tag{3.12}$$

which represents two waves travelling in opposite directions. Assuming an initial Gaussian wave profile centred at $s = 1/2$, the wave travelling towards the rotation axis (the 'incoming' wave) at time $t = 0$ is

$$u_\phi(s,0) \approx \frac{1}{2}\sum_{j=1}^{\infty} N_j \sqrt{\frac{2}{\pi k_j s}} \cos\left(k_j s - \frac{3\pi}{4}\right). \tag{3.13}$$

At time $t = 1$, this incoming wave packet has reflected at the rotation axis and is again centred at $s = 1/2$ and travelling outwards towards $s = 1$. The outgoing wave profile is

$$u_\phi(s,1) \approx \frac{1}{2}\sum_{j=1}^{\infty} N_j \sqrt{\frac{2}{\pi k_j s}} \cos\left(k_j (s-1) - \frac{3\pi}{4}\right), \tag{3.14}$$

which has undergone a phase shift of $-k_j$ in each mode with respect to the incoming wave. Using the asymptotic expansion of J_1 given by equation (3.11), we find an expression for the zeroes

$$k_j \approx \frac{3\pi}{4} + \left(j - \frac{1}{2}\right)\pi, \tag{3.15}$$

which implies the following index-dependent phase shift at the rotation axis

$$\psi = \begin{cases} \frac{\pi}{4} & j \text{ even}, \\ -\frac{3\pi}{4} & j \text{ odd} \end{cases}. \tag{3.16}$$

Note that at time $t = 0$, both the incoming and outgoing waves are described by equation (3.13). Wave behaviour at the outer boundary, $s = 1$, is considered by comparing the initial outgoing wave with the incoming wave profile at time $t = 1$, which gives a phase shift of $+k_j$ in every mode.

In the above analysis, we have used the asymptotic approximations to torsional normal modes in a cylinder to investigate the predicted phase shift at the rotation axis and at the outer boundary (for a no-slip boundary condition). These predicted phase shifts are not uniform, but depend on the mode under consideration. Since the normal mode solutions to the torsional wave equation in a cylinder are known, it is of interest to compare these analytic solutions with the wave profiles approximated by their phase shifted asymptotic form, which is given by equations (3.12) and (3.16). The initial wave profile described by equation (2.60), with $\sigma = 0.1$, was projected onto the first twenty normal modes of the system and evolved through time. Figs. 3.19a and 3.19b show, respectively, the travelling wave solution given by the normal mode projections

(blue line) and their phase shifted asymptotic form (red line) for reflections at $s = 0$ and $s = 1$. In both cases, the two wave profiles are very similar, which indicates that the reflections are adequately described by the k_j (index-dependent) phase shift of the asymptotic approximations. Interestingly, the index-dependent phase shifts reproduce the analytic normal mode wave behaviour for both the rotation axis and $s = 1$, despite the former being a singular point and the latter a physical boundary.

Powell (1994) investigated the phase shift of waves on a circular membrane when passing through, or reflecting from, the focal point. By considering normal modes and their periodic approximations, he found that the divergent (outgoing) waveform is found by phase shifting the convergent (incoming) waveform by $-\pi/2$ in every mode. As a uniform $\pi/2$ phase shift of a waveform constitutes its Hilbert transform (the sign of the phase shift depends on the convention, e.g. Shearer (2009; pp. 155)), Powell (1994) concluded that the focal shift of waves on a circular membrane is equivalent to the Hilbert transform of the converging wave. In the remainder of this section, we attempt to recover this result for torsional normal mode projections and for travelling waves in forward models. For narrower initial profiles than those shown in Figs. 3.19a and 3.19b, which used $\sigma = 0.1$, we recover this result for our normal mode projections. Although the normal mode projections and their phase shifted asymptotic approximations remain very similar, the outgoing wave after reflection at the rotation axis also strongly resembles the Hilbert transform of the incoming wave profile, which in this case, converts the cosines in equation (3.12) to sines. It seems that, for a sufficiently narrow pulse, the overall wave behaviour of the predicted phase shift, for which some normal modes are shifted by $\pi/4$ and others by $-3\pi/4$, averages to mimic the behaviour of a uniform $\pi/2$ phase shift.

We might expect to recover a similar result in our torsional wave models because the region near to the rotation axis in a spherical geometry is well-approximated by a cylinder (constant z_T). For our torsional wave models, which are in a full sphere and an equatorially symmetric spherical shell, there is empirical evidence to suggest that the Hilbert transform is recovered for narrow pulses after reflection at the rotation axis. Fig. 3.20a shows the wave profiles 1 year before (blue line) and after (red line) in the previously discussed full sphere model (ii), with the Hilbert transform of the blue profile drawn in black. For this initial profile, with $\sigma = 0.1$, we see that although the

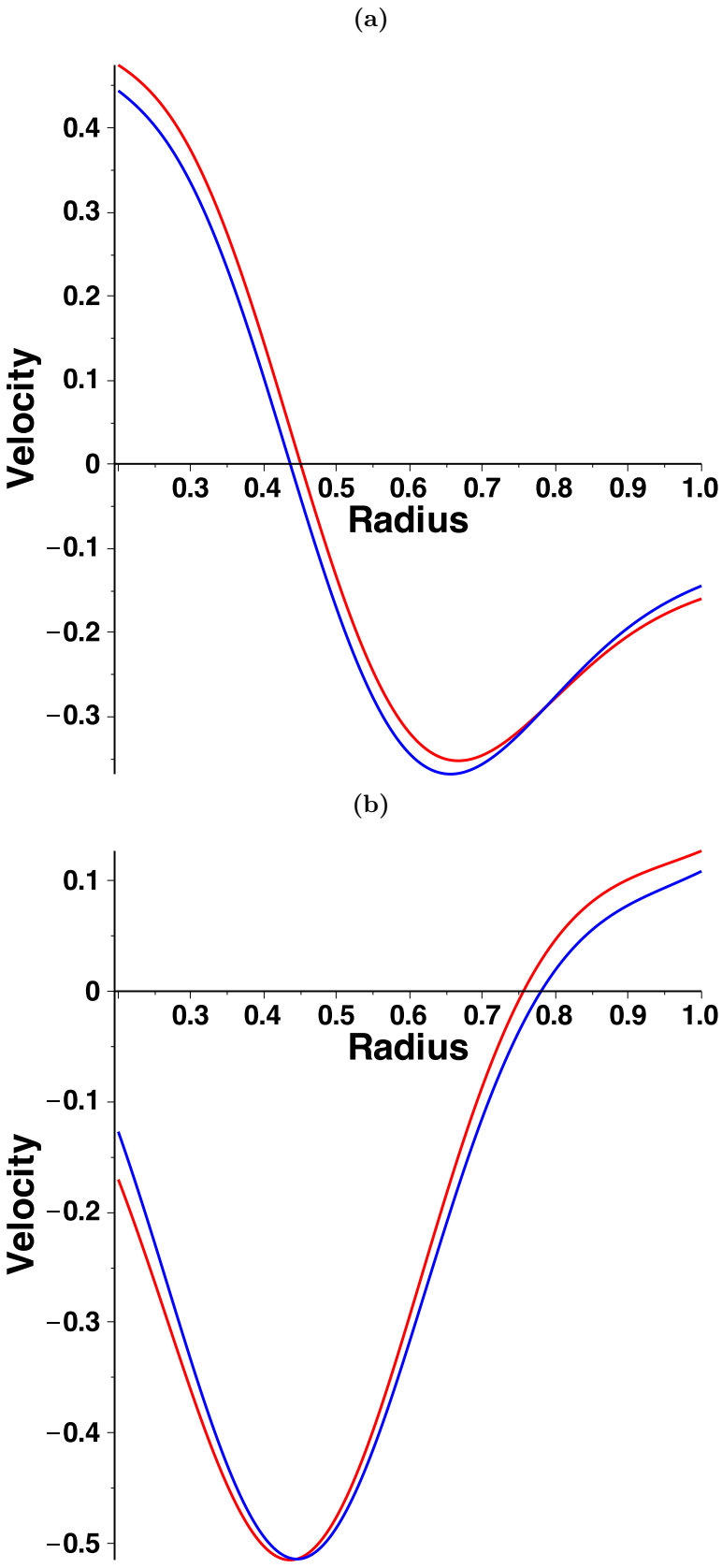

Figure 3.19: (a) Comparison of the outgoing wave in a cylinder of radius 1 at time $t = 1$ (after reflection at the rotation axis) according to the normal mode solution given by equation (3.10) (blue line) and the phase shifted asymptotic approximation to the normal mode solutions, given by equations (3.12) and (3.16) (red line). (b) Comparison of the incoming wave in a cylinder of radius 1 at time $t = 1$ (after reflection at the outer boundary $s = 1$) according to the normal mode solution given by equation (3.10) (blue line) and the phase shifted asymptotic approximation to the normal mode solutions, given by equations (3.12) and (3.16) (red line).

general shape of the Hilbert transform matches the reflected wave profile, the required regularity condition is not met at the rotation axis, which implies that the wave has undergone a more complex reflection than a uniform $\pi/2$ phase shift. However, when the initial profile is much narrower, as shown in Fig. 3.20b for a σ value of 0.01, the shape of the Hilbert transform and reflected wave profile match more closely and the Hilbert transform better matches the regularity condition at $s = 0$. From this we conclude that while some narrow initial pulses appear to undergo a uniform phase shift at the rotation axis, in general, an arbitrary initial pulse will undergo a more complicated phase shift that cannot readily be understood as a Hilbert transform.

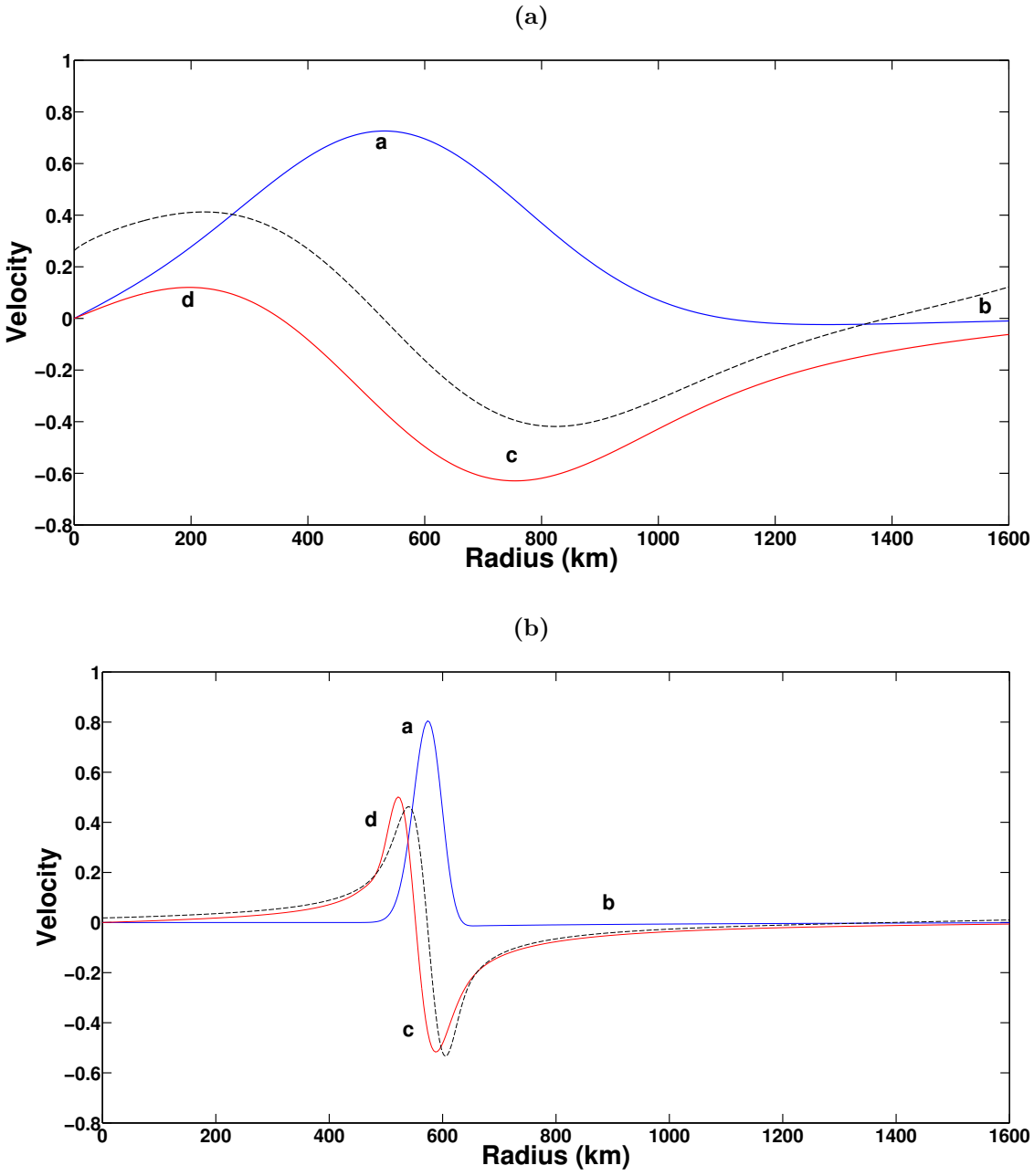

Figure 3.20: (a) Velocity profiles of the waves one year before (blue) and after (red) reflection at the rotation axis in the full sphere model (ii). The annotations correspond to those in Fig. 3.5 and the times at which the profiles were taken are shown in that figure as two vertical black lines. The black dashed line is the Hilbert transform of the incoming wave (the blue line). Note that the Hilbert transform is somewhat similar to the outgoing wave (the red line). (b) Velocity profiles of the waves one year before (blue) and after (red) reflection at the rotation axis in a full sphere model with a narrow initial profile ($\sigma = 0.01$). The black dashed line is the Hilbert transform of the incoming wave (the blue line). Note the increased similarity of the Hilbert transform to the outgoing wave (the red line).

3.11 Implications for torsional waves in the Earth's core

In the Earth's interior, the inner core is thought to have strong electromagnetic coupling with the outer core, which was not included in our models. In that case, one would expect the core fluid above and below the inner core (regions II and III in Fig. 1.4b) to rotate rigidly inside the tangent cylinder at the same speed as the inner core. Electromagnetic coupling to the inner core would quickly dissipate torsional waves entering the tangent cylinder and, consequently, waves would not exist long enough to reflect from the rotation axis and reenter the outer core as they do in our models. The reflection at the tangent cylinder observed in Fig. 3.13 is an interesting feature that may have implications for torsional waves in the geophysical context. If a torsional wave were generated outside the tangent cylinder in the Earth's core by a local impulse in space and time, as opposed to a temporally periodic global forcing, we could only expect to observe the outwards travelling pulse once at the CMB before it is reflected back into the core and absorbed on the tangent cylinder. However, as the discontinuity in the derivative of the cylinder height causes waves to be partially reflected at the tangent cylinder, it is possible that they could be observed at the CMB at regular intervals and may then be linked with decade variations in SV and/or ΔLOD . Another possible source of internal reflections of torsional waves in the Earth's core are strong gradients in the radial magnetic field, as seen in Fig. 3.16 (pulse B). However, the reflection coefficients for pulses A and B are both very small and it is possible that these internally reflected pulses would immediately be damped or dispersed upon reaching the CMB such that regular observation is impossible.

The analysis by Dumberry (2009) reproduced in section 3.8 implies that short wavelength torsional normal modes, corresponding to high wave numbers, are non-dispersive. Our findings are consistent with that conclusion because we find that, for travelling torsional waves, narrow (short wavelength) wave profiles are less dispersive than wider pulses, see Fig. 3.15. This result may be particularly important when studying torsional waves in the Earth's core because those inferred from SV data appear to be relatively long wavelength. For example, the smallest features of torsional waves presented in Gillet et al. (2010) occupy approximately one fifth of the core radius and those presented in Hide et al. (2000) occupy almost the entire core radius. Our analyses of dispersive regions and the evolution of our modelled waves suggest that torsional

waves in the core may undergo a significant dispersion process that arises solely as a result of core geometry. This geometric dispersion is an effect that has previously been neglected in torsional wave studies. Recent work by Schaeffer et al. (2012) discusses Alfvén wave reflection properties and energy dissipation in boundary layers based on the ratio of kinematic viscosity to magnetic diffusion (the magnetic Prandtl number, P_m). They argue that for geophysically relevant liquid metals, corresponding to $P_m \ll 1$, little energy is dissipated during a single reflection at $s = r_c$ but that many successive reflections may lead to significant dissipation. Dissipative processes are damping mechanisms for waves; they dissipate wave energy and decrease wave amplitude. Schaeffer et al. (2012) define a quality factor for reflected waves and conclude that torsional wave normal modes could survive in the Earth's core for a few periods of the fundamental modes, which they take as 6 years. Given that successive reflections from the boundaries significantly changes the shape of wave pulses in our models, as seen in Figs. 3.5 and 3.6 for example, we suggest that terrestrial torsional waves would undergo significant dispersion (energy spreading) irrespective of, and in addition to, any dissipative (damping) effects and therefore may not survive as distinct pulses for several transits of the Earth's core.

Chapter 4

Geophysical signatures of torsional waves

In the previous chapter, we presented the results of forward models of torsional waves and discussed their propagation in Earth's core. The key features observed in the models were dispersion, phase shifts and internal reflections. Torsional waves involve the interaction of zonal fluid flow and the ambient magnetic field in the core. Consequently, they perturb the background magnetic field and induce a secondary magnetic field. The subject of this chapter is the magnetic signals induced by the torsional waves in the previously presented forward models. In §1.3, we discussed observations of the geomagnetic field and the resulting spherical harmonic magnetic field models that are constructed using potential theory. Using a steady background magnetic field from observationally constrained field models and azimuthal velocities from torsional wave forward models, we solve an induction equation for the wave-induced secular variation. Treating both the background field and the wave-induced perturbation as potential fields allows us to calculate their spherical harmonic coefficients and reconstruct their North, East and radial components. We construct time series and maps of wave-induced SV and investigate how the propagation characteristics identified in the previous chapter manifest in the magnetic signals. As torsional waves have previously been linked with geomagnetic jerks (Bloxham et al., 2002), we apply a method developed by Brown et al. (2013) to search for jerk-like signals in the synthetic time series. Finally, we examine the amplitudes of the torsional wave-induced SV and use the amplitude of observed SV signals to place constraints on torsional waves in the core.

4.1 Torsional waves and geomagnetic jerks

Geomagnetic jerks are abrupt jumps in the second time-derivative (secular acceleration, SA) of Earth's magnetic field, which corresponds to sharp changes in the trend of the the first time-derivative of the magnetic field (the SV) (Courtillot et al., 1978). Jerks separate periods of almost steady SA so that the SV appears as a series of straight-line segments separated by the jerk itself, see Fig. 4.1. Several jerks are known to have occurred in the 20th and 21st centuries, including those in 1969 (Courtillot et al., 1978, Malin et al., 1983, Whaler, 1987), 1978 (Gubbins & Tomlinson, 1986, Davis & Whaler, 1997), 1991 (Macmillan, 1996), 1999 (Mandea et al., 2000) and 2003 (Olsen & Mandea, 2007). According to Alexandrescu et al. (1996), who used wavelet analysis to detect and characterise worldwide jerk occurrences, some are observed globally and others in only small regions, and all occur within differential time delays of about two years at Earth's surface.

Pinheiro et al. (2011) described a method for applying a two-part linear regression to the SV of observatory data (i.e. fitting a 'V' shape to the SV) and generating a probability density function (PDF) of potential jerk occurrence times. The technique was designed for use on a single component of SV data and two-part linear regression is iterated across the window, with each time step considered a potential jerk occurrence. Brown et al. (2013) extended this method to use a sliding window for the two-part linear regression and applied the modified method to monthly mean data from observatories spanning the period 1957-2008. Their study provided quantitative uncertainty estimates on jerk occurrence times and amplitudes with minimal *a priori* information. They identified frequent events fitting their definition of jerks throughout the period of study, though relative peaks in the global number of jerk occurrences were found in 1968-71, 1973-74, 1977-79, 1983-85, 1989-93, 1995-98 and 2002-03, coinciding with previously established jerk events. They also found further, poorly sampled, events in the early 1960s and late 2000s. The jerks in that study often occurred only in one component of the magnetic field and were not globally contemporaneous. The regional jerks had no consistent occurrence pattern, though Brown et al. (2013) identified possible periodic trends in Europe and N. America.

Despite many attempts, the physical origin of geomagnetic jerks is yet to be established,

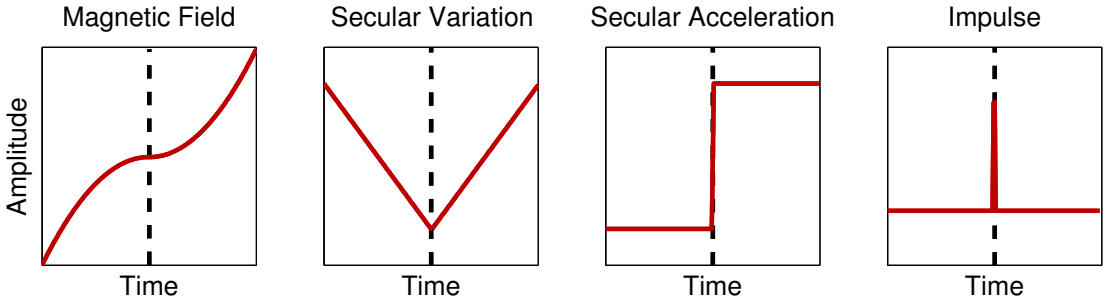

Figure 4.1: The general morphology of a geomagnetic jerk as seen in, from left to right, the magnetic field, the SV (first time-derivative of the field), the SA (second time-derivative of the field) and the impulse (third time-derivative of the field).

see Mandea et al. (2010) for a recent review of this topic. Malin & Hodder (1982) used spherical harmonic analysis to establish that jerks are of internal origin, but none of the subsequently proposed generating mechanisms has proved completely successful. The previous interpretations of jerks include core flows (e.g. Le Huy et al., 1998, Wardinski et al., 2008, Silva & Hulot, 2012), torsional oscillations (Bloxham et al., 2002) and instability of an Ekman-Hartman boundary layer at the CMB (Desjardins et al., 2001). Of particular interest to this work are those interpretations that rely upon zonal core flows and/or torsional waves.

Several authors (Waddington et al., 1995, Bloxham et al., 2002, Olsen & Mandea, 2008) have shown that no steady flow can produce jerk-like features, nor can a steady flow in a drifting frame (Holme & Whaler, 2001). This implies that a steady flow of the magnitude typically assumed for core flow, $\mathcal{O}(10^{-4})$ m/s, is not able to produce the strong SA associated with jerks and that flow acceleration is likely an important contribution to jerks (Waddington et al., 1995). Bloxham et al. (2002) relaxed the steady flow constraint and showed that jerks can be explained by the combination of a steady flow and a simple time-varying, axisymmetric, equatorially symmetric, toroidal zonal flow. Such flows are consistent with torsional oscillations (torsional normal modes) and give an excellent fit to many jerk features, particularly in Europe. The authors also noted that the SV generated by simple core flows depends on the local morphology of the ambient magnetic field, as we shall see in §4.4. This is a crucial point because it means that large-scale core flow can produce localised signals at magnetic observatories and thus there is no need to invoke a small-scale core flow to explain those jerk events that are observed on a regional scale. However, whilst the simple zonal flows consistent with torsional waves are likely an important contribution to jerks, less restrictive flows,

such as toroidal or tangentially geostrophic flows, are needed to reproduce all of the observed features (e.g. Wardinski et al., 2008, Silva & Hulot, 2012). Toroidal flows have no radial (poloidal) component and are consistent with a stratified layer at the top of the outer core, which was first proposed by, among others, Whaler (1980) and Braginsky (1999). More recently, various authors (e.g. Helffrich & Kaneshima, 2013, Gubbins & Davies, 2013, Buffett, 2014) have advocated a stratified layer in the outer core using seismological evidence, geomagnetic observations and material properties of liquid iron at high temperature and pressure. Tangentially geostrophic flows neglect the Lorentz term in the force balance at the top of the core, implying a zeroth order balance between the horizontal components of the pressure gradient and the Coriolis force (Le Mouël, 1984). This flow is also consistent with a stratified layer beneath the CMB (Jault & Le Mouël, 1991), though this constraint is less restrictive than the purely toroidal case because it allows a poloidal component. An intermediary flow that is more general than pure torsional oscillations but more restrictive than tangential geostrophy is also able to explain observed SV, including geomagnetic jerks. These are called quasi-geostrophic flows (Gillet et al., 2009) and are almost invariant along the rotation axis.

Given the proposed link between torsional oscillations, zonal flows and geomagnetic jerks, it is of interest to take velocity data from torsional wave forward models and investigate whether our modelled travelling torsional waves are capable of producing SV signals that resemble jerks in terms of amplitude and timescale. In order to do this, we first calculate the torsional wave-induced SV and then apply the jerk detection method developed by Brown et al. (2013) to the resulting synthetic time series.

4.2 Method

Under the frozen-flux approximation, fluid in the outer core is assumed to be perfectly conducting and magnetic field lines are tied into the fluid. Since the mantle is presumed to be an electrical insulator, there is a jump in electrical conductivity across this boundary which means only the radial component of the magnetic field is guaranteed to be continuous across the CMB (e.g. Whaler & Holme, 2007). Fluid motions interact with B_r through the radial component of the diffusionless version of the induction equation discussed in chapter 1.4.1, equation (1.6). The frozen-flux form of the

induction equation at the CMB is

$$\frac{\partial B_r}{\partial t} = -\boldsymbol{\nabla_H} \cdot (\boldsymbol{u} B_r), \tag{4.1}$$

e.g. Canet et al. (2009), where $\boldsymbol{\nabla_H}\cdot$ is the horizontal divergence operator. For an arbitrary vector, $\boldsymbol{A}$, defined in spherical coordinates (r, θ, ϕ), $\boldsymbol{\nabla_H} \cdot \boldsymbol{A} = \frac{1}{r\sin\theta}\frac{\partial A_\theta \sin\theta}{\partial\theta} + \frac{1}{r\sin\theta}\frac{\partial A_\phi}{\partial\phi}$.

The total magnetic field, previously denoted $\boldsymbol{B}$, is the sum of the steady background field $\boldsymbol{B}$ and a small perturbation $\boldsymbol{b}$. In the following discussion, we assume that this perturbation to the magnetic field is caused by flow associated with torsional waves, u_ϕ. Therefore, the equation to be solved is a linearisation of (4.1) when $\boldsymbol{u}$ and $\boldsymbol{b}$ are small:

$$\frac{\partial b_r}{\partial t} = -\frac{u_\phi}{s}\frac{\partial B_r}{\partial \phi} \tag{4.2}$$

where s is the radius in cylindrical coordinates and is linked to the radius in a spherical coordinate system by the relation $s = r\sin\theta$.

Since the mantle is presumed electrically insulating, the vector fields $\boldsymbol{B}$ and $\boldsymbol{b}$ can both be expressed as scalar potential fields, V and v respectively, such that

$$\boldsymbol{B} = -\nabla V, \tag{4.3}$$

$$\nabla^2 V = 0, \tag{4.4}$$

$$\boldsymbol{b} = -\nabla v \tag{4.5}$$

and

$$\nabla^2 v = 0. \tag{4.6}$$

These scalar fields, evaluated at a radius r, are expressed as sums of spherical harmonics and Gauss coefficients such that

$$V = r\sum_{l=1}^{\infty}\sum_{m=0}^{l}\left(\frac{a}{r}\right)^{l+1}\left[G_l^m \cos m\phi + H_l^m \sin m\phi\right] P_l^m(\cos\theta), \tag{4.7}$$

where a is the radius of the Earth, $P_l^m(\cos\theta)$ is the associated Legendre function in

$\cos\theta$ of degree l and order m and G_l^m and H_l^m are the Gauss coefficients. These are usually denoted using lower case g_l^m and h_l^m, but we use upper case letters here to avoid confusion with the expansion of b_r below, which uses a different set of Gauss coefficients denoted g_l^m and h_l^m.

The radial component of the steady background magnetic field is

$$B_r = -\frac{\partial V}{\partial r}, \tag{4.8}$$

which expands to give

$$B_r = \sum_{l=1}^{\infty}\sum_{m=0}^{l}(l+1)\left(\frac{a}{c}\right)^{l+2}\left[G_l^m\cos m\phi + H_l^m\sin m\phi\right]P_l^m(\cos\theta) \tag{4.9}$$

when evaluated at the CMB $r = c$.

The ϕ derivative of this component is therefore

$$\frac{\partial B_r}{\partial \phi} = \sum_{l=1}^{\infty}\sum_{m=0}^{l} m(l+1)\left(\frac{a}{c}\right)^{l+2}\left[-G_l^m\sin m\phi + H_l^m\cos m\phi\right]P_l^m(\cos\theta). \tag{4.10}$$

Using a similar expansion for the perturbation to the main field gives an expression for b_r at the CMB

$$\begin{aligned} b_r &= -\frac{\partial v}{\partial r} \\ &= \sum_{l=1}^{\infty}\sum_{m=0}^{l}(l+1)\left(\frac{a}{c}\right)^{l+2}\left[g_l^m\cos m\phi + h_l^m\sin m\phi\right]P_l^m(\cos\theta) \end{aligned} \tag{4.11}$$

and its time derivative

$$\frac{\partial b_r}{\partial t} = \sum_{l=1}^{\infty}\sum_{m=0}^{l}(l+1)\left(\frac{a}{c}\right)^{l+2}\left[\dot{g}_l^m\cos m\phi + \dot{h}_l^m\sin m\phi\right]P_l^m(\cos\theta). \tag{4.12}$$

where g_l^m and h_l^m are the Gauss coefficients associated with $\boldsymbol{b}$ and $\dot{g}_l^m$ and $\dot{h}_l^m$ denote their temporal derivative.

Substituting equations (4.10) and (4.12) into (4.2) gives

$$\sum_{l=1}^{\infty}\sum_{m=0}^{l}(l+1)\left(\frac{a}{c}\right)^{l+2}\left[\dot{g}_l^m\cos m\phi+\dot{h}_l^m\sin m\phi\right]P_l^m(\cos\theta)=$$
$$-\frac{u_\phi}{r\sin\theta}\sum_{l=1}^{\infty}\sum_{m=0}^{l}m(l+1)\left(\frac{a}{c}\right)^{l+2}\left[-G_l^m\sin m\phi+H_l^m\cos m\phi\right]P_l^m(\cos\theta). \quad (4.13)$$

This expression can be greatly simplified by using the Schmidt quasi-normalised spherical harmonics defined by

$$Y_l^m(\theta,\phi)=\sqrt{\frac{(2l+1)(l-m)!}{4\pi(l+m)!}}P_l^m(\cos\theta)\left[\cos m\phi+i\sin m\phi\right] \quad (4.14)$$

and exploiting their orthogonality properties

$$\int_0^{2\pi}\int_0^{\pi}Y_l^mY_{l'}^{m'*}\sin\theta d\theta d\phi=\frac{4\pi}{2l+1}\delta_{ll'}\delta_{mm'} \quad (4.15)$$

where * denotes the complex conjugate and δ is the Kronecker delta.

Multiplying equation (4.13) by $P_{l'}^{m'}(\cos\theta)\cos m'\phi$ and integrating over a spherical surface (the CMB) gives

$$\int_0^{2\pi}\int_0^{\pi}\sum_{l=1}^{\infty}\sum_{m=0}^{l}m(l+1)\left(\frac{a}{c}\right)^{l+2}\Big[\dot{g}_l^m\cos m\phi\cos m'\phi P_l^m(\cos\theta)P_{l'}^{m'}(\cos\theta)+$$
$$\dot{h}_l^m\sin m\phi\cos m'\phi P_l^m(\cos\theta)P_{l'}^{m'}(\cos\theta)\Big]\sin\theta d\theta d\phi=$$
$$-\int_0^{2\pi}\int_0^{\pi}\frac{u_\phi}{r\sin\theta}\sum_{l=1}^{\infty}\sum_{m=0}^{l}m(l+1)\left(\frac{a}{c}\right)^{l+2}\Big[-G_l^m\sin m\phi+$$
$$H_l^m\cos m\phi\Big]\cos m'\phi P_l^m(\cos\theta)P_{l'}^{m'}(\cos\theta)\sin\theta d\theta d\phi \quad (4.16)$$

which simplifies to

$$\frac{4\pi l'}{2l'+1}(l'+1)\left(\frac{a}{c}\right)^{l'+2}\dot{g}_{l'}^{m'}=-\int_0^{\pi}\frac{u_\phi}{r\sin\theta}\Bigg[\sum_{l\geq m'}^{\infty}(l+1)\left(\frac{a}{c}\right)^{l+2}$$
$$H_l^{m'}P_l^{m'}(\cos\theta)\Bigg]m'P_{l'}^{m'}(\cos\theta)\sin\theta d\theta\underbrace{\int_0^{2\pi}\cos^2 m'\phi d\phi}_{=\pi\text{ for }m'>0\text{ or }=2\pi\text{ for }m'=0}. \quad (4.17)$$

Therefore

$$\frac{4\pi l'}{2l'+1}(l'+1)\left(\frac{a}{c}\right)^{l'+2}\dot{g}_{l'}^{m'} = -\int_0^\pi \frac{u_\phi \pi}{r\sin\theta}\left[\sum_{l\geq m'}^{\infty}(l+1)\left(\frac{a}{c}\right)^{l+2}\right.$$
$$\left. H_l^{m'}P_l^{m'}(\cos\theta)\right] m' P_{l'}^{m'}(\cos\theta)\sin\theta d\theta. \tag{4.18}$$

The 1-D torsional wave models previously discussed in chapters 2 and 3 give the azimuthal velocities as a function of cylindrical radius s. We must now map these velocities $u_\phi(s)$ onto a grid in θ and ϕ so that all of the RHS of the above equation is defined on a spherical surface. This projection onto spherical harmonics is performed in a similar manner to the normal mode projections described in §2.2.1. We begin by assuming that the velocity may be represented as a linear sum of zonal spherical harmonics ($m = 0$) such that

$$u_\phi(s) = \sum_{k=1}^{\infty} a_k P_k^0(\cos\theta), \tag{4.19}$$

where a_k is the contribution of a particular mode k. We may then use orthogonality properties to derive an expression for each coefficient a_k up to the maximum number of modes used in the projection, which is chosen to give a converged solution (see §4.4 for a discussion of resolution testing).

For each order m', we then calculate the sum in square brackets at each θ node, we denote the sum $\beta(\theta)$ such that

$$\dot{g}_{l'}^{m'} = -\frac{2l'+1}{4a(l'+1)}\left(\frac{c}{a}\right)^{l'+2} m' \int_0^\pi \frac{u_\phi}{r\sin\theta}\beta P_{l'}^{m'}(\cos\theta)\sin\theta d\theta. \tag{4.20}$$

A similar expression for the $\dot{h}_l^m$ coefficients is obtained by multiplying equation (4.13) by $P_{l'}^{m'}(\cos\theta)\sin m'\phi$ and again using the orthogonality properties of the spherical harmonics to simplify the resulting expression. We then have

$$-\frac{4\pi l'}{2l'+1}(l'+1)\left(\frac{a}{c}\right)^{l'+2}\dot{h}_{l'}^{m'} = -\int_0^\pi \frac{u_\phi}{r\sin\theta}\left[\sum_{l\geq m'}^{\infty}(l+1)\left(\frac{a}{c}\right)^{l+2}\right.$$
$$\left. G_l^{m'}P_l^{m'}(\cos\theta)\right] m' P_{l'}^{m'}(\cos\theta)\sin\theta d\theta \underbrace{\int_0^{2\pi}\sin^2 m'\phi d\phi}_{=\pi} \tag{4.21}$$

which gives a final expression for $\dot{h}_{l'}^{m'}$

$$\dot{h}_{l'}^{m'} = \frac{2l'+1}{4a(l'+1)}\left(\frac{c}{a}\right)^{l'+2} m' \int_0^{\pi} \frac{u_\phi}{r\sin\theta}\beta P_{l'}^{m'}(\cos\theta)\sin\theta d\theta, \tag{4.22}$$

where the coefficient $G_l^{m'}$, rather than $H_l^{m'}$, now appears in the sum β.

Since we know the value of the integrand everywhere on the spherical surface, we can use Gauss Legendre quadrature (GLQ) to evaluate the above integral. GLQ is a numerical integration method that approximates the value of a definite integral using a weighted sum of function values at specified points in the integral domain such that

$$\int_{-1}^{1} f(x)dx \approx \sum_{i=1}^{N} w_{n,i} f(x_{n,i}) \tag{4.23}$$

where the $x_{n,i}$ are the quadrature points and the $w_{n,i}$ are the weights (e.g. Abramowitz & Stegun (1984)). The quadrature point $x_{n,i}$ is the i-th root of the Legendre polynomial of degree n ($P_n(x)$) and its weight is

$$w_{n,i} = \frac{2}{(1-x_{n,i}^2)\left[P_n'(x_{n,i})\right]^2} \tag{4.24}$$

where $P_n'(x)$ is the derivative of the Legendre polynomial $P_n(x)$ with respect to x. The abscissae for quadrature occur symmetrically about 0, and the number of quadrature points, N, is chosen to yield a converged representation of a polynomial of degree n.

Once the $\dot{g}_l^m$ and $\dot{h}_l^m$ coefficients have been obtained, they are then substituted back into equation (4.12) to give a time series of $\dot{\boldsymbol{b}}$ at the CMB. This time series will then be investigated using the method detailed in Brown et al. (2013).

4.3 Background magnetic fields

The production of synthetic data relies upon zonal velocities obtained from our torsional wave forward models and upon a background magnetic field defined by Gauss coefficients (G_l^m and H_l^m in the previous section) obtained from a field model. The choice of background field will obviously influence the wave-induced SV (see equation (4.2) and Bloxham et al. (2002)), so we investigated the effects of choosing one field

model over another, and of using a snapshot of the observed field as opposed to a time-averaged field. As discussed in §1.3, several such magnetic field models exist, each spanning different time periods and constrained by different observational datasets. For example, the CALSxk series of models uses archaeomagnetic and lake sediment data spanning several millennia (Korte & Constable, 2003, Korte et al., 2005, 2011), the historical *gufm1* model uses shipping logs and observatory data spanning the period 1540-1990 (Jackson et al., 2000), and the CHAOS series of models uses satellite data spanning less than 20 years (e.g. Olsen et al., 2006, 2009, 2010b, 2014).

As torsional waves are thought to occur on decadal timescales, and have been associated with 6 year signals in ΔLOD and SV, and with geomagnetic jerks, this work only considers magnetic field models with high spatial and temporal resolution. High spatial resolution permits investigation of small-length scale features, and high temporal resolution is required because we consider the effects of using a single snapshot of the field versus a time-averaged field. Two magnetic field models were chosen as the starting point for the steady background field required for torsional wave-induced SV; CHAOS-4 by Olsen et al. (2014) and COV-OBS by Gillet et al. (2013). The CHAOS-4 model covers the period 1997-2013 and is constrained by Ørsted, CHAMP and SAC-C satellite data, augmented by monthly mean values from observatories. The time variations of the core-generated field are described by 6th order splines and the third time derivative of the squared radial magnetic field component is regularised at the CMB. Such regularisation forces the expansions in the spatial and time domains to converge, but also hinders the calculation of reliable second order statistics that are required for inferring the core dynamics responsible for observed SV. The COV-OBS family of models, spanning the period 1840-2010, takes a stochastic approach that uses time covariance functions to integrate some prior information on the time evolution of the geomagnetic field. The time series of spherical harmonic coefficients are considered as realisations of a continuous and differentiable stochastic process, which is chosen such that it is not twice differentiable. This property allows for sharper changes in SV, such as geomagnetic jerks, than are permitted in previous regularised field models, which were designed to penalise sharp changes.

Despite the fundamental differences in model construction between the CHAOS-4 and COV-OBS models, the resulting magnetic fields look remarkably similar when evaluated

using Gauss coefficients from both models for the same time interval. Indeed, when the radial magnetic field, B_r, is constructed at the CMB for the same time, the fields differed by only a few nanotesla. This led to the conclusion that there is no reason to prefer one model over the other when looking at single snapshots of the geomagnetic field because their spatial structure is very similar. In terms of temporal variations, the background magnetic field is considered constant over the timescales of torsional wave evolution in our models. A consideration is whether a single snapshot for the field at a particular time is consistent with waves on decadal timescales; the field snapshot may actually contain features that are caused by torsional waves. In order to assess whether a snapshot or a time-averaged field should be used in the calculations, we compared the radial magnetic field at the CMB in three cases: a snapshot in 2010, a 50 year time-average (1960-2010) and a 130 year time-average (1840-2010) according to COV-OBS, see Fig. 4.2. The figure shows that the three fields are very similar in both spatial structure and in amplitude, with only a few small length scale features vanishing from the 130 year average compared to the modern snapshot. Rather than small-scale features being absent from the field prior to 1960, it is likely that observational limitations and spatial coverage at the time were not sufficient to resolve them. From this, it seems that the choice between the two field models, and between a snapshot of the radial field at the CMB and a time-averaged field, is unlikely to greatly influence the results. As such, we chose the 2010 radial field according to COV-OBS for our synthetic data production, see Fig. 4.3. For the forward models of the previous chapter, we required a profile for the cylindrical average of the background magnetic field inside the core, $\{B_s^2\}$. As observationally-constrained field models describe the geomagnetic field above the core surface, and only up to degree 14, such models provide no constraint on the profile of $\{B_s^2\}$ inside the core. Therefore, there is no inconsistency between the $\{B_s^2\}$ profiles used in the forward models and the COV-OBS background magnetic field used for wave-induced SV calculations.

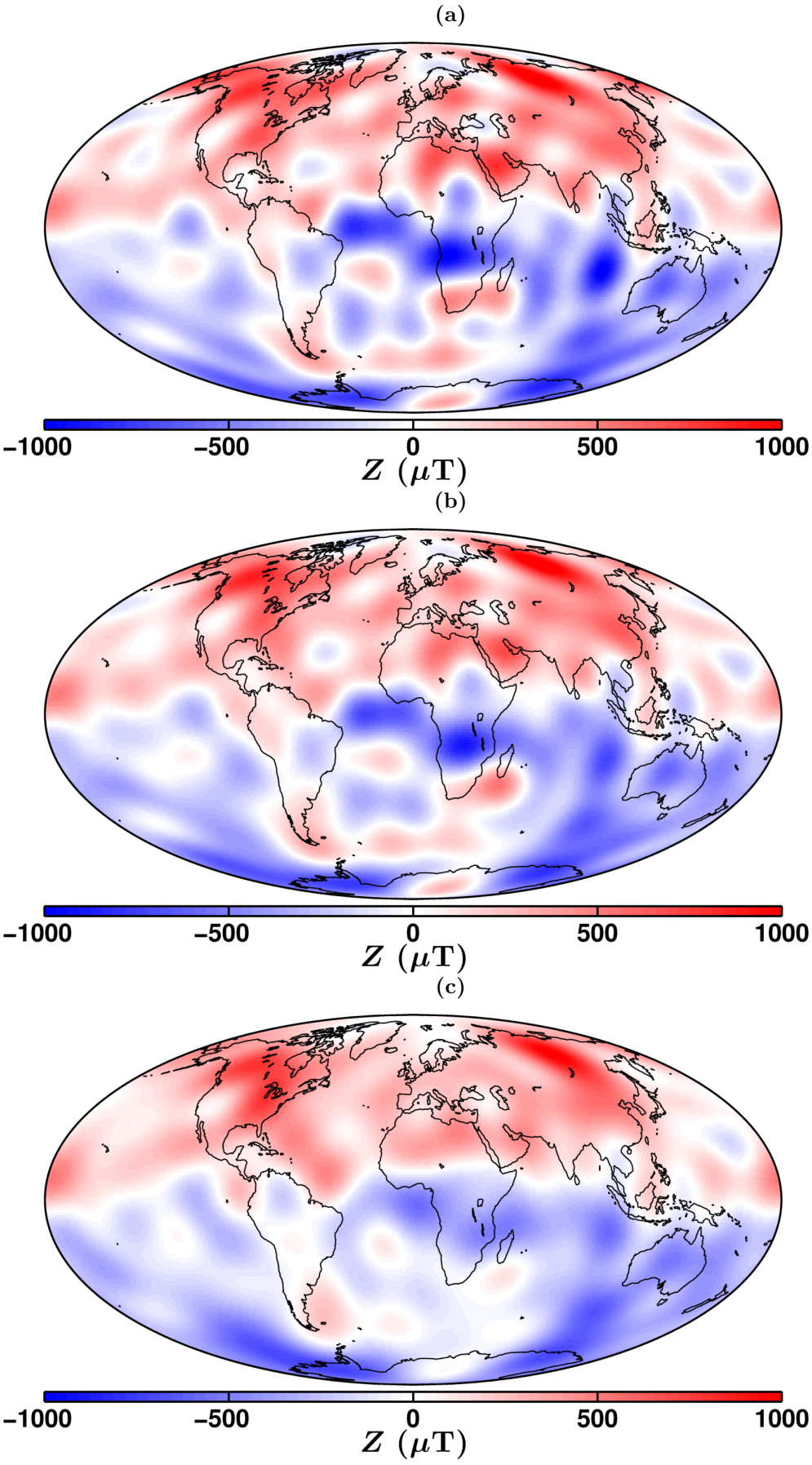

Figure 4.2: The Z $(= -B_r)$ component of the geomagnetic field at the CMB according to the COV-OBS field model Gillet et al. (2013) (a) Snapshot of the field in 2010 (b) 50 year time-averaged field (1960-2010) and (c) 130 year time-averaged field (1840-2010). The scale is in μT; red indicates positive field (entering the core) and blue indicates negative field (exiting the core).

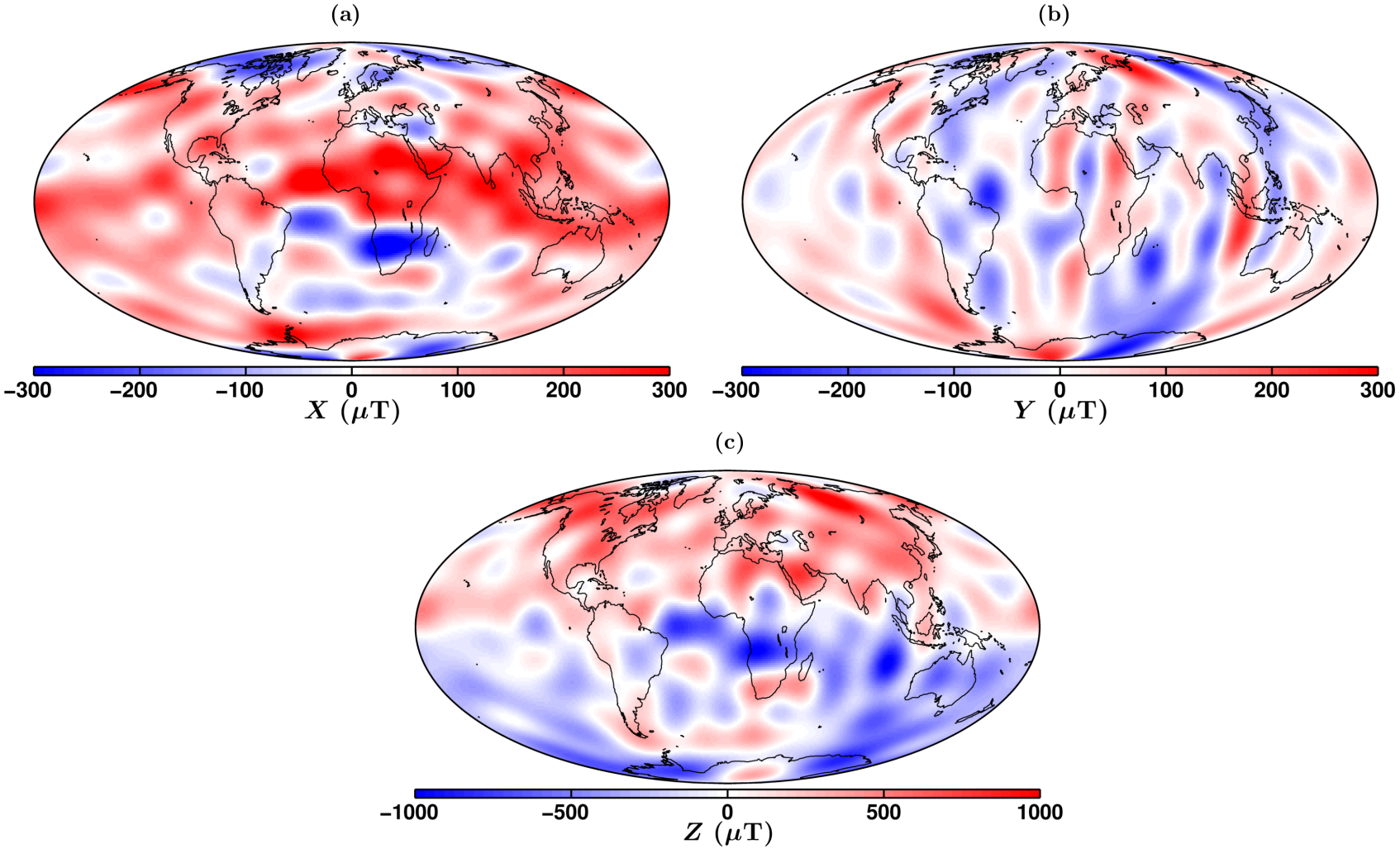

Figure 4.3: The (a) X, (b) Y and (a) Z components of the geomagnetic field at the CMB in 2010 according to the COV-OBS field model Gillet et al. (2013). The Gauss coefficients up to spherical harmonic degree 14 were used to calculate the field. The scale is in μT; red indicates positive field and blue indicates negative field.

4.4 Benchmarking and resolution testing

Numerical results for torsional wave-induced SV were obtained using a code written in Matlab that takes as inputs the wave velocities in the spatial domain, $u_\phi(s)$, and the Gauss coefficients of the background magnetic field at the CMB, G_l^m and H_l^m. The background magnetic field $\boldsymbol{B}$ is specified up to spherical harmonic degree 14, which is the maximum degree to which the internally generated field is robustly determined in field models. The Gauss nodes and weights were computed using the eigenvalue method of Golub & Welsch (1969) and, in all models, sufficient nodes were used to ensure convergence of the projection of $u_\phi(s)$ onto spherical harmonics. The code projects the wave velocities onto spherical harmonics and solves equations (4.20) and (4.22) for the Gauss coefficients of the scalar potential v describing the wave-induced SV $\dot{\boldsymbol{b}}$. The Matlab script was benchmarked against a Maple script that performs the required integrations analytically when the input velocities and background field are expressed explicitly as associated Legendre functions. The Maple code outputs the Gauss coefficients for v and can evaluate the values of any component of $\dot{\boldsymbol{b}}$ at a given point. We compared values for the Gauss coefficients and magnetic field values output by the two independent codes and found they were in excellent agreement.

Fig. 4.4 shows the initial wave profile, given by equation (2.60) in cylindrical coordinates, mapped onto the collocation points for GLQ (top), in the theta domain, and the spatial power spectrum of the velocity (bottom). The single pulse in the spatial domain maps into two pulses on the Gauss nodes due to the equatorial symmetry of torsional waves (e.g. see Figs 1.4a and 1.5). When the single pulse splits into two, such as the torsional waves shown in Fig. 3.5 of §3.3, this manifests as four pulses on the Gauss nodes (see Fig. 4.5). This equatorial symmetry also explains the power spectra in Figs 4.4 and 4.5; only even spherical harmonic degrees are present because only harmonics with $l - m$ even have this property. As the velocities are axisymmetric ($m = 0$), this leaves only spherical harmonics of even degree available. Convergence of the velocity expansion was ensured by calculating the spatial power spectra (the squared magnitude of the spherical harmonic coefficients at each degree, see equation (1.1)) and comparing the power contained at low and high spherical harmonic degrees at different times during wave propagation. From the calculated spectra, examples of which are shown in Figs 4.4 and 4.5, we chose to project u_ϕ onto spherical harmonics up to degree

40, anticipating that the magnitudes of higher degree coefficients are negligibly small. Similarly, spatial power spectra were used to compare the magnitudes of the Gauss coefficients of the calculated wave-induced SV (see the next sections for figures) and determine the resolution required for the calculation of $\dot{\boldsymbol{b}}$. The power spectrum of $\dot{\boldsymbol{b}}$ was calculated at different times throughout the wave evolution in order to ensure that the resolution required for the SV induced by the initial profile is sufficient to resolve the SV induced by the waves at any time in the model. We also performed the numerical integration using different numbers of quadrature points between 20 and 200, in order to verify convergence of the solutions. Following this convergence testing, a value of $N = 100$ was chosen so as to be large enough to ensure convergence but small enough to avoid inaccuracies associated with calculating the eigenvalues of large matrices in Matlab.

Figure 4.4: The initial wave profile given by equation (2.60) in cylindrical coordinates mapped onto 100 collocation points (Gauss nodes) for GLQ (top) and the spatial power spectrum of the velocity (bottom). The spectrum has no units because the velocity has no intrinsic scale.

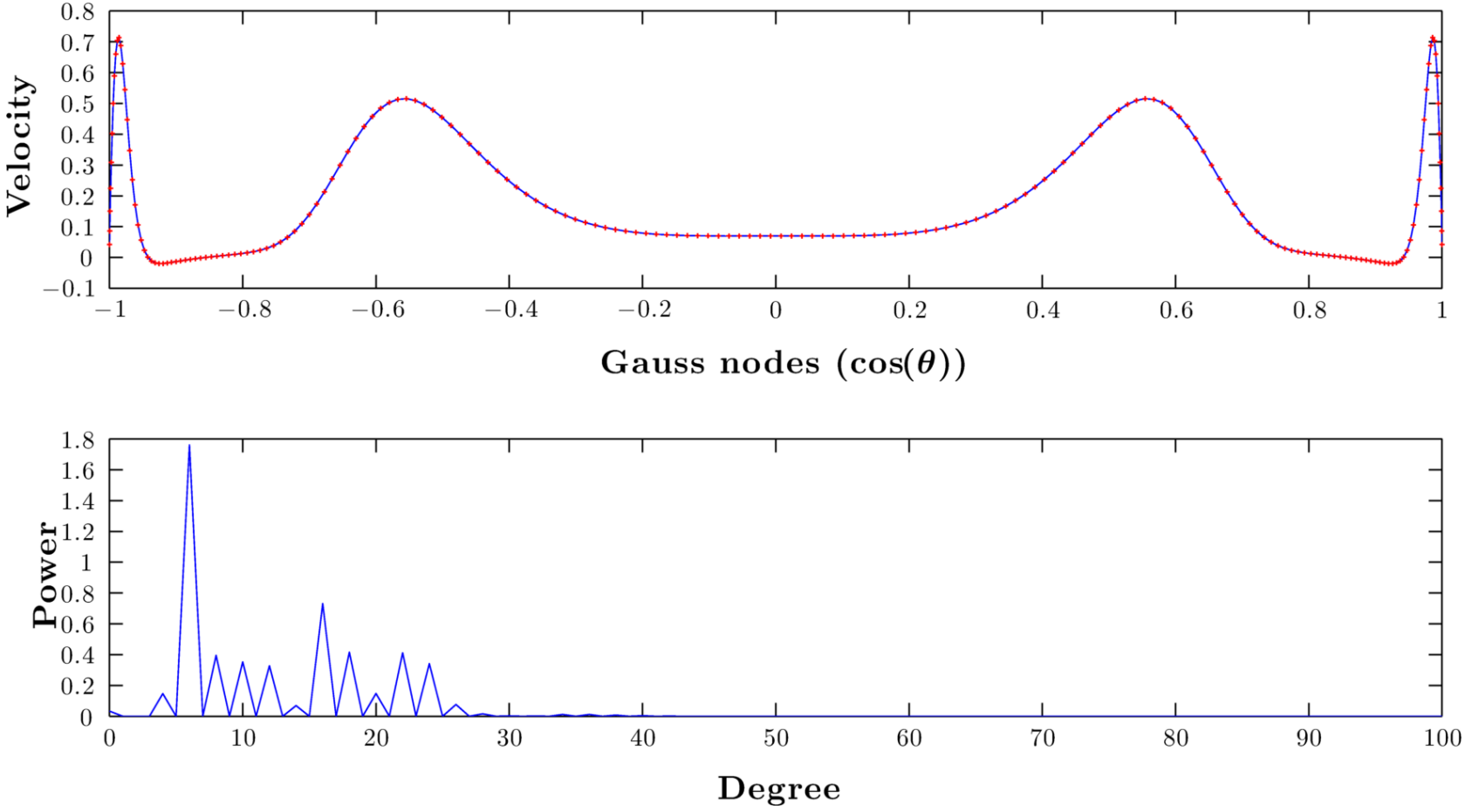

Figure 4.5: A torsional wave that has split into two pulses, see $t = 2$ yr of Fig. 3.5 in §3.3, mapped onto 100 collocation points (Gauss nodes) for GLQ (top) and the spatial power spectrum of the velocity (bottom). The spectrum has no units because the velocity has no intrinsic scale.

Two further tests of the code were carried out: first, using an axisymmetric magnetic field and second, a sensitivity test for a bulk rotation of the core fluid. Equation (4.1) shows that zonal flow-induced secular variation depends upon the azimuthal (longitudinal) variations in the background magnetic field, which means that an axisymmetric magnetic field should be unaffected by torsional waves. We verified that both the Matlab and Maple codes give all Gauss coefficients for v as zero for any axisymmetric background field.

For a bulk rotation of the core fluid with respect to the mantle (constant ω_g), the SV obtained can be predicted from equation (4.2); differentiating the background B_r (from the field model) with respect to ϕ and multiplying by $-\omega_g$ shows the pattern of SV that is expected to arise when all of the fluid in the core is perturbed equally. Not only does this sensitivity test provide another means of benchmarking the numerical solutions, it highlights those regions of the field at the CMB that are sensitive to zonal core flow, and which regions are unaffected by zonal core flow.

4.5 SV patterns

As Bloxham et al. (2002) noted in the first paper linking geomagnetic jerks to torsional oscillations, local magnetic field morphology dictates whether a particular location is sensitive to zonal core flow. This is an important point because some jerks are observed globally, while others are seen on regional scales, which has previously hindered identification of a common physical origin for these events.

Fig. 4.6a shows the ϕ-derivative of the radial component of the selected background magnetic field shown in Fig. 4.3. The red and blue regions show where zonal flow will induce a signal in the SV, whilst the white areas indicate regions that are not sensitive to zonal flow because there are no azimuthal gradients in the radial field at that location. The middle figure, 4.6b, shows the SV pattern that would be induced by a bulk rotation of the core fluid with respect to the mantle and, as expected, the pattern matches that of Fig. 4.6a. An interesting point is that the pattern is also very similar to the observed SV at the same time (see Fig. 4.6c), particularly in the equatorial Atlantic region, which implies that much of the observed SV can be accounted for by a general zonal core flow. A bulk rotation of $-0.2864°$/yr was needed to match the amplitudes

of the observed SV. The observed westward drift of the historical geomagnetic field at a rate of approximately 0.2°/yr has long been associated with a general westward flow at the top of the core (Bullard et al., 1950, Jackson, 1997, Jault et al., 1988, Dumberry & Finlay, 2007). More recent work by Livermore et al. (2013) has even linked the flows responsible for the westward drift of the magnetic field with the shuffling superrotation of the inner core observed by Tkalčić et al. (2013).

In order to produce time series and maps of torsional wave-induced SV, the torsional wave velocities u_ϕ must be scaled by an appropriate amplitude; recall that the torsional wave equation has no intrinsic scale. Having chosen the internal magnetic field amplitude to give a core transit time of approximately 6 years in order to be consistent with Gillet et al. (2010), we chose to scale our torsional waves to match their amplitude as well. As shown in Fig. 1.8, the torsional waves in that study had maximum amplitudes of approximately 0.4 km/yr. When this amplitude is used, the resulting SV is relatively small; the amplitudes of $\dot{x}$ and $\dot{y}$ are generally less than ± 20 nT/yr at the CMB. The radial component of $\dot{\boldsymbol{b}}$ is a factor of 2-3 larger than the other components, and so the rest of this section will focus upon the pattern of signals in $\dot{z}$. Having discussed these patterns, we will then investigate the wave amplitudes and timescales needed to match SV observations and produce jerk-like signals.

When both the velocity and magnetic fields are expressed in spherical harmonics, the interactions between different magnetic and velocity modes are non-zero only when certain selection rules are satisfied (Bullard & Gellman, 1954). For example, when the velocity is purely toroidal everywhere ($u_r = 0$), the induction equation has no non-trivial solution and dynamo action cannot be sustained. However, in general, starting with any magnetic field and velocity field, an infinite sequence of other harmonics will be excited. Since no general statement can be made, we must resort to numerical methods to solve (4.2) and ensure that the calculations are converged and account for most of the wave-induced SV. Fig. 4.7 shows the spatial power spectrum of the calculated potential field, v, pertaining to $\dot{\boldsymbol{b}}$ up to spherical harmonic degree 50. An interesting feature of these spectra is a step down in power at $l = 14$, which corresponds to the end of the background magnetic field expansion. The spectrum is calculated at different times throughout the wave evolution in order to ensure that the initial resolution is sufficient for the whole calculation. A resolution of 40 spherical harmonics was chosen

for the SV calculations discussed in the this chapter, as the power had dropped several orders of magnitude from its maximum by this degree.

Fig. 4.8 shows the SV induced by the torsional waves of the forward model in the previous chapter, see Fig. 3.5 for the contour map of u_ϕ for the full sphere model. As previously discussed, the single pulse of the initial profile in Fig. 4.8a, which is placed at the midpoint of the core radius ($s = r_c/2$), manifests as two bands of SV at mid to high-latitudes. The location of these bands is equatorially symmetric due to the symmetry of the columnar flow comprising torsional waves, but the bands themselves are not equatorially symmetric because the local magnetic field morphology differs in the northern and southern hemispheres. The locations of the lines of zero wave-induced SV match those in Figs. 4.6a and 4.6b, which describe where the background magnetic field has no longitudinal variations and these differ in each hemisphere. After 1 year, the wave has split into two smaller pulses that begin to move away from the initial pulse position ($s = r_c/2$), see Fig. 4.8b. The two velocity pulses now manifest as four bands of SV, two at slightly lower latitudes than before and two at slightly higher latitudes than the initial bands. Fig. 4.8c shows the wave profile after 2 years when one pulse has moved towards the rotation axis and the other towards the equator of the CMB. Due to the geometry of torsional waves, the pulse near the rotation axis perturbs the magnetic field in the polar regions and the pulse near the equator of the CMB perturbs the field in equatorial regions. Fig. 4.8d shows the wave profile at 3 years, during the first reflections and phase shifts of the pulses. The strong SV in the equatorial region is due to the waves being high amplitude during the reflection at the stress-free boundary. The band is wider than in the previous figures because the wave is no longer a distinct pulse at the equator; at least the outermost 500 km of the core fluid is perturbed. The wave pulse near the rotation axis is smaller than before the phase shift and of the opposite polarity, which explains the sign reversal of the SV and lower amplitude signal. The SV signals are seen across the whole planet as the wave becomes dispersed and the energy spreads through the domain, see Figs. 4.8e and 4.8f for the wave profiles and corresponding SV signals after 4 and 5 years respectively. The white lines of zero wave-induced SV arise from two effects; first, the background field has no longitudinal variations in some locations and second, the velocity profile crosses $u_\phi = 0$ at several radii throughout the core whilst changing polarity, which results in no induced SV along certain bands of latitude.

As the dynamics of the waves in the forward models were very similar, we shall focus on the full sphere model in this chapter; the effects of changing geometry to that of a spherical shell or adding a spatially varying $\{B_s^2\}$ profile would result in only minor differences in the SV maps. In the previous chapter, we also considered the effect of wavelength on torsional wave propagation, finding that long wavelength features are more dispersive than short wavelength features, though the general dynamics of the modelled waves were very similar for all wavelengths. Increasing the wavelength of the initial pulse results in wider bands of SV because the wave occupies more of the core and perturbs a larger portion of the ambient magnetic field. Conversely, narrower initial pulses than that shown in Fig. 4.8a occupy less of the core and therefore perturb less of the magnetic field, resulting in narrower bands of SV. The amplitude of the SV is unchanged by varying the wavelength because it is determined only by the amplitude of the torsional wave.

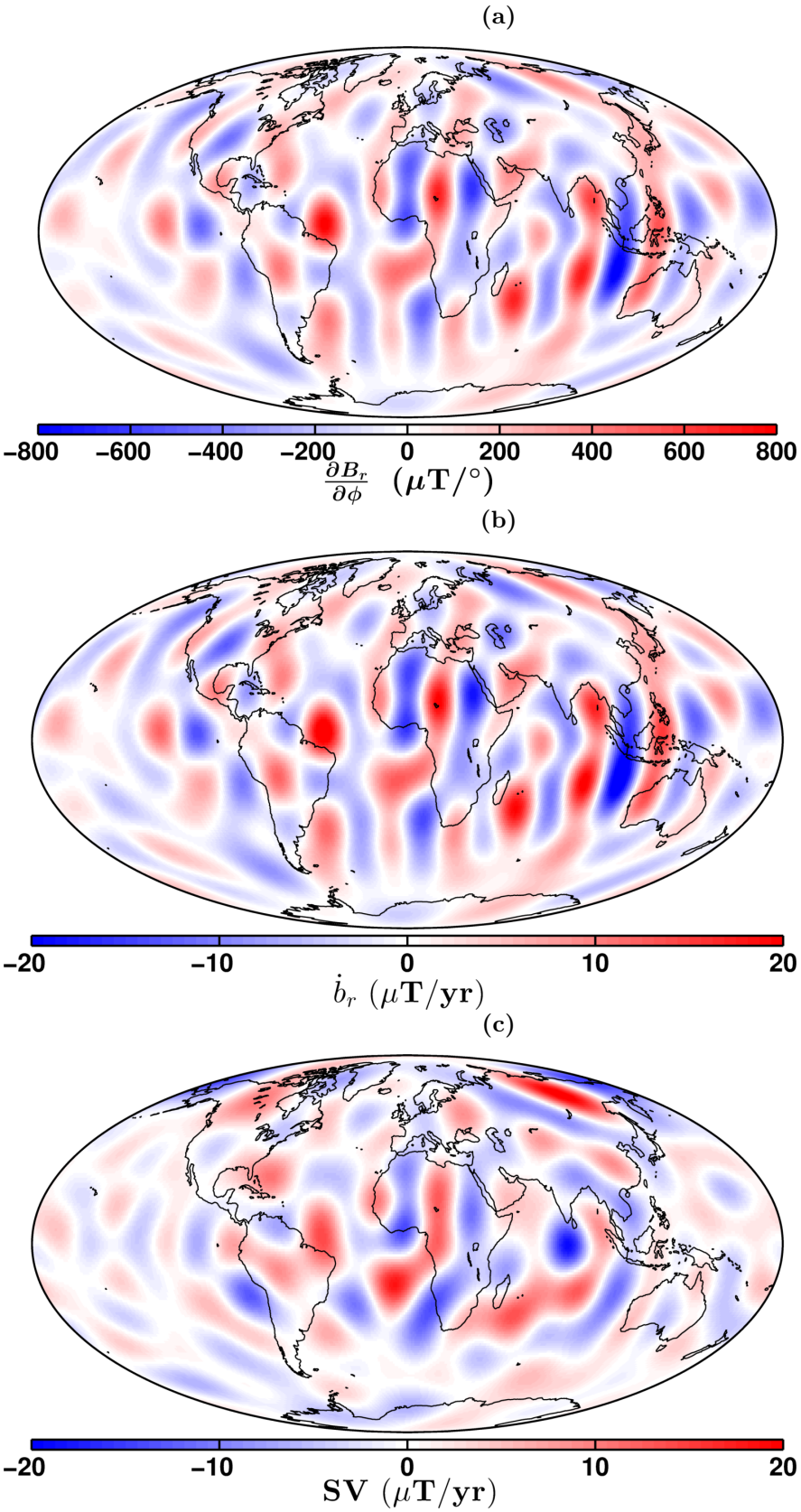

Figure 4.6: (a) The ϕ-derivative of the radial component of the geomagnetic field at the CMB in 2010 according to the COV-OBS field model Gillet et al. (2013) (b) The radial SV, $\dot{b}_r$, induced by the interaction of the field shown in (a) with a bulk rotation of the core fluid with respect to the mantle of -0.005 rad/yr (-0.2864°/yr) (c) The radial SV of the geomagnetic field at the CMB in 2010 according to the COV-OBS field model. The scale is in μT/yr; red indicates more positive field (more exiting the core) and blue indicates more negative field (more entering the core).

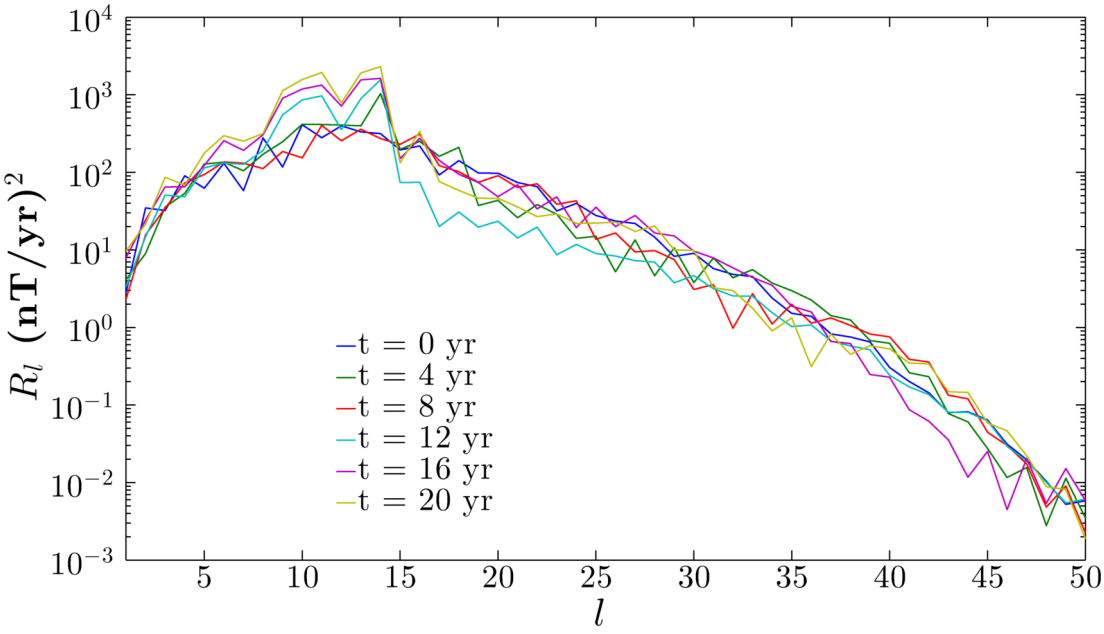

Figure 4.7: The spatial power spectrum, evaluated at the CMB radius, of torsional wave-induced SV. The waves in this model had a core transit time of 6 yr and an initial pulse amplitude of 0.4 km/yr.

(a) $t = 0$

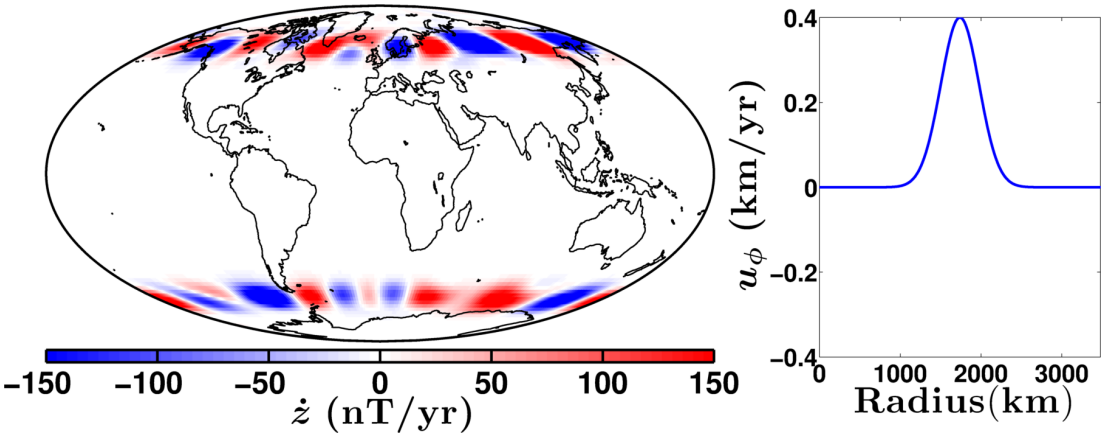

(b) $t = 1$ yr

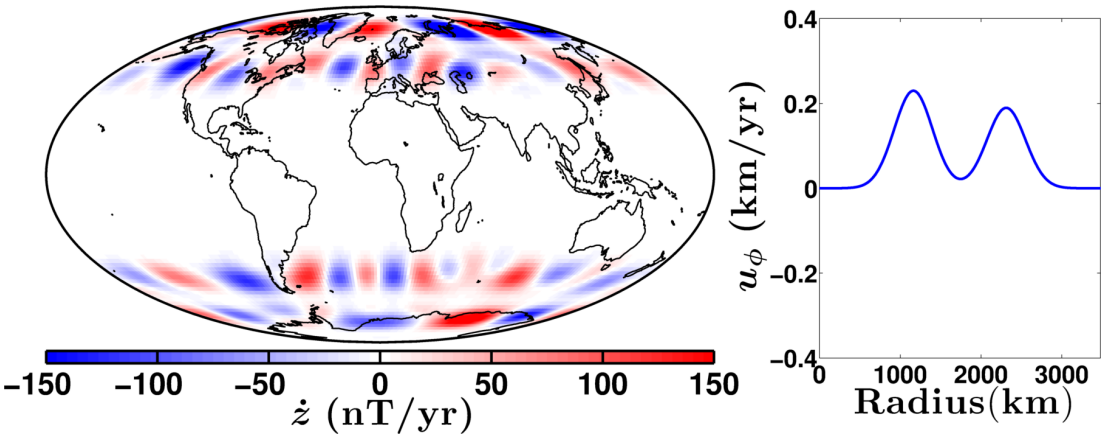

(c) $t = 2$ yr

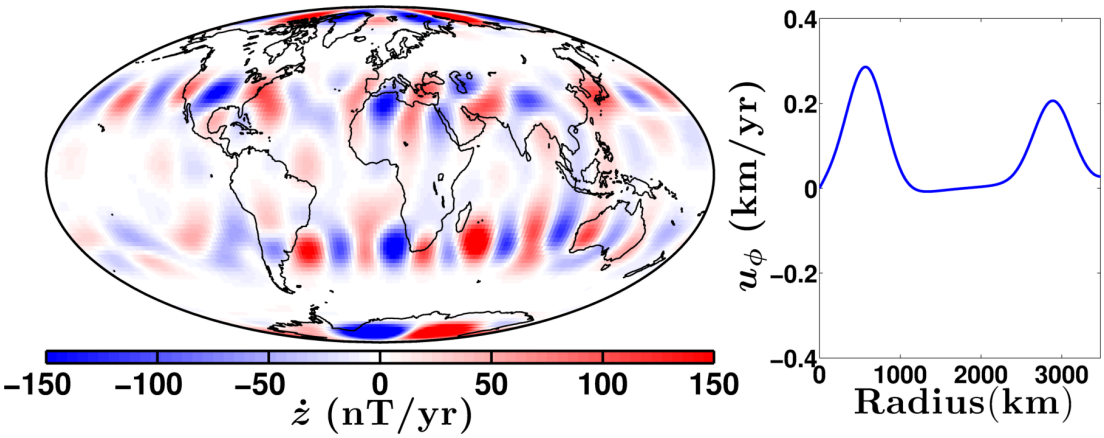

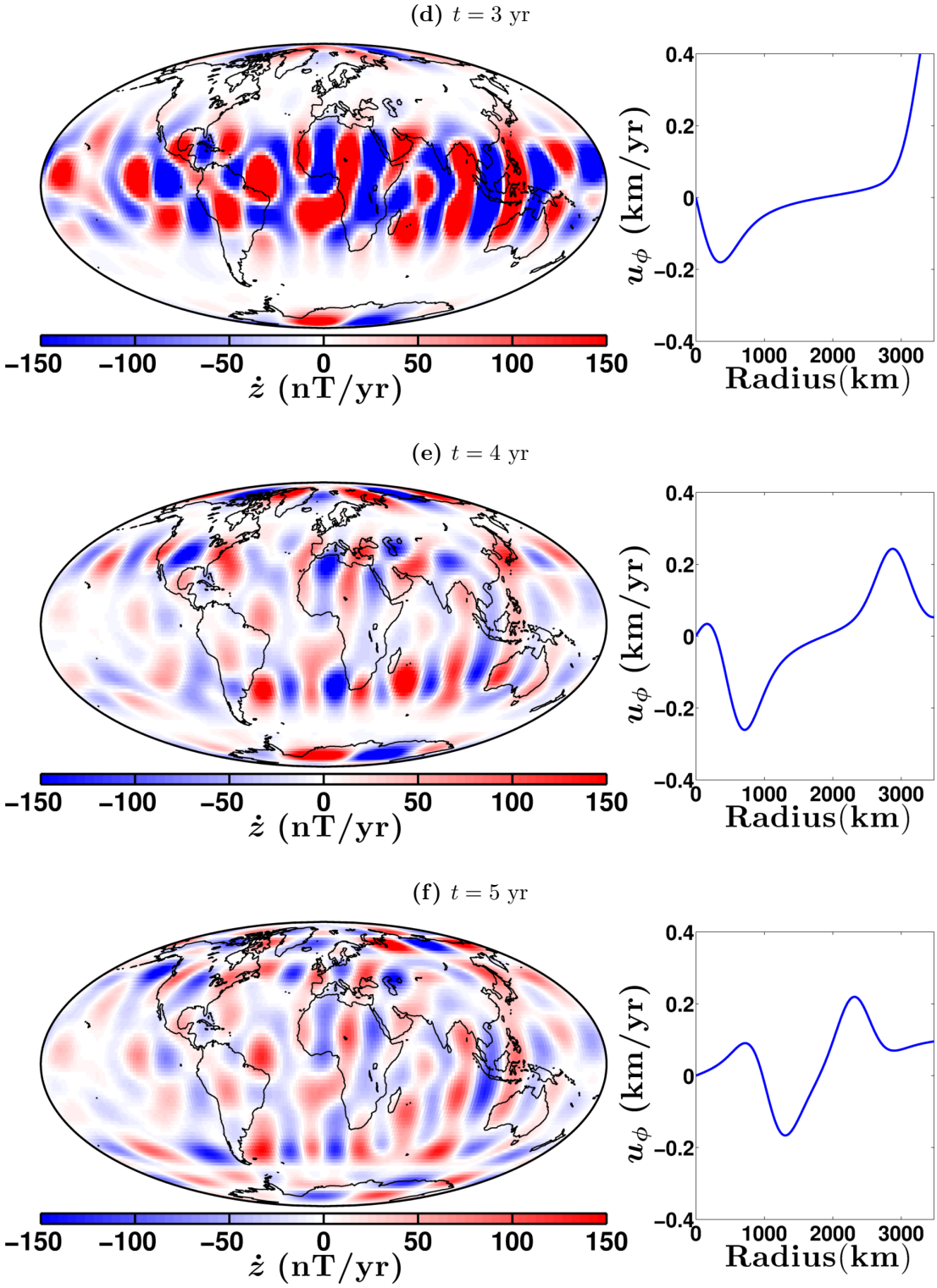

Figure 4.8: Maps of the radial component of the SV induced by torsional waves with a 6 yr core transit time and an initial wave pulse amplitude of 0.4 km/yr. The SV is evaluated at the CMB and the colour scale is from −150 nT/yr to 150 nT/yr. The torsional wave profile is shown on the right, with cylindrical radius (km) on the horizontal axis and zonal velocity (km/yr) on the vertical axis.

4.6 Synthetic observatory data

Having examined the general structure of SV induced by torsional waves travelling through the core, it is now of interest to investigate the signals that would be observed at particular locations throughout wave evolution. Fig. 4.9 shows the locations of the 24 magnetic observatories at which synthetic SV time series are produced. These observatories are a sample of the total number of observatories worldwide and were chosen to give maximum spatial coverage. We first calculate the wave-induced SV at the CMB radius, using the real observatory latitudes and longitudes, and subsequently look at the signals at Earth's surface.

The figures in Appendix B show time series of the z component of wave-induced SV at the 24 observatory locations (at CMB radius) for the first 20 yr of torsional wave evolution in the full sphere model; for illustrative purposes, a selection of these figures is provided in this section. As previously discussed, all of the observatories record different SV signals, but all share two common traits: first, the amplitudes are quite small and second, the timescales are very short. Also, where signals are recorded, they show some periodicity because the waves travel beneath the same location approximately every six years.

For example, Fig. 4.10a shows the signal recorded at the Bangui observatory in the Central African Republic, at CMB radius. At this station, the SV signals are relatively large compared to other stations, approximately 200 nT/yr, and vary on timescales of 6 yr. Fig. 4.10b shows that very little is recorded at the Eskdalemuir observatory in Scotland. One of the objectives of this work was to investigate whether the torsional waves in our forward models produce signals that resemble geomagnetic jerks. Of course, we do not observe jerks at the CMB, but at observatories on Earth's surface and via satellite observations. The synthetic data were upward continued to the Earth's surface (taken as 6371 km) in order to permit comparison with real magnetic data, see Fig. 4.11 for time series of the SV at the same three observatories shown in Fig. 4.10. Note the very small amplitudes ($<$3 nT/yr) compared to the maximum amplitude of observed SV at Earth's surface ($\sim$ 200 nT/yr) and the rapid timescales of the signals.

Using the the wave amplitude and timescales of Gillet et al. (2010), we must conclude

Figure 4.9: The locations of the 24 magnetic observatories at which synthetic time series of wave-induced SV will be produced.

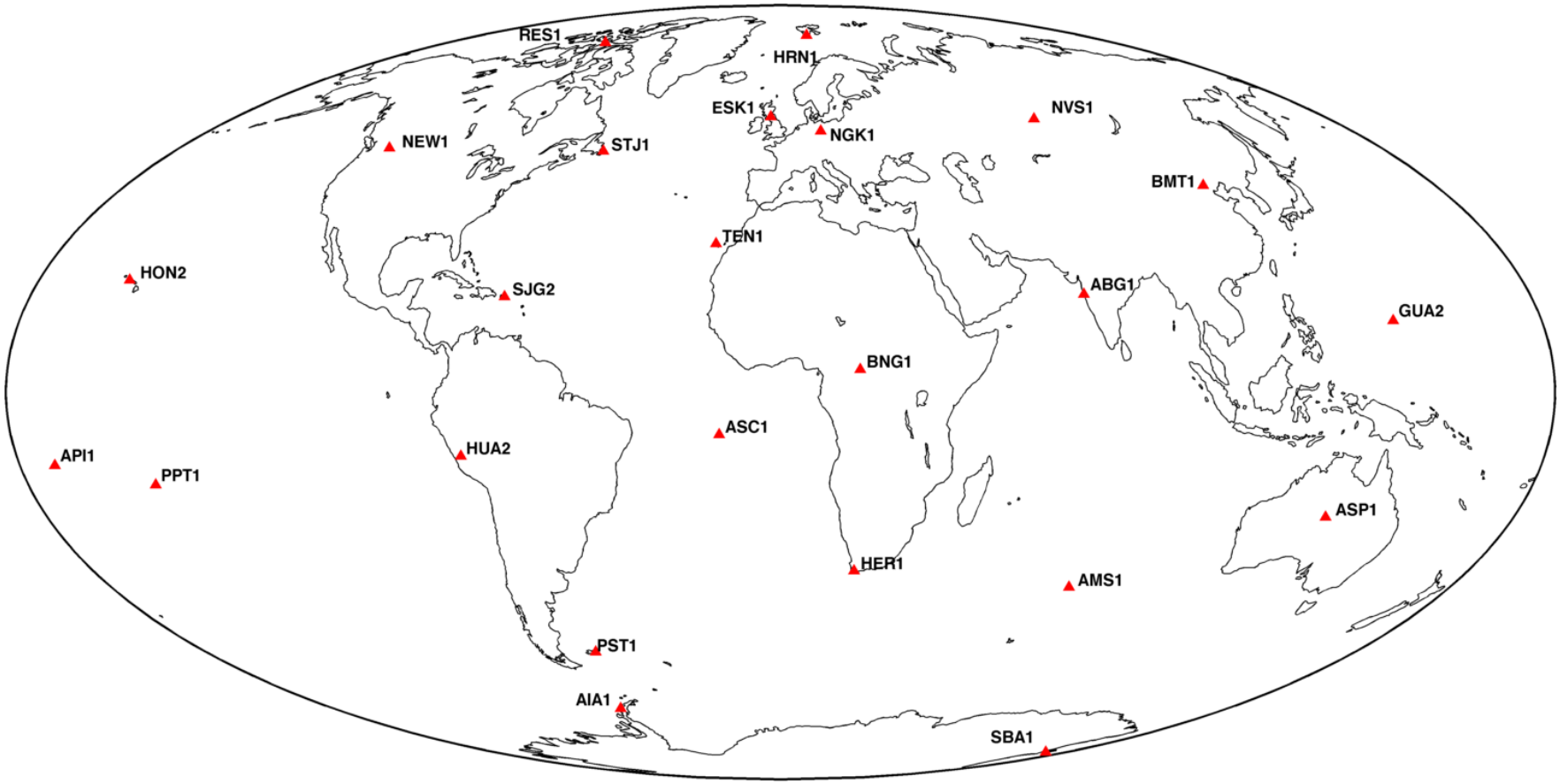

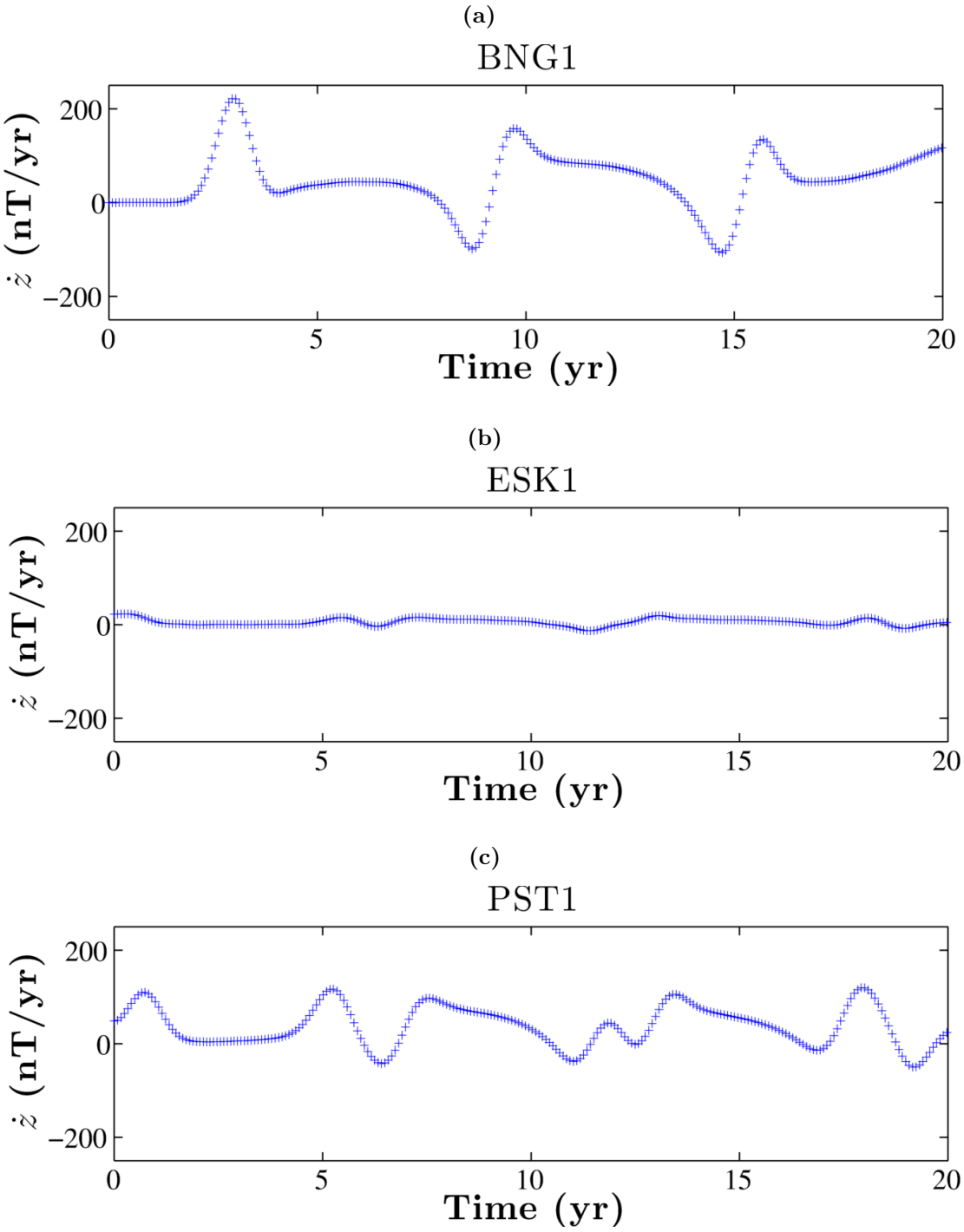

Figure 4.10: Time series of the z component of the SV induced at the CMB by torsional waves with a 6 yr core transit time and an initial pulse amplitude of 0.4 km/yr at (top) Bangui, (middle) Eskdalemuir and (bottom) Port Stanley.

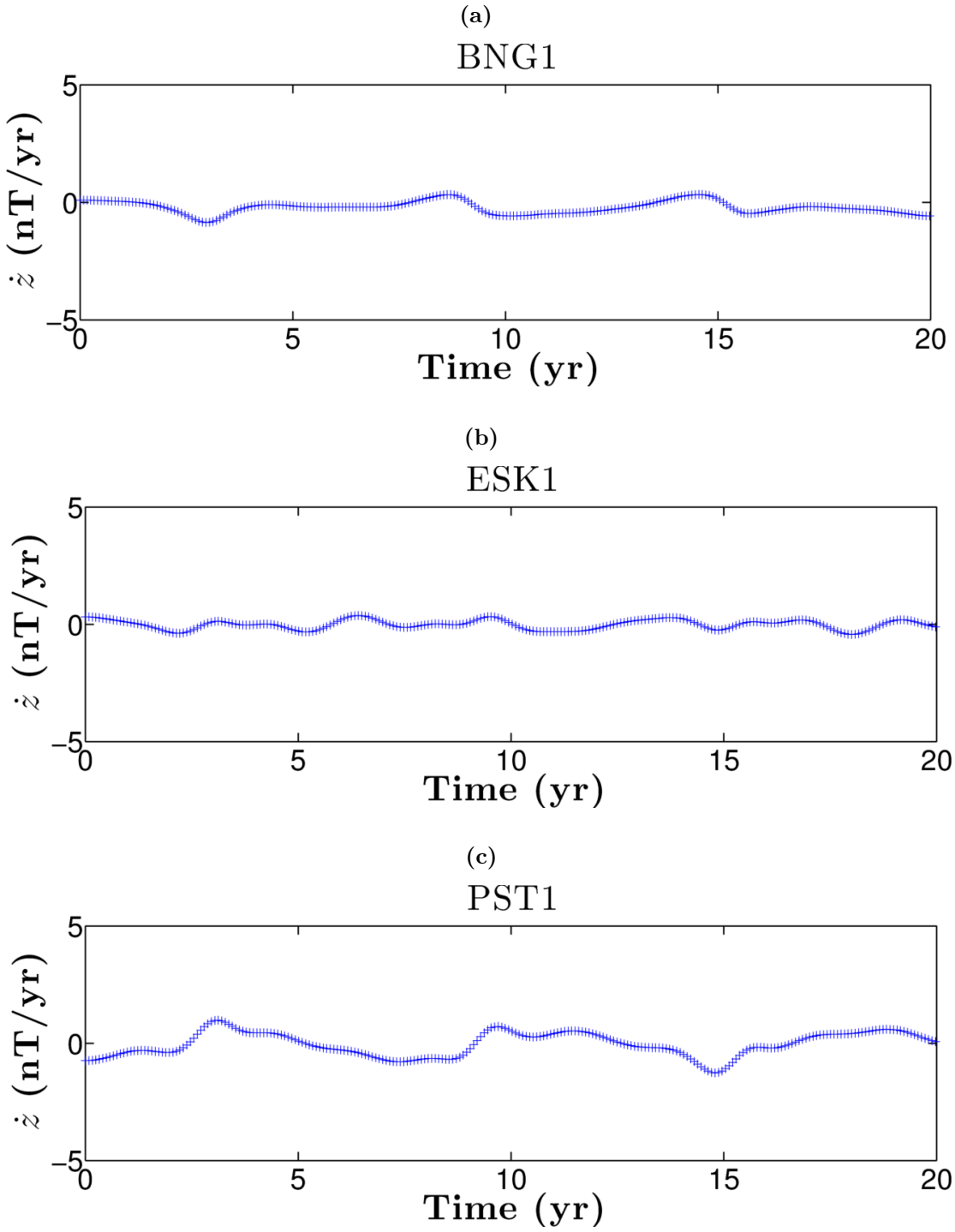

Figure 4.11: Time series of the z component of the SV induced at Earth's surface by torsional waves with a 6 yr core transit time and an initial pulse amplitude of 0.4 km/yr at (top) Bangui, (middle) Eskdalemuir and (bottom) Port Stanley.

that the waves do not produce jerk-like signals because the timescales of the synthetic SV are much too rapid and at Earth's surface, the signals are too small. Jerks in real SV data generally consist of two linear segments of data that are several years (or decades) long, with the jerk event being the very rapid (<1 yr) change from one gradient to the other, as shown in Fig. 4.1. In the synthetics, the SV does change slope very rapidly in many of the time series, particularly in the time series evaluated at CMB radius, but these changes do not separate long periods of SV of constant slope; the rapid changes are bracketed by linear SV segments of only a few months and, often, two rapid changes occur in quick succession due to the wave passing beneath a particular location and then changing direction, after reflection for example, and passing beneath the same point shortly afterwards. For example, see the signals predicted at Bangui at the CMB in Fig. 4.10a and at Port Stanley in the Falkland Islands, Fig. 4.10c at CMB radius and Fig. 4.11c at Eath's surface. Applying the jerk detection method of Brown et al. (2013) that was described in §4.1 required parameters far removed from those applied to real SV data in order to identify 'jerks'. At Earth's surface, the jerk algorithm could only detect 'jerks' if the amplitude threshold was considerably lower than that used for real SV data. The algorithm could detect jerk-like signals at the CMB, due to the larger signals at this radius, but the signals identified were the very rapid 'wiggles' described above, and required very short sliding windows of less than 2 yr to be detected. For comparison, window lengths of 5-20 yr were used by Brown et al. (2013) in their study of magnetic data from 1958-2008. Another point for consideration is that real jerks can be observed in any component of the magnetic field, but the synthetic data produced very small signals in all three components at Earth's surface, which would likely be within the noise threshold of observational data (see Wardinski & Holme (2011) for details on the techniques used to denoise geomagnetic data for SV studies). For comparison, the radial SV at the CMB is on the order of 20 μT/yr (see Fig. 4.6c), which is two orders of magnitude larger than the wave-induced SV shown in Fig. 4.8, and the radial SV at Earth's surface is on the order of $\sim$ 200 nT/yr compared to the wave-induced SV of a few nanotesla.

The selected wave amplitude and timescale were chosen for consistency with a recent study on torsional waves by Gillet et al. (2010). Those waves were much faster than the waves in previous works and of relatively small amplitude, which raises the question of whether matching torsional waves in previous studies might yield results that bear

more resemblance to real SV data. The first study of torsional oscillations in Earth's core by Braginsky (1970) theoretically predicted torsional oscillations with a period of approximately 60 years. The same period was recently advocated by Roberts et al. (2007), based on empirical mode decomposition of ΔLOD and SV data. Zatman & Bloxham (1997) identified two torsional modes with periods of 76 and 53 years, respectively, based on observational data, giving an average period of 60-65 years. A subsequent study by Hide et al. (2000), also based on observations, identified a robust 65 year torsional oscillation period. The theoretical study of Mound & Buffett (2005) used Green's functions to show how torsional oscillations might be excited in the core, and a subsequent study by the same authors identified several periods associated with torsional oscillations (Mound & Buffett, 2007). Their first four modes had approximate periods of 80, 46, 32 and 24 years respectively. Dickey & de Viron (2009) reviewed the leading modes of torsional oscillations found in previous studies, from both observational and theoretical methods, and also isolated some additional modes using core angular momentum data from the core flow (Hide et al., 2000) reconstructed from Jackson et al. (1993). Their first two modes were in agreement with the previous results by Zatman & Bloxham (1997) and Mound & Buffett (2007).

Based on the above overview of previously determined torsional oscillation periods, a forward model of torsional waves with a revised core transit time and wave amplitude was run, see Fig. 4.12 for the contour plot of the azimuthal velocity for the first 200 years of wave evolution. The amplitude of the initial wave pulse was set to 4 km/yr, for consistency with previously determined torsional wave amplitudes (e.g. Zatman & Bloxham, 1997) and the core transit time was 60 yr. Note that recent work by Buffett (2014) has attributed the 60 yr core signal to another type of waves, called Magneto-Archimedes-Coriolis (MAC) waves, that may propagate in a stably stratified layer at the top of the outer core. However, as discussed above, there is a substantial body of work linking the 60 yr signal with torsional waves and for the purposes of this study, we will assume that the signal is indeed related to torsional waves.

Having rescaled our torsional wave timescales and amplitudes, we produced synthetic time series of the induced SV at the previously discussed observatories. The spatial SV patterns at the CMB are the same as discussed in the previous section, and the temporal scales are now elongated compared to the previous model. As seen in Fig. 4.8 and the

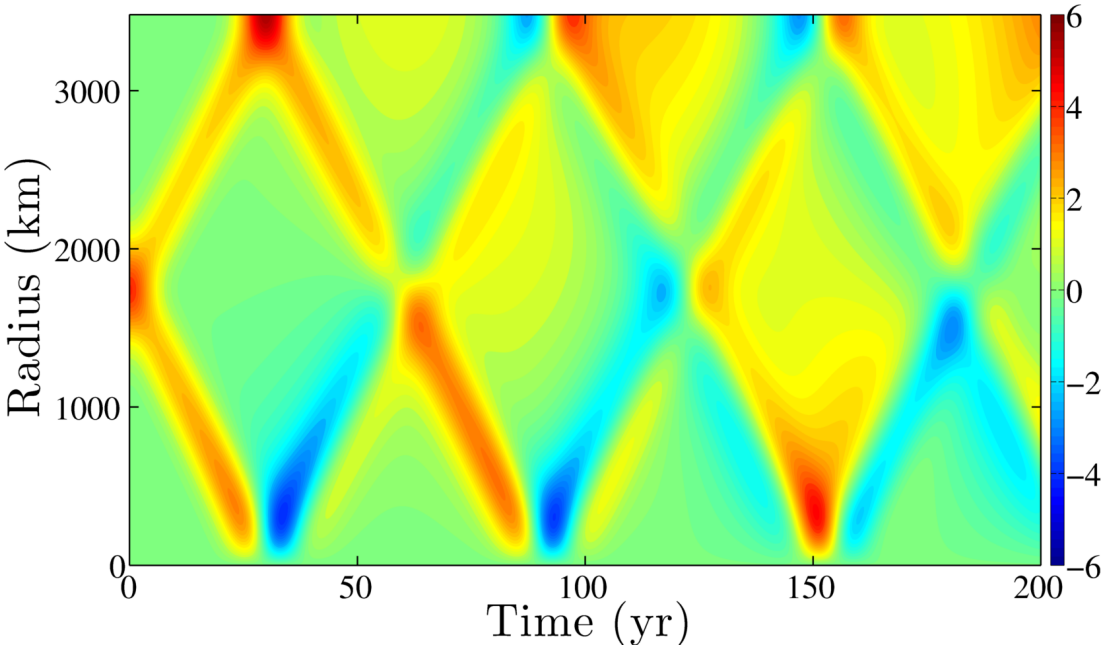

Figure 4.12: Contour plot of the velocity u_ϕ of torsional waves in a full sphere, with time on the horizontal axis and cylindrical radius on the vertical axis. Red corresponds to positive velocity and blue corresponds to negative velocity. The colour scale is from -6 km/yr to 6 km/yr; the initial wave pulse had an amplitude of 4 km/yr and the waves have a 60 yr core transit time.

spectra in Fig. 4.7, much of the wave-induced SV is small length scale at the CMB. At Earth's surface, many of the small length scale (high spherical harmonic degree) features of the induced SV have been filtered out during the upward continuation and the majority of the SV is of degree $l < 5$, see the spectra in Fig. 4.16. Maps of the x, y and z components of the torsional wave-induced SV at six different times during the first core transit time are shown in Figs. 4.13, 4.14 and 4.15. This filtering out of small length scales would be increased in the case of the mantle containing any electrically conducting material. This screening by conductive material is an effect that is typically neglected in models, but the presence of such material is thought likely for parts of Earth's lower mantle (e.g. Shankland et al., 1993).

The magnitudes of the synthetic SV are an order of magnitude larger than in the previous model, due to the increased torsional wave amplitude, and all three components are large enough to be resolved in observations (see the amplitude of the observed SV at the Earth's surface in Fig. 1.3a and Wardinski & Holme (2011), Brown et al. (2013)). We applied the jerk detection method of Brown et al. (2013) to the synthetic time series evaluated at Earth's surface. As previously discussed, that method was based

on a study by Pinheiro et al. (2011), which described a method for identifying jerks by applying a two-part linear regression to a window of a single component of observatory SV data and generating a PDF of the 'likeliness' of potential jerk occurrence times. A potential jerk occurrence is considered at each time step as the linear regression is iterated across the window of data, and the misfit of the regression to the data is used to build the PDF. Estimates of the uncertainties in jerk occurrence times and amplitudes may then be calculated, assuming Gaussian error distributions in the 'peaks of likeliness'. Events are classified as jerks if a 68% confidence window (± one standard deviation) may be defined about the most likely occurrence time in the PDF, whilst no jerks are identified if the confidence interval cannot be defined about the peak in likeliness or if no peak in likeliness occurs within the window of data.

As the previously described method uses a static window of data, Brown et al. (2013) proposed that the jerk identification may be biased due to inherent limitations in the extent and time of potential jerks considered, and suggested that a more robust method would use the whole time series of data (e.g. Stewart & Whaler, 1995, Alexandrescu et al., 1996, De Michelis & Tozzi, 2005), rather than requiring prior data selection. Therefore, they modified the method to use a sliding window that acts as in Pinheiro et al. (2011), but shifts one time step per iteration along the time series of data and calculates the PDF repeatedly. The summation of the resulting overlapping probability functions is then normalised to an integral of 1, so as to produce a continuous PDF for the entire series of data under consideration. The modified method uses the same procedure for estimating time uncertainties as described in Pinheiro et al. (2011), but Brown et al. (2013) introduced a threshold probability above which an event may be considered 'significantly likely' compared to the background level of 'likeliness' that arises from the misfit of the regression to the variability in the data. Their method also requires a minimum jerk amplitude below which an event is not considered significant compared to the background noise level of the data.

For consistency, we used the same parameters on the synthetics as Brown et al. (2013) used on the real magnetic data for the period 1958-2008. These parameters include a PDF threshold cut-off (taken as 0.2 in Brown et al. (2013), based on trade-off curve of the number of jerks detected versus the probability cut-off threshold above which peaks in probability are considered jerks), a minimum jerk amplitude (3 $\mathrm{nT/yr^2}$) and

the window length for the linear regression. Four different window lengths (5, 10, 15 and 20 yr) were applied to each individual component of the SV time series, and a two-part linear regression was fitted to the series at every potential jerk occurrence time (taken as 0.001 yr so as to be smaller than the monthly (0.08 yr) synthetic data sampling).

The jerk detection method identified several jerk events at Earth's surface, according to the criteria specified by Brown et al. (2013). As previously discussed in relation to the previous synthetic series, the signals retain some periodicity due to waves travelling beneath some locations periodically. This periodicity results in several successive jerks being observed at some observatories, but there is only weak evidence for such periodic jerks in real magnetic data (Brown et al., 2013). Figures of all results from this method may be found in Appendix B, Figs. B.2 to B.10; a few example figures are also included in this chapter for ease of discussion. The top panel of these figures shows a time series of a single component of the SV signal (in nT/yr) at a particular observatory throughout the 200 years of the torsional wave forward model shown in Fig. 4.12. The observatory name and the window length are displayed at the top of each figure, and any identified jerk events are shown as a red 'V' shape fitted to the synthetic SV series. The bottom panel shows the calculated PDF from the two-part linear regression, with the chosen threshold cut-off value shown as a green line, and the positive and negative errors on the PDF are filled in underneath the PDF curve in red and black respectively. As described in Brown et al. (2013), the PDF values are normalised to a value of one across the entire window to account for any jerk events being identified in several windows during the sliding regression. Note that for narrow PDF curves, the values of the PDF are very high (>100) because the algorithm normalises the area of a spike.

In general, the identified jerk events occurred in single components of the SV and were localised to small regions. Since the torsional waves perturb the ambient magnetic field in two equatorially symmetric bands of latitude, the waves do not produce signals that are observed everywhere at the same time, which precludes the generation of global jerk events such as that observed in 1969 (Courtillot et al., 1978, Malin et al., 1983, Whaler, 1987). However, more observatories see signals simultaneously towards the end of the wave model because the wave energy has dispersed through the domain, though these signals tend to be low amplitude and smoothly varying. As the wave

energy disperses through the core, the SV signals become broader and weaker, which at some observatories, such as at Hermanus in South Africa (Fig. 4.17a), results in fewer jerk events being identified during the final core transit time in the model. In other locations, jerk events are identified whenever the wave passes beneath the observatory, see San Juan, USA in Fig. 4.17b.

(a) $t = 0$

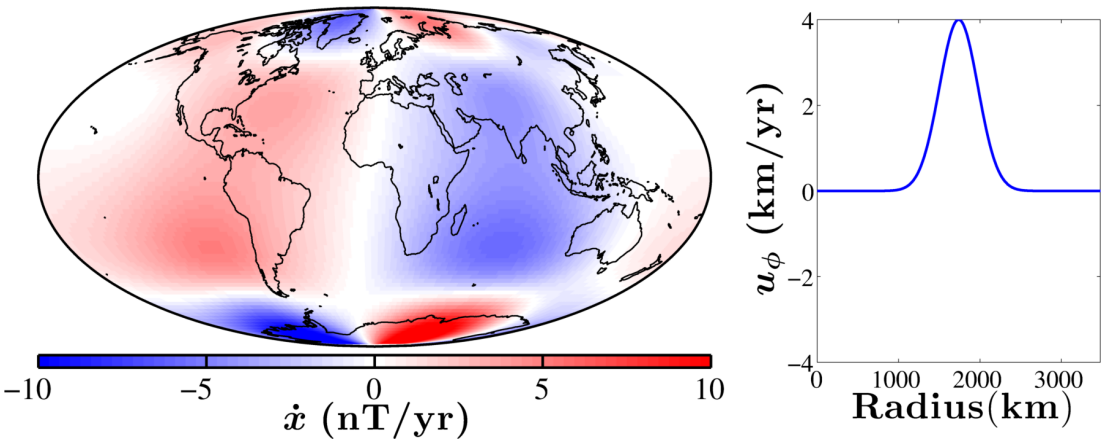

(b) $t = 10$ yr

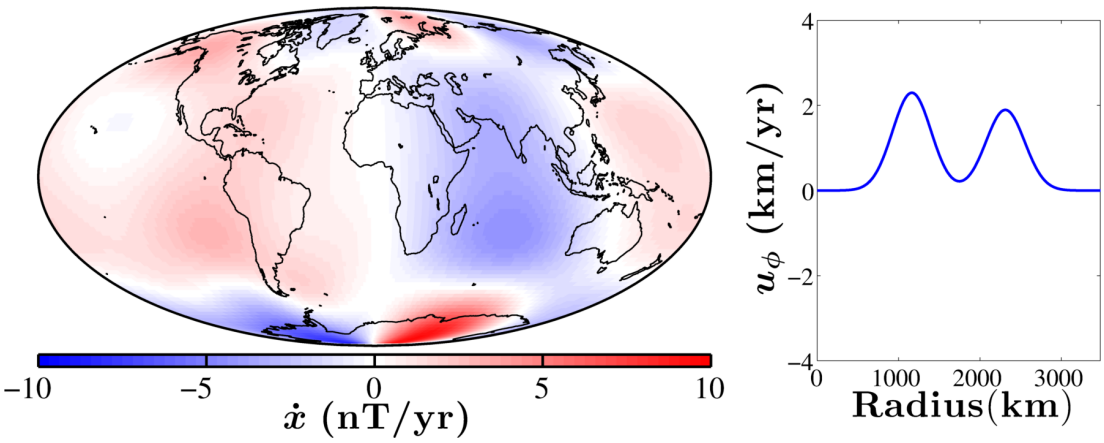

(c) $t = 20$ yr

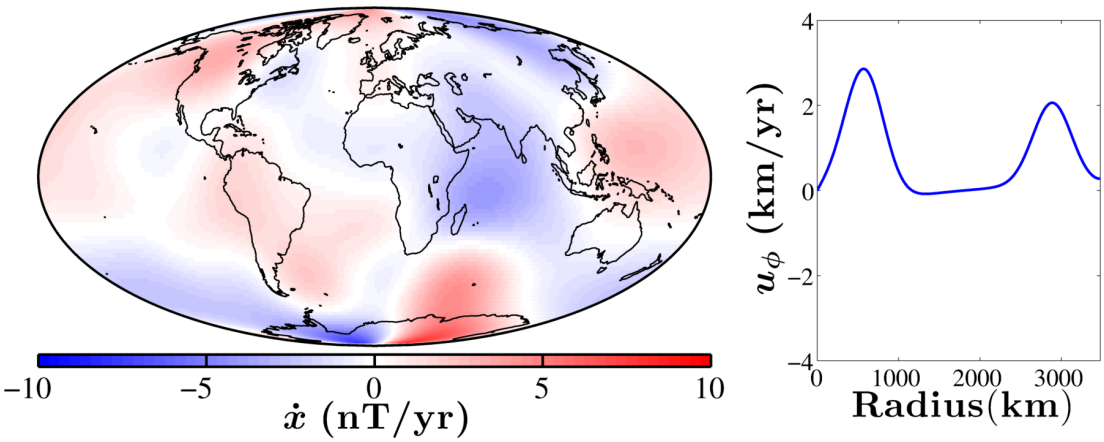

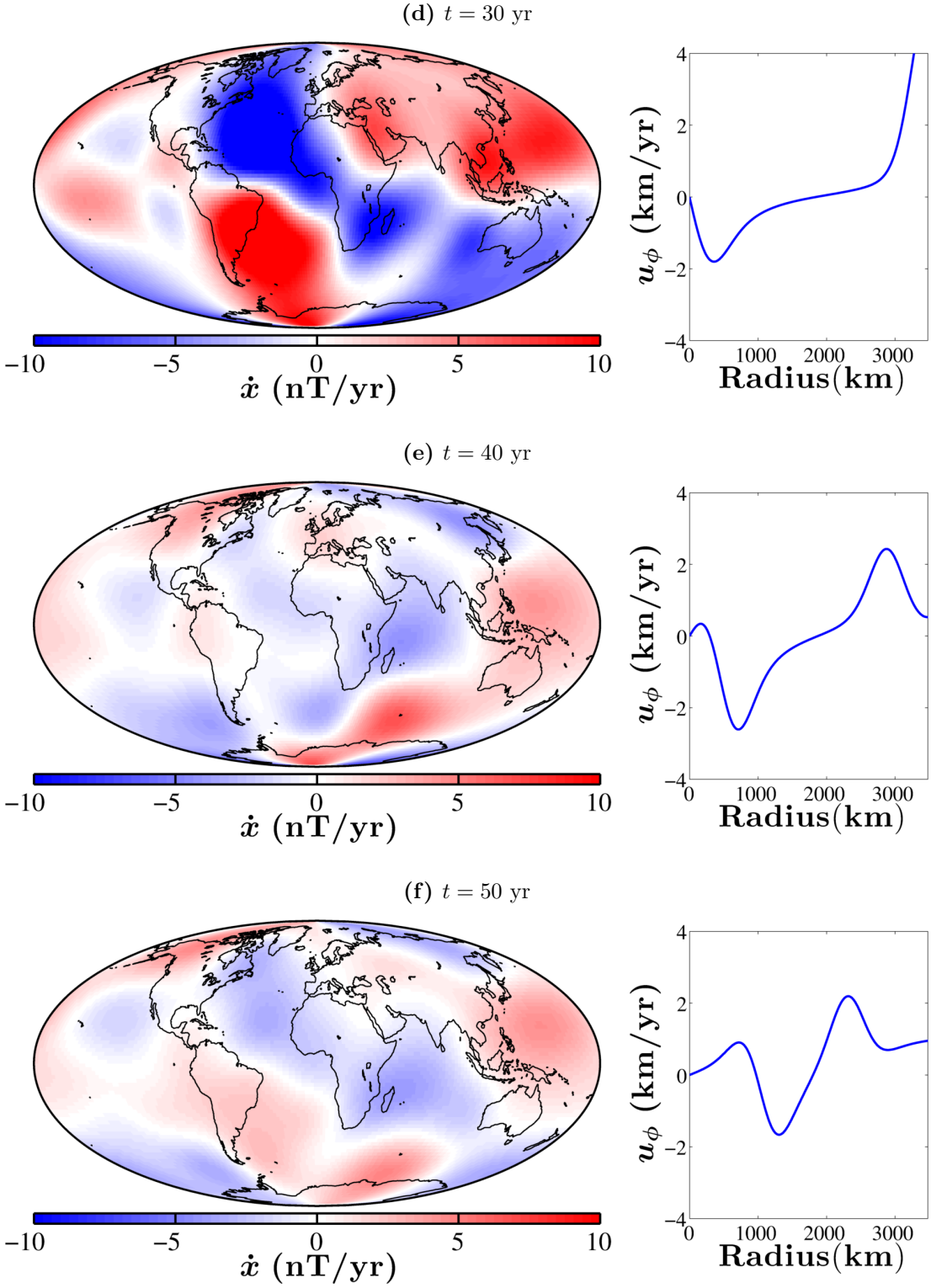

Figure 4.13: Maps of the x component of the SV induced by torsional waves with a 60 yr core transit time and an initial wave pulse amplitude of 4 km/yr. The SV is evaluated at the Earth's surface and the colour scale is from −10 nT/yr to 10 nT/yr. The torsional wave profile is shown on the right, with cylindrical radius (km) on the horizontal axis and zonal velocity (km/yr) on the vertical axis.

(a) $t = 0$

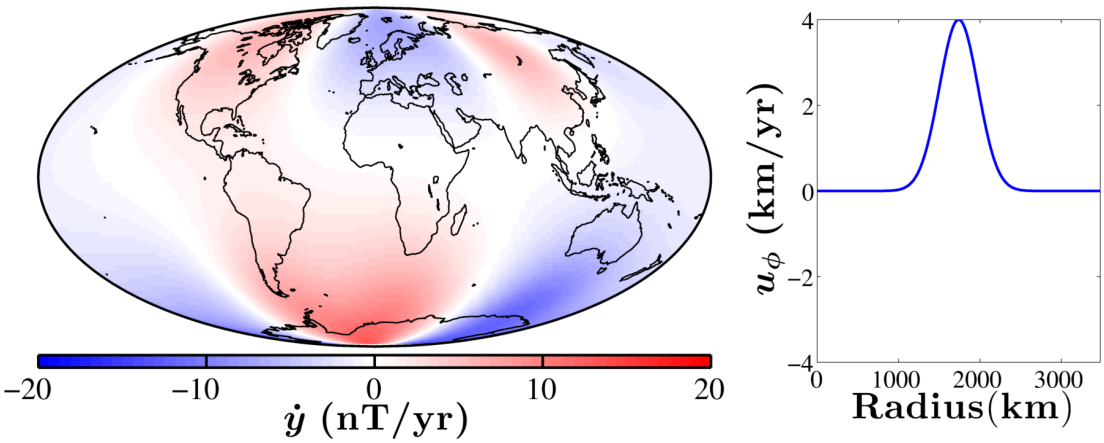

(b) $t = 10$ yr

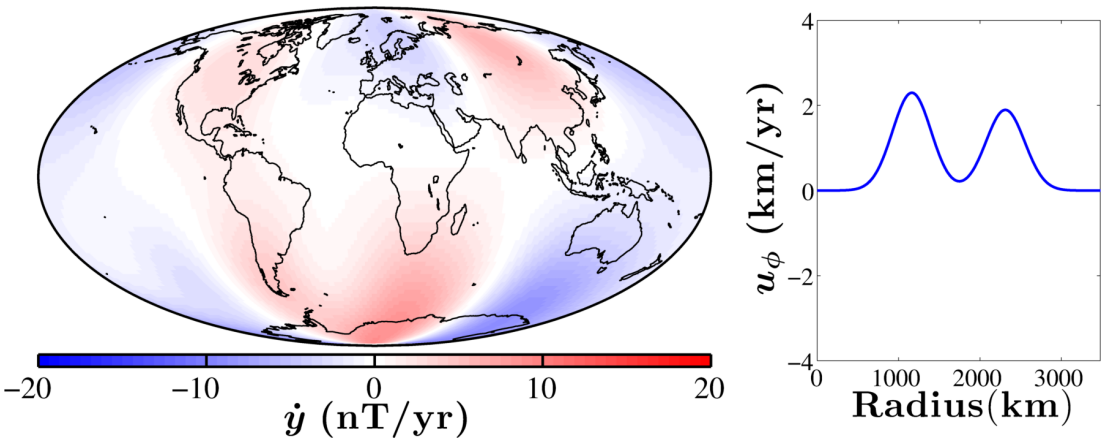

(c) $t = 20$ yr

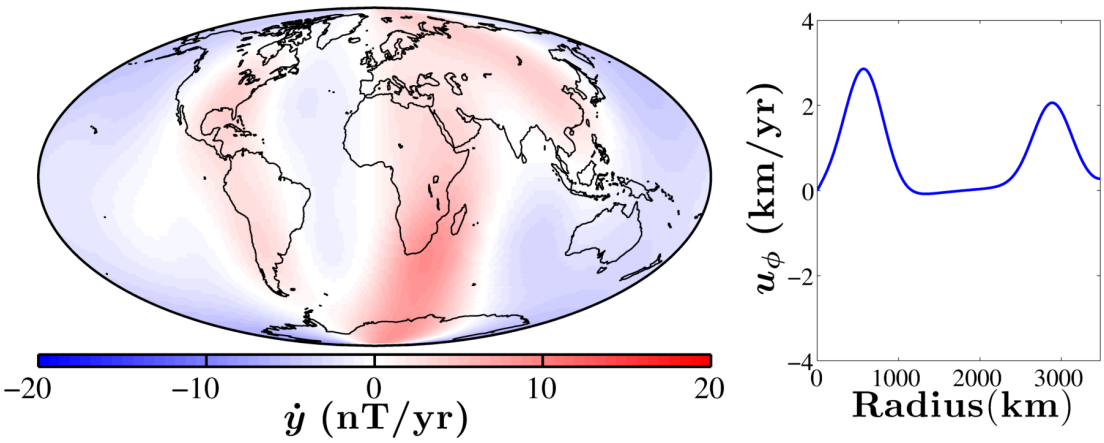

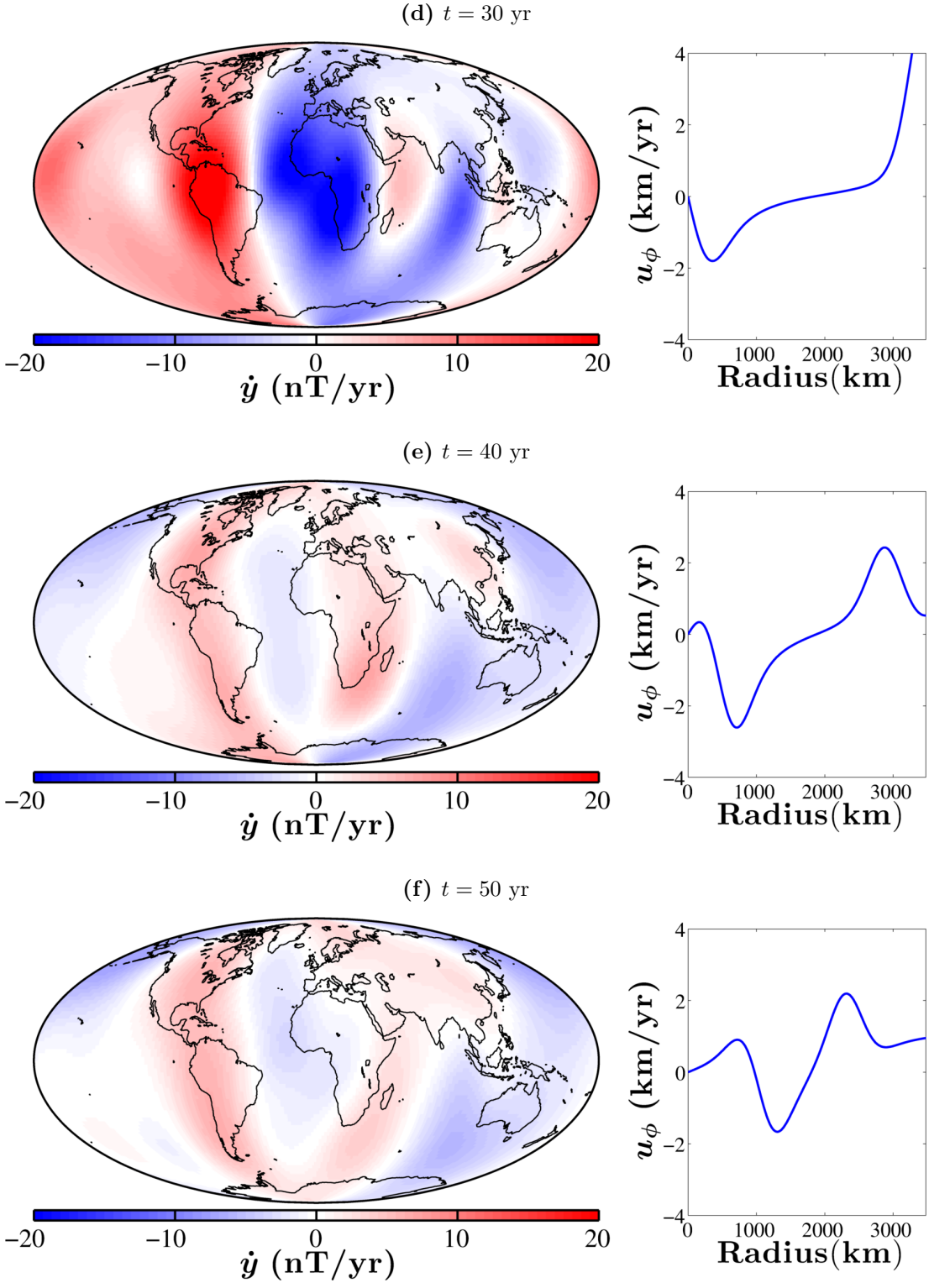

Figure 4.14: Maps of the y component of the SV induced by torsional waves with a 60 yr core transit time and an initial wave pulse amplitude of 4 km/yr. The SV is evaluated at the Earth's surface and the colour scale is from −20 nT/yr to 20 nT/yr. The torsional wave profile is shown on the right, with cylindrical radius (km) on the horizontal axis and zonal velocity (km/yr) on the vertical axis.

(a) $t = 0$

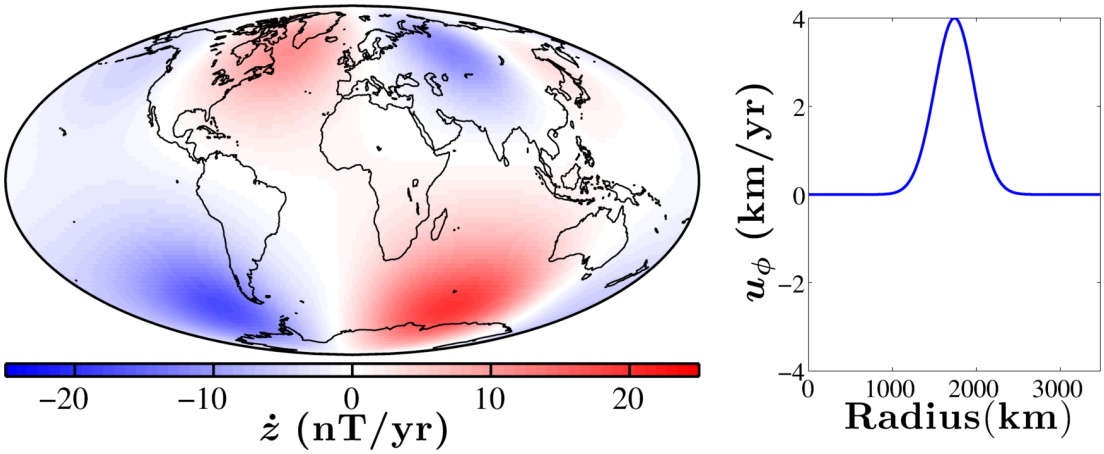

(b) $t = 10$ yr

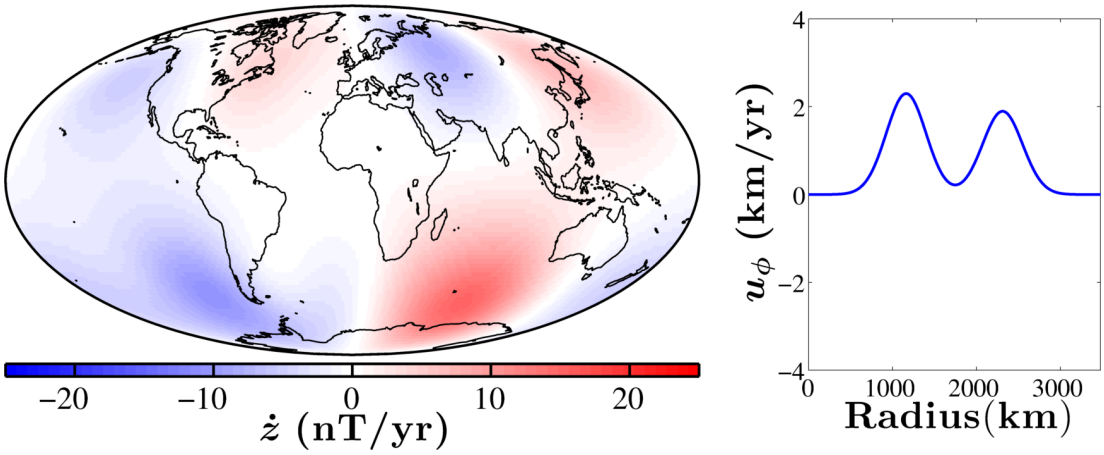

(c) $t = 20$ yr

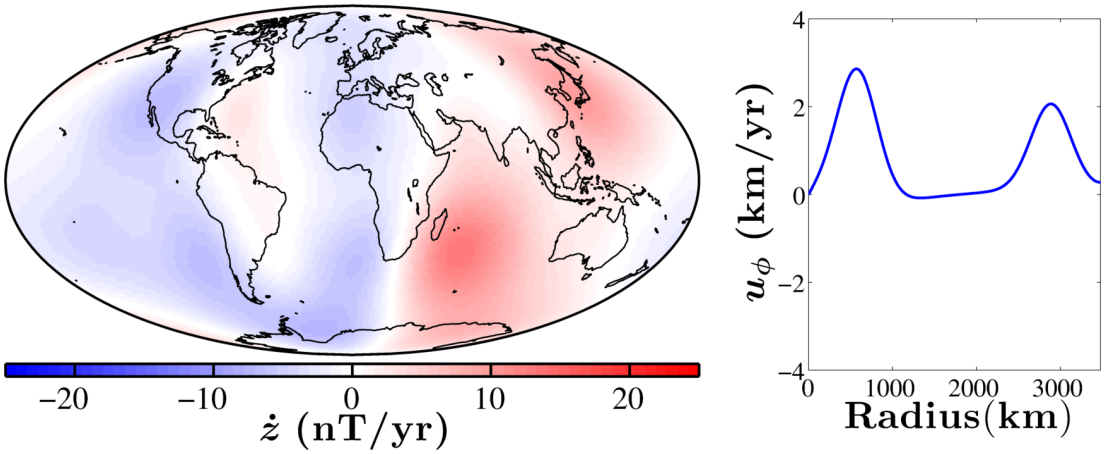

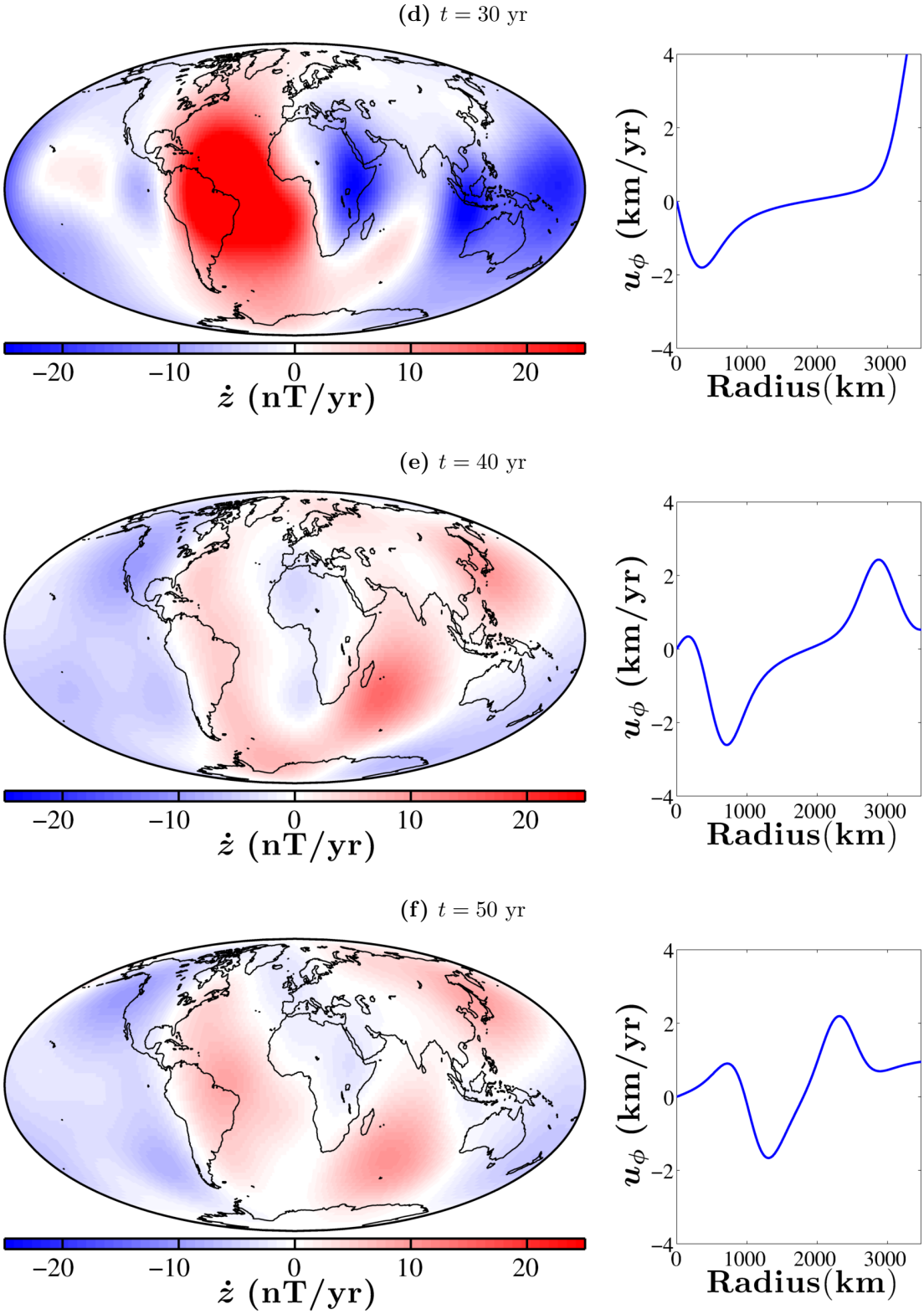

Figure 4.15: Maps of the z component of the SV induced by torsional waves with a 60 yr core transit time and an initial wave pulse amplitude of 4 km/yr. The SV is evaluated at the Earth's surface and the colour scale is from −25 nT/yr to 25 nT/yr. The torsional wave profile is shown on the right, with cylindrical radius (km) on the horizontal axis and zonal velocity (km/yr) on the vertical axis.

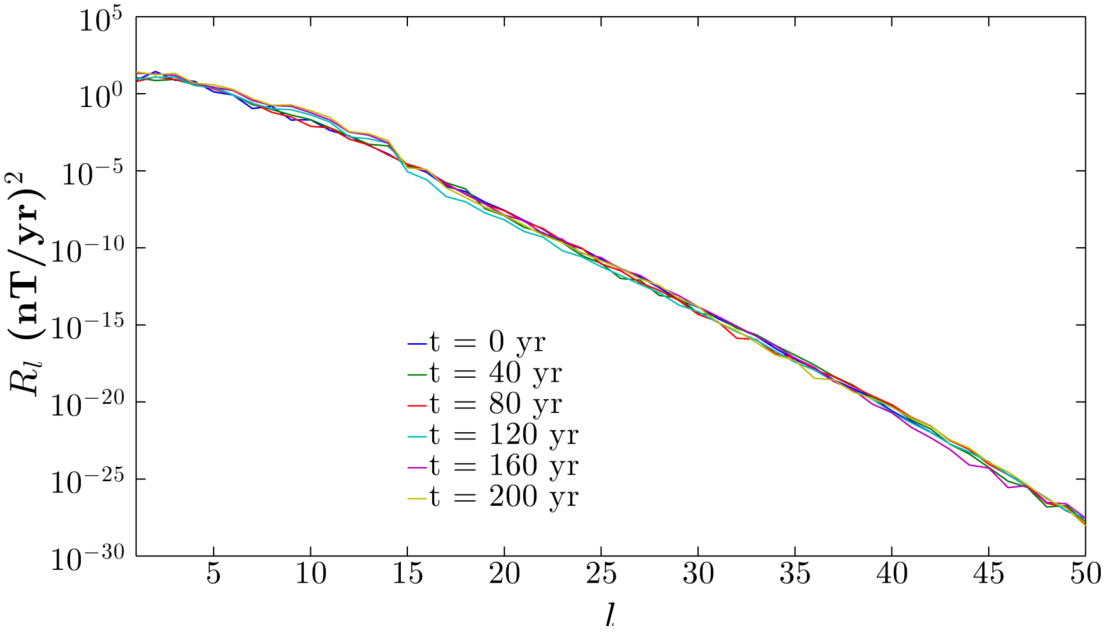

Figure 4.16: The spatial power spectrum, evaluated at Earth's surface, of torsional wave-induced SV. The waves in this model had a core transit time of 60 yr and an initial pulse amplitude of 4 km/yr.

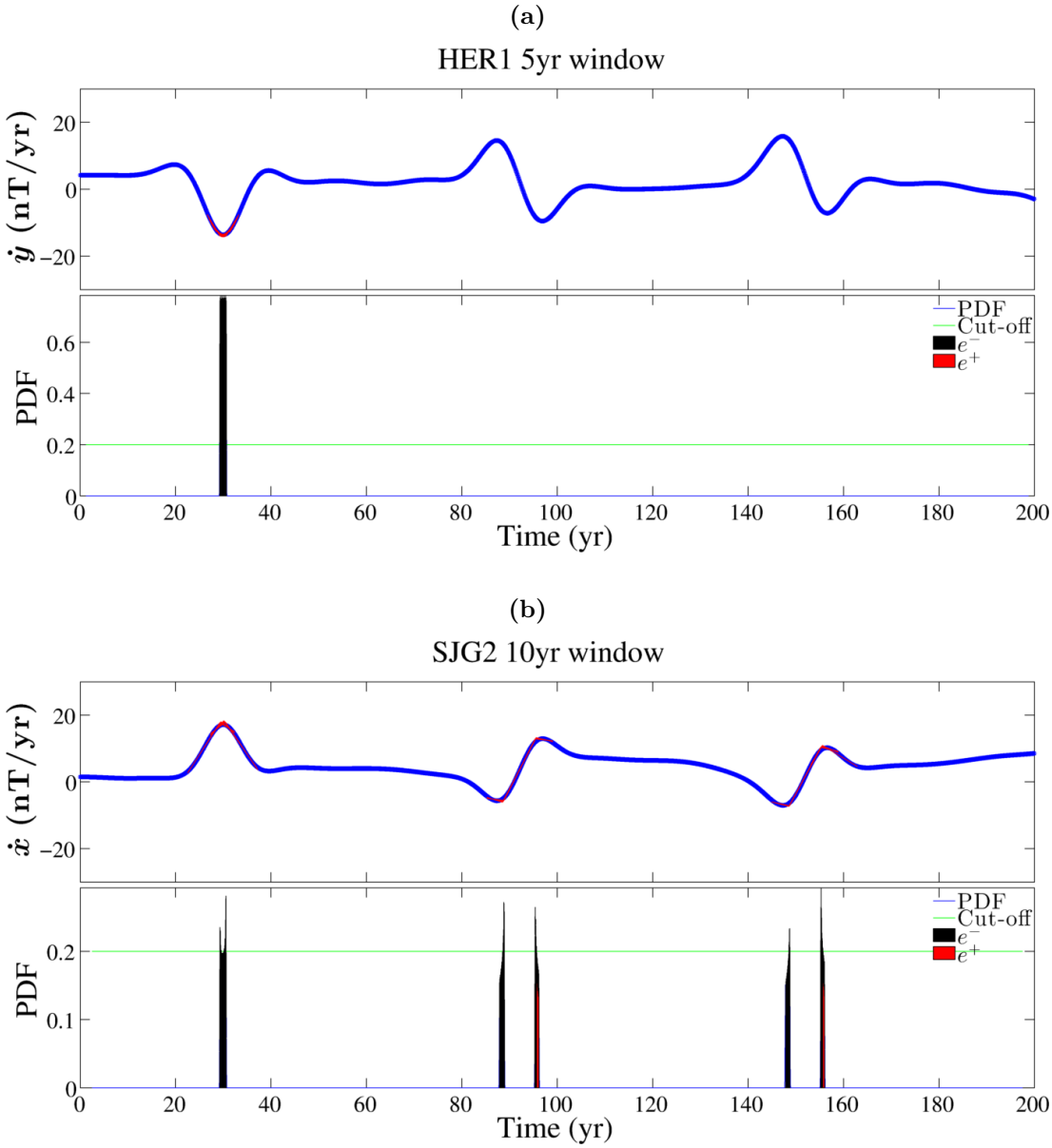

Figure 4.17: The top panel of these figures shows a time series of a single component of the SV signal (in nT/yr) at (a) Hermanus and (b) San Juan throughout the 200 years of the torsional wave forward model shown in Fig. 4.12. The observatory name and window length are displayed at the top of each subfigure, and identified jerk events are shown as a red 'V' shape fitted to the SV series. The bottom panel shows the calculated PDF from the two-part linear regression, with the chosen threshold cut-off value of 0.2 shown as a green line. The positive and negative errors on the PDF are filled in underneath the PDF curve in red and black, respectively

4.7 Discussion and conclusions

In this chapter, we have used the induction equation under the frozen flux assumption and velocities from torsional wave forward models to produce maps and synthetic time series of wave-induced SV. The required background fields were taken from the COV-OBS model by Gillet et al. (2013), though the effects of using different field models and/or time-averaged fields were investigated and found to give equivalent results. We conducted a sensitivity test of the magnetic field to a bulk rotation of the core fluid, finding that global zonal core flows produce SV signals that strongly depend on the local magnetic field morphology and in particular, on the field's longitudinal variations. As Bloxham et al. (2002) noted in the first paper suggesting that geomagnetic jerks are caused by torsional oscillations, the local effects of field structure may explain why some jerk events are only observed on regional scales and implies that small length scale core flow need not necessarily be the cause of regional SV signals. However, some geomagnetic jerks, such as the event in 1969, were observed at a global scale (Courtillot et al., 1978, Malin et al., 1983, Whaler, 1987), but not all parts of Earth's magnetic field are sensitive to zonal core flows at any particular time. Since torsional waves (or other zonal flow) cannot produce global contemporaneous SV signals, we concur with previous studies (e.g. Wardinski et al., 2008, Silva & Hulot, 2012) that suggested geomagnetic jerks cannot be caused by zonal flows alone, even though such flows are an important contributor to the observed SV. An interesting point to note from the sensitivity test, is that the observed SV and that induced by a bulk rotation of the core fluid are remarkably similar, particularly in the equatorial regions. The amplitude of the bulk rotation required to match the observed SV amplitudes was approximately 0.3°/yr, which is similar to many estimates of the rate of westward drift of the geomagnetic field in the equatorial Atlantic (e.g. Bullard et al., 1950).

We set out to investigate whether the torsional waves in our forward models can produce SV signals that resemble geomagnetic jerks. Several studies have linked the origin of jerks to torsional oscillations and/or toroidal core flows (e.g. Waddington et al., 1995, Bloxham et al., 2002, Olsen & Mandea, 2008, Wardinski et al., 2008, Silva & Hulot, 2012). When the torsional wave amplitudes and timescales are chosen to match a recent study of the 6 yr signal in ΔLOD by Gillet et al. (2010), the resulting SV signals were very small (<3 nT/yr at Earth's surface) and would not be resolved in magnetic

data. The timescales of the induced SV signals are very short, due to the waves having a 6 yr core transit time, and are consequently too rapid to be considered as jerks because observed jerks punctuate relatively long (years to decades) periods of constant SV. However, torsional oscillations have most often been linked to decadal signals in geophysical data with higher amplitudes (e.g. Braginsky, 1970, Zatman & Bloxham, 1997, 1999, Hide et al., 2000, Roberts et al., 2007, Dickey & de Viron, 2009), and so we recalculated the SV signals induced by torsional waves with a 60 yr core transit time and an increased amplitude of 4 km/yr.

We applied the jerk detection method of Brown et al. (2013) to the synthetic SV series evaluated at Earth's surface, using the same parameters as they used on real magnetic data. Various signals were identified as jerks in the synthetic data, according to the criteria described in Brown et al. (2013), though they do not appear to resemble SV signals that have traditionally been identified as jerks. At all observatories, the SV signals are smoothly-varying and do not resemble the sharp 'V' shape that is usually associated with geomagnetic jerks, see Fig. 4.1. However, despite the prevalence of this definition, not all authors agree that jerks should be defined as sharp changes in SV and a corresponding step in the second time derivative of the magnetic field and spike in the third time derivative (e.g. Alldredge, 1984, 1985). Demetrescu & Dobrica (2005) decomposed the geomagnetic field variation into its multidecadal ingredients, which include a 'steady variation' and three quasi-periodic signals of ∼11 yr, ∼22 yr and ∼80 yr. The steady variation and 80 yr signals are related to main field evolution, the 11 yr is of external origin and 22 yr signal has both internal and external sources. When considering the 22 yr signal to be of purely external origin, Demetrescu & Dobrica (2005) suggested that a jerk results from the superposition of the 11 yr and 22 yr variations on the 80-yr variation, and this superposition of quasi-periodic signals affects jerk timing, magnitude, and duration. In a subsequent paper, in which the authors made the distinction between the external 22 yr signal and the (larger) internal 22 yr signal, the authors found that jerks arise from the combination of the internal 22 yr and 80 yr signals (Demetrescu & Dobrica, 2014). They argue that since jerks are caused by smoothly-varying periodic signals, they are not inherently sharp SV signals and that contamination by the external 22 yr signal causes the often reported 'V' shape on very short timescales, and also influences the amplitude and timing of the jerk. The smoothly varying SV signals induced by our torsional waves seem to be more consistent

with the results of Demetrescu & Dobrica (2005, 2014) than other works requiring very sharp SV variations.

Many of the signals are only identified in a single component of the field, and the several jerks often occur in quick succession due to the periodic propagation of waves under particular locations. Despite attempts by Brown et al. (2013), such periodicities have not been identified in jerk occurrences in observatory data. If torsional waves in the core are related to geomagnetic jerks, it could be that the waves are generated in one region of the core, the tangent cylinder for example (Livermore & Hollerbach, 2012, Teed et al., 2015), and are damped out in another region so that the waves do not reflect from the core boundaries (Schaeffer et al., 2012). If the base of the lower mantle were electrically conducting, the waves would likely be rapidly attenuated at the top of the core (e.g. Dumberry & Mound, 2008) and so would be unable to produce the periodic signals seen in our forward models. Despite several suggestions, the excitation mechanism of torsional waves in the core has not yet been confirmed. The waves could be continually generated, periodically generated or irregularly generated, depending on the physical processes that excites them, and each of these scenarios would result in very different SV signals.

Chapter 5

Concluding remarks

This thesis has focussed upon torsional Alfvén waves in Earth's core and their influence on geomagnetic secular variation. This chapter collects the principal results obtained in the previous chapters and returns to the questions posed in chapter 1. Finally, we discuss some remaining gaps in knowledge of torsional waves and make suggestions as to how these could be addressed in future studies.

5.1 Conclusions

What are the fundamental propagation characteristics of torsional Alfvén waves?

In chapter 3, we presented the results of our 1-D forward models of torsional waves in a cylinder of fluid, a sphere of fluid and an equatorially symmetric spherical shell. The key propagation features of the torsional waves in our models are: dispersion, phase shifts and internal reflections.

We found that torsional waves undergo significant dispersion during propagation that arises due to their geometric setting, and that the waves are increasingly dispersed with time. Using the various 'geometric' terms in the torsional wave equation, we quantified and characterised this dispersion, concluding that long wavelength features are more dispersive than short wavelength features. An additional source of dispersion in the models is the presence of a low amplitude wake trailing behind sharply defined pulses after the initial wave pulse has split apart. We attributed these negative wakes to

the failure of Huygens' principle in even spatial dimensions, hypothesising that despite their 1-D mathematical description, torsional waves involve 2-D physics due to their convergence upon an axis.

Having observed unexpected wave behaviour at the Earth's rotation axis, we performed a similar analysis to that detailed in Morse & Feshbach (1953) for torsional normal modes and showed that phase shifts can explain the observed wave behaviour. We also investigated the possibility of torsional waves undergoing a Hilbert transform at the rotation axis, a phenomenon that was first reported by Powell (1994) for waves passing through the focal point of a circular membrane. From these analyses, we concluded that while some narrow initial pulses appear to undergo a uniform phase shift at the rotation axis, in general, an arbitrary initial pulse will undergo a more complicated phase shift that cannot readily be understood as a Hilbert transform.

We investigated the effects on torsional wave propagation of using a spatially varying profile of the cylindrically averaged magnetic field and observed all of the features contained in previous models, plus three additional propagation features. First, the pulse trajectories are curved due to variations in the local Alfvén wave group velocity. Second, we observed an internal wave reflection, which we attributed to relatively steep magnetic field gradient at the same location. Third, we observed several pulses of alternating polarity near to both the rotation axis and the equator of the CMB after the first reflection of torsional waves at the boundaries. We noted that this effect is particularly prominent near the rotation axis, where the gradient of the magnetic field profile is steep, and concluded that these strong field gradients cause continual reflections of propagating waves in this region of the model, resulting in waves becoming partially trapped.

What are the implications of these propagation characteristics on torsional waves in Earth's core?

The main propagation characteristics of torsional waves in our forward models all act to significantly change the shape of an initial wave pulse. For travelling torsional waves, narrow (short wavelength) wave profiles are less dispersive than wider pulses, which may be particularly important when studying torsional waves in the Earth's core because those inferred from SV data appear to be relatively long wavelength. For example, the torsional waves presented in Gillet et al. (2010) occupy at least one

fifth of the core radius and those presented in Hide et al. (2000) occupy almost the entire core radius. Our analyses of dispersive regions and the evolution of our modelled waves suggested that torsional waves in the core may undergo a significant dispersion process that arises solely as a result of core geometry, an effect that has previously been neglected in torsional wave studies. Given that successive reflections from the boundaries significantly changes the shape of wave pulses in our models, we suggested that terrestrial torsional waves would undergo significant dispersion (energy spreading) irrespective of, and in addition to, any dissipative (damping) effects such as those proposed by Schaeffer et al. (2012), and therefore may not survive as distinct pulses for several transits of the Earth's core. The phase shifts and internal reflections also contribute to this effect, resulting in the initial pulse being unrecognisable after only a few core transits. Perhaps the most obvious implication of these combined dispersive effects is that if torsional waves were observed in geophysical data, they may not shed much light on their excitation mechanism as it would be difficult to recover the originally generated wave.

How do torsional waves perturb the ambient magnetic field, and are torsional wave-induced signals resolvable in SV data?

Using torsional wave velocities from our forward models and a background magnetic field taken from an observationally-constrained model, we investigated which regions of the geomagnetic field are most sensitive to zonal core flow and produced maps and synthetic time series of wave-induced SV. A sensitivity test of the magnetic field to a bulk rotation of the core fluid highlighted two important considerations. First, it has reiterated a point previously made by Bloxham et al. (2002) that local magnetic field morphology is a key factor in determining whether a particular location could observe an SV signal generated by zonal core flow and second, that a bulk rotation of $\sim 0.3^\circ$/yr with respect to the mantle can explain much of the observed SV signal.

Torsional wave time scales and amplitudes that are consistent with a recent investigation of the 6 yr signal in ΔLOD (Gillet et al., 2010) produced very small SV signals that likely could not be resolved in data and very rapid variations that are inconsistent with observed jerk events. Waves with 6 yr core transit time and an initial pulse amplitude of 0.4 km/yr gave SV signals that were, at most, approximately 20 nT/yr at the CMB, which is very small compared to the amplitude of the observed SV (approx-

imately 20 μT/yr). At Earth's surface, the x and y components of wave-induced SV were less than 1 nT/yr, and the radial component was less than 3 nT/yr, compared to the maximum ∼200 nT/yr amplitude of the observed radial SV. However, this scaling for the waves is only one of many possible choices. Scaling the waves such that they are consistent with other previous works (e.g. Zatman & Bloxham, 1997, Hide et al., 2000), gave more promising results. Torsional waves with a 60 yr core transit time and an initial pulse amplitude of 4 km/yr gave SV signals that are an order of magnitude larger than the previous scaling. At Earth's surface, all three components of the SV reach amplitudes of approximately 20 nT/yr, which could be resolved in SV data.

Can torsional waves produce signals in secular variation that are consistent with geomagnetic jerks?

We applied the jerk detection method developed by Pinheiro et al. (2011) and extended by Brown et al. (2013) to the synthetic SV data at Earth's surface. Application to the fast torsional waves required parameters that were far removed from those used for real SV data. Not only were the SV amplitudes small, the timescales were much too rapid to be consistent with jerks. Observed jerks tend to punctuate two relatively long periods (years to decades) of steady SV, with the jerk itself taking place very quickly. Due to the rapid core transit time of the waves, the synthetic data had no long periods of steady SV and so could not replicate jerk signals. However, using a different torsional wave scaling with a 60 yr core transit time and an initial pulse amplitude of 4 km/yr produces SV signals that are identified as jerks when the two-part linear regression method developed by Brown et al. (2013) is applied to the resulting synthetic SV time series. The signals tend to occur in only one SV component and are only observed on regional scales. As the local magnetic field morphology dictates which regions are sensitive to zonal core flow, and not all regions are sensitive at the same time, the torsional waves in the models are not able to induce global contemporaneous jerk events such as that observed in 1969 (Courtillot et al., 1978, Malin et al., 1983, Whaler, 1987). Also, the identified events are periodic due to waves passing beneath locations periodically and the SV signals are smoothly varying rather than the sharp 'V' shapes that are typically associated with geomagnetic jerks. These smooth signals are more consistent with the geomagnetic jerks envisaged by Demetrescu & Dobrica (2005, 2014) than other works requiring very sharp SV variations.

5.2 Future extensions

This work has focussed upon 1-D forward models of torsional waves that are initiated by a single velocity perturbation and propagate in an outer core that is not coupled to the inner core or to the mantle. The most obvious extensions to these models would be to use different forcing mechanisms to generate the torsional waves, add damping mechanisms to account for core-mantle and inner-outer core coupling mechanisms and/or extend them to higher dimensions.

The torsional waves in our forward models were initiated by an initial wave pulse and then left to propagate. As the excitation mechanism of torsional waves in the core has not yet been confirmed, forward models present an opportunity to investigate the effects of various forcing mechanisms on wave dynamics and their signals in SV. For example, the modelled waves could be periodically generated, excited at random times, or excited by adding random velocity perturbations. These generation mechanisms would produce very different SV signals, which could then be studied using methods such as the jerk detection code employed in this work.

Earth's outer core is thought to have strong electromagnetic (EM) coupling with the inner core and a weaker EM coupling with the lower mantle due to the presence of electrically conducting material in that region. Other core-mantle coupling mechanisms, such as gravitational, topographic or viscous, are also possible and could be included in future forward models. In the case of strong EM coupling with the inner core, one would expect the core fluid above and below the inner core (regions II and III in Fig. 1.4b) to rotate rigidly inside the tangent cylinder at the same speed as the inner core. The coupling would quickly dissipate torsional waves entering the tangent cylinder and so the waves would not exist long enough to reflect from the rotation axis and reenter the outer core as they do in our models. EM coupling with the inner core could be included in models by adding a magnetic diffusion layer to the ICB. Outer core-mantle coupling could be included in the models by adding an electrically conducting layer at the CMB. The thicknesses and material properties of these layers could then be varied in order to investigate the damping times and the effects of damping on wave dynamics, and to identify the most efficient damping mechanism and the best location for wave excitation. The wave-induced SV signals could then be filtered through the conducting

layer at the CMB by using a conductivity profile of Earth's interior to solve a magnetic diffusion equation, in a similar study to that of Pinheiro & Jackson (2008).

Although we have made extensive use of the 1-D torsional wave equation derived by Braginsky (1970), some aspects of torsional wave propagation cannot be thoroughly investigated using 1-D models. For example, Teed et al. (2013) reported that some torsional waves in their 3-D geodynamo simulations are transmitted through the tangent cylinder and others are dissipated when travelling towards the rotation axis. An interesting feature of the transmitted waves is that they appear to propagate into either the northern or southern hemisphere inside the tangent cylinder (regions II or III in Fig. 1.4b), but not into both hemispheres. An investigation of torsional wave behaviour at the tangent cylinder would require a developed theory of how to match the three regions of the core. In particular, if the wave velocities in regions II and III differ from each other, what does the velocity in region I match to? In the absence of a known matching condition, 1-D models such as those described in this work must be restricted to a full sphere of fluid or to an equatorially symmetric spherical shell, which precludes an investigation of this hemispherical preference of the waves.

References

Abramowitz, M. & Stegun, I. A., 1984. *Pocketbook of mathematical functions*, Verlag Harri Deutsch.

Alexandrescu, M., Gibert, D., Hulot, G., Le Mouël, J.-L., & Saracco, G., 1996. Worldwide wavelet analysis of geomagnetic jerks, *Journal of Geophysical Research: Solid Earth*, **101**(B10), 21975–21994.

Alfè, D., Gillan, M. J., & Price, G. D., 2000. Constraints on the composition of the Earth's core from ab initio calculations, *Nature*, **405**(6783), 172–175.

Alldredge, L. R., 1984. A discussion of impulses and jerks in the geomagnetic field, *Journal of Geophysical Research: Solid Earth (1978–2012)*, **89**(B6), 4403–4412.

Alldredge, L. R., 1985. More on the alleged 1970 geomagnetic jerk, *Phys. Earth Planet. Int.*, **39**(4), 255–264.

Asselin, R., 1972. Frequency Filter for Time Integrations, *Mon. Weather Rev.*, **100**(6), 487490.

Backus, G., 1968. Kinematics of geomagnetic secular variation in a perfectly conducting core, *Phil. Trans. R. Soc. Lond. A*, **263**, 239–266.

Biggin, A. J., de Wit, M. J., Langereis, C. G., Zegers, T. E., Voûte, S., Dekkers, M. J., & Drost, K., 2011. Palaeomagnetism of archaean rocks of the onverwacht group, barberton greenstone belt (southern africa): Evidence for a stable and potentially reversing geomagnetic field at ca. 3.5 Ga, *Earth and Planetary Science Letters*, **302**(3), 314–328.

Birch, F., 1964. Density and composition of mantle and core, *Journal of Geophysical Research*, **69**(20), 4377–4388.

Bloxham, J., Gubbins, D., & Jackson, A., 1989. Geomagnetic secular variation, *Phil. Trans. R. Soc. Lond. A*, **329**(1606), 415–502.

Bloxham, J., Zatman, S., & Dumberry, M., 2002. The origin of geomagnetic jerks, *Nature*, **420**, 65–68.

Boas, M. L., 2006. *Mathematical Methods in the Physical Sciences*, Wiley, 3rd edn.

Braginsky, S. I., 1970. Torsional magnetohydrodynamic vibrations in the Earth's core and variations in the length of day, *Geomagnetism and Aeronomy*, **10**, 1–10.

Braginsky, S. I., 1984. Short-period geomagnetic secular variation, *Geophys. Astrophys. Fluid Dyn.*, **30**, 1–78.

Braginsky, S. I., 1999. Dynamics of the stably stratified ocean at the top of the core, *Phys. Earth Planet. Int.*, **111**, 21–34.

Brown, W., Mound, J., & Livermore, P., 2013. Jerks abound: An analysis of geomagnetic observatory data from 1957 to 2008, *Physics of the Earth and Planetary Interiors*, **223**(0), 62 – 76, SI:13th SEDI conference.

Buffett, B., 2014. Geomagnetic fluctuations reveal stable stratification at the top of the earth's core, *Nature*, **507**(7493), 484–487.

Buffett, B. A., 2010. Tidal dissipation and the strength of the Earth's internal magnetic field, *Nature*, **468**, 952–954.

Buffett, B. A., Mound, J., & Jackson, A., 2009. Inversion of torsional oscillations for the structure and dynamics of Earth's core, *Geophys. J. Int.*, **177**, 878–890.

Bullard, E. C. & Gellman, H., 1954. Homogeneous dynamos and terrestrial magnetism, *Phil. Trans. R. Soc. Lond. A*, **247**, 213–278.

Bullard, E. C., Freedman, C., Gellman, H., & Nixon, J., 1950. The Westward Drift of the Earth's Magnetic Field, *Phil. Trans. R. Soc. Lond. A*, **243**, 67–92.

Canet, E., Fournier, A., & Jault, D., 2009. Forward and adjoint quasi-geostrophic models of the geomagnetic secular variation, *J. Geophys. Res.*, **114**, B11101.

Christensen, U. & Wicht, J., 2007. Numerical Dynamo Simulations, *in Treatise on Geophysics, Ed. P. Olson, Elsevier*, **8**, 245–279.

Cole, D., 2003. Space weather: Its effects and predictability, in *Advances in Space Environment Research*, pp. 295–302, eds Chian, A.-L., Cairns, I., Gabriel, S., Goedbloed, J., Hada, T., Leubner, M., Nocera, L., Stening, R., Toffoletto, F., Uberoi, C., Valdivia, J., Villante, U., Wu, C.-C., & Yan, Y., Springer Netherlands.

Constable, C. G., 2000. On rates of occurrence of geomagnetic reversals, *Phys. Earth Planet. Int.*, **118**, 181–193.

Courant, R. & Hilbert, D., 1962. *Methods of Mathematical Physics*, vol. II, Wiley.

Courtillot, V. & Valet, J.-P., 1995. Secular variation of the earth's magnetic field: from jerks to reversals, *Comptes rendus de l'Académie des sciences. Série 2. Sciences de la terre et des planètes*, **320**(10), 903–922.

Courtillot, V., Ducruix, J., & Le Mouël, J., 1978. Sur une accélération récente de la variation séculaire du champ magnétique terrestre, *CR Acad. Sci. D*, **287**, 1095–1098.

Cowling, T. G., 1934. The magnetic field of sunspots, *Mon. Not. R. Astr. Soc.*, **94**, 39–48.

Cox, G. A., Livermore, P. W., & Mound, J. E., 2014. Forward models of torsional waves: dispersion and geometric effects, *Geophysical Journal International*, **196**(3), 1311–1329.

Davidson, P. A., 2001. *An introduction to magnetohydrodynamics*, CUP.

Davies, C. J., Gubbins, D., & Jimack, P. K., 2011. Scalability of pseudospectral methods for geodynamo simulations, *Concurrency and Computation: Practice and Experience*, **23**(1), 38–56.

Davis, R. G. & Whaler, K. A., 1997. The 1969 geomagnetic impulse and spin-up of the Earth's liquid core, *Phys. Earth Planet. Int.*, **103**(3), 181–194.

De Michelis, P. & Tozzi, R., 2005. A local intermittency measure LIM approach to the detection of geomagnetic jerks, *Earth Planet. Sci. Lett.*, **235**(1), 261–272.

de Wijs, G. A., Kresse, G., Vocadlo, L., Dobson, D., Alfè, D., Gillan, M. J., & Price, G. D., 1998. The viscosity of liquid iron at the physical conditions of the Earth's core, *Nature*, **392**(6678), 805–807.

Demetrescu, C. & Dobrica, V., 2005. Recent secular variation of the geomagnetic field. new insights from long series of observatory data, *Rev. Roum. Geophys*, **49**, 22–33.

Demetrescu, C. & Dobrica, V., 2014. Multi-decadal ingredients of the secular variation of the geomagnetic field. insights from long time series of observatory data, *Phys. Earth Planet. Int.*, **231**, 39–55.

Desjardins, B., Dormy, E., & Grenier, E., 2001. Instability of Ekman-Hartmann boundary layers, with application to the fluid flow near the core-mantle boundary, *Physics of the Earth and Planetary Interiors*, **123**(1), 15–26.

Dickey, J. O. & de Viron, O., 2009. Leading modes of torsional oscillations within the Earth's core, *Geophysical Research Letters*, **36**(15).

Dumberry, M., 2009. Taylor's constraint and torsional oscillations, in *Les Houches, session LXXXVIII: Dynamos*, pp. 383–401, eds Cardin, P. & Cugliandolo, L. F., Elsevier.

Dumberry, M. & Bloxham, J., 2003. Torque balance, Taylor's constraint and torsional oscillations in a numerical model of the geodynamo, *Phys. Earth Planet. Int.*, **140**(1-3), 29–51.

Dumberry, M. & Finlay, C. C., 2007. Eastward and westward drift of the Earth's magnetic field for the last three millennia, *Earth and Planetary Science Letters*, **254**(1), 146–157.

Dumberry, M. & Mound, J. E., 2008. Constraints on core-mantle electromagnetic coupling from torsional oscillation normal modes, *J. Geophys. Res.*, **113**, B03102.

Durran, D. R., 1991. The third-order Adams-Bashforth method: An attractive alternative to leapfrog time differencing, *Monthly Weather Review*, **119**(3), 702–720.

Dziewonski, A. & Anderson, D., 1981. Preliminary reference Earth model, *Phys. Earth Planet. Int.*, **25**, 297–356.

Elsasser, W., 1946. Induction effects in Terrestrial magnetism I, *Phys. Rev.*, **69**(3-4), 106–116.

Gauss, C. F., 1832. Intensitas vis magneticae terrestris ad mensuram absolutam revocata (anzeige), *Göttinger Gelehrte Anzeigen*, pp. 2041–2058.

Gauss, C. F., 1834. Mesure absolue de lintensité du magnétisme terrestre, *Ann. Chim. Phys*, **57**, 1–69.

Gauss, C. F., 1839. Allgemeine theorie des erdmagnetismus. resultate ans den beobachtungen des magnetischen verein im jahre 1838.

Gauss, C. F. & Weber, W., 1840. *Atlas des Erdmagnetismus*, Weidemann.

Gillet, N., Pais, M., & Jault, D., 2009. Ensemble inversion of time-dependent core flow models, *Geochemistry, Geophysics, Geosystems*, **10**(6).

Gillet, N., Jault, D., Canet, E., & Fournier, A., 2010. Fast torsional waves and strong magnetic field within the Earth's core, *Nature*, **465**(74), 74–77.

Gillet, N., Jault, D., Finlay, C. C., & Olsen, N., 2013. Stochastic modeling of the Earth's magnetic field: Inversion for covariances over the observatory era, *Geochemistry, Geophysics, Geosystems*, **14**(4), 766–786.

Glatzmaier, G. A. & Roberts, P. H., 1995. A three-dimensional self-consistent computer simulation of a geomagnetic field reversal, *Nature*, **377**, 203–209.

Golub, G. H. & Welsch, J. H., 1969. Calculation of Gauss quadrature rules, *Mathematics of Computation*, **23**(106), 221–230.

Gomi, H., Ohta, K., Hirose, K., Labrosse, S., Caracas, R., Verstraete, M. J., & Hernlund, J. W., 2013. The high conductivity of iron and thermal evolution of the Earth's core, *Physics of the Earth and Planetary Interiors*, **224**, 88–103.

Gubbins, D., 1987. Mechanism for geomagnetic polarity reversals, *Nature*, **326**(6109), 167–169.

Gubbins, D. & Davies, C., 2013. The stratified layer at the core–mantle boundary caused by barodiffusion of oxygen, sulphur and silicon, *Physics of the Earth and Planetary Interiors*, **215**, 21–28.

Gubbins, D. & Roberts, P. H., 1987. Magnetohydrodynamics of the Earth's Core, *In Geomagnetism, Ed. Jacobs, J.A.*, **2**, 1–183.

Gubbins, D. & Tomlinson, L., 1986. Secular variation from monthly means from Apia and Amberley magnetic observatories, *Geophysical Journal International*, **86**(2), 603–616.

Hadamard, J., 1923. *Lectures on Cauchy's problem in linear partial differential equations*, Yale University Press.

Halley, E., 1692. On the cause of the change in the variation of the magnetic needle, with a hypothesis of the structure of the internal parts of the Earth, *Phil. Trans. R. Soc. Lond.*, **17**, 470–478.

Helffrich, G. & Kaneshima, S., 2013. Causes and consequences of outer core stratification, *Physics of the Earth and Planetary Interiors*, **223**, 2–7.

Hide, R., 1978. How to locate the electrically conducting fluid core of a planet from external magnetic observations, *Nature*, **271**, 640–641.

Hide, R. & Malin, S. R. C., 1981. On the determination of the size of the Earth's core from observations of the geomagnetic secular variation, *Proceedings of the Royal Society of London A: Mathematical, Physical and Engineering Sciences*, **374**(1756), 15–33.

Hide, R., Boggs, D. H., & Dickey, J. O., 2000. Angular momentum fluctuations within the Earth's liquid core and torsional oscillations of the core-mantle system, *Geophys. J. Int.*, **143**, 777–786.

Hirose, K., Labrosse, S., & Hernlund, J., 2013. Composition and state of the core, *Annual Review of Earth and Planetary Sciences*, **41**(1), 657.

Hollerbach, R., 1996. On the theory of the geodynamo, *Phys. Earth Planet. Int.*, **98**, 163–185.

Holme, R., 2007. Large-Scale Flow in the Core, *in Treatise on Geophysics, Ed. G. Schubert*, **8**, 107–130.

Holme, R. & de Viron, O., 2013. Characterization and implications of intradecadal variations in length of day, *Nature*, **499**, 202–204.

Holme, R. & Whaler, K., 2001. Steady core flow in an azimuthally drifting reference frame, *Geophysical Journal International*, **145**(2), 560–569.

Iitaka, T., Hirose, K., Kawamura, K., & Murakami, M., 2004. The elasticity of the $MgSiO_3$ post-perovskite phase in the Earth's lowermost mantle, *Nature*, **430**(6998), 442–445.

Jackson, A., 1997. Time-dependency of tangentially geostrophic core surface motions, *Phys. Earth Planet. Int.*, **103**, 293–311.

Jackson, A., Bloxham, J., & Gubbins, D., 1993. Time-dependent flow at the core surface and conservation of angular momentum in the coupled core-mantle system, *Dynamics of Earth's Deep Interior and Earth Rotation, Geophysical Monograph*, **72**, 97–107.

Jackson, A., Jonkers, A. R. T., & Walker, M. R., 2000. Four centuries of geomagnetic secular variation from historical records, *Phil. Trans. R. Soc. Lond. A*, **358**, 957–990.

Jault, D. & Le Mouël, J., 1991. Physical properties at the top of the core and core surface motions, *Physics of the Earth and Planetary Interiors*, **68**(1), 76–84.

Jault, D. & Légaut, G., 2005. Alfvén waves within the Earth's core, in *Fluid Dynamics and Dynamos in Astrophysics and Geophysics*, The Fluid Mechanics of Astrophysics and Geophysics, pp. 277–293, eds Soward, A. M., Jones, C. A., Hughes, D. H., & Weiss, N. O., CRC Press.

Jault, D., Gire, C., & Le Mouël, J. L., 1988. Westward drift, core motions and exchanges of angular momentum between core and mantle, *Nature*, **333**(26), 353–356.

Jeffreys, H., 1926. The rigidity of the Earth's central core, *Geophysical Journal International*, **1**, 371–383.

King, E. M. & Buffett, B. A., 2013. Flow speeds and length scales in geodynamo models: The role of viscosity, *Earth and Planetary Science Letters*, **371-372**(0), 156 – 162.

Korte, M. & Constable, C., 2003. Continuous global geomagnetic field models for the past 3000 years, *Phys. Earth Planet. Int.*, **140**, 73–89.

Korte, M., Genevey, A., Constable, C., Frank, U., & Schnepp, E., 2005. Continuous geomagnetic field models for the past 7 millennia: 1. a new global data compilation, *Geochemistry, Geophysics, Geosystems*, **6**(2).

Korte, M., Constable, C., Donadini, F., & Holme, R., 2011. Reconstructing the Holocene geomagnetic field, *Earth and Planetary Science Letters*, **312**(3), 497–505.

Kuang, W., 1999. Force balances and convective states in the Earth's core, *Phys. Earth Planet. Int.*, **116**, 65–79.

Kuang, W. & Bloxham, J., 1997. An Earth-like numerical dynamo model, *Nature*, **389**, 371–374.

Langlais, B., Amit, H., Larnier, H., Thébault, E., & Mocquet, A., 2014. A new model for the (geo) magnetic power spectrum, with application to planetary dynamo radii, *Earth and Planetary Science Letters*, **401**, 347–358.

Larmor, J., 1919. How could a rotating body such as the sun become a magnet?, *Rept. Brit. Assoc. Adv. Sci.*, pp. 159–160.

Le Huy, M., Alexandrescu, M., Hulot, G., & Le Mouël, J.-L., 1998. On the characteristics of successive geomagnetic jerks, *Earth, planets and space*, **50**(9), 723–732.

Le Mouël, J. L., 1984. Outer-core geostrophic flow and secular variation of Earth's geomagnetic field, *Nature*, **311**(5988), 734–735.

Le Mouël, J. L., Gire, C., & Madden, T., 1985. Motions at core surface in the geostrophic approximation, *Phys. Earth Planet. Int.*, **39**, 270–287.

Légaut, G., 2005. *Ondes de torsion dans le noyau terrestre*, Ph.D. thesis, Laboratoire de Géophysique Interne et Tectonophysique.

Lehmann, I., 1936. P', *Bur. Centr. Seism. Internat. Serie A*, **14**, 87–115.

Lewis, H. R. & Bellan, P. M., 1990. Physical constraints on the coefficients of Fourier expansions in cylindrical coordinates, *J. Math. Phys.*, **31**(11), 2592–2596.

Li, J. & Fei, Y., 2003. Experimental constraints on core composition, *Treatise on Geochemistry*, **2**, 521–546.

Livermore, P. W. & Hollerbach, R., 2012. Successive elimination of shear layers by a hierarchy of constraints in inviscid spherical-shell flows, *J. Math. Phys.*, **53**(7), 073104.

Livermore, P. W., Ierley, G., & Jackson, A., 2011. The evolution of a magnetic field subject to Taylor's constraint using a projection operator, *Geophysical Journal International*, **187**(2), 690–704.

Livermore, P. W., Hollerbach, R., & Jackson, A., 2013. Electromagnetically driven westward drift and inner-core superrotation in Earth's core, *Proceedings of the National Academy of Sciences*.

Lowes, F. J., 1974. Spatial power spectrum of the main geomagnetic field, and extrapolation to the core, *Geophys. J. R. Astr. Soc.*, **36**, 717–730.

Macmillan, S., 1996. A geomagnetic jerk for the early 1990s, *Earth Planet. Sci. Lett.*, **137**(1), 189–192.

Malin, S. R. C. & Hodder, B. M., 1982. Was the 1970 geomagnetic jerk of internal or external origin?, *Nature*, **296**(5859), 726–728.

Malin, S. R. C., Hodder, B. M., & Barraclough, D. R., 1983. Geomagnetic secular variation: a jerk in 1970, in *Scientific Contributions in Commemoration of Ebro Observatory's 75th Anniversary*, vol. 1, pp. 239–256.

Mandea, M., Bellanger, E., & Le Mouël, J.-L., 2000. A geomagnetic jerk for the end of the 20th century?, *Earth and Planetary Science Letters*, **183**(3), 369–373.

Mandea, M., Holme, R., Pais, A., Pinheiro, K., Jackson, A., & Verbanac, G., 2010. Geomagnetic jerks: rapid core field variations and core dynamics, *Space science reviews*, **155**(1-4), 147–175.

McDonough, W. & Sun, S., 1995. The composition of the earth, *Chemical Geology*, **120**(34), 223 – 253, Chemical Evolution of the Mantle.

McElhinny, M. W. & Senanayake, W. E., 1980. Paleomagnetic evidence for the existence of the geomagnetic field 3.5 Ga ago, *Journal of Geophysical Research: Solid Earth*, **85**(B7), 3523–3528.

Merrill, R. T. & McFadden, P. L., 1999. Geomagnetic polarity transitions, *Rev. Geophys.*, pp. 201–226.

Morse, P. & Feshbach, H., 1953. *Methods of theoretical physics*, vol. 1, McGraw-Hill.

Mound, J. & Buffett, B., 2007. Viscosity of the Earth's fluid core and torsional oscillations, *J. Geophys. Res.*, **112**, B05402.

Mound, J. E. & Buffett, B. A., 2005. Mechanisms of core-mantle angular momentum exchange and the observed spectral properties of torsional oscillations, *Journal of Geophysical Research: Solid Earth (1978-2012)*, **110**(B8).

Murakami, M., Hirose, K., Kawamura, K., Sata, N., & Ohishi, Y., 2004. Post-perovskite phase transition in $MgSiO_3$, *Science*, **304**(5672), 855–858.

Oganov, A. R. & Ono, S., 2004. Theoretical and experimental evidence for a post-perovskite phase of $MgSiO_3$ in Earth's D" layer, *Nature*, **430**(6998), 445–448.

Oldham, R. D., 1906. The constitution of the interior of the Earth, as revealed by earthquakes, *Quarterly Journal of the Geological Society*, **62**(1-4), 456–475.

Olsen, N. et al., 2006. CHAOS – a model of the Earth's magnetic field derived from CHAMP, Ørsted, and SAC-C magnetic satellite data, *Geophys. J. Int.*, **166**, 67–75.

Olsen, N. & Mandea, M., 2007. Investigation of a secular variation impulse using satellite data: The 2003 geomagnetic jerk, *Earth and Planetary Science Letters*, **255**(1), 94–105.

Olsen, N. & Mandea, M., 2008. Rapidly changing flows in the Earth's core, *Nature Geoscience*, **1**, 390–394.

Olsen, N. & Stolle, C., 2012. Satellite geomagnetism, *Annual Review of Earth and Planetary Sciences*, **40**(1), 441–465.

Olsen, N., Mandea, M., Sabaka, T. J., & Tøffner-Clausen, L., 2009. CHAOS-2a geomagnetic field model derived from one decade of continuous satellite data, *Geophysical Journal International*, **179**(3), 1477–1487.

Olsen, N., Glassmeier, K.-H., & Jia, X., 2010a. Separation of the magnetic field into external and internal parts, *Space Science Reviews*, **152**(1-4), 135–157.

Olsen, N., Mandea, M., Sabaka, T. J., & Tøffner-Clausen, L., 2010b. The CHAOS-3 geomagnetic field model and candidates for the 11th generation IGRF, *Earth Planets and Space*, **62**(10), 719.

Olsen, N., Lühr, H., Finlay, C. C., Sabaka, T. J., Michaelis, I., Rauberg, J., & Tøffner-Clausen, L., 2014. The CHAOS-4 geomagnetic field model, *Geophysical Journal International*, **197**(2), 815–827.

Pais, A. & Hulot, G., 2000. Length of day decade variations, torsional oscillations and inner core superrotation: evidence from recovered core surface zonal flows, *Phys. Earth Planet. Int.*, **118**, 291–316.

Pinheiro, K. & Jackson, A., 2008. Can a 1-d mantle electrical conductivity model generate magnetic jerk differential time delays?, *Geophysical Journal International*, **173**(3), 781–792.

Pinheiro, K., Jackson, A., & Finlay, C., 2011. Measurements and uncertainties of the occurrence time of the 1969, 1978, 1991, and 1999 geomagnetic jerks, *Geochemistry, Geophysics, Geosystems*, **12**(10).

Poirier, J.-P., 1994. Light elements in the Earth's outer core: A critical review, *Phys. Earth Planet. Int.*, **85**(34), 319 – 337.

Powell, A., 1994. The focal phase shift of waves of a circular membrane, applied to underexpanded supersonic jet structure, *J. Acoust. Soc. Am.*, **97**(2), 927–932.

Pozzo, M., Davies, C., Gubbins, D., & Alfè, D., 2012. Thermal and electrical conductivity of iron at earth's core conditions, *Nature*, **485**, 355–358.

Press, W. H., Teukolsky, S. A., Vetterling, W. T., & Flannery, B. P., 1992. *Numerical Recipes in Fortran 77*, CUP, 2nd edn.

Proudman, J., 1916. On the motion of solids in a liquid possessing vorticity, *Proceedings of the Royal Society of London. Series A, Containing Papers of a Mathematical and Physical Character*, pp. 408–424.

Robert, A. J., 1966. The integration of a low-order spectral form of the primitive meteorological equations, *J. Meteor. Soc. Japan*, **44**, 237–244.

Roberts, P., 2007. 8.03 - Theory of the Geodynamo, in *Treatise on Geophysics*, pp. 67 – 105, ed. in Chief: Gerald Schubert, E., Elsevier, Amsterdam.

Roberts, P. & Scott, S., 1965. On analysis of the secular variation. a hydromagnetic constraint: Theory, *J. Geomagn. Geolect.*, **17**(2), 137–151.

Roberts, P., Yu, Z., & Russell, C., 2007. On the 60 year signal from the core, *Geophysical and Astrophysical Fluid Dynamics*, **101**(1), 11–35.

Roberts, P. H. & Aurnou, J. M., 2011. On the theory of core-mantle coupling, *Geophys. Astrophys. Fluid Dyn.*, **106**(2), 157–230.

Romanowicz, B., 2008. Using seismic waves to image Earth's internal structure, *Nature*, **451**, 266–268.

Rotvig, J. & Jones, C., 2002. Rotating convection-driven dynamos and low Ekman number, *Phys. Rev. E*, **66**, 056308.

Sagnotti, L., Scardia, G., Giaccio, B., Liddicoat, J. C., Nomade, S., Renne, P. R., & Sprain, C. J., 2014. Extremely rapid directional change during Matuyama-Brunhes geomagnetic polarity reversal, *Geophysical Journal International*, **199**(2), 1110–1124.

Schaeffer, N., Jault, D., Cardin, P., & Drouard, M., 2012. On the reflection of Alfvèn waves and its implication for Earth's core modelling, *Geophys. J. Int.*, **191**(2), 508–516.

Shankland, T. J., Peyronneau, J., & Poirer, J. P., 1993. Electrical conductivity of the Earth's lower mantle, *Nature*, **366**, 453–455.

Shearer, P., 2009. *Introduction to seismology*, Cambridge University Press, 2nd edn.

Shearer, P. M., 1995. Seismic studies of the upper mantle and transition zone, *Reviews of Geophysics*, **33**(S1), 321–324.

Shimizu, H., Poirier, J., & Mouël, J. L., 2005. On crystallization at the inner core boundary, *Phys. Earth Planet. Int.*, **151**(12), 37 – 51.

Silva, L. & Hulot, G., 2012. Investigating the 2003 geomagnetic jerk by simultaneous inversion of the secular variation and acceleration for both the core flow and its acceleration, *Physics of the Earth and Planetary Interiors*, **198**, 28–50.

Stellmach, S. & Hansen, U., 2004. Cartesian convection driven dynamos at low Ekman numbers, *Phys. Rev. E*, **70**, 056312.

Stewart, D. N. & Whaler, K. A., 1995. Optimal piecewise regression analysis and its application to geomagnetic time series, *Geophys. J. Int.*, **121**(3), 710–724.

Takahashi, F., Matsushima, M., & Honkura, Y., 2005. Simulations of a Quasi-Taylor State Geomagnetic Field Including Polarity Reversals on the Earth Simulator, *Science*, **309**, 459–461.

Taylor, G. I., 1917. Motion of solids in fluids when the flow is not irrotational, *Proceedings of the Royal Society of London. Series A, Containing Papers of a Mathematical and Physical Character*, pp. 99–113.

Taylor, J. B., 1963. The magneto-hydrodynamics of a rotating fluid and the Earth's dynamo problem, *Proc. R. Soc. A*, **9**, 274–283.

Teed, R. J., Jones, C. A., & Tobias, S. M., 2013. The dynamics and excitation of torsional waves in geodynamo simulations, *Geophys. J. Int.*.

Teed, R. J., Jones, C. A., & Tobias, S. M., 2015. The transition to Earth-like torsional oscillations in magnetoconvection simulations, *Earth Planet. Sci. Lett.*, **419**(0), 22 – 31.

Terra-Nova, F., Amit, H., Hartmann, G. A., & Trindade, R. I. F., 2015. The time-dependence of reversed archeomagnetic flux patches, *Journal of Geophysical Research: Solid Earth*.

Tkalčić, H., Young, M., Bodin, T., Ngo, S., & Sambridge, M., 2013. The shuffling rotation of the Earth's inner core revealed by earthquake doublets, *Nature Geoscience*, **6**, 497–502.

Waddington, R., Gubbins, D., & Barber, N., 1995. Geomagnetic field analysis V. determining steady core-surface flows directly from geomagnetic observations, *Geophysical Journal International*, **122**(1), 326–350.

Wardinski, I. & Holme, R., 2011. Signal from noise in geomagnetic field modelling: denoising data for secular variation studies, *Geophys. J. Int.*, **185**(2), 653–662.

Wardinski, I., Holme, R., Asari, S., & Mandea, M., 2008. The 2003 geomagnetic jerk and its relation to the core surface flows, *Earth and Planetary Science Letters*, **267**(3), 468–481.

Whaler, K., 1980. Does the whole of the Earth's core convect?, *Nature*, **287**, 528–530.

Whaler, K. A., 1987. A new method for analysing geomagnetic impulses, *Phys. Earth Planet. Int.*, **48**(3), 221–240.

Whaler, K. A. & Holme, R., 2007. Consistency between the flow at the top of the core and the frozen-flux approximation, *Earth, planets and space*, **59**(12), 1219–1229.

Wicht, J. & Christensen, U. R., 2010. Torsional oscillations in dynamo simulations, *Geophys. J. Int.*, **181**, 1367–1380.

Zatman, S. & Bloxham, J., 1997. Torsional oscillations and the magnetic field within the Earth's core, *Nature*, **388**, 760–763.

Zatman, S. & Bloxham, J., 1999. On the dynamical implications of models of b_s in the Earth's core, *Geophys. J. Int.*, **138**(3), 679–686.

Zhang, P., Cohen, R., & Haule, K., 2015. Effects of electron correlations on transport properties of iron at Earth's core conditions, *Nature*, **517**(7536), 605–607.

Appendix A

Derivation of the torsional wave equation

In §1.4.2 we derived Taylor's constraint, equation (1.16), which specifies that the Lorentz torque vanishes when averaged over cylindrical surfaces. When the magnetic field does not precisely satisfy Taylor's constraint, inertia may be reintroduced into equation (1.16) and used to balance the azimuthal Lorentz force to obtain

$$\rho_0 \int_z \oint \frac{\partial \boldsymbol{u}_g}{\partial t} s d\phi dz = \int_z \oint (\boldsymbol{J} \times \boldsymbol{B})_\phi s d\phi dz, \tag{A.1}$$

for an incompressible fluid. The above equation is defined in cylindrical polar coordinates (s, ϕ, z), where s is cylindrical radius, ϕ is azimuth and z is height. The symbol $\boldsymbol{u}_g$ represents the geostrophic flow, $\boldsymbol{J}$ is the electric current density, B is the magnetic field and ρ_0 is the hydrostatic reference density. Since we have integrated in the ϕ and z directions, the problem collapses to one dimension and the above equation (A.1), along with the induction equation, may be used to derive an equation for the time derivative of the geostrophic flow. The resulting 1-D torsional wave equation was first established by Braginsky (1970), though the following derivation is that found in Légaut (2005) and Jault & Légaut (2005). See Braginsky (1970) and Roberts & Aurnou (2011) for alternative derivations.

Equation (A.1) relates the geostrophic fluid velocity $\boldsymbol{u}_g$ to the magnetic field $\boldsymbol{B}$. Substituting $\boldsymbol{u}_g = s\omega_g(s,t)\boldsymbol{e}_{\boldsymbol{\phi}}$ yields

$$4\pi\rho_0 s z_T \frac{\partial \omega_g}{\partial t} = \int_z \oint (\boldsymbol{J} \times \boldsymbol{B})_\phi d\phi dz, \tag{A.2}$$

which now couples the angular speed ω_g and the magnetic field. In order to derive the torsional wave equation, we also need an equation that describes the evolution of

the magnetic field. As the timescales of interest for torsional waves (years to decades) are much less than the electromagnetic diffusion timescale of the core (approximately 200 000 yr), we use the frozen-flux form of the induction equation

$$\frac{\partial \boldsymbol{B}}{\partial t} = \nabla \times (\boldsymbol{u} \times \boldsymbol{B}). \tag{A.3}$$

Since $\boldsymbol{u}_g = (0, u_\phi, 0)$ and $\boldsymbol{B} = (B_s, B_\phi, B_z)$ in cylindrical coordinates,

$$\boldsymbol{u}_g \times \boldsymbol{B} = u_\phi B_z \boldsymbol{e}_s - u_\phi B_s \boldsymbol{e}_z,$$

and

$$\nabla \times (\boldsymbol{u} \times \boldsymbol{B}) = \begin{cases} -\omega_g \frac{\partial B_s}{\partial \phi} \\ s\omega_g \left(\frac{1}{s} \frac{\partial}{\partial s}(sB_s) + \frac{\partial B_z}{\partial z} \right) + sB_s \frac{\partial \omega_g}{\partial s}. \\ -\omega_g \frac{\partial B_z}{\partial \phi} \end{cases} \tag{A.4}$$

Using the solenoidal condition $\nabla \cdot \boldsymbol{B} = \frac{1}{s}\frac{\partial}{\partial s}(sB_s) + \frac{1}{s}\frac{\partial B_\phi}{\partial \phi} + \frac{\partial B_z}{\partial z} = 0$, equation (A.3) may be written as

$$\frac{\partial \boldsymbol{B}}{\partial t} = sB_s \frac{\partial \omega_g}{\partial s} \boldsymbol{e}_\phi - \omega_g \left(\frac{\partial B_s}{\partial \phi} + \frac{\partial B_\phi}{\partial \phi} + \frac{\partial B_z}{\partial \phi} \right), \tag{A.5}$$

which is a second equation relating the fluid speed and the magnetic field. The two coupled equations (A.2) and (A.5) may now be used to derive the canonical part of the torsional wave equation. That is, the simplest form of the wave equation to which more complicated contributions may be added, such as coupling to the mantle or solid inner core. Roberts & Aurnou (2011) provide a thorough review of the possible coupling mechanisms between the mantle and outer and inner cores. These processes include thermal interactions, viscosity, gravity, topography and magnetic field. The authors of that study also derive solutions to the torsional wave equation in a dissipative core and discuss the various mechanical and magnetic boundary layers that affect torsional waves when core-mantle coupling mechanism are taken into account. These additional contributions will not be considered in this thesis.

We now denote the meridian field $\boldsymbol{B}_M = \boldsymbol{B} - B_\phi \boldsymbol{e}_\phi$ and note that

$$(\mu_0 \boldsymbol{J} \times \boldsymbol{B})_\phi = \frac{1}{s} \nabla \cdot (s \boldsymbol{B}_M B_\phi) + \frac{1}{s} \underbrace{\left(B_\phi \frac{\partial B_\phi}{\partial \phi} - B_s \frac{\partial B_s}{\partial \phi} - B_z \frac{\partial B_z}{\partial \phi} \right)}_{\oint \frac{\partial}{\partial \phi}(B_\phi^2 - B_s^2 - B_z^2) d\phi = 0}$$

which yields

$$\oint (\boldsymbol{J} \times \boldsymbol{B})_\phi d\phi = \frac{1}{\mu_0 s} \oint \nabla \cdot (s \boldsymbol{B}_M B_\phi) d\phi. \tag{A.6}$$

Using $\nabla \cdot (s\boldsymbol{B}_M B_\phi) = \frac{\partial}{\partial s}(s^2 B_s B_\phi) + s\frac{\partial}{\partial z}(B_z B_\phi)$ and integrating (A.6) with respect to z over the entire cylinder height gives

$$\int_{-z_T}^{+z_T} \oint (\boldsymbol{J} \times \boldsymbol{B})_\phi d\phi dz = \frac{1}{\mu_0 s} \int_z \oint \left(\underbrace{\frac{\partial}{\partial s}(s^2 B_s B_\phi)}_{\text{(a)}} + s\frac{\partial}{\partial z}(B_z \phi) \right) d\phi dz, \tag{A.7}$$

Term (a) of the above is evaluated by taking the differential operator outside the integral and using the Leibniz integral rule

$$\frac{\partial}{\partial s}\int_{-z_T}^{+z_T} (s^2 B_s B_\phi) dz = \int_{-z_T}^{+z_T} \frac{\partial}{\partial s}(s^2 B_s B_\phi) dz + \frac{\partial z_T}{\partial s}(s^2 B_s B_\phi)\Big|_{+z_T} - \frac{\partial(-z_T)}{\partial s}(s^2 B_s B_\phi)\Big|_{-z_T},$$

which gives

$$\int_{-z_T}^{+z_T} \oint (\boldsymbol{J} \times \boldsymbol{B})_\phi d\phi dz = \frac{1}{s^2 \mu_0}\frac{\partial}{\partial s}\left(s^2 \int_{-z_T}^{+z_T} \oint B_s B_\phi d\phi dz \right) + \frac{1}{\mu_0}\oint B_s B_\phi\Big|_{+z_T}\frac{\partial z_T}{\partial s} d\phi$$

$$+ \frac{1}{\mu_0}\oint B_s B_\phi\Big|_{-z_T}\frac{\partial z_T}{\partial s} d\phi + \frac{1}{\mu_0 s}\underbrace{\int_{-z_T}^{+z_T} \oint s\frac{\partial}{\partial z}(B_z B_\phi) d\phi dz}_{\text{(A)}}. \tag{A.8}$$

Term (A) in the above is

$$\int_{-z_T}^{+z_T} \oint s\frac{\partial}{\partial z}(B_z B_\phi) d\phi dz = sB_z B_\phi\Big|_{+z_T} - sB_z B_\phi\Big|_{-z_T}$$

which yields

$$\int_{-z_T}^{+z_T} \oint (\boldsymbol{J} \times \boldsymbol{B})_\phi d\phi dz = \frac{1}{s^2 \mu_0}\frac{\partial}{\partial s}\left(s^2 \int_{-z_T}^{+z_T} \oint B_s B_\phi d\phi dz \right)$$

$$+ \frac{1}{\mu_0}\oint \left(B_s B_\phi\Big|_{+z_T}\frac{\partial z_T}{\partial s} + B_s B_\phi\Big|_{-z_T}\frac{\partial z_T}{\partial s} \right) d\phi + \frac{1}{\mu_0}\oint \left(B_z B_\phi\Big|_{+z_T} - B_z B_\phi\Big|_{-z_T} \right) d\phi. \tag{A.9}$$

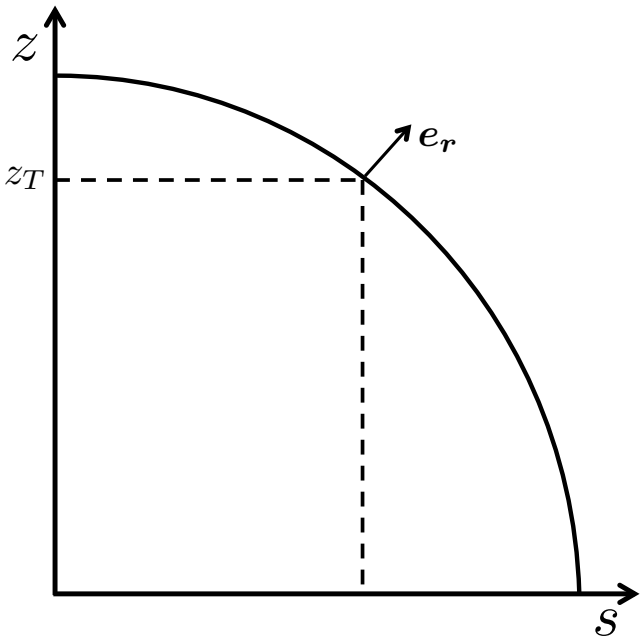

Figure A.1: Simplified geometry of the core

$$z_T = \sqrt{r_c^2 - s^2} \tag{A.10}$$

$$\frac{\partial z_T}{\partial s} = \frac{-s}{\sqrt{r_c^2 - s^2}} = \frac{-s}{z_T} \tag{A.11}$$

$$B_r = \boldsymbol{e}_r \cdot \boldsymbol{B} = \frac{s}{r_c} B_s + \frac{z}{r_c} B_z \tag{A.12}$$

$$r_c B_r(+z_T) = s B_s + z_T B_z \tag{A.13}$$

$$r_c B_r(-z_T) = s B_s - z_T B_z \tag{A.14}$$

Equation (A.9) may now be rewritten using equations (A.11), (A.13) and (A.14)

$$\int_{-z_T}^{+z_T} \oint (\boldsymbol{J} \times \boldsymbol{B})_\phi d\phi dz = \frac{1}{s^2 \mu_0} \frac{\partial}{\partial s} \left(s^2 \int_{-z_T}^{+z_T} \oint B_s B_\phi d\phi dz \right)$$

$$+ \frac{1}{\mu_0} \oint \left(B_s B_\phi \Big|_{+z_T} \frac{\partial z_T}{\partial s} + B_z B_\phi \Big|_{+z_T} \right.$$

$$\left. + B_s B_\phi \Big|_{-z_T} \frac{\partial z_T}{\partial s} - B_z B_\phi \Big|_{-z_T} \right) d\phi$$

with the second integral on the right-hand side

$$\frac{B_\phi}{z_T} \underbrace{(s B_s + z B_z)}_{B_r} \Big|_{z_T} + \frac{B_\phi}{z_T} \underbrace{(s B_s - z B_z)}_{B_r} \Big|_{-z_T}$$

simplifying to give

$$\int_{-z_T}^{+z_T} \oint (\boldsymbol{J} \times \boldsymbol{B})_\phi d\phi dz = \frac{1}{s^2 \mu_0} \frac{\partial}{\partial s} \left(s^2 \int_{-z_T}^{+z_T} \oint B_s B_\phi d\phi dz \right)$$

$$+ \frac{1}{\mu_0} \oint \left(\frac{B_r B_\phi}{z_T} \bigg|_{z_T} + \frac{B_r B_\phi}{z_T} \bigg|_{-z_T} \right) d\phi, \tag{A.15}$$

where the radial magnetic field component, B_r, is defined using the geometry in Fig. A.1. We now introduce a perturbation $\boldsymbol{b}$ to the background magnetic field $\boldsymbol{B}$ such that the total field, previously denoted $\boldsymbol{B}$, is now $\boldsymbol{B} + \boldsymbol{b}$. Differentiating (A.15) with respect to time and considering that the background field is constant over the short periods of interest (much less than the magnetic diffusion time), equation (A.15) becomes

$$\frac{\partial}{\partial t} \int_{-z_T}^{+z_T} \oint (\boldsymbol{J} \times \boldsymbol{B})_\phi d\phi dz = \frac{1}{s^2 \mu_0} \frac{\partial}{\partial s} \left(s^2 \int_{-z_T}^{+z_T} \oint \underbrace{\left(B_s \frac{\partial b_\phi}{\partial t} + \frac{\partial b_s}{\partial t} B_\phi \right)}_{\text{(a)}} d\phi dz \right)$$

$$+ \frac{1}{\mu_0 z_T} \oint \left(\left(B_r \frac{\partial b_\phi}{\partial t} + \frac{\partial b_r}{\partial t} B_\phi \right) \bigg|_{+z_T} \right.$$

$$\left. + \left(B_r \frac{\partial b_\phi}{\partial t} + \frac{\partial b_r}{\partial t} B_\phi \right) \bigg|_{-z_T} \right) d\phi. \tag{A.16}$$

Term (a) is calculated using the frozen-flux form of the induction equation for the perturbation $\boldsymbol{b}$

$$\frac{\partial \boldsymbol{b}}{\partial t} = \nabla \times (\boldsymbol{u} \times \boldsymbol{B}), \tag{A.17}$$

assuming that the velocity perturbations are small and that the background flow is zero.

$$B_s \frac{\partial b_\phi}{\partial t} + \frac{\partial b_s}{\partial t} B_\phi = s B_s^2 \frac{\partial \omega_g}{\partial s} - \omega_g \underbrace{\left(B_s \frac{\partial B_\phi}{\partial \phi} + B_\phi \frac{\partial B_s}{\partial \phi} \right)}_{\oint \frac{\partial}{\partial \phi} (B_s B_\phi) d\phi = 0.} = s B_s^2 \frac{\partial \omega_g}{\partial s} \tag{A.18}$$

Substituting the above into (A.16) gives the equation

$$\frac{\partial}{\partial t}\int_{-z_T}^{+z_T}\oint(\boldsymbol{J}\times\boldsymbol{B})_\phi d\phi dz = \frac{1}{s^2\mu_0}\frac{\partial}{\partial s}\left(s^2\int_{-z_T}^{+z_T}\oint\left(sB_s^2\frac{\partial\omega_g}{\partial s}\right)d\phi dz\right)$$

$$+\frac{1}{\mu_0 z_T}\oint\left(\left(B_r\frac{\partial b_\phi}{\partial t}+\frac{\partial b_r}{\partial t}B_\phi\right)\Big|_{+z_T}+\left(B_r\frac{\partial b_\phi}{\partial t}+\frac{\partial b_r}{\partial t}B_\phi\right)\Big|_{-z_T}\right)d\phi \tag{A.19}$$

which may then be simplified by introducing the notation $\{B_s^2\}=\frac{1}{4\pi z_T}\int_{-z_T}^{+z_T}\oint B_s^2 d\phi dz$,

$$\frac{\partial}{\partial t}\int_{-z_T}^{+z_T}\oint(\boldsymbol{J}\times\boldsymbol{B})_\phi d\phi dz = \frac{4\pi}{s^2\mu_0}\frac{\partial}{\partial s}\left(s^3 z_T\frac{\partial\omega_g}{\partial s}\{B_s^2\}\right)$$

$$+\frac{1}{\mu_0 z_T}\oint\left(\left(B_r\frac{\partial b_\phi}{\partial t}+\frac{\partial b_r}{\partial t}B_\phi\right)\Big|_{+z_T}+\left(B_r\frac{\partial b_\phi}{\partial t}+\frac{\partial b_r}{\partial t}B_\phi\right)\Big|_{-z_T}\right)d\phi. \tag{A.20}$$

Substituting equation (A.2) into the LHS of the above equation gives the 1-D torsional wave equation coupling the angular speed and the magnetic field

$$\frac{\partial^2\omega_g}{\partial t^2} = \frac{1}{s^3\mu_0\rho_0 z_T}\frac{\partial}{\partial s}\left(s^3 z_T\{B_s^2\}\frac{\partial\omega_g}{\partial s}\right)$$

$$+\frac{1}{\mu_0 z_T}\oint\left(\left(B_r\frac{\partial b_\phi}{\partial t}+\frac{\partial b_r}{\partial t}B_\phi\right)\Big|_{+z_T}+\left(B_r\frac{\partial b_\phi}{\partial t}+\frac{\partial b_r}{\partial t}B_\phi\right)\Big|_{-z_T}\right)d\phi. \tag{A.21}$$

For an electrically insulating mantle, the second term on the RHS is thought to be small due to the cancellation of different harmonics of $\boldsymbol{B}$ and $\boldsymbol{b}$ during the integration in ϕ and is therefore usually neglected in numerical studies of torsional waves in Earth's core (Légaut, 2005). Although, Roberts & Aurnou (2011) and Légaut (2005) have verified its small magnitude for all magnetic fields used in their work, there appears to be no mathematical proof that this term may always be neglected. According to Roberts & Aurnou (2011), if the second term on the RHS of (A.21) were not negligibly small but nevertheless omitted from numerical studies, the angular momentum of the core would not be conserved in the models. With this in mind, we will follow other works in using the 'canonical' torsional wave equation, which includes only the first term on the RHS of (A.21). We will subsequently verify the conservation of angular momentum in our torsional wave models, which should provide some *a posteriori* justification for the omission of the additional terms.

Appendix B

Synthetic SV series and jerk results

Figure B.1 shows the z component of the SV signal recorded at each of the 24 observatories shown in Fig. 4.9, evaluated at the CMB radius, when the torsional wave scalings are chosen to be consistent with Gillet et al. (2010). Time (in yr) is on the horizontal axis, the SV (in nT/yr) is on the vertical axis and the observatory name is at the top of each subfigure. Figures B.2 to B.10 show the results of applying the jerk detection method of Brown et al. (2013) to the synthetic SV data generated by torsional waves with a 60 yr core transit time and an initial pulse amplitude of 4 km/yr. The figures are organised first by window length (5, 10, 15 and 20 yr) and then by SV component (x, y and z). The top panel of these figures shows a time series of a single component of the SV signal (in nT/yr) at a particular observatory throughout the 200 years of the torsional wave forward model. The observatory name and the window length are displayed at the top of the figure, and any identified jerk events are shown as a red 'V' shape fitted to the synthetic SV series. The bottom panel shows the calculated PDF from the two-part linear regression, with the chosen threshold cut-off value shown as a green line, and the positive and negative errors on the PDF are filled in underneath the PDF curve in red and black respectively. As described in Brown et al. (2013), the PDF values are normalised to a value of one across the entire window to account for any jerk events being identified in several windows during the sliding regression. For narrow PDF curves, the values of the PDF are very high (>100) because the regression is attempting to normalise the area of a spike.

(a)

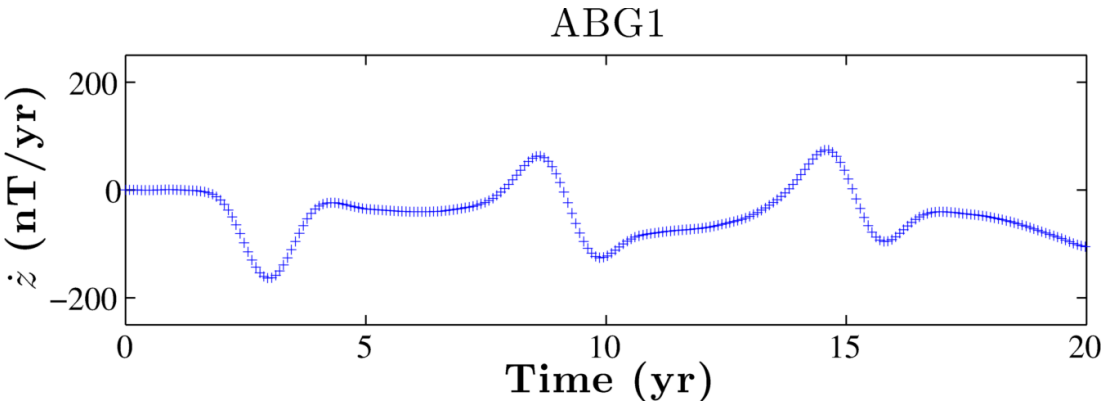
ABG1
200
0
−200
$\dot{z}$ (nT/yr)
0
5
10
15
20
Time (yr)

(b)

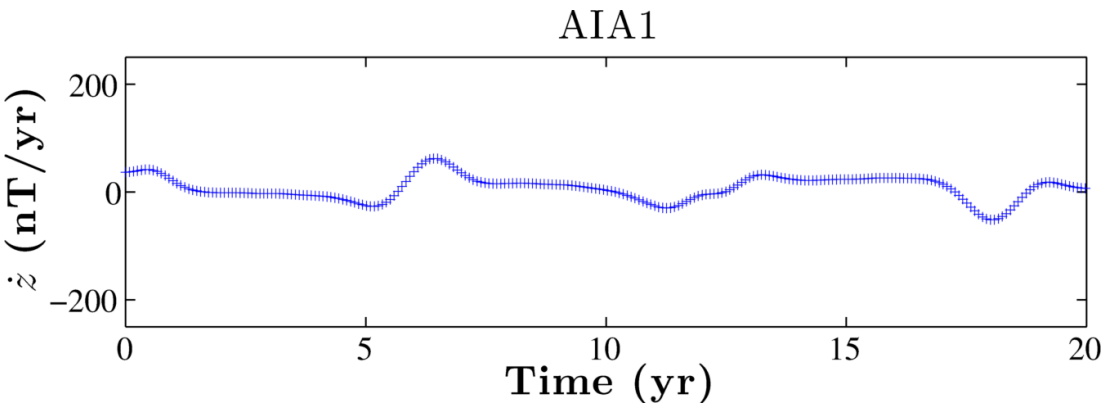
AIA1
200
0
−200
$\dot{z}$ (nT/yr)
0
5
10
15
20
Time (yr)

(c)

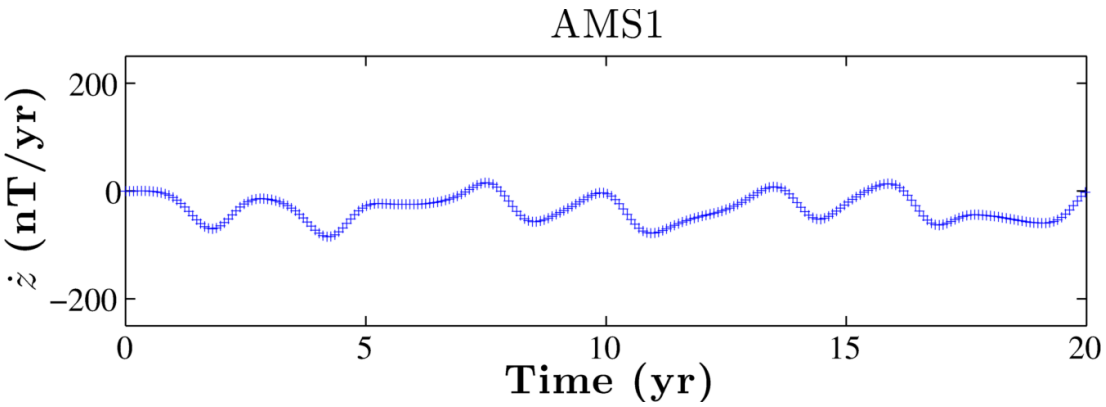
AMS1
200
0
−200
$\dot{z}$ (nT/yr)
0
5
10
15
20
Time (yr)

(d)

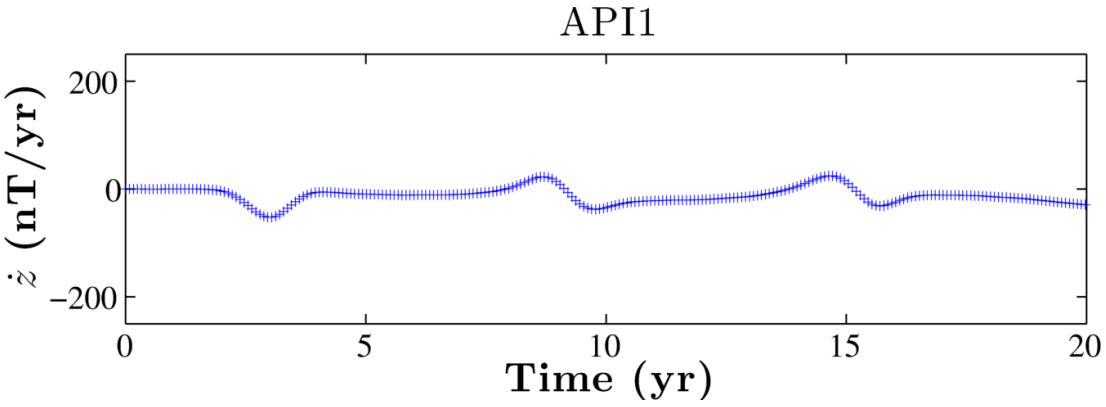
API1
200
0
−200
$\dot{z}$ (nT/yr)
0
5
10
15
20
Time (yr)

(a)

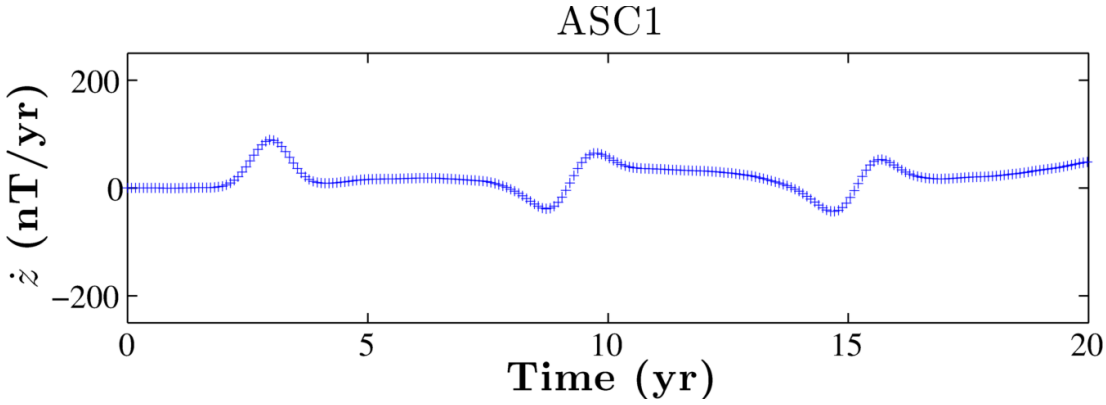
ASC1
200
0
−200
$\dot{z}$ (nT/yr)
0
5
10
15
20
Time (yr)

(b)

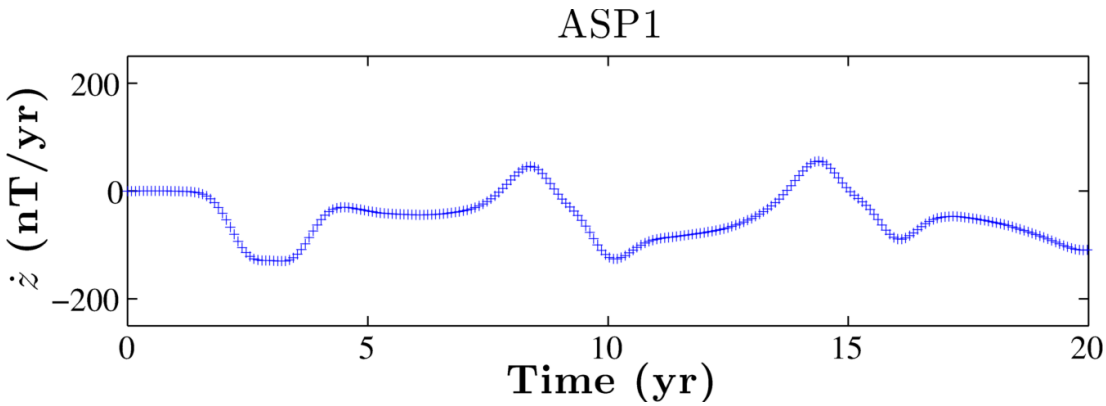
ASP1
200
0
−200
$\dot{z}$ (nT/yr)
0
5
10
15
20
Time (yr)

(c)

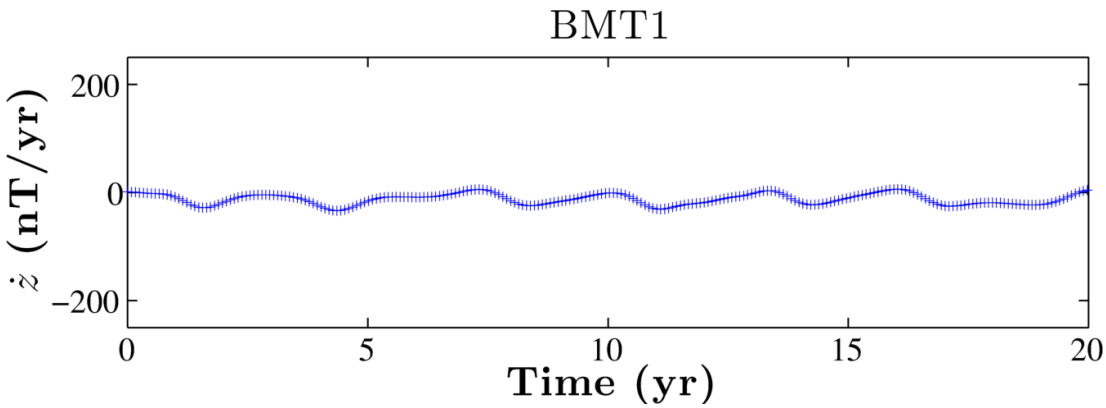
BMT1
200
0
−200
$\dot{z}$ (nT/yr)
0
5
10
15
20
Time (yr)

(d)

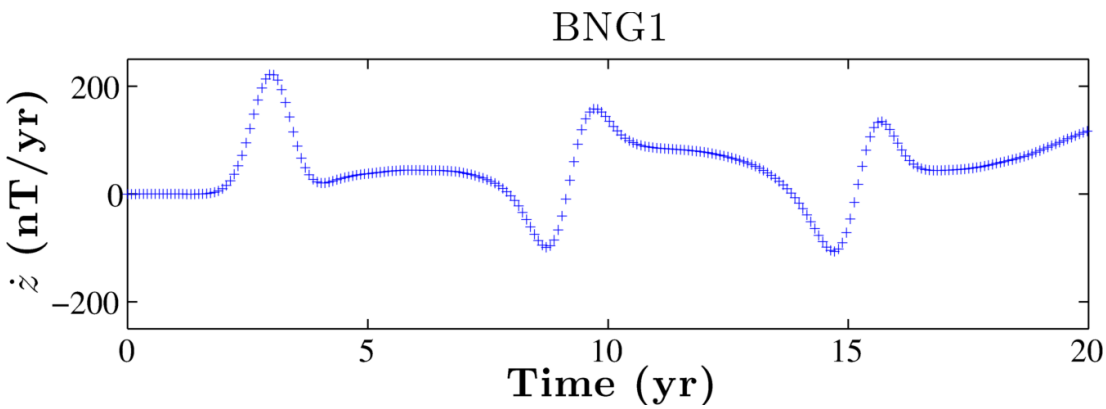
BNG1
200
0
−200
$\dot{z}$ (nT/yr)
0
5
10
15
20
Time (yr)

(a)

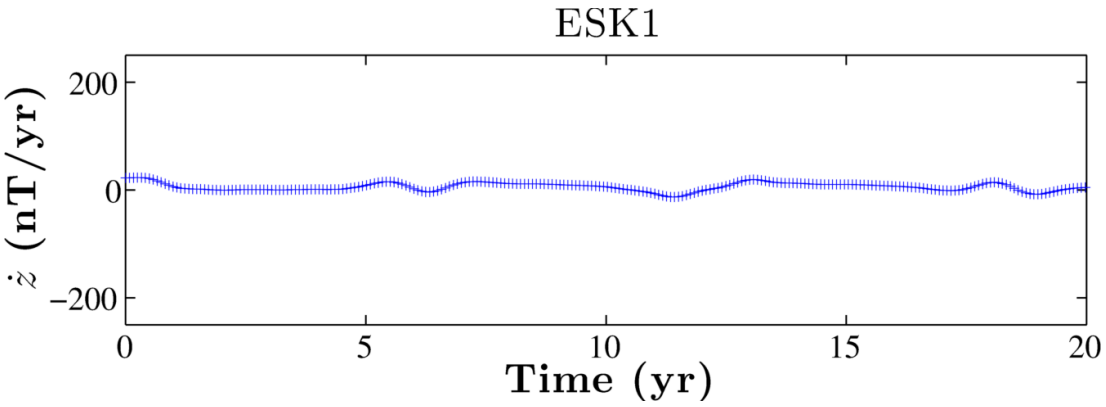
ESK1
200
0
−200
$\dot{z}$ (nT/yr)
0
5
10
15
20
Time (yr)

(b)

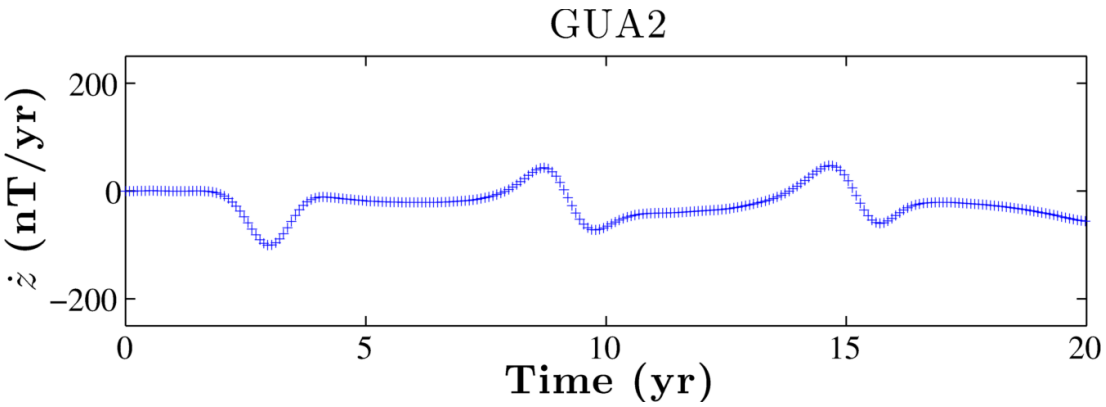
GUA2
200
0
−200
$\dot{z}$ (nT/yr)
0
5
10
15
20
Time (yr)

(c)

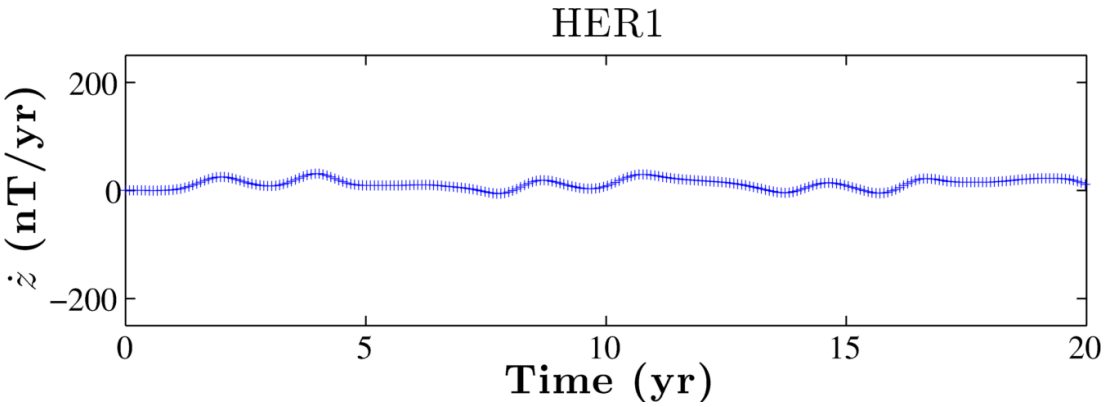
HER1
200
0
−200
$\dot{z}$ (nT/yr)
0
5
10
15
20
Time (yr)

(d)

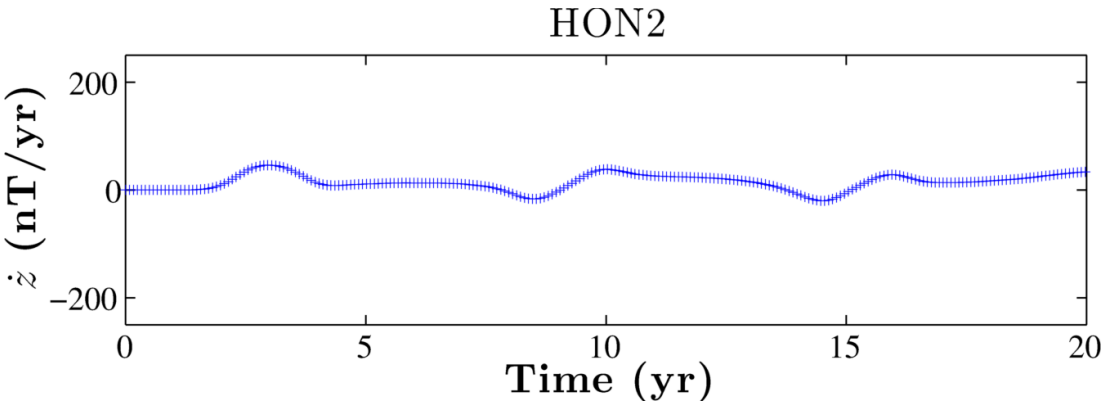
HON2
200
0
−200
$\dot{z}$ (nT/yr)
0
5
10
15
20
Time (yr)

(a)

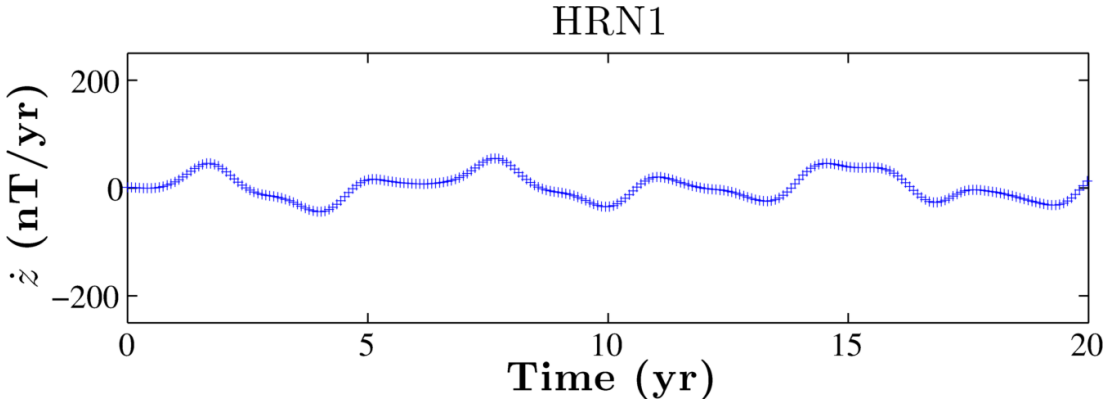
HRN1
200
0
−200
$\dot{z}$ (nT/yr)
0
5
10
15
20
Time (yr)

(b)

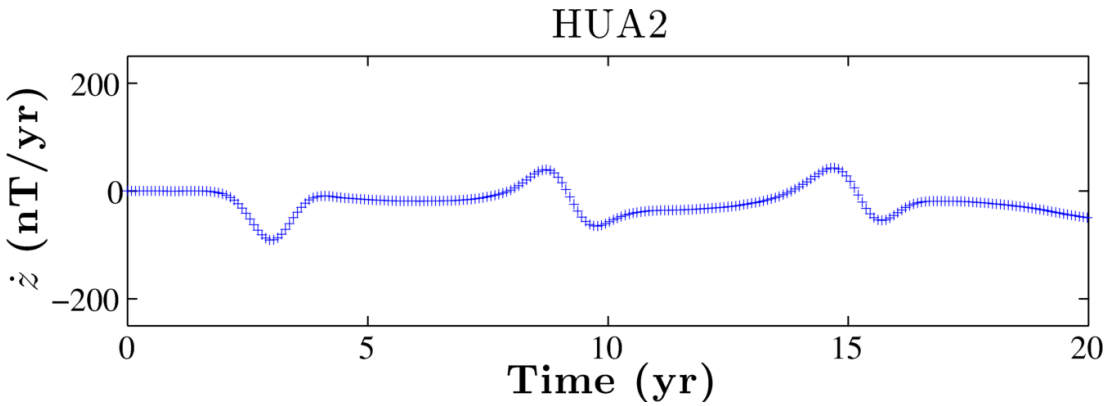
HUA2
200
0
−200
$\dot{z}$ (nT/yr)
0
5
10
15
20
Time (yr)

(c)

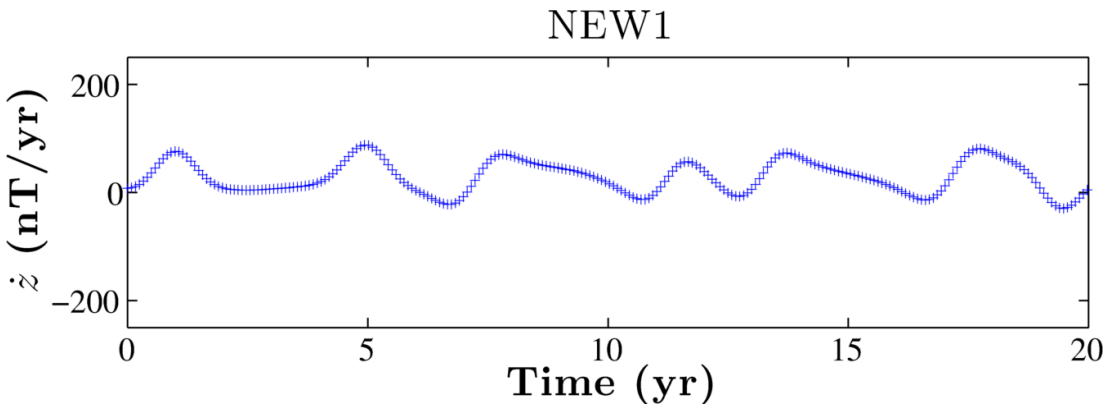
NEW1
200
0
−200
$\dot{z}$ (nT/yr)
0
5
10
15
20
Time (yr)

(d)

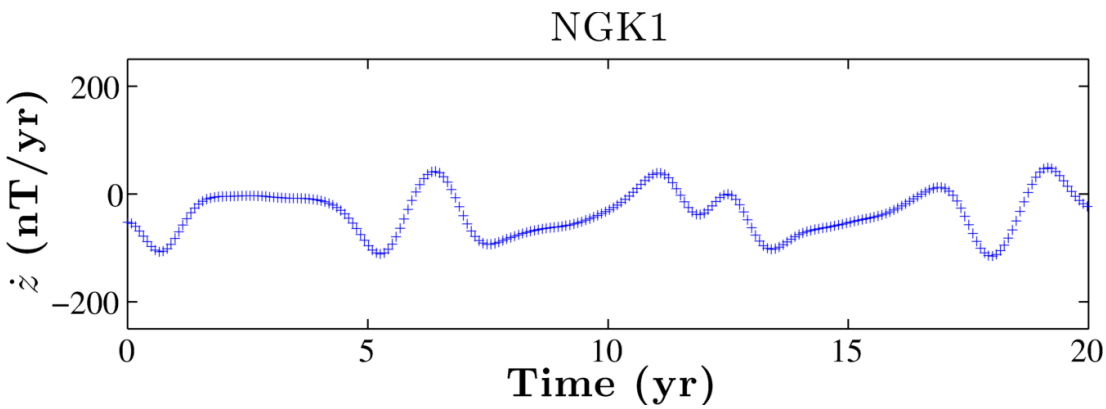
NGK1
200
0
−200
$\dot{z}$ (nT/yr)
0
5
10
15
20
Time (yr)

(a)

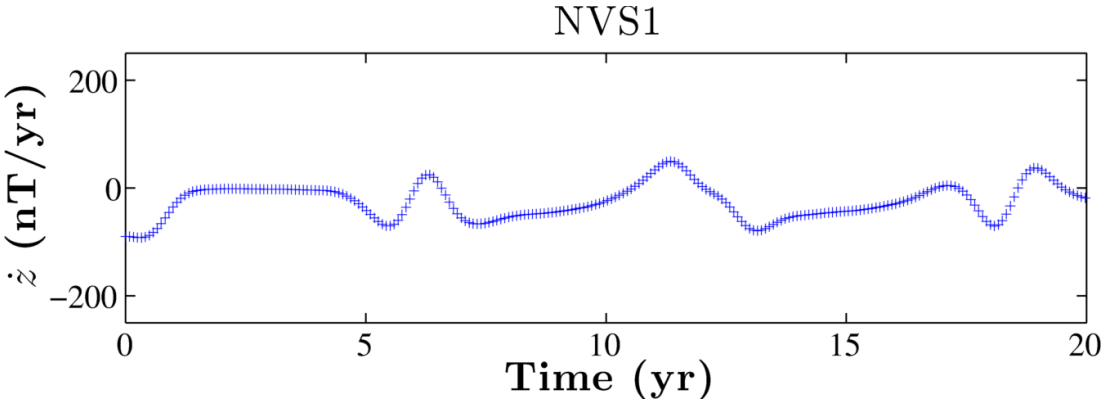
NVS1
200
0
−200
$\dot{z}$ (nT/yr)
0
5
10
15
20
Time (yr)

(b)

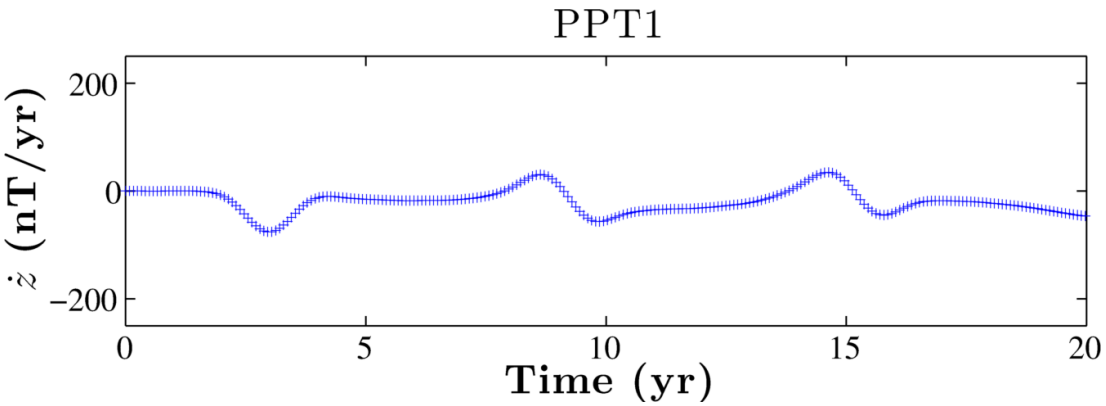
PPT1
200
0
−200
$\dot{z}$ (nT/yr)
0
5
10
15
20
Time (yr)

(c)

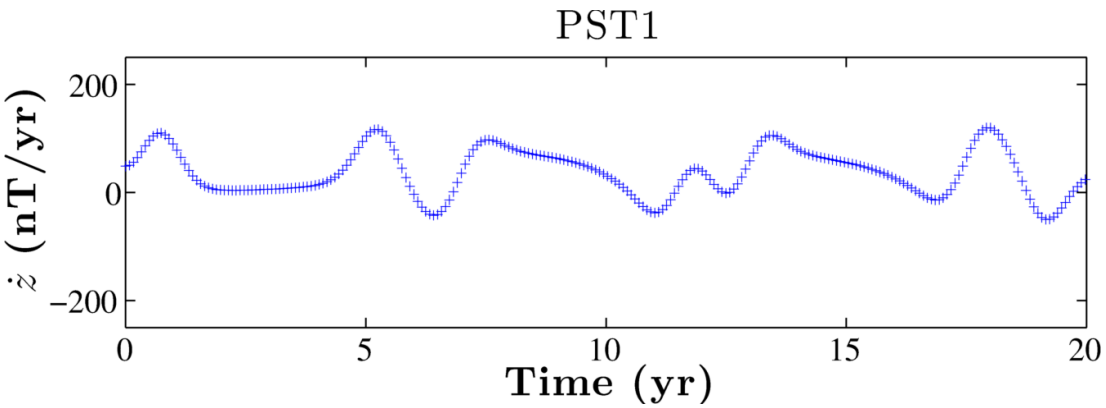
PST1
200
0
−200
$\dot{z}$ (nT/yr)
0
5
10
15
20
Time (yr)

(d)

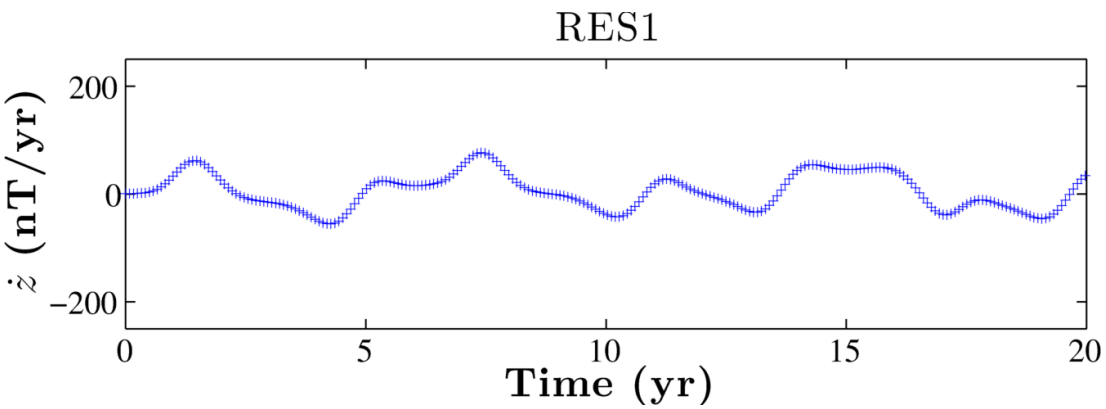
RES1
200
0
−200
$\dot{z}$ (nT/yr)
0
5
10
15
20
Time (yr)

(a)

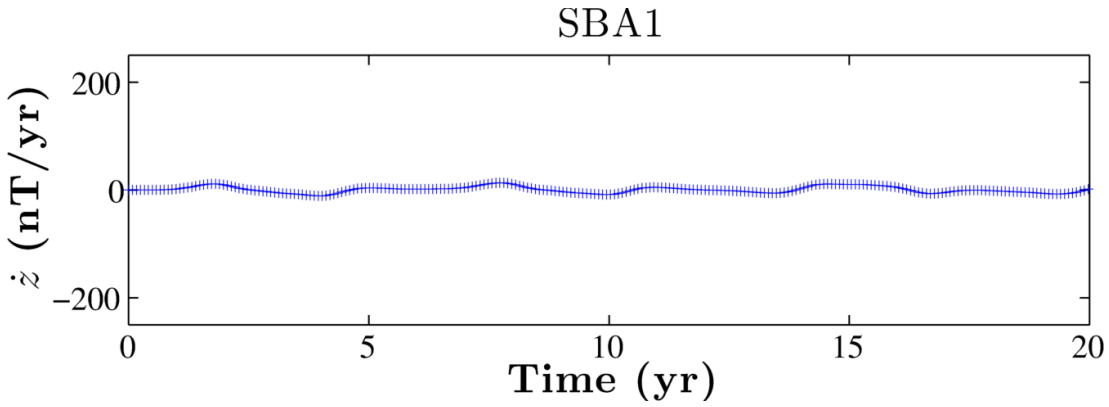
SBA1
200
0
−200
$\dot{z}$ (nT/yr)
0
5
10
15
20
Time (yr)

(b)

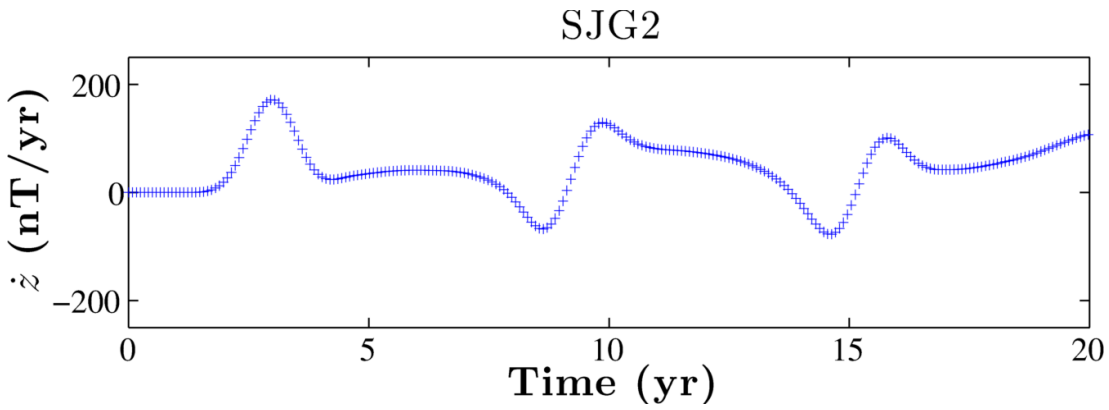
SJG2
200
0
−200
$\dot{z}$ (nT/yr)
0
5
10
15
20
Time (yr)

(c)

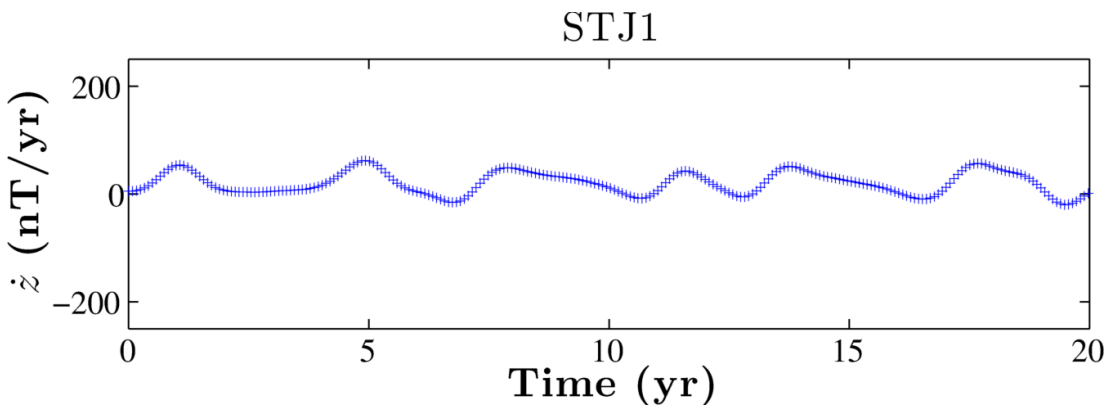
STJ1
200
0
−200
$\dot{z}$ (nT/yr)
0
5
10
15
20
Time (yr)

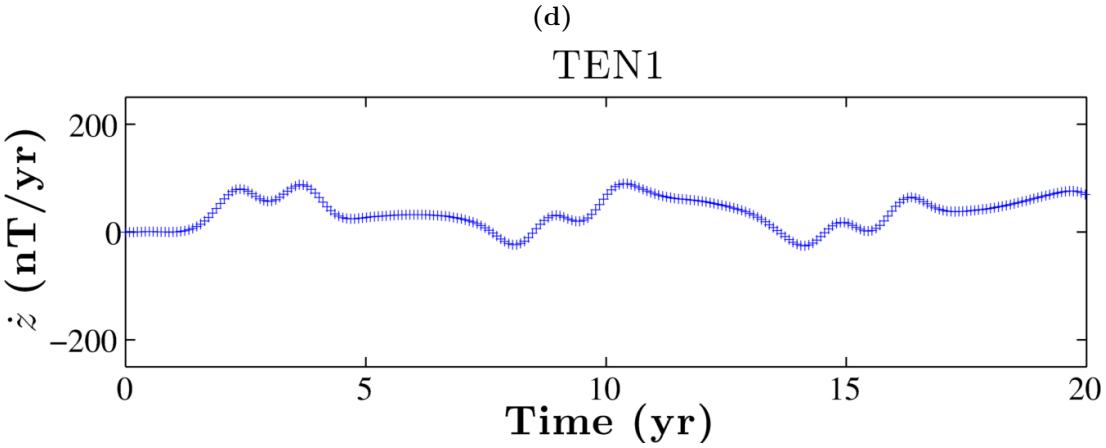

Figure B.6: The z component of the SV induced at the CMB by torsional waves with a 6 yr core transit time and an initial pulse amplitude of 0.4 km/yr. Time is on the horizontal axis, SV is on the vertical axis and the observatory name is at the top of each subfigure. The locations of the observatories are shown in Fig. 4.9.

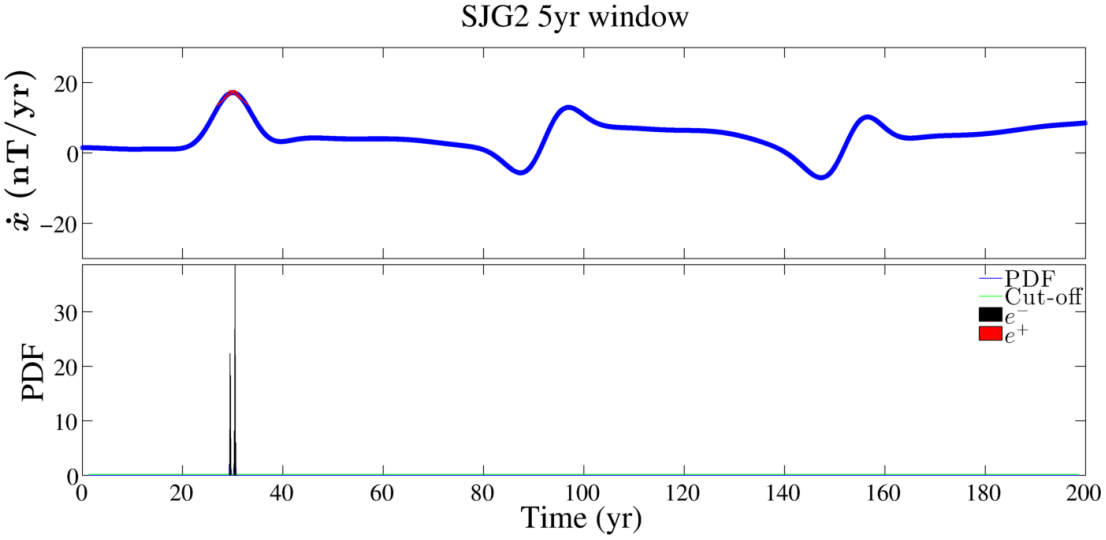

Figure B.7: Jerk identification in the $\dot{x}$ component at Earth's surface with a 5 yr window.

(a)

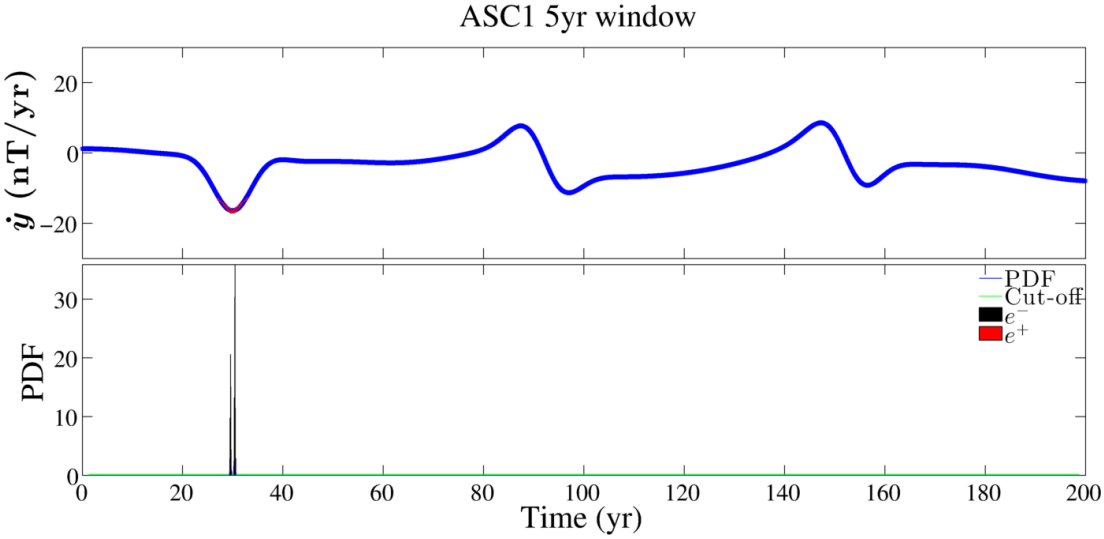
ASC1 5yr window
$\dot{y}$ (nT/yr)
PDF
Time (yr)
PDF
Cut-off
e^-
e^+

(b)

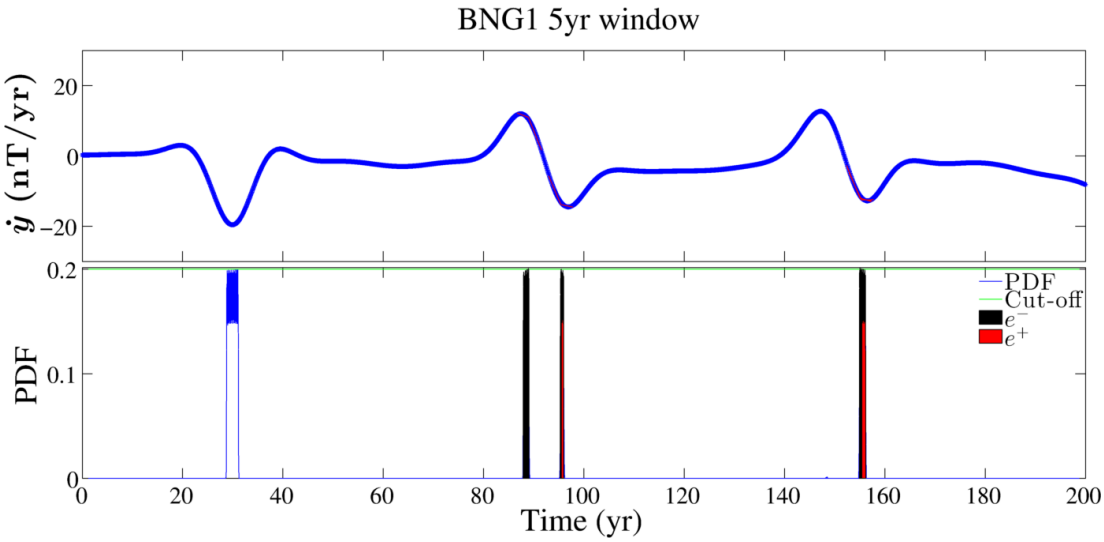
BNG1 5yr window
$\dot{y}$ (nT/yr)
PDF
Time (yr)
PDF
Cut-off
e^-
e^+

(c)

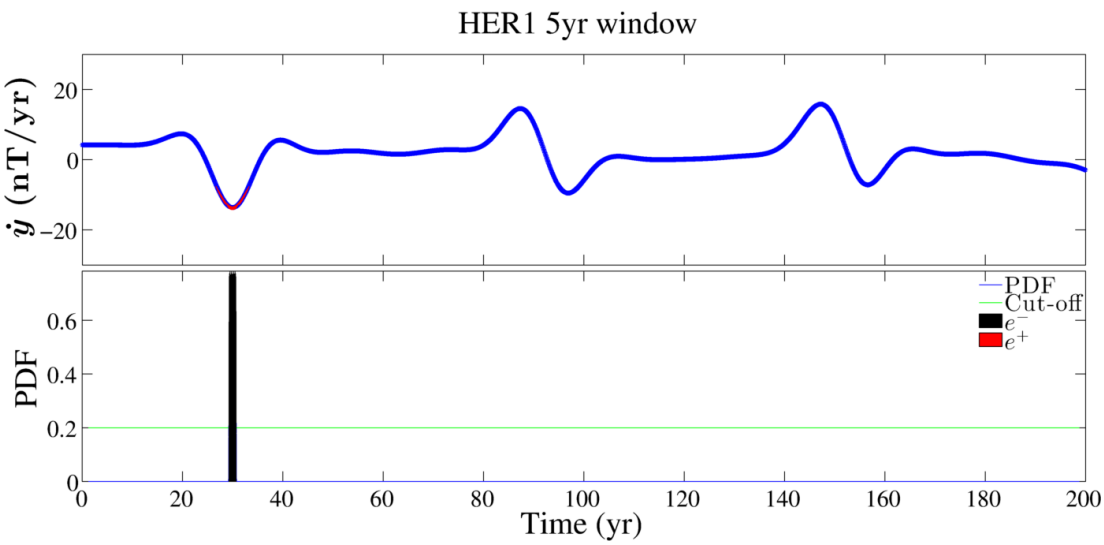
HER1 5yr window
$\dot{y}$ (nT/yr)
PDF
Time (yr)
PDF
Cut-off
e^-
e^+

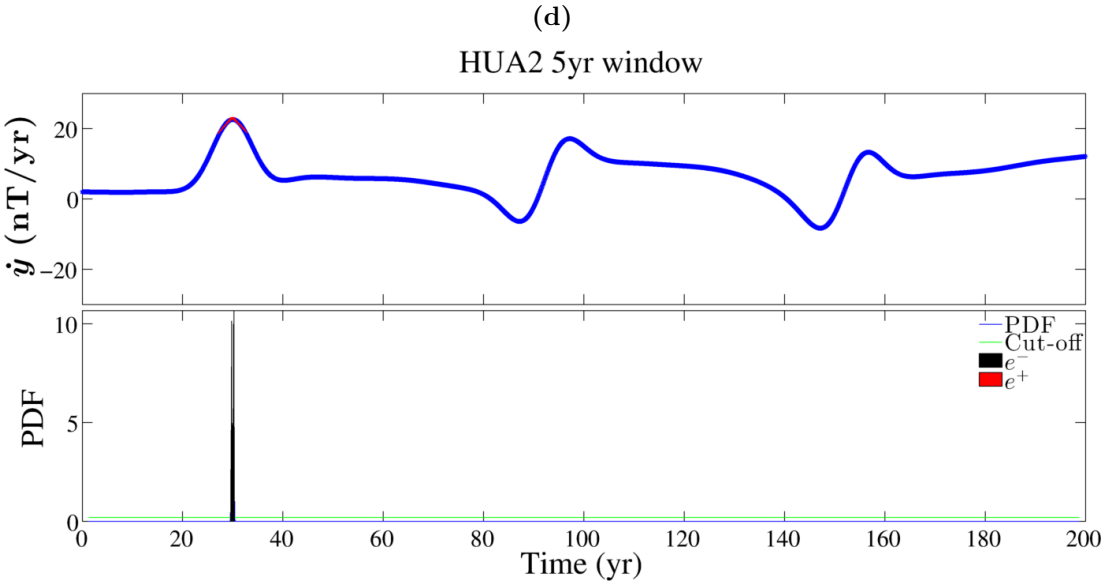

Figure B.8: Jerk identification in the $\dot{y}$ component at Earth's surface with a 5 yr window.

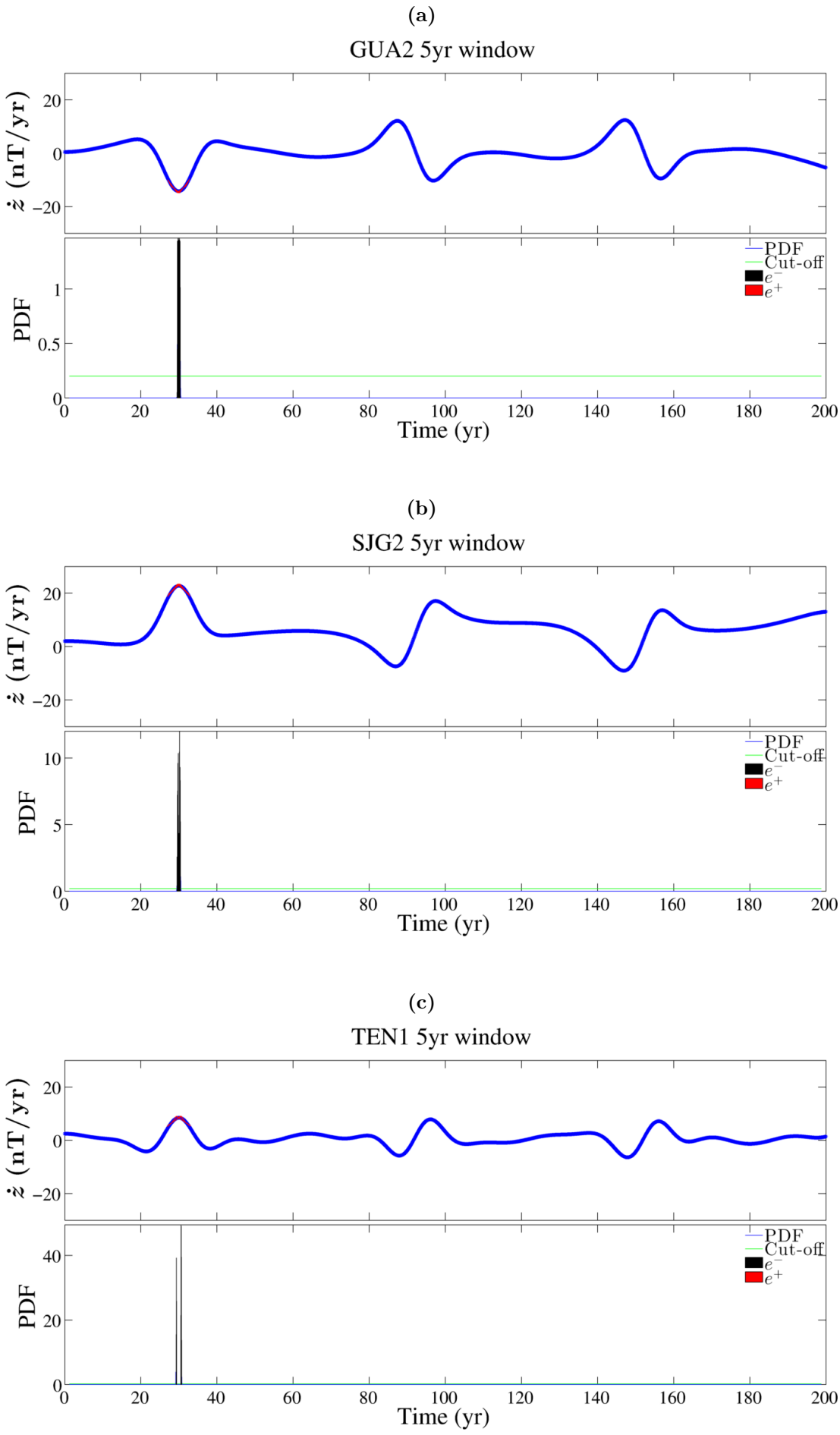

Figure B.9: Jerk identification in the $\dot{z}$ at Earth's surface component with a 5 yr window.

(a)

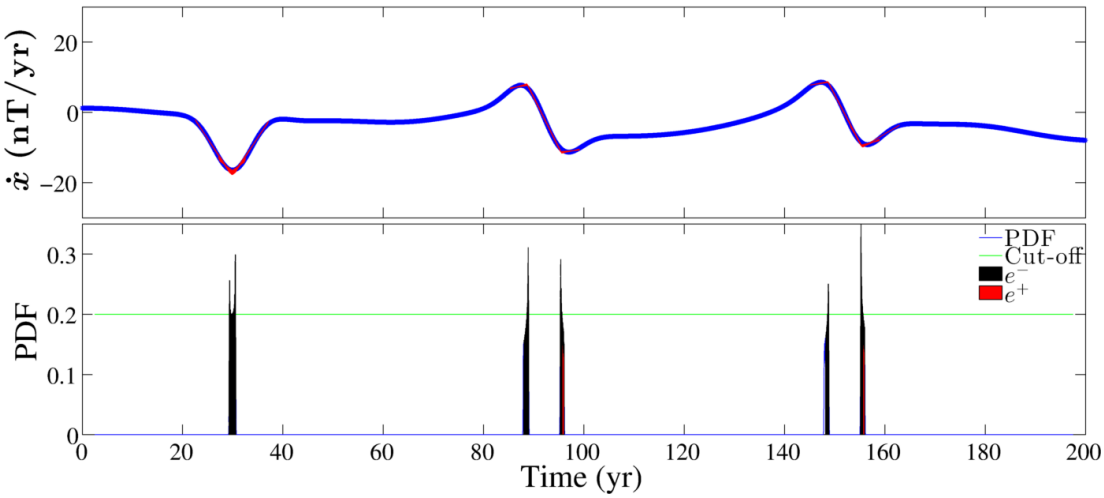
ASC1 10yr window
$\dot{x}$ (nT/yr)
PDF
Cut-off
e^-
e^+
Time (yr)

(b)

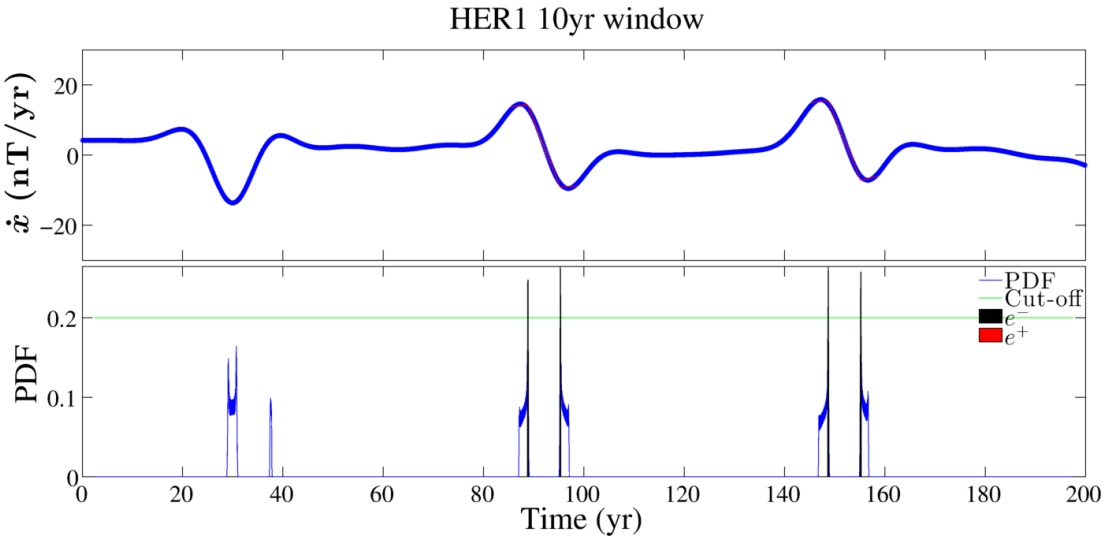
HER1 10yr window
$\dot{x}$ (nT/yr)
PDF
Cut-off
e^-
e^+
Time (yr)

(c)

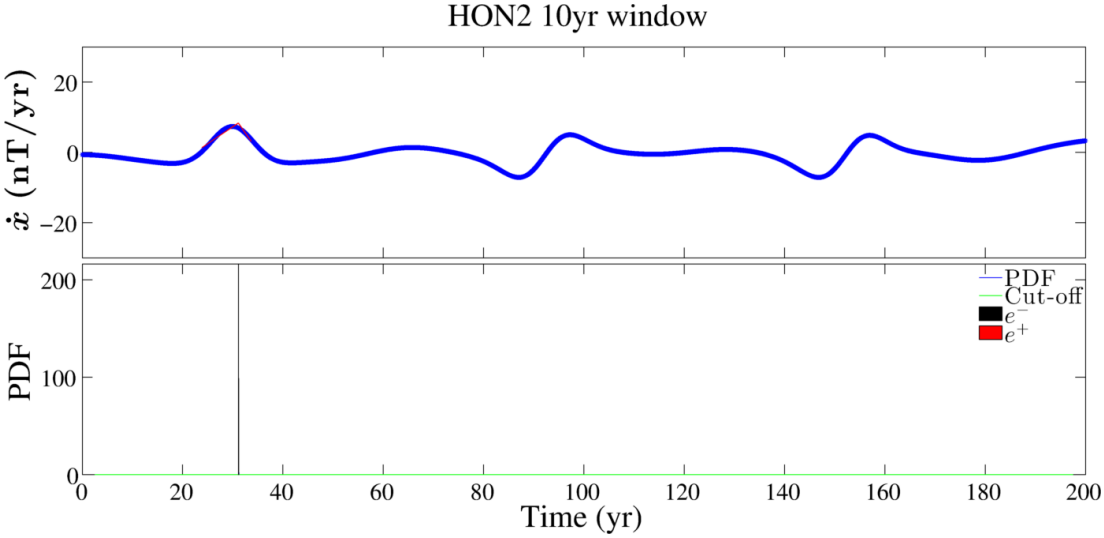
HON2 10yr window
$\dot{x}$ (nT/yr)
PDF
Cut-off
e^-
e^+
Time (yr)

(a)

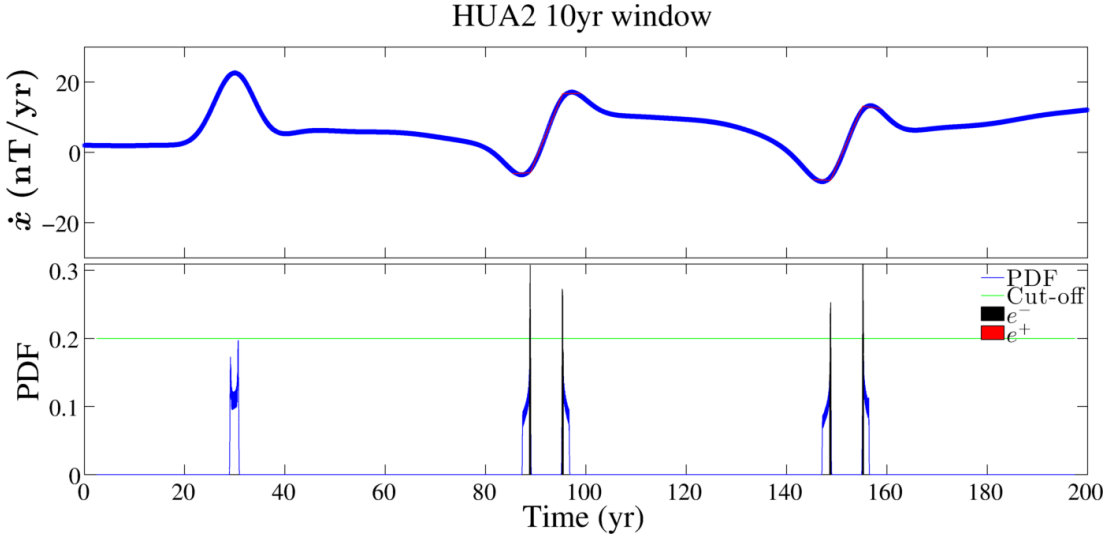
HUA2 10yr window
$\dot{x}$ (nT/yr)
PDF
Time (yr)
PDF
Cut-off
e^-
e^+

(b)

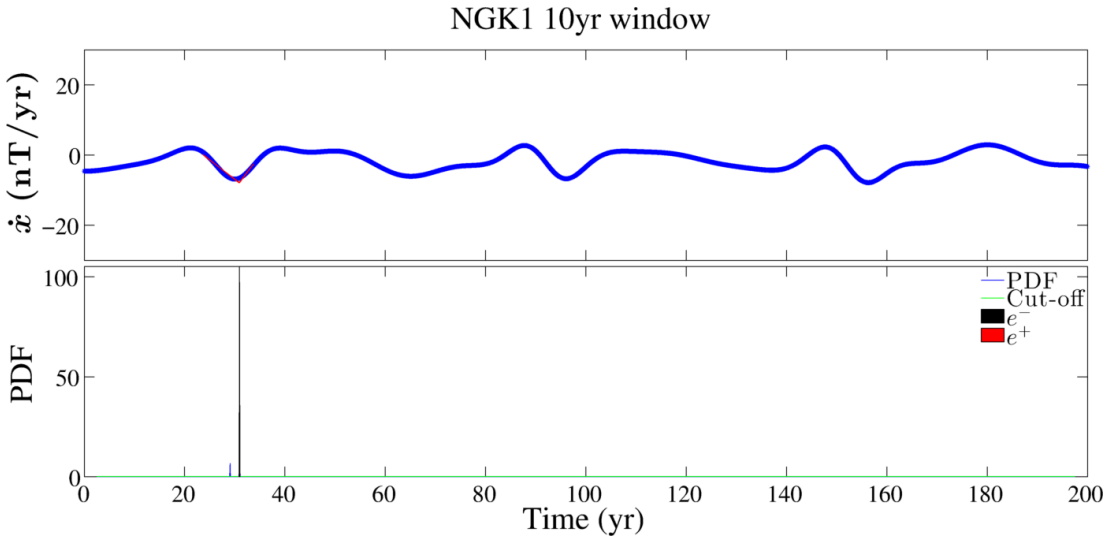
NGK1 10yr window
$\dot{x}$ (nT/yr)
PDF
Time (yr)
PDF
Cut-off
e^-
e^+

(c)

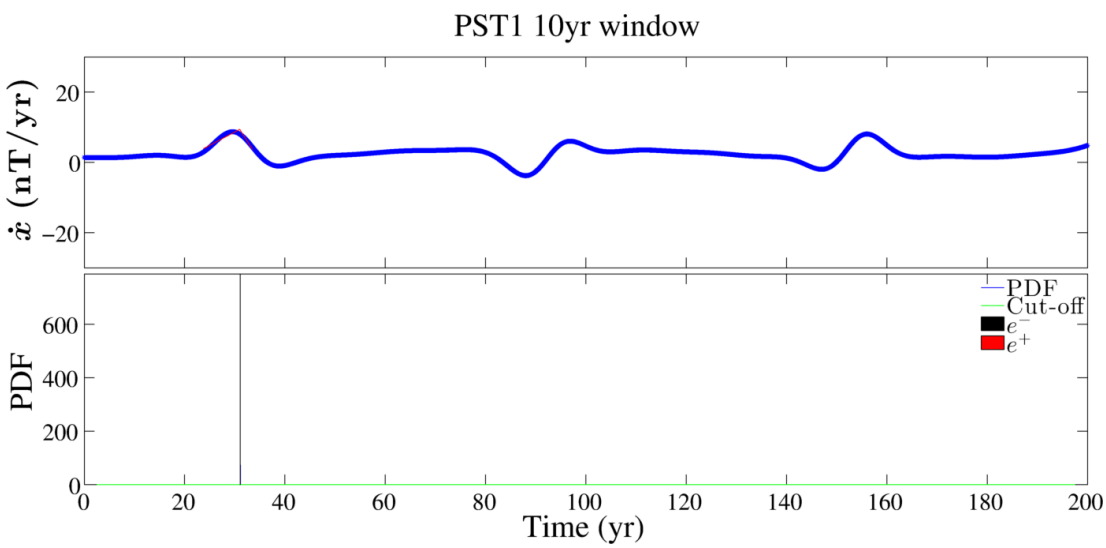
PST1 10yr window
$\dot{x}$ (nT/yr)
PDF
Time (yr)
PDF
Cut-off
e^-
e^+

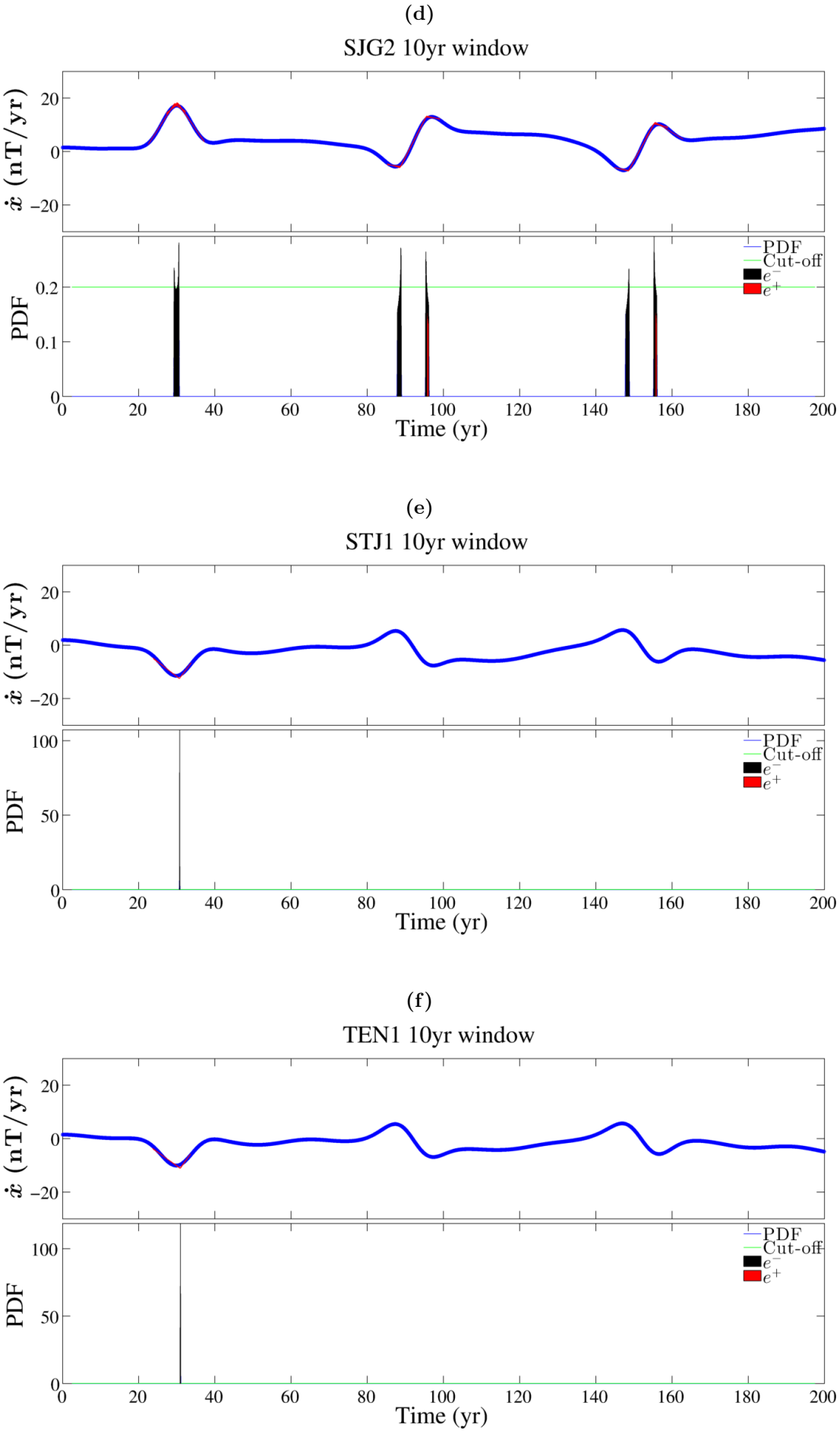

Figure B.11: Jerk identification in the $\dot{x}$ component at Earth's surface with a 10 yr window.

(a)

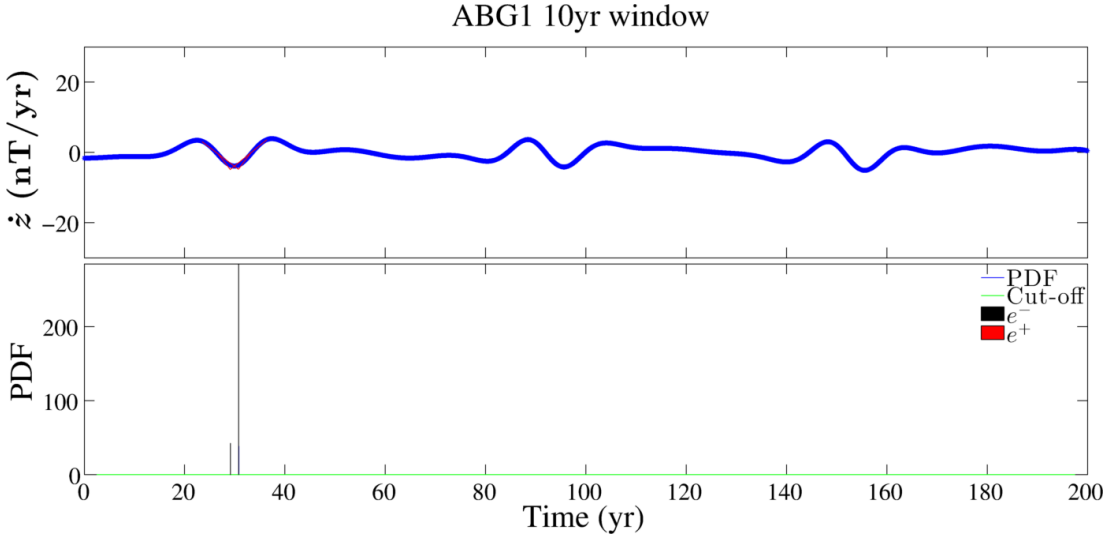
ABG1 10yr window
$\dot{z}$ (nT/yr)
PDF
Cut-off
e^-
e^+
Time (yr)

(b)

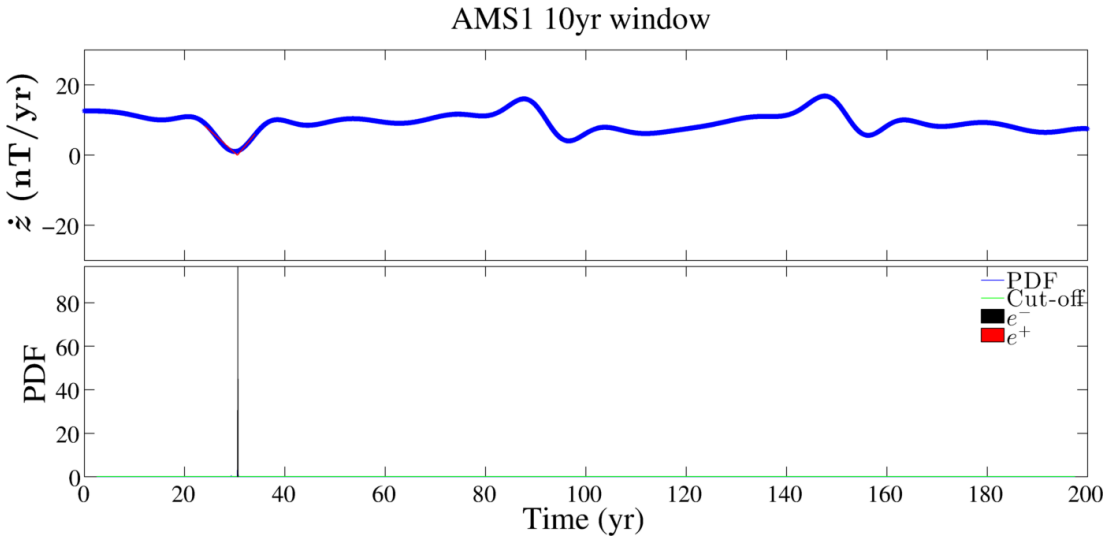
AMS1 10yr window
$\dot{z}$ (nT/yr)
PDF
Cut-off
e^-
e^+
Time (yr)

(c)

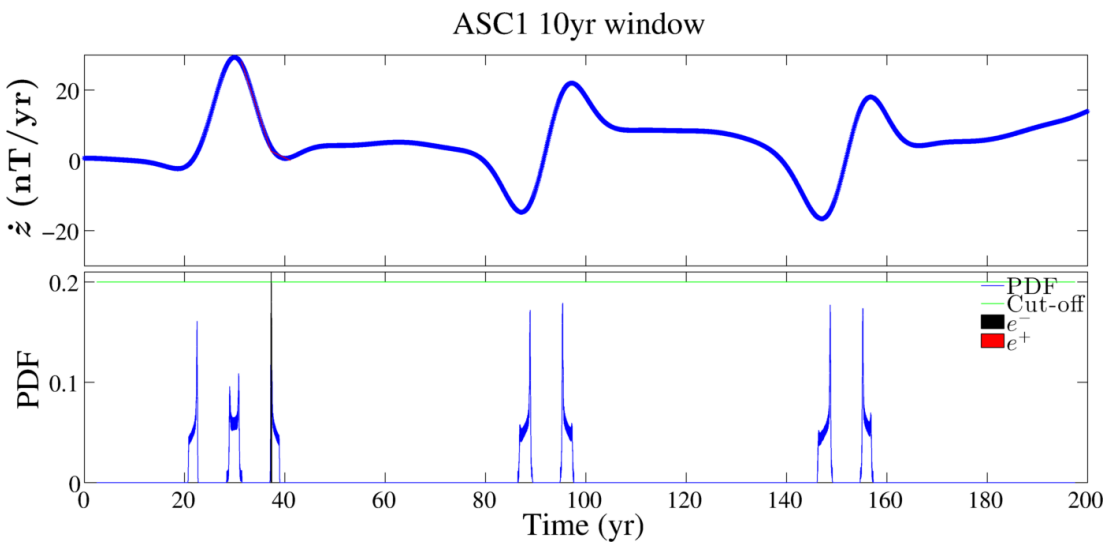
ASC1 10yr window
$\dot{z}$ (nT/yr)
PDF
Cut-off
e^-
e^+
Time (yr)

(a)

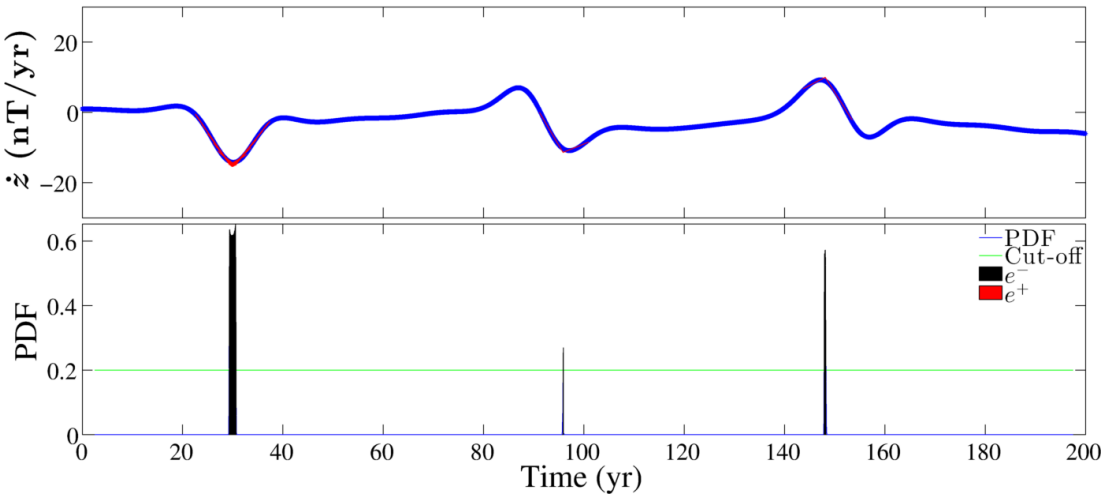
ASP1 10yr window
$\dot{z}$ (nT/yr)
PDF
PDF
Cut-off
e^-
e^+
Time (yr)

(b)

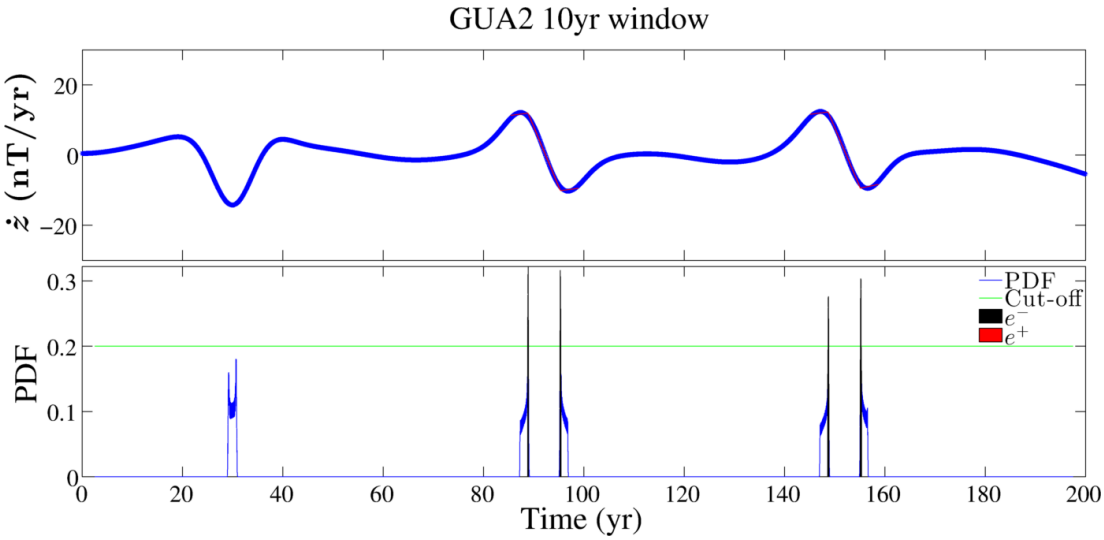
GUA2 10yr window
$\dot{z}$ (nT/yr)
PDF
PDF
Cut-off
e^-
e^+
Time (yr)

(c)

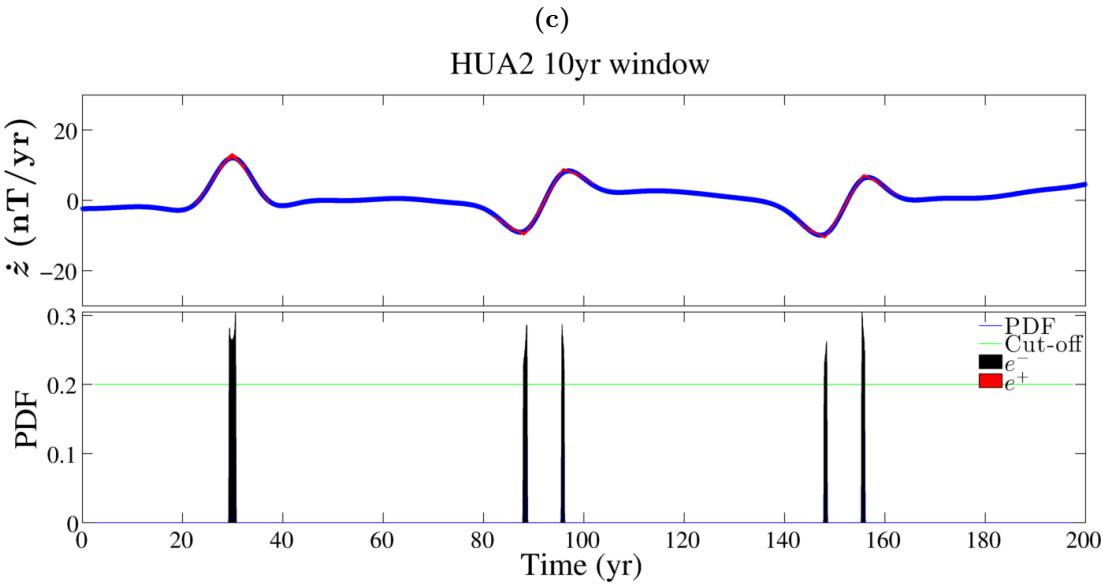
HUA2 10yr window
$\dot{z}$ (nT/yr)
PDF
PDF
Cut-off
e^-
e^+
Time (yr)

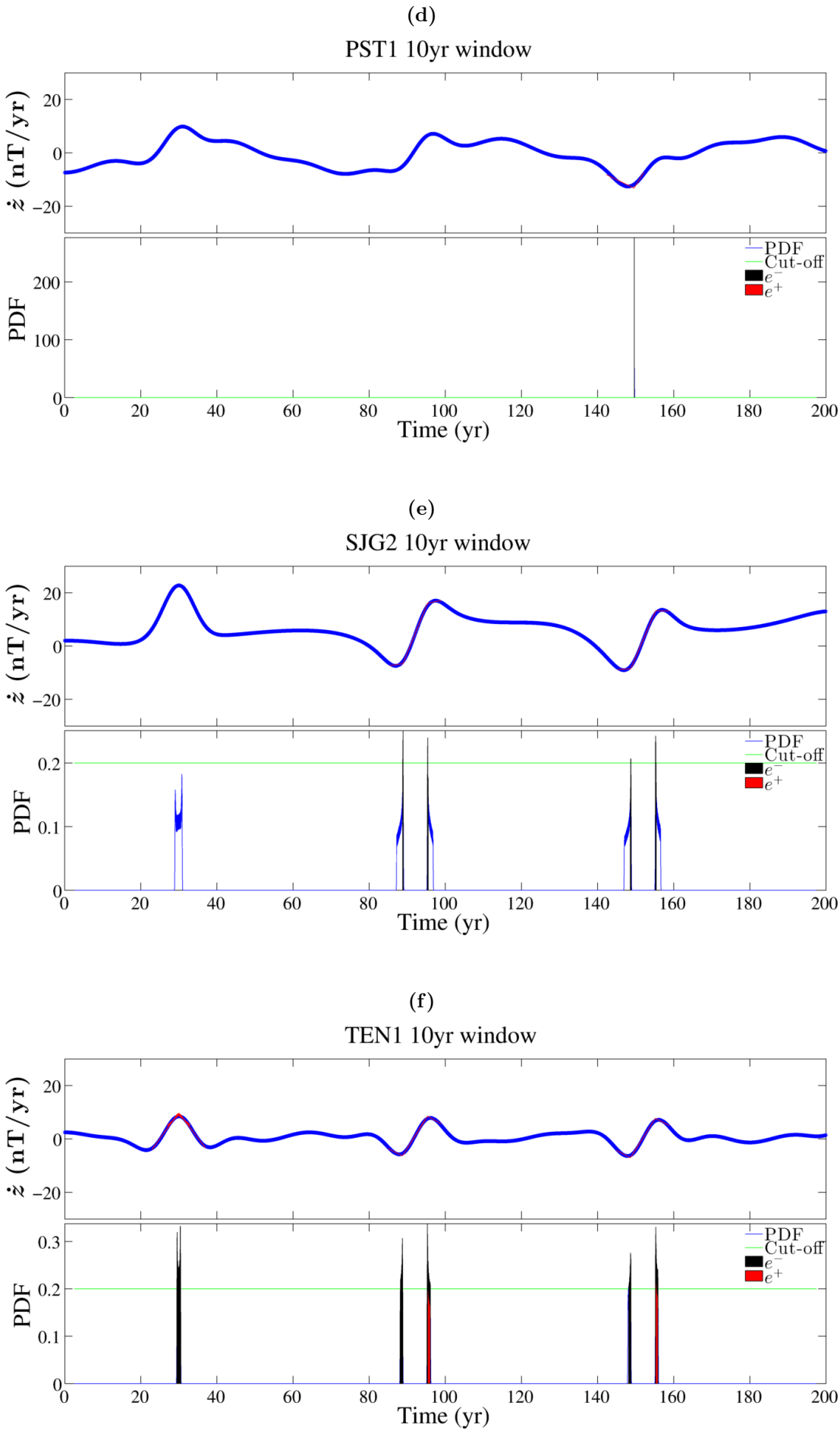

Figure B.13: Jerk identification in the $\dot{z}$ component at Earth's surface with a 10 yr window.

(a)

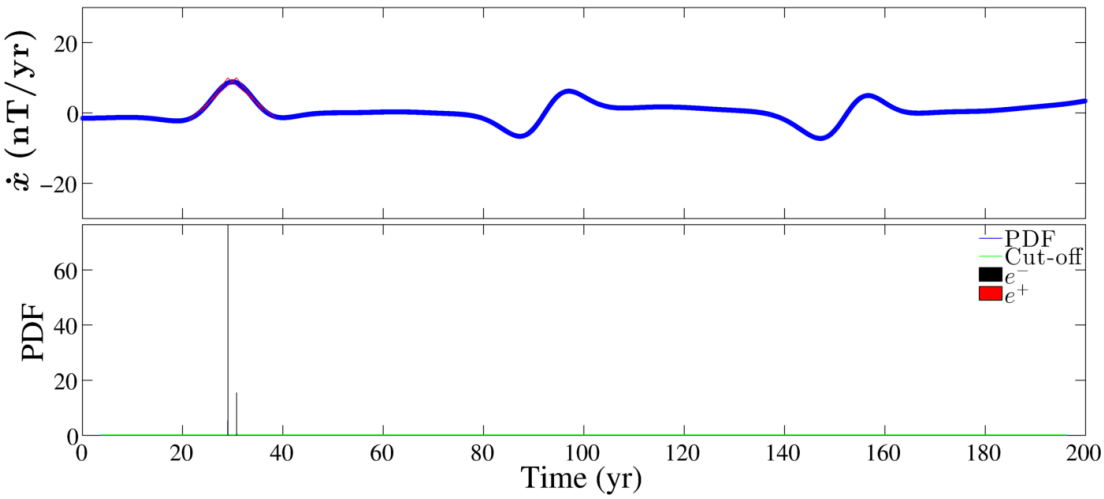
API1 15yr window
$\dot{x}$ (nT/yr)
PDF
Cut-off
e^-
e^+
Time (yr)

(b)

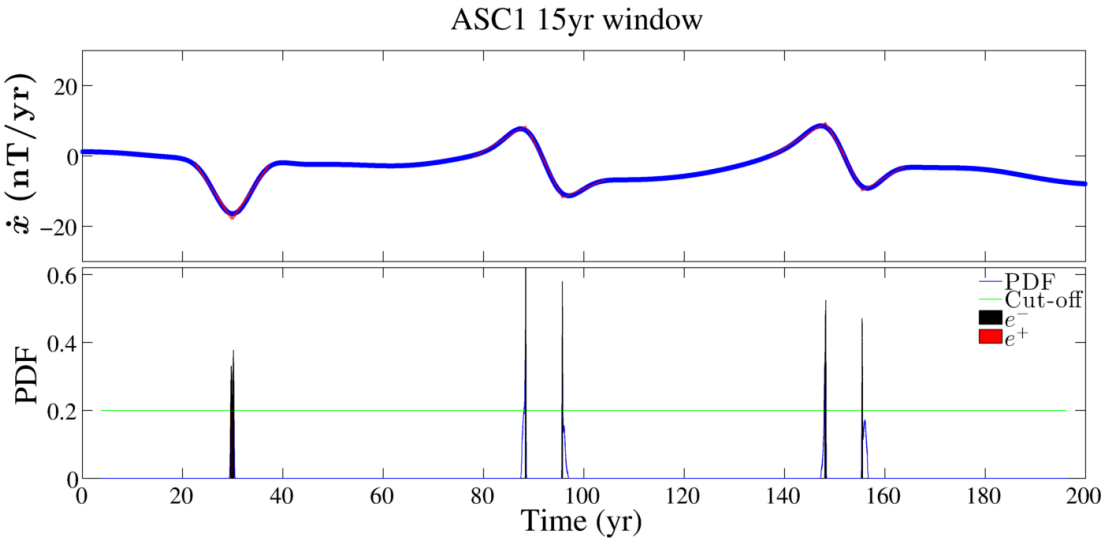
ASC1 15yr window
$\dot{x}$ (nT/yr)
PDF
Cut-off
e^-
e^+
Time (yr)

(c)

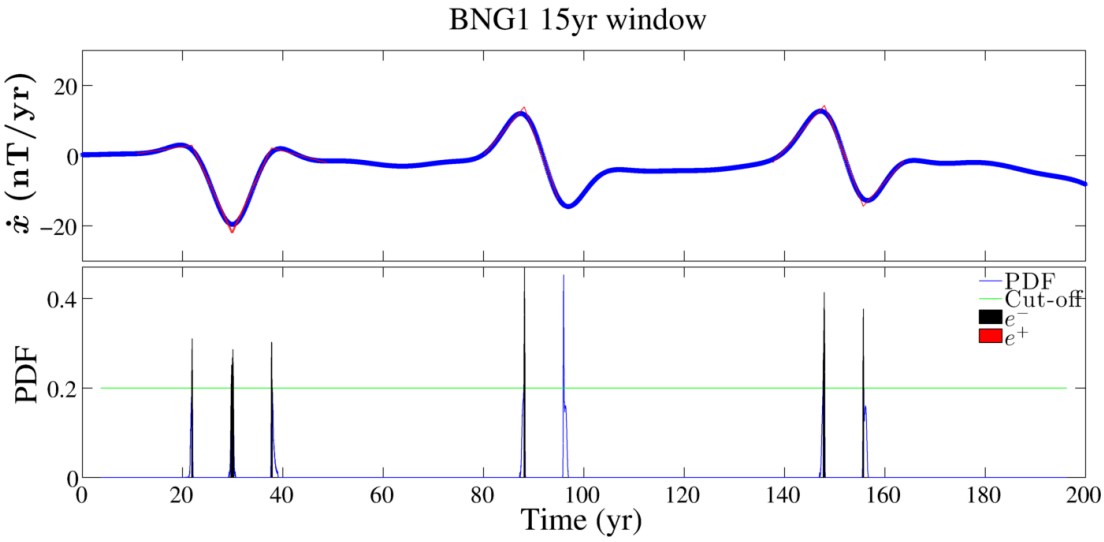
BNG1 15yr window
$\dot{x}$ (nT/yr)
PDF
Cut-off
e^-
e^+
Time (yr)

(a)

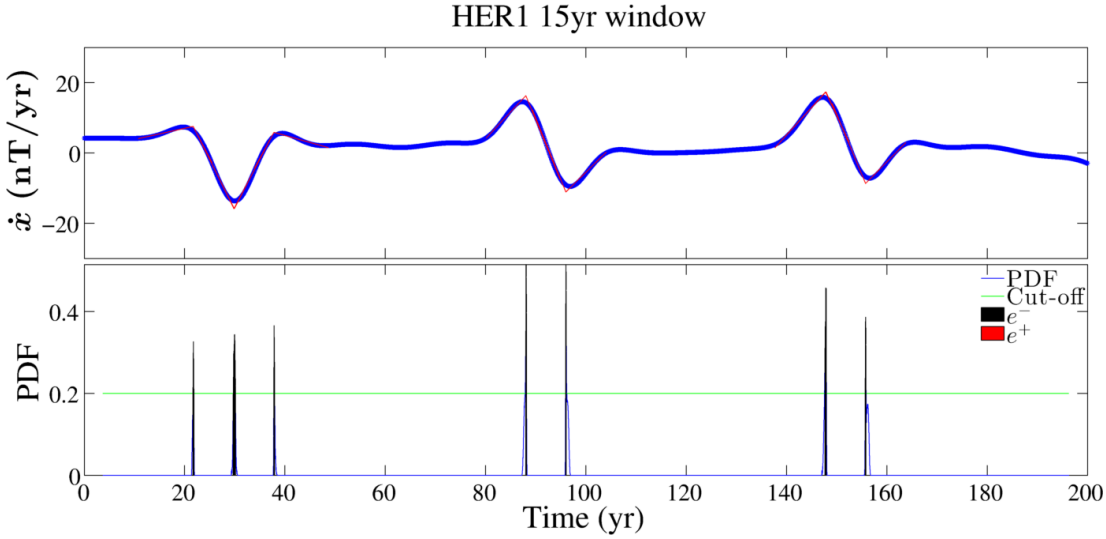
HER1 15yr window
$\dot{x}$ (nT/yr)
PDF
Time (yr)
PDF
Cut-off
e^-
e^+

(b)

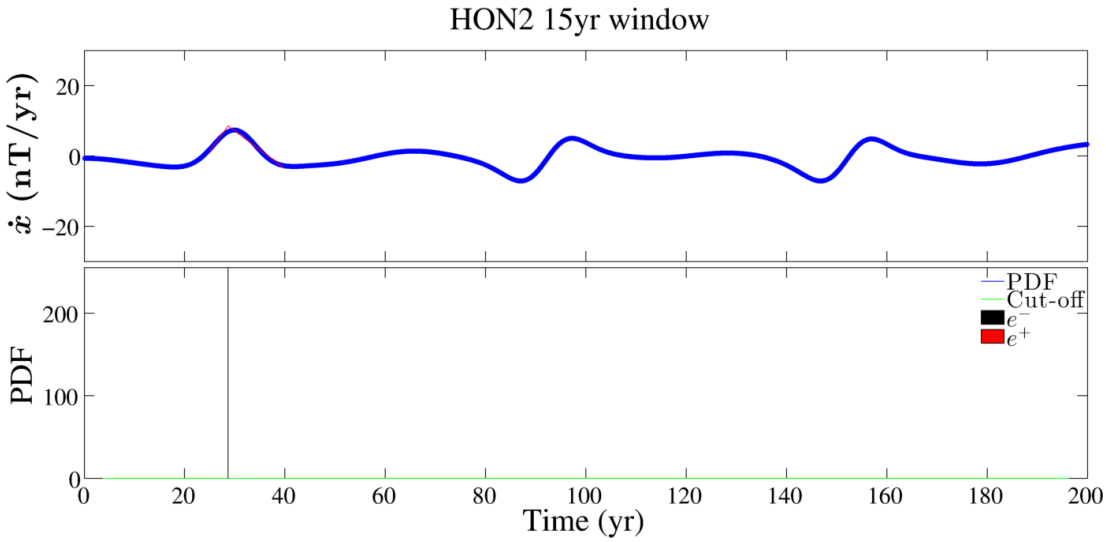
HON2 15yr window
$\dot{x}$ (nT/yr)
PDF
Time (yr)
PDF
Cut-off
e^-
e^+

(c)

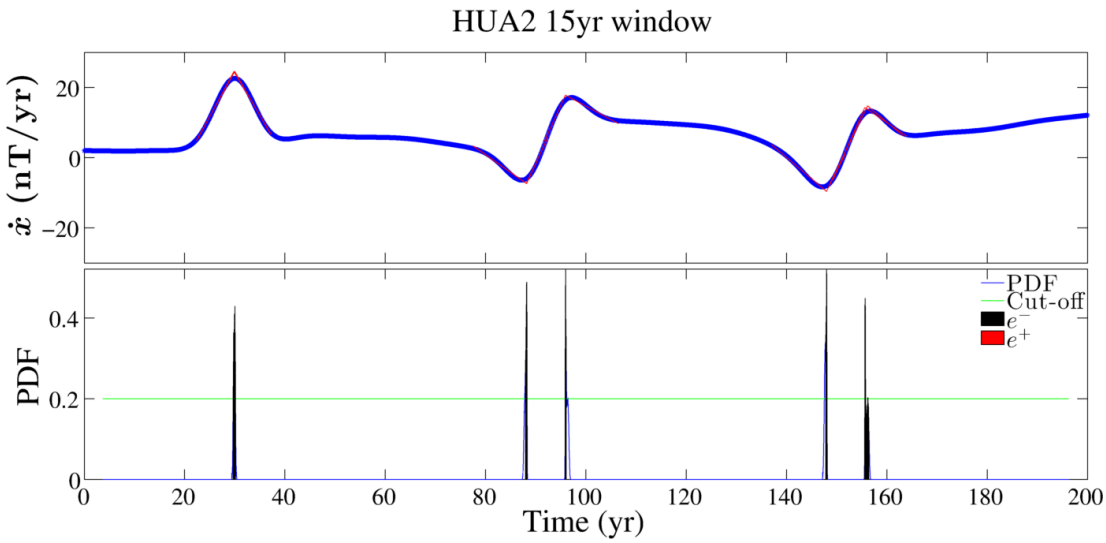
HUA2 15yr window
$\dot{x}$ (nT/yr)
PDF
Time (yr)
PDF
Cut-off
e^-
e^+

(a)

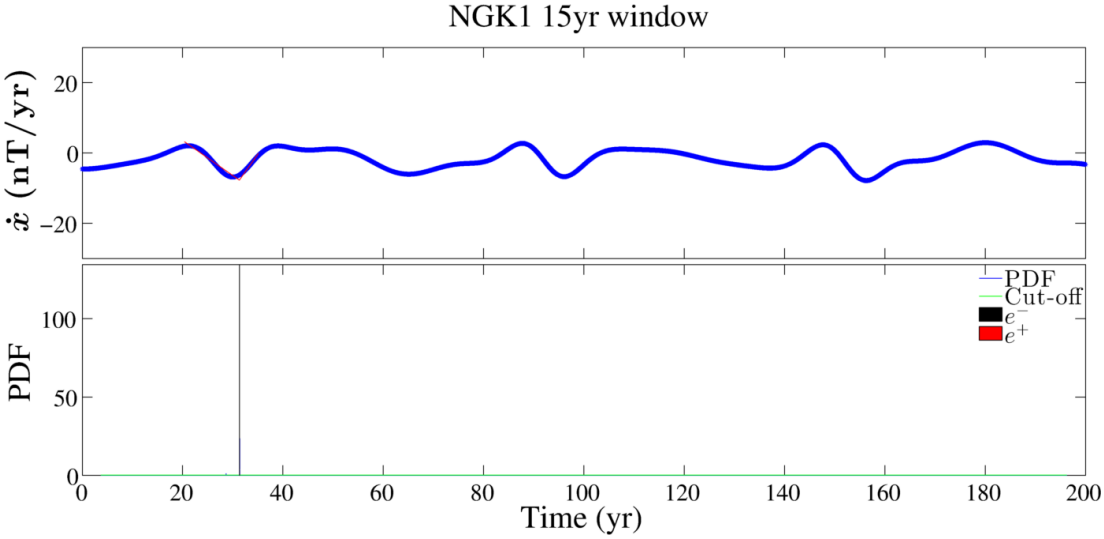
NGK1 15yr window
$\dot{x}$ (nT/yr)
PDF
Cut-off
e^-
e^+
Time (yr)

(b)

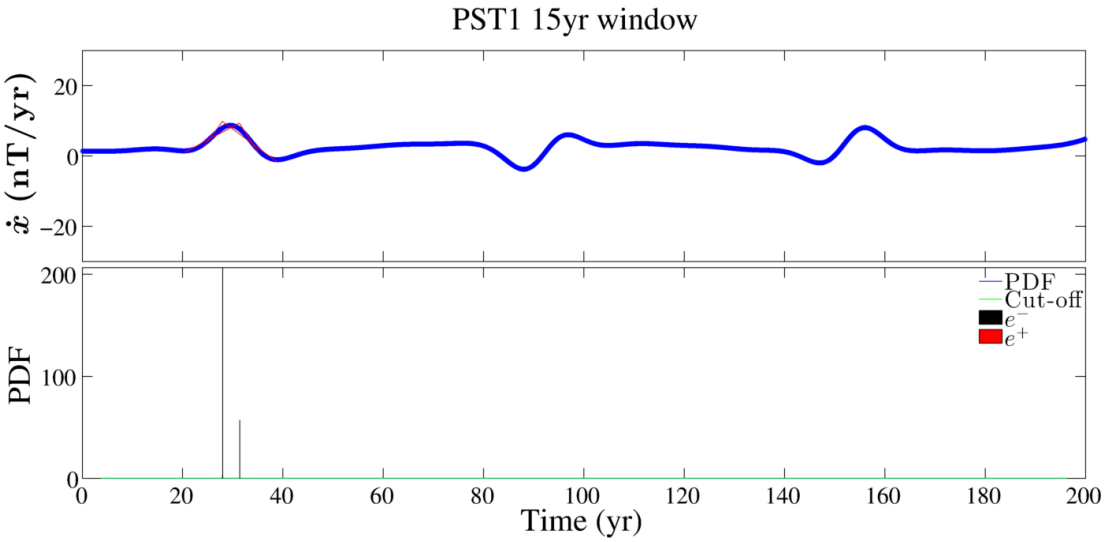
PST1 15yr window
$\dot{x}$ (nT/yr)
PDF
Cut-off
e^-
e^+
Time (yr)

(c)

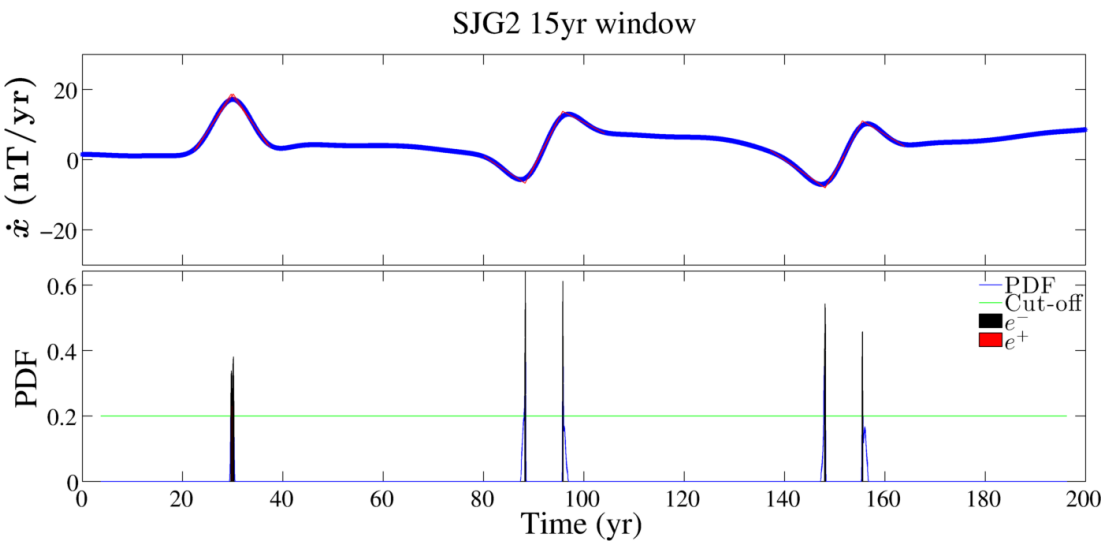
SJG2 15yr window
$\dot{x}$ (nT/yr)
PDF
Cut-off
e^-
e^+
Time (yr)

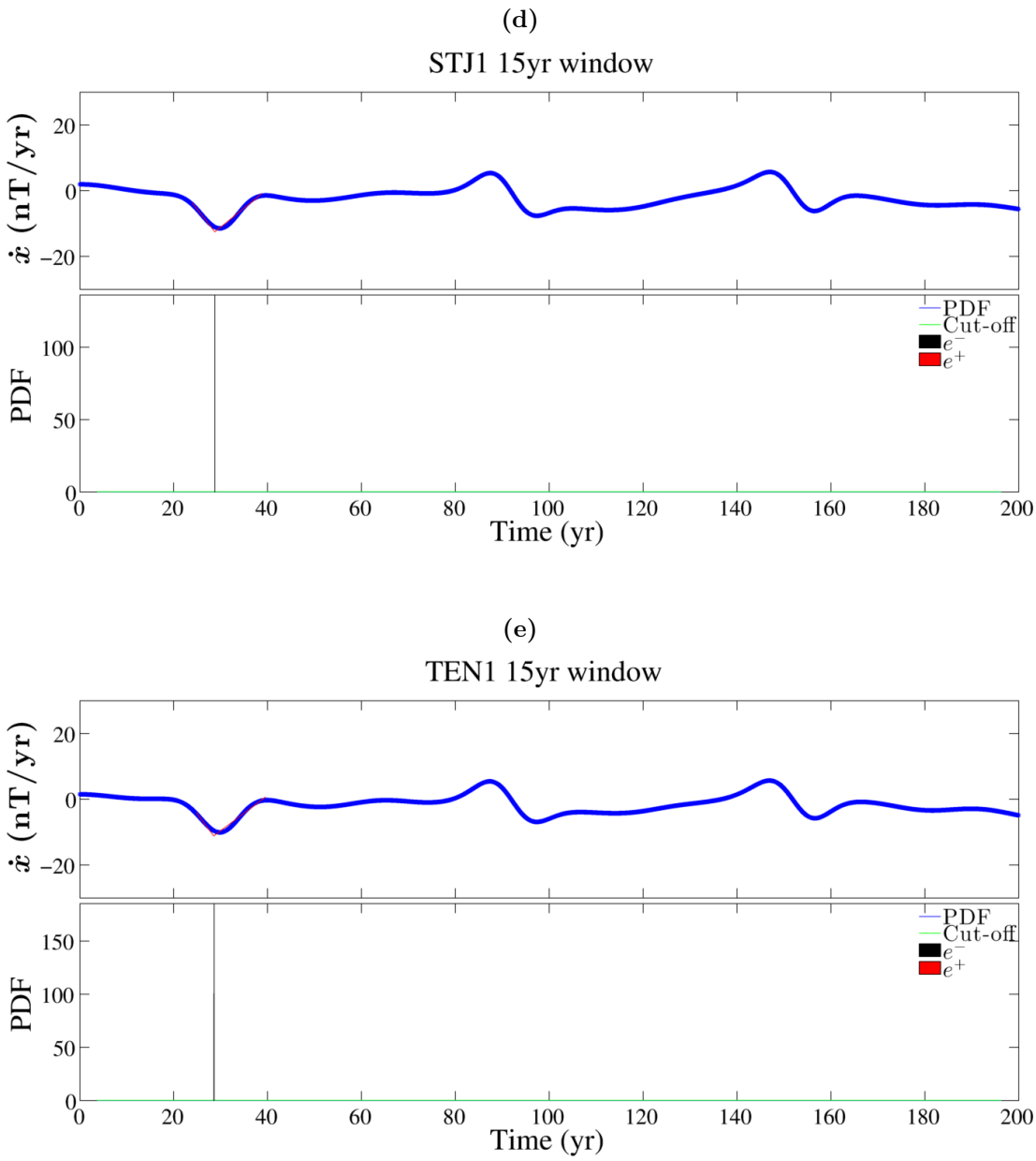

Figure B.16: Jerk identification in the $\dot{x}$ component at Earth's surface with a 15 yr window.

(a)

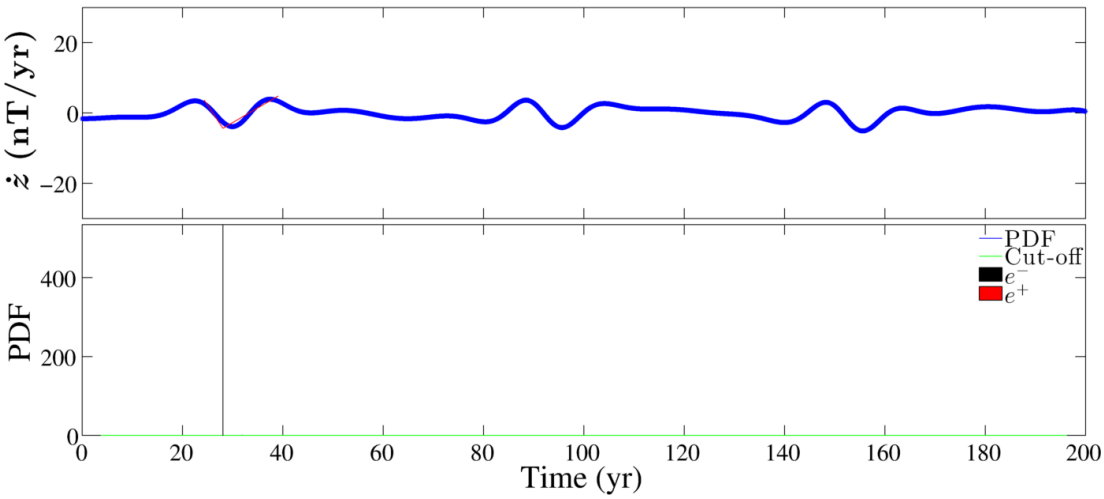
ABG1 15yr window
$\dot{z}$ (nT/yr)
PDF
Cut-off
e^-
e^+
Time (yr)

(b)

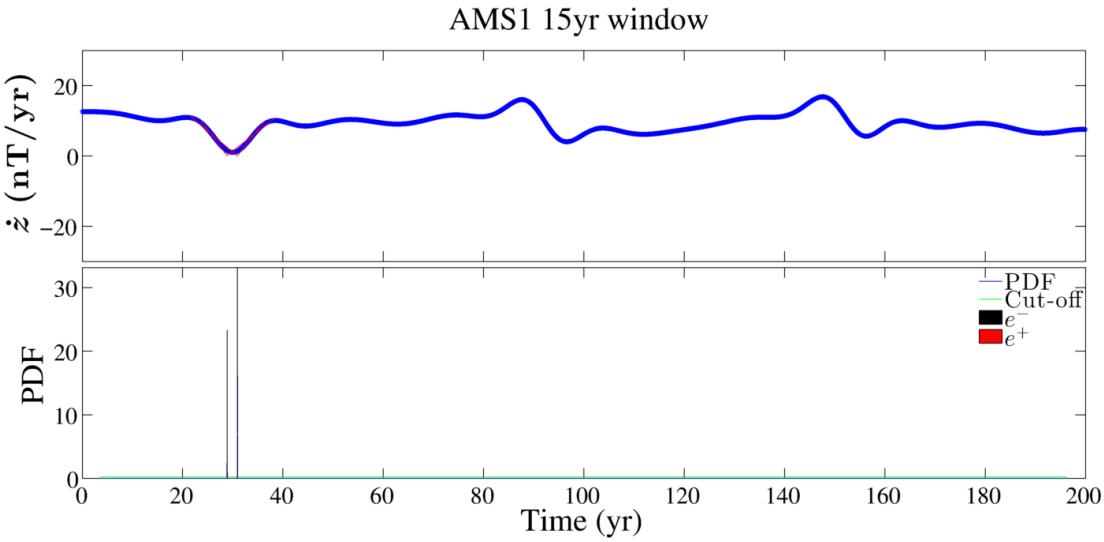
AMS1 15yr window
$\dot{z}$ (nT/yr)
PDF
Cut-off
e^-
e^+
Time (yr)

(c)

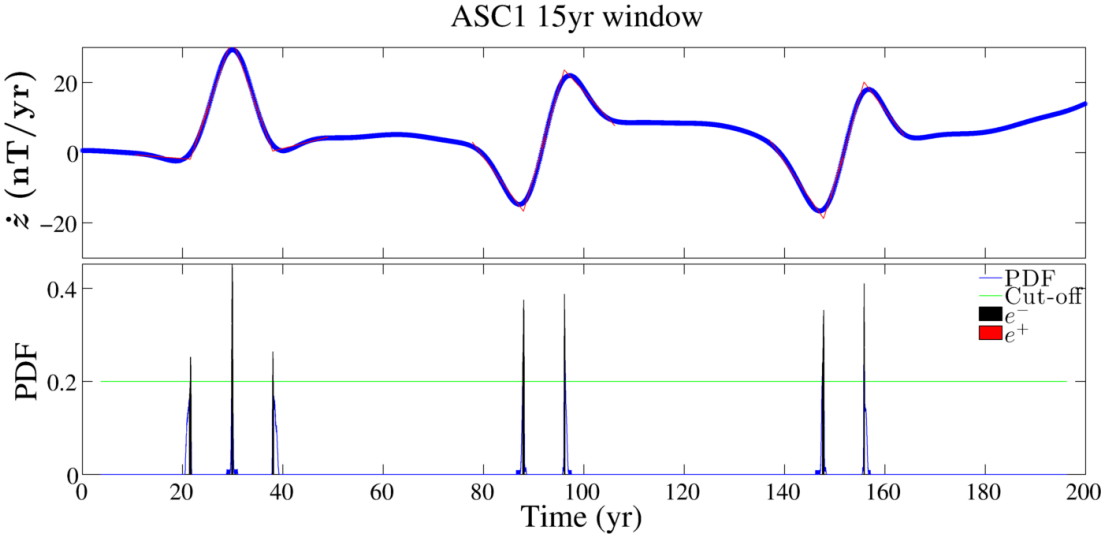
ASC1 15yr window
$\dot{z}$ (nT/yr)
PDF
Cut-off
e^-
e^+
Time (yr)

(a)

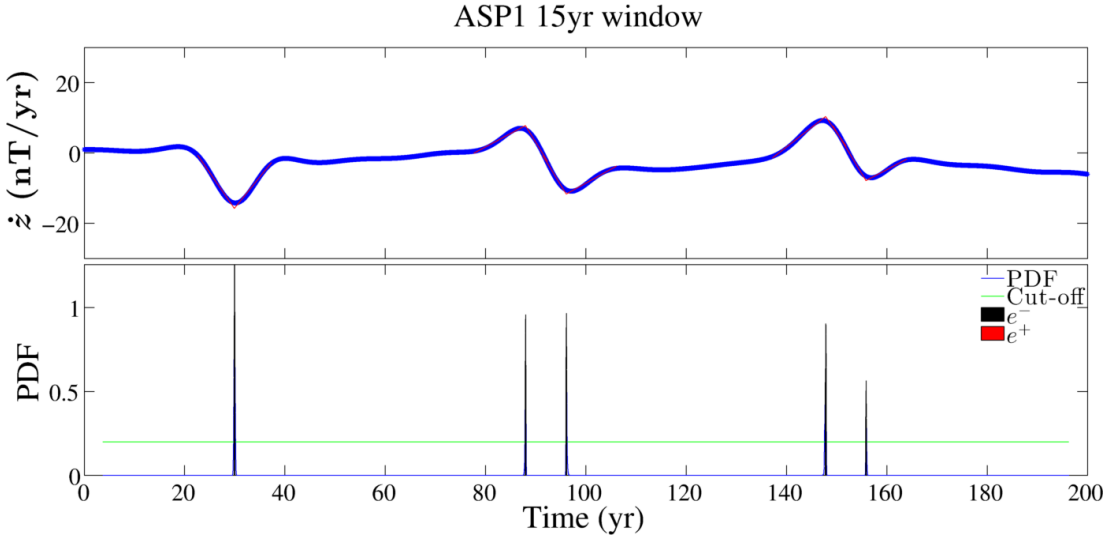
ASP1 15yr window
$\dot{z}$ (nT/yr)
PDF
Cut-off
e^-
e^+
Time (yr)

(b)

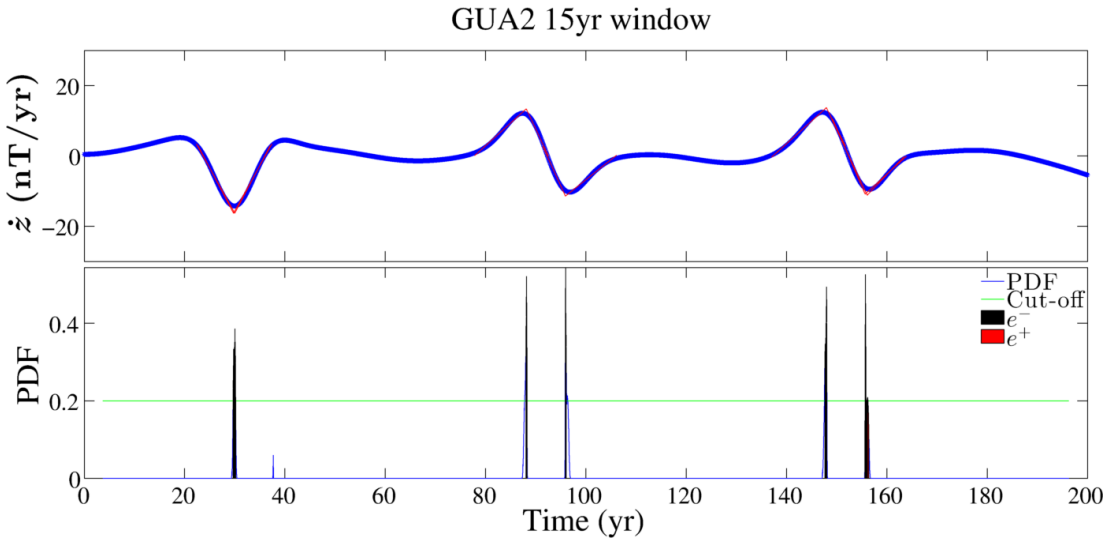
GUA2 15yr window
$\dot{z}$ (nT/yr)
PDF
Cut-off
e^-
e^+
Time (yr)

(c)

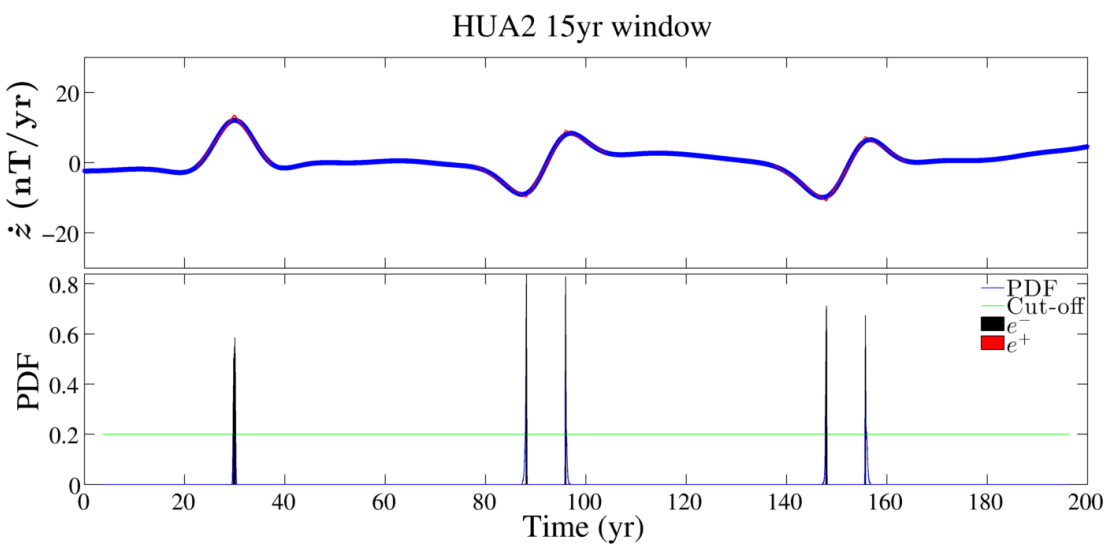
HUA2 15yr window
$\dot{z}$ (nT/yr)
PDF
Cut-off
e^-
e^+
Time (yr)

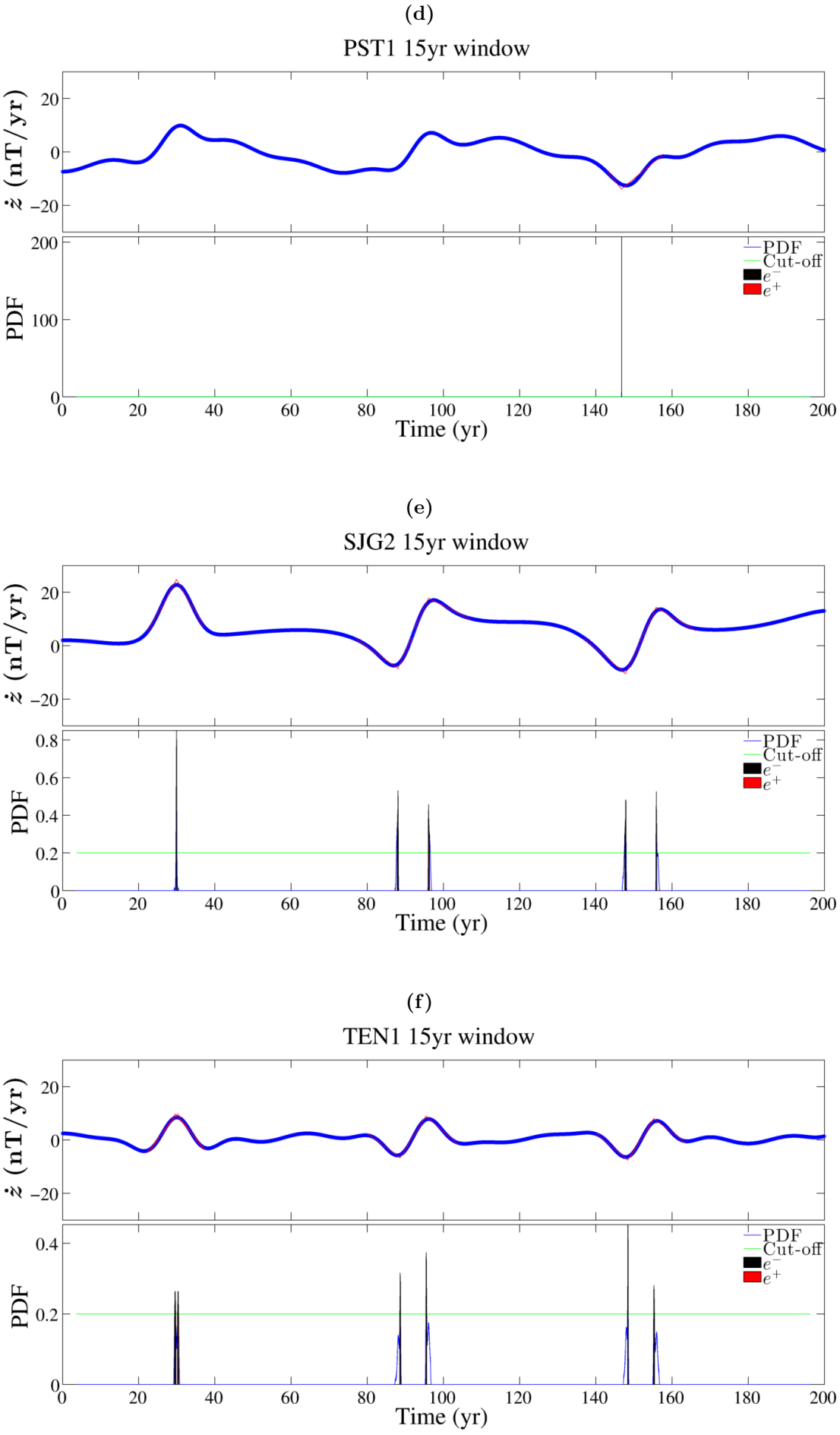

Figure B.18: Jerk identification in the $\dot{z}$ component at Earth's surface with a 15 yr window.

(a)

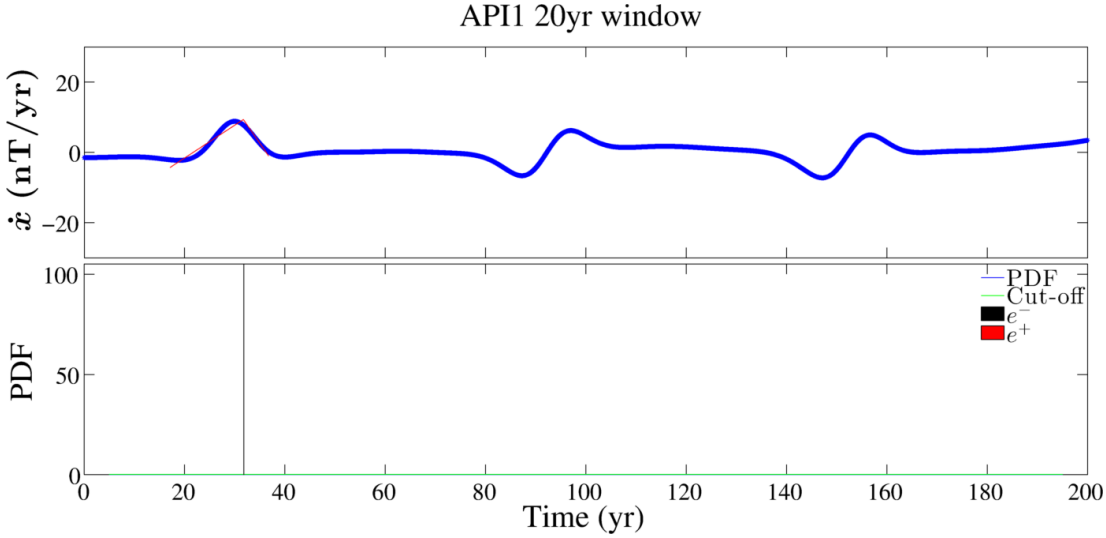
API1 20yr window
$\dot{x}$ (nT/yr)
PDF
Cut-off
e^-
e^+
Time (yr)

(b)

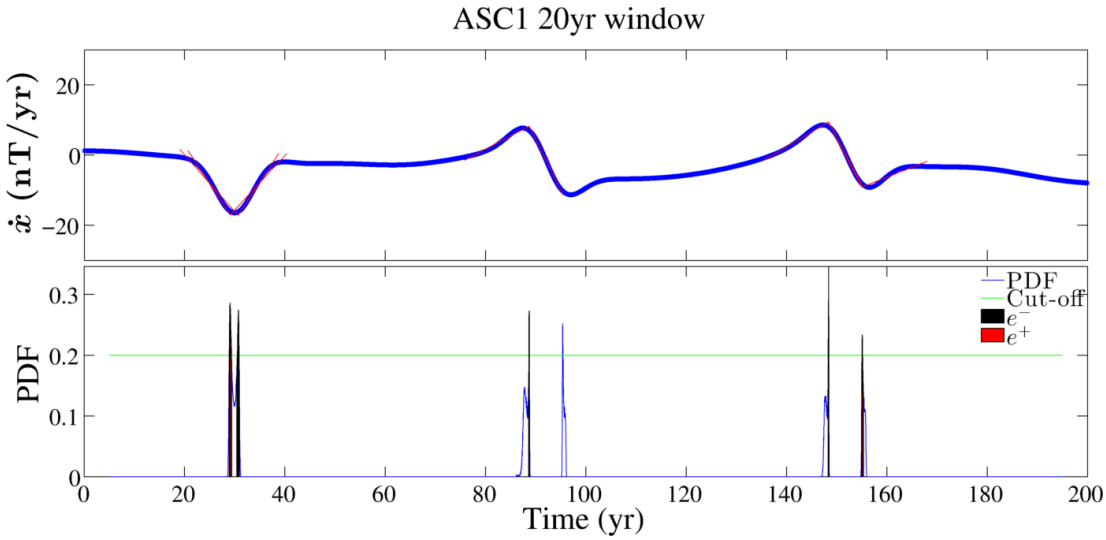
ASC1 20yr window
$\dot{x}$ (nT/yr)
PDF
Cut-off
e^-
e^+
Time (yr)

(c)

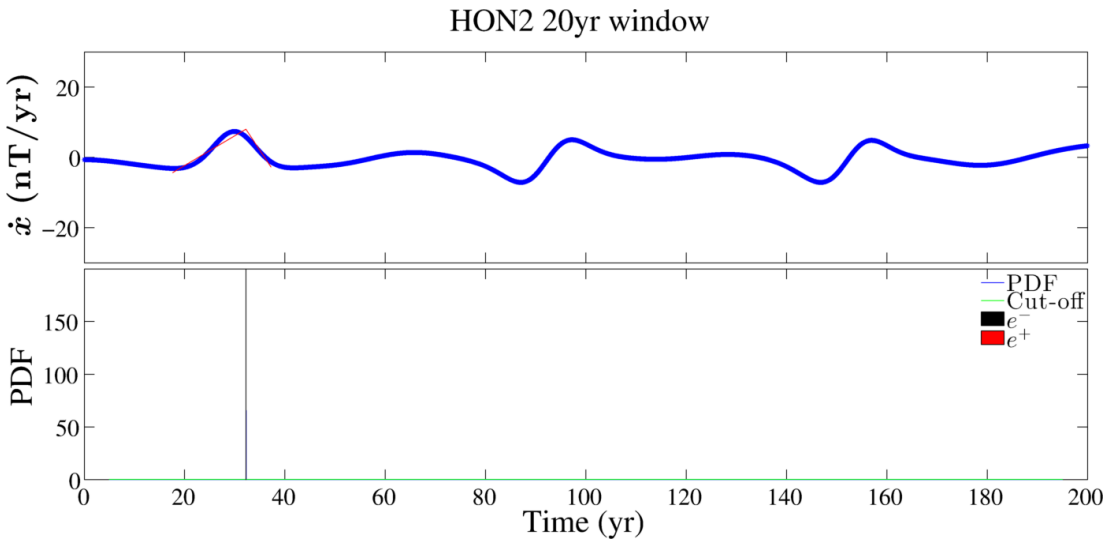
HON2 20yr window
$\dot{x}$ (nT/yr)
PDF
Cut-off
e^-
e^+
Time (yr)

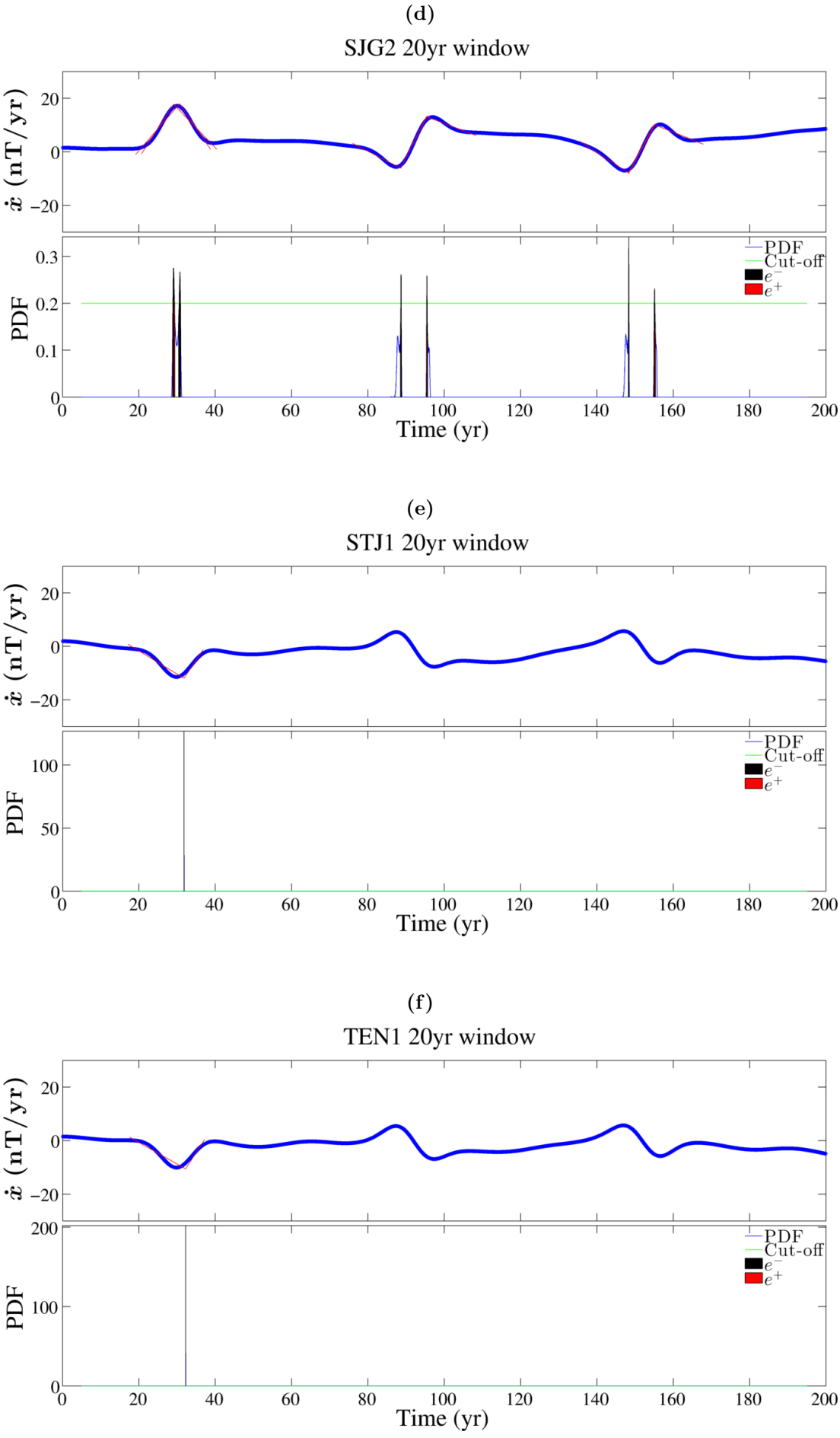

Figure B.19: Jerk identification in the $\dot{x}$ component at Earth's surface with a 20 yr window.

(a)

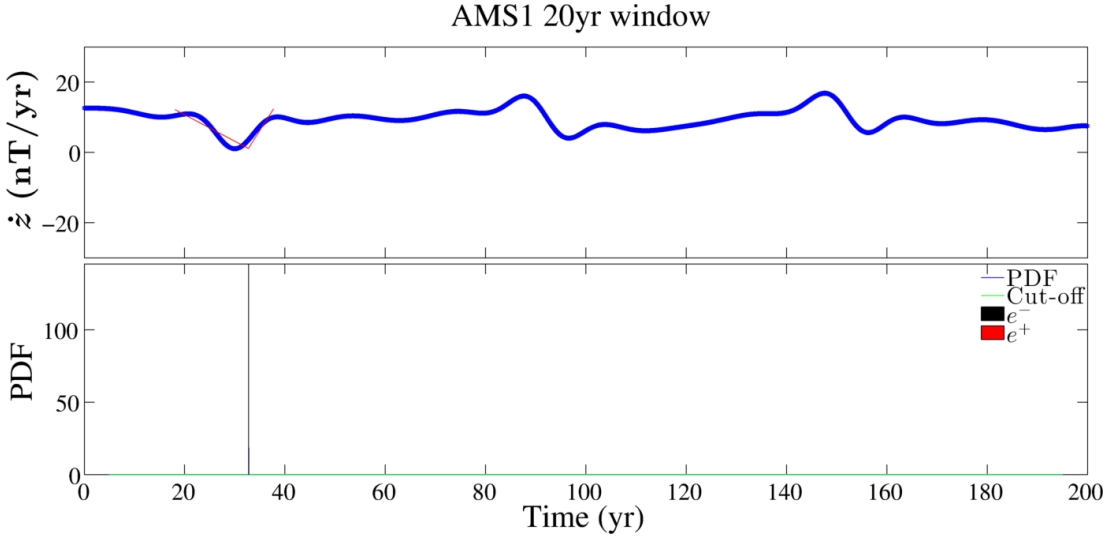
AMS1 20yr window
$\dot{z}$ (nT/yr)
PDF
Cut-off
e^-
e^+
Time (yr)

(b)

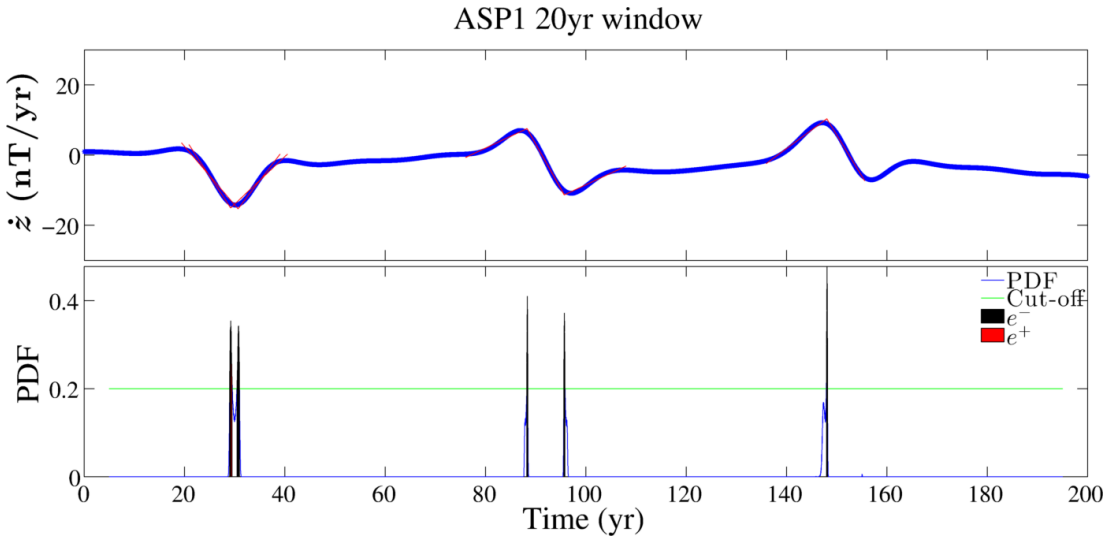
ASP1 20yr window
$\dot{z}$ (nT/yr)
PDF
Cut-off
e^-
e^+
Time (yr)

(c)

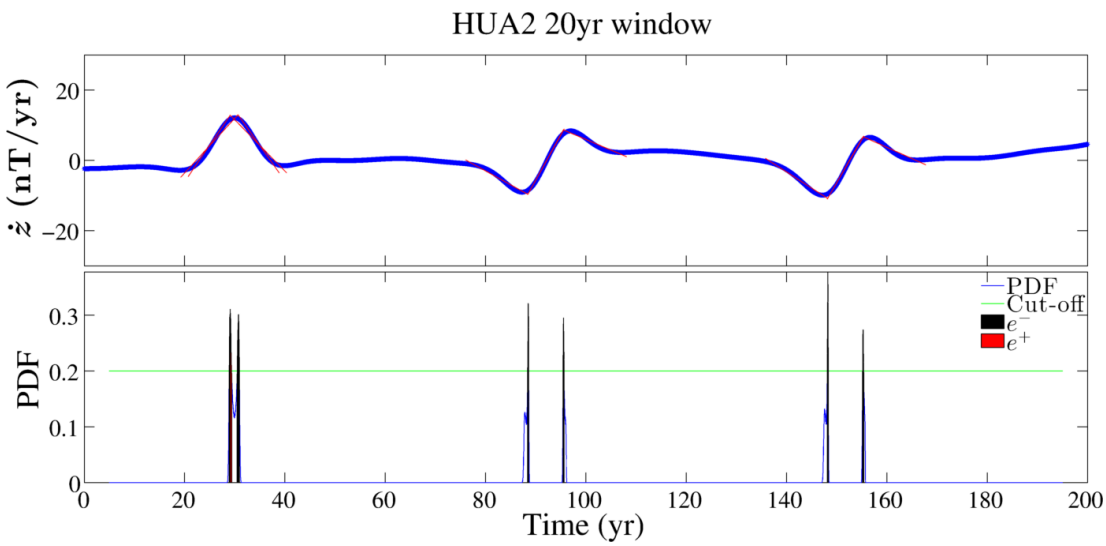
HUA2 20yr window
$\dot{z}$ (nT/yr)
PDF
Cut-off
e^-
e^+
Time (yr)

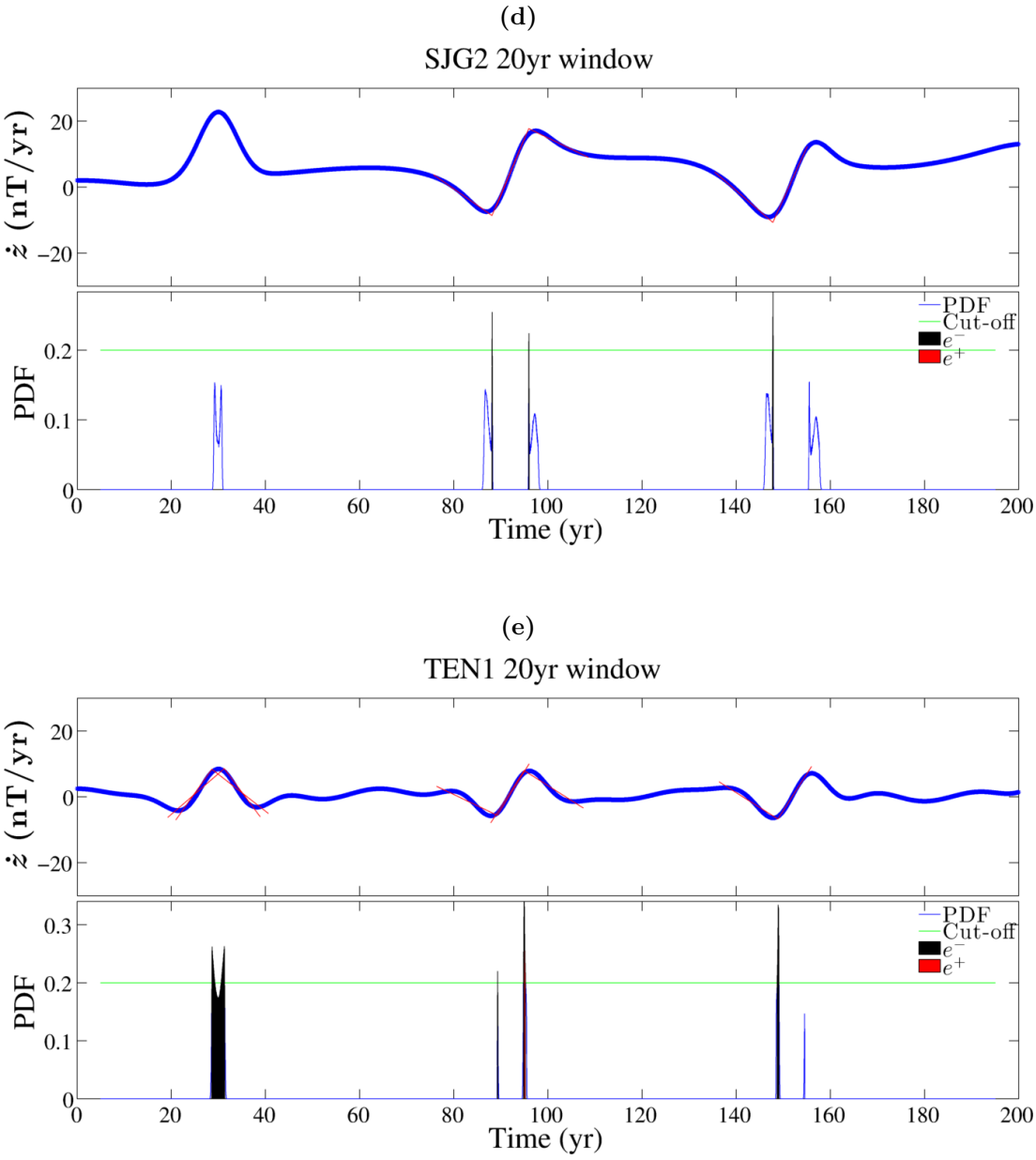

Figure B.20: Jerk identification in the $\dot{z}$ component at Earth's surface with a 20 yr window.